ABSTRACT

Title of dissertation: A MEASUREMENT OF THE STRANGE QUARK CONTRIBUTIONS TO THE ELECTROMAGNETIC FORM FACTORS OF THE NUCLEON

Jianglai Liu, Doctor of Philosophy, 2006

Dissertation directed by: Professor Elizabeth J. Beise
Department of Physics

G^0 is a parity violating electron scattering program at the Thomas Jefferson National Accelerator Facility, and its forward angle measurement is reported in this thesis. In this experiment, parity violating asymmetries of elastic electron-proton scattering were measured over a range of four-momentum transfer from 0.12 to 1.0 $(\mathrm{GeV/c})^2$. From these asymmetries, linear combinations of the strange electric and magnetic form factors of the nucleon, $G_E^s + \eta G_M^s$, are extracted over the same kinematic range. These results, combined with existing data from other experiments, indicate that both G_E^s and G_M^s are non-zero and dependent on the four-momentum transfer, which imply non-trivial strange quark contributions to the low energy electromagnetic properties of the nucleon.

A MEASUREMENT OF THE STRANGE QUARK CONTRIBUTIONS TO THE ELECTROMAGNETIC FORM FACTORS OF THE NUCLEON

by

Jianglai Liu

Dissertation submitted to the Faculty of the Graduate School of the
University of Maryland, College Park in partial fulfillment
of the requirements for the degree of
Doctor of Philosophy
2006

Advisory Committee:

Professor Elizabeth J. Beise, Chair/Advisor
Doctor Herbert Breuer
Professor Xiangdong Ji
Professor Alice C. Mignerey
Professor Philip G. Roos

Dedication

To the loving memory of my grandfather

Zhicheng Liu

1919-2000

ACKNOWLEDGMENTS

I am indebted to so many people that have helped me complete this Ph.D. dissertation. I would like to begin by thanking my advisor, Betsy Beise, who has been a dedicated teacher and mentor to my career, as well as a supportive friend and a truly respectful person. I admire Betsy for being an honest and unbiased physicist, from whom I have learned not only physics, but also the right attitude towards scientific research. Over the years, Betsy has given me freedom and trust to work on my own, and always takes time to offer me guidance when I need it. Besides being an achieved leader in the field, Betsy is also a hands-on experimenter, who helped me debugging my incomprehensible Fortran programs in my early days, took my share of overnight G^0 shifts (although being an unusual early riser!), and helped me moving the ladder and lead blocks when we installed the LUMI detectors. I am extremely fortunate to be Betsy's student.

My special regards also go to Doug Beck, the spokesman of the G^0 experiment, who gave me the opportunity, trust and supports to work on this challenging and rewarding project for my dissertation. Doug's vision and his exceptional leadership have been the primary driving force to push this project along over the years, and his views on physics is truly inspirational. Although being a busy "big boss", Doug worked very closely with me on a few difficult experimental problems, and I vividly recall that so many times Doug saved me out of frustration when I had run out of things to try. Although not officially, I regard Doug as my coadivsor.

I acknowledge all my defense committee members: Betsy Beise, Herbert Breuer, Xiangdong Ji, Alice Mignerey and Phil Roos for taking the time reading this thesis. I particularly appreciate Betsy, Herbert and Phil's tremendous efforts of turning this lengthy writing full of language errors into a useful document.

The people in the experimental nucleon physics group at Maryland are a spe-

cial group of people that make my experience both educational and enjoyable. The faculty members, Betsy Beise, Herbert Breuer, George Chang, Nick Chant, Jim Kelly and Phil Roos are all wonderful people to interact with. I am grateful to Phil, who recruited me into the group after I had worked as his teaching assistant for a semester. Phil's intuitive way of thinking about physics always reminds me "not to use fancy mathematics". The progress that G^0 has made is indispensable from Phil's oversight as the deputy spokesman. I thank George for driving me to Jefferson Lab during my first summer in the group, and introduced the gigantic Hall A spectrometers to me, which got me excited about the field. I particularly wish to thank Herbert for teaching me the experimental aspects of nuclear physics. From working on the "paddle" detector in the dark room when I just got started, to the long night-time discussions about the background correction, Herbert's meticulous attitude towards physics sets a good example that big science is made by the understanding of every little detail. I am grateful to our group secretary, Judy Myrick, who always keeps everything on track and saved my expenses in a few occasions. I am privileged to have my years in the group overlapping with former and present graduate students Kenneth Gustafsson, Damon Spayde, Nikolai Savvinov, Tanja Horn, Chad Galley, Colleen Ellis and Jon Miller, and undergraduates Mary Claire Herda, Kristin Kiriluk, Ken Rossato, Erick Andrade and Andrew Parker. I thank my seniors, Kenneth and Damon, who were very helpful and patient to help me get on track in my early days, and Damon in particular (who later became an Illinois postdoc on G^0) for helping me to learn C++, ROOT and SQL. My appreciations also go to Tanja, who helped by taking so many G^0 shifts, and had been a good officemate when I was at the Jefferson Lab.

My three years at the Jefferson Lab is truly memorable. I thank all the people in the lab that I have directly or indirectly interact with. Especially, I would like to thank two postdoctoral associates, Julie Roche and Paul King. Julie always has time in her busy schedule for a discussion with me, and keeps reminding me to be careful and thorough when dealing with a problem. Her excellent job for being the scout leader for a group of wondering graduate students is highly acknowledged. Paul,

who was a Maryland postdoc, had helped me in every little step in my development. I particularly thank him for teaching me the analysis software and how to beat the linux system into submission. I also thank Paul and Julie for inviting me over for dinners a number of times. The Hall C staff members, under the leadership of Rolf Ent, have offered crucial support to the G^0 experiment and educated me many "survival skills". I thank Allison Lung for her tireless management of the project, Steve Wood for helping me with the computers, Dave Mack for allowing me to work in the detector huts of the HMS and SOS, and teaching me about the phototubes, Dave Gaskell for lots of interesting physics discussions and for sharing a common "student" language, Greg Smith for his help on my LUMI project, Bill Vulcan for advices on the LUMIs and loaning me electronics, Roger Carlini for a few long and interesting debates, and Walter Kellner and his crew for helping me getting the LUMI detectors onto the beam pipe.

The Jefferson Lab management and the accelerator group have done an exceptional job of keeping the experiment on schedule, providing the infrastructure, and delivering high quality G^0 beam. I thank them for their hard and fruitful work.

The G^0 collaboration is made up by a group of extremely talented physicists. The success of the forward angle measurement is truly due to the collective efforts from the entire collaboration. Here I would like to present my most sincere acknowledgment to all collaboration members. Besides those who I have mentioned, my special thanks also go to Wolgang Korsch, for getting me started on the "formidable" G^0 analyzer, and for always replying to my email questions within an hour, and Mark Pitt for teaching me about the "parity" beam and the LUMIs, and calming me down in a few occasions when I was swearing out of frustration in the counting room. I would like to express my deep regards to Illinois magnet experts (Steve Williamson, Damon Spayde, Kaz Nakahara, et al.), and the target "black belts" (Greg Smith, Silviu Covrig, Lars Hannelius, et al.), who lost so many nights of sleep to maintain the normal operation of these key components, and forgave me when I phoned from the counting room 3 am in the morning asking for help. I am also grateful to Dave Armstrong, Angela Biselli, Christophe Furget, Larry Lee,

Jeff Martin, Jean-Sebastien Real, and Steve Wells for insightful discussions. I had a fun experience working with Dominique Marchand, who was always patient and thorough in explaining to me the French electronics. I enjoyed sharing an office with Retief Neveling for half a year, and will always remember our beer nights and biking trips. I acknowledge Klaus Grimm for helping me with the LUMI detectors, offering me his prototype of the famous "goat++" code, and I enjoyed the dinners at he and Sabine's house. I also would like to thank Russel Clark and Brian Quinn for teaching me about electronic deadtime, and Brian in particular for his tireless email replies (usually at midnights), and his "peculiar" taste of humor. I appreciate Bob McKeown's careful reading of my overlong notes, and his helpful suggestions before we publicized the results. I thank Serge Kox for reminding me that there is always different approaches to solving a problem, and for bringing jokes, laughs and the monstrous whipping sounds into the counting room. I admire Jacques Arvieux for his Marathon running, and being the most senior run coordinate in the lab at a very crucial (and extended) period of the experiment. This list goes on and on, ..., and I better stop here to avoid having this acknowledgment longer than the main text. I apologize to any collaborator whose name I have not mentioned, particularly those who have been "sliently" pushing the backward experiment in these years, and please be assured that I do highly appreciate your effort and help.

Be patient, my fellow students, I have not forgot you guys. The "unrested young guys" not only contribute tremendous amount to this project, but also make my journey a very fun one. I congratulate Silviu Covrig, Hayko Guler, Jeff Secrest, Guillaume Batigne and Benoit Guillon for being the "lucky ones", who have somehow got out from the "slavery" earlier than me, and I wish the best to the doctor-to-bes: Stephanie Bailey, Lars Hannelius, Tanja Horn, Ameya Kolarkar, Bryan Moffit, Mat Muether, Kaz Nakahara, Vince Sulkosky, and Sarah Phillips. I particularly acknowledge Kaz ("SUNK") Nakahara, for his heroic contribution to the G^0 beam, which was absolutely crucial to make this experiment work, and for his amusing anecdotes during the experiment, well, I better not to make them public. I like to thank Jeff's interesting stories and Silviu's unique "philosophical" speeches, which

always make me smile even during the most stressful days. I thank Lars and Benoit for always coming up with good points in discussions, and not making fun of my desperate swears. I appreciate Sarah for feeding colors to our student lives, and I am sure that everyone enjoys the dinner-and-movie night at Sarah's place. Numerous undergraduates worked on G^0 during the summers and filled up the shifts; their efforts are highly appreciated. Thank you all, guys, and keep up the good work!

I thank Maryland group's NSF fund which has made me survive during these years. I also acknowledge the fellowship support from Jefferson Lab/SURA during my stay at the Jefferson Lab.

I can not imagine what my life might be without my Chinese physics friends back home and in the US. I thank my college buddies Yi Yang's and Chu Nie's long distance support during these years that we are apart. I am grateful to my friends at Maryland, Yuanzhen Chen, Jianyang Li, Chengang Tao, Bo Xu, Chi Zhang and Lubo Zhou, for sharing the pain of the E&M, QFT and GR classes, for keeping my Chinese more fluent than my stuttering English, for dinning with me at the China Cafe everyday, and for drinking beer and playing squash with me whenever I feel like a stress relief. I also feel obliged to thank the storekeepers of the China Cafe, Hailin and Linda, for always bringing me an extra soup and snacks.

Finally, I wish I could use appropriate words to express my gratitude to my family. I thank my brother Jianghuai, who, as a fellow scientist, shares the joys in my work, and always brings his professional encouragement when I get frustrated, and as an elder brother and my best friend, gives me selfless love and support. I thank my dear parents, Yingsheng and Chun, and my grandparents in Nanjing and Shanghai, for their unconditional love and care throughout my entire life. Sadly, in my first year at Maryland, my grandfather Zhicheng passed away. I dedicate this thesis to the memory of him, and wish that he could see this small achievement of his grandson from the other world with a proud smile, and he would know that his grandson has been trying to be a useful, honest and respectful person like him.

TABLE OF CONTENTS

LIST OF TABLES

LIST OF FIGURES

Chapter 1

Physics Motivation

1.1 Introduction

"Strangeness" was introduced in the 1950's by Gell-Mann and Nishijima as a new quantum number besides isospin that describes the strong interaction [Gel55, Nis53]. A larger symmetry, SU(3), was postulated between nucleons and hyperons, as well as between mesons. As a by-product, the naive quark model was developed [Gel64]. In this model, there are three flavors of quarks, u, d and s, which form an SU(3) symmetric flavor space. All baryons and mesons are made up from these constituents. Nucleons are among those "strangeless" particles in the sense that their net strangeness quantum numbers are zero. Deep inelastic scattering (DIS) experiments at SLAC in the late 60s and early 70s provided strong experimental evidence that there exist point-like Dirac particles (partons or quarks) inside the nucleons. Quantum Chromodynamics (QCD) was developed soon after to describe the interaction between quarks, which introduces a gauge color force between quarks carried by gluons. The theory turned out to be a great success. By now QCD has become the only non-trivial theory for the strong interaction, and it is a part of the "Standard Model" (SM) for elementary particle physics. In the SM, quarks have six different flavors: u (up), d (down), s (strange), c (charm), b (beauty) and t (top), in order of increasing mass. For low energy hadron properties, only u, d and s quarks are relevant.

From the perspective of QCD, nucleons are made up of "valence quarks" (u and d as in the naive quark picture) and the so-called QCD vacuum, which is formed by "sea quarks" ($\bar{u}u$, $\bar{d}d$, $\bar{s}s$,...) and gluons. Generally, it is difficult to distinguish the sea u and d quark contributions from their valence counterparts. On the other hand, the s quarks in the nucleon are completely from the sea. Although the net strangeness of nucleons is zero, it could have a non-uniform space-time distribution,

just as the charge distribution inside the neutron.

The significance of the QCD vacuum can be appreciated by noting the analogous (perturbative) vacuum phenomena in the quantum electrodynamics (QED), such as the anomalous magnetic moment of electron or muon $(g-2)$, and the "Lamb shift" in the hydrogen atom [HM84], which played crucial roles in the development of QED. For the nucleon strangeness, the QED analogy would be a photon fluctuating into a $\mu^+\mu^-$ pair in the hydrogen atom, of which the contribution would be further suppressed compared to the already tiny Lamb shift. However, due to the non-perturbative nature of the color force, such vacuum fluctuations in QCD could be significant, and they remain challenging to be calculated reliably, despite decades of efforts from the theoreticians.

1.2 Different Aspects of the Strangeness Content of Nucleons

Experimental evidence for the contribution of strange quarks to nucleon[†] structure will be briefly reviewed in this section. Despite the difficulty and model dependence in interpreting these experimental results, the latter have triggered great theoretical and experimental interest in the field.

1.2.1 Strangeness Contribution to the Nucleon's Longitudinal Momentum

The existence of s quark flavor in the nucleon can be established via deep inelastic neutrino-nucleon scattering. The idea is that the charged current weak interaction between muon neutrinos ν_μ and quarks are predominantly sensitive to the s quarks. The experimental observables are defined in terms of quark distribution functions. In the so-called infinite momentum frame (in which time dilation has slowed down the interaction between quarks so that they would scatter incoherently),

[†]Although we discuss the structure of nucleons in general, most of the observations that have been made are limited to protons only, since a free neutron target does not exist in nature. Charge symmetry is assumed so the strangeness content of the neutron is the same as that of the proton (see Eqn. 2.26).

the (unpolarized) quark distribution function $q_i(x)$ is defined as the number density of finding quark flavor i carrying a fraction of x of the nucleon momentum [†]. From the measurements of the NuTeV experiment at the Fermi Lab, the ratio of the total fraction of the momentum of the nucleon carried by strange sea quarks (s and $\bar{s}$) to that by the "non-strange" sea was extracted to be [Ada99]

$$\frac{1}{2}\frac{\int_0^1 s(x)+\bar{s}(x)dx}{\int_0^1 \bar{u}(x)+\bar{d}(x)dx} = 0.42 \pm 0.07 \pm 0.06\,, \tag{1.1}$$

at $Q^2 = 16$ (GeV/c)^2. It was also found that $s(x)(\bar{s}(x))$ is significant at $x < 0.1$, and the total fraction of the nucleon momentum carried by strange (anti-strange) quarks, is roughly 2%. Therefore, this result is an unambiguous observation of the existence of the strange sea in the nucleon. However the momentum fraction in the parton model is theoretically difficult to connect with ordinary observables.

1.2.2 The Scalar Matrix Element and Its Contribution to the Nucleon Mass

In the language of quantum mechanics, the mass of the nucleon is given by the matrix element $M_N = \langle N|\mathcal{H}_{QCD}|N\rangle$, where $\mathcal{H}_{QCD}$ is the QCD Hamiltonian of a nucleon and $|N\rangle$ is the (same) initial and final state of the nucleon (here the normalization that $\langle N|N\rangle = 1$ is taken). The quark mass term in $\mathcal{H}_{QCD}$ is $\sum_i m_i\bar{q}_i q_i$, in which m_i is the Dirac mass of quark flavor i. In the chiral limit, in which all quark masses are zero, the mass of the nucleon approaches a non-zero value M_0, corresponding to the gluon and $\bar{q}q$ condensate. When the masses of the quarks are turned on, additional terms of the scalar matrix element show up as

$$M_N = M_0 + \hat{\sigma} + \sigma_s + \text{heavy quark terms} \tag{1.2}$$

$$\hat{\sigma} = \hat{m}\langle N|\bar{u}u + \bar{d}d|N\rangle\,, \quad \sigma_s = m_s\langle N|\bar{s}s|N\rangle\,, \tag{1.3}$$

[†] This simple physical definition of x (or so-called Feynman x_F) [Fey69], turns out to be identical with a dimensionless kinematic variable $x_B \equiv \frac{Q^2}{M\nu}$ that Bjorken introduced as the scaling variable of the nucleon structure functions [Bjo69].

where $\hat{m} = \dfrac{m_u + m_d}{2}$. Note that both $\hat{\sigma}$ and σ_s are scalar form factors that depend only on the momentum transfer. As the mass terms, however, zero momentum transfer is implicit in both of them. We shall neglect the heavy quark terms in the following discussion, although they could also contribute to the nucleon mass to some level [Shi78].

The first constraint on these scalar matrix elements comes from the hyperon mass splitting due to the SU(3) flavor symmetry breaking effect [Che88]. At leading order,

$$\frac{1}{3}(\hat{m} - m_s)\langle N|\bar{u}u + \bar{d}d - 2\bar{s}s|N\rangle = M_\Lambda - M_\Xi \,, \tag{1.4}$$

where M_Λ and M_Ξ are the masses of Λ and Ξ hyperons respectively. It is convenient to define a quantity y to reflect the strange content of the nucleon as

$$y = \frac{2\langle N|\bar{s}s|N\rangle}{\langle N|\bar{u}u + \bar{d}d|N\rangle} \,. \tag{1.5}$$

So Eqn. 1.4 becomes

$$\frac{1}{3}(1 - \frac{m_s}{\hat{m}})(1 - y)\hat{\sigma} = M_\Lambda - M_\Xi \,. \tag{1.6}$$

If one takes the canonical ratio that $m_s/\hat{m} \sim 26$ [Gas85], and assumes that the strange matrix element is zero ($y = 0$), then $\hat{\sigma} \sim 25$ MeV. Higher order chiral corrections increase its value to $\hat{\sigma} \sim 35$ MeV [Gas91].

The second constraint comes from the analysis of the so-called $\pi-N$ "sigma term", $\Sigma_{\pi N}$. Experimentally, $\Sigma_{\pi N}$ is related to the isospin even $\pi-N$ scattering amplitude $\bar{D}^+$ (leading Born term subtracted) at the "Cheng-Dashen" point [CD71]:

$$\Sigma_{\pi N} = F_\pi^2 \bar{D}^+(s = M_N^2, t = 2m_\pi^2) \,, \tag{1.7}$$

in which $F_\pi \sim 92.4$ MeV is the pion decay constant, s is the invariant mass of the $\pi-N$ system, and t is the four-momentum transfer squared to the nucleon ($t < 0$ for physical region). In the lowest order of chiral perturbation theory, a low energy

theorem states that [CD71]

$$\Sigma_{\pi N} \simeq \hat{\sigma}(t = 2m_\pi^2)\,. \tag{1.8}$$

However, the Cheng-Dashen point ($s = M_N^2, t = 2m_\pi^2$) is unphysical, therefore one has to extrapolate the experimental data using phase-shift analysis and dispersion calculations [Rey74]. In a comprehensive analysis in [Gas91], the authors concluded that $\Sigma_{\pi N} \simeq \hat{\sigma}(t = 2m_\pi^2) \sim 60$ MeV. Extrapolating this value to zero momentum transfer ($t = 0$) to get the mass term is also quite involved; higher order chiral perturbation terms are significant. In the accompanying paper [Gas91b], the authors applied dispersion relations and found that the t dependence of $\hat{\sigma}(t)$ is remarkably large. Extrapolating it to $t = 0$ lowered the value of $\hat{\sigma}$ to ~ 45 MeV.

If the strange quark does not contribute to the scalar matrix element, or $y = 0$, then one would expect $\hat{\sigma}$ obtained via the two approaches to agree. The discrepancy between 35 and 45 MeV implies that $y \sim 0.2$. Taking a typical average light quark mass to be $\hat{m} \sim 5$ MeV (see, for example, [Bij95]) and $m_s/\hat{m} \sim 26$ [Gas85] would yield

$$\sigma_s = m_s \langle N|\bar{s}s|N\rangle \sim 130 \text{ MeV}\,, \tag{1.9}$$

which suggests that the strange quarks contribute a sizable amount to the nucleon mass. However, the uncertainty of this result could be quite large due to the experimental uncertainties and inconsistency of the $\pi-N$ data, the extrapolation of the data to the unphysical region, the inaccuracy of the higher order chiral corrections to hyperon mass relations, and the uncertainty in the quark mass ratio $\frac{m_s}{\hat{m}}$. Indeed, a recent lattice calculation gave $\hat{\sigma}(t = 0) \sim 53$ MeV, which leads to $y = 0.36 \pm 0.03$ [Don96], and another two-flavor dynamic QCD lattice calculation yielded $\hat{\sigma}(t = 0) = 45 - 55$ MeV [LTW00]. A recent global analysis including the new experimental inputs suggests that $\hat{\sigma}(t = 2m_\pi^2) \sim 90 \pm 8$ MeV [Pav99]. Another analysis based a dispersive sum rule relying on the threshold parameters yields $\hat{\sigma}(t = 2m_\pi^2) \sim 70 \pm 9$ MeV [Ols00], also significantly larger than previous values. Without consensus on these results, the uncertainty of the strange scalar

matrix element $\langle N|\bar{s}s|N\rangle$ is probably at 100% level.

Lastly, it is worth noting another (suggestive) piece of experimental evidence — the excessive ϕ meson production in the $\bar{p}p$ annihilation. One of the explanations involves an intrinsic $\bar{s}s$ component in the proton wave function that gets rearranged during the reaction [Ell95], although further investigation is needed in this regard.

1.2.3 The Axial Matrix Element and the Strangeness in the Nucleon Spin

The unpolarized quark structure function $q_i(x)$ has been defined in Sec. 1.2.1. For a polarized nucleon, $q_i(x)$ can be decomposed into $q_i(x) = q_i^{\uparrow}(x) + q_i^{\downarrow}(x)$, with the superscript $\uparrow$ ($\downarrow$) reflecting that the spin of the quark is aligned (anti-aligned) to that of the nucleon. Then the overall contribution of quark flavor i to the spin of the nucleon is

$$\Delta q_i = \int_0^1 [q_i^{\uparrow}(x) - q_i^{\downarrow}(x)]\, dx\,, \tag{1.10}$$

where q_i could be either a quark or anti-quark of a certain flavor i (u,d,s,...). Note that if only quarks are responsible for the nucleon spin, then $\sum_i \Delta q_i = 1$. Δq_i can be related to the one-nucleon axial current matrix element as

$$\Delta q_i \sigma_\mu = \langle p, \vec{\sigma}|\bar{q}_i \gamma_\mu \gamma_5 q_i|p, \vec{\sigma}\rangle\,, \tag{1.11}$$

which is closely related to the axial form factor of the nucleon (see Secs. 2.3.2 and 6.1.2).

Experimental constraints can be put on Δu, Δd and Δs. The first constraint comes from polarized *inclusive* DIS of the electron (or muon) from the nucleon, for which the cross section is characterized by two polarized structure functions, $g_1(x, Q^2)$ and $g_2(x, Q^2)$. During the last two decades, a number of experiments have been carried out at CERN [Ash89, Ada97], SLAC [Abe98, Ant00] and DESY [Air98] to determine g_1 over a large range of x and Q^2. To the leading order in the parton

model, g_1 is independent of Q^2 and one has

$$g_1(x) = \frac{1}{2}\sum_i e_{q_i}^2 \left[q_i^{\uparrow}(x) - \bar{q}_i^{\uparrow}(x)\right] . \tag{1.12}$$

So if c, b and t quarks are ignored, one gets a g_1 sum rule of

$$\Gamma_1 = \int_0^1 g_1(x)\, dx = \frac{1}{2}\left(\frac{4}{9}\Delta u + \frac{1}{9}\Delta d + \frac{1}{9}\Delta s\right) , \tag{1.13}$$

in which the contributions of a quark and anti-quark of a given flavor are combined. As an example, the result for Γ_1 of the proton at $Q^2 = 3(\mathrm{GeV/c})^2$ from E143 [Abe98] is

$$\Gamma_1^p = 0.132 \pm 0.010 . \tag{1.14}$$

The parton model, combined with strong isospin symmetry, enables us to re-derive the Bjorken sum rule[†], which puts a second constraint on Δu and Δd as [TW00]

$$\Delta u - \Delta d = F + D = -\frac{g_A}{g_V} . \tag{1.15}$$

Extending SU(2) isospin to SU(3) flavor symmetry leads to [TW00]

$$\Delta u + \Delta d - 2\Delta s = 3F - D \equiv 2\sqrt{3} g_A^8 . \tag{1.16}$$

F and D in these two equations are phenomenological parameters to characterize the charged current matrix element of the baryon octet [Cab63, Wil64], and can be determined through beta decays of baryons. g_A and g_V are the charged current weak axial and vector charges of the neutron; $F+D \equiv -g_A/g_V = 1.2695 \pm 0.0029$ [PDG04] is well-established by neutron beta decay. $2\sqrt{3}g_A^8 \equiv 3F - D$ is the 8th octet axial charge of the baryon; a recent analysis of hyperon beta decay data yields $3F - D = 0.585 \pm 0.025$ [Got00].

Naively combining Eqns. 1.13, 1.15 and 1.16 with the values of Γ_1, g_A/g_V and

[†] Originally Bjorken derived the sum rule based on the current algebra [Bjo66].

$3F - D$ given above yields

$$\Delta u = 0.76 \pm 0.03\,, \quad \Delta d = -0.51 \pm 0.03\,, \quad \Delta s = -0.17 \pm 0.03\,, \tag{1.17}$$

indicating that the overall contribution of quarks to the nucleon spin is quite small and Δs is small and negative. In reality, however, extracting Δq is a very involved and model dependent process. First, the data must be extrapolated to $x = 0$ and $x = 1$ in order to compute Γ_1. Second, when taking into account the next-to-leading-order (NLO) corrections to Eqn. 1.13, the evolution of g_1 with four-momentum transfer introduces uncertainties. The result also depends on the renormalization scheme and scale. Third, the gluon contribution to Eqn. 1.13 introduces some ambiguity. Fourth, Eqn. 1.16 assumes SU(3) flavor symmetry, which is not exact in real world. Nonetheless, most of the NLO analyses tend to give small and negative values for Δs [LLS02, LLS03, BB03, HKS04].

The model dependence in the flavor separation for polarized inclusive DIS results can be partly overcome by the "flavor tagging" technique in polarized semi-inclusive DIS experiment. Unlike inclusive reactions, in a semi-inclusive DIS the scattered lepton and one of the hadrons in the final state are detected in coincidence, and the flavor content of the hadron "tags" the flavor of the struck quark. This implies that strange quark contribution to the nucleon spin can be isolated by looking at the kaon channels in polarized semi-inclusive DIS. In a recent paper by the HERMES collaboration [Air05], Δs measured by this means was reported to be consistent with zero within the kinematical range of $0.023 < x < 0.3$. The discrepancy between this result and those from inclusive DIS indicates the size of model uncertainty in Δs.

Besides the polarized DIS, neutral weak probes also have sensitivities to Δs. As shall be discussed in Sec. 6.1.2, Δs contributes to parity violating elastic electron scattering, however its sensitivity is suppressed due to the smallness of electron's weak charge. On the other hand the contribution of Δs is not suppressed in elastic neutrino-nucleon ($\nu - N$) scattering, and it can be determined by fitting the cross

section data with nucleon EM form factors as inputs. This analysis was first attempted in [Ahr87] based on $\nu-p$ and $\bar{\nu}-p$ data taken by BNL734, and later refined in [GLW93]. Both analyses obtained Δs in agreement with the results from the DIS, but with larger uncertainties due to the limited precision of the $\nu-N$ cross section data.

1.2.4 The Vector Matrix Element and Strangeness in the Charge and Magnetization Distributions of the Nucleon

With the electromagnetic interaction, the most ordinary observables of the nucleon are its charge and magnetic moment. That the proton has one unit of charge and the neutron is charge neutral have long been built into our intuition. But it is less so for the magnetic moment. In 1933, Stern and collaborators carried out a pioneering experiment and found, surprisingly, that the proton's magnetic moment was $\mu_p \sim 2.5\mu_N$ [FS33]. In 1940, Alvarez and Bloch determined the neutron's magnetic moment to be $\mu_n \sim -1.93\mu_N$ [AB40], where $\mu_N = \frac{e\hbar}{2M_pc}$ is the nucleon Bohr magneton. That the μ_p is not unity and μ_n is non-zero are probably the earliest evidence that the nucleons are not fundamental particles. In the 1950's, Hofstadter and collaborators launched the far-reaching electron-proton scattering program [Hof55], which used the electromagnetic interaction as a probe to determine the internal structure of the proton. The electromagnetic form factors, in field theory language, are related to the matrix element of a Lorentz vector current operator $\hat{\mathcal{J}}^{\mu,N}_{\rm EM}$ as

$$\langle N|\hat{\mathcal{J}}^{\mu,N}_{\rm EM}|N\rangle = \bar{\mathcal{U}}(p')\left[\gamma^\mu G_M^\gamma - (p'+p)^\mu \frac{1}{2M}\frac{G_M^\gamma - G_E^\gamma}{1+\tau}\right]\mathcal{U}(p)\,, \tag{1.18}$$

in which p and p' are the initial and final four-momenta of the nucleon. G_E^γ and G_M^γ are the nucleon's electric and magnetic form factors, which describe the distribution of charge and magnetization inside the nucleon. To date, the electromagnetic (EM) form factors of the nucleons are well-measured over a wide range of kinematics.

It is then natural to ask how much the strange quark contribution is to these nucleon EM form factors. Formally this is to determine the matrix element of the

strange vector current $\langle N|\bar{s}\gamma^{\mu}s|N\rangle$. Similarly to Eqn. 1.18, one can write it in terms of the strange electric and magnetic form factors, G_E^s and G_M^s.

In 1988, Kaplan and Manohar suggested that one could access G_E^s and G_M^s by measuring the neutral weak EM form factor $G_{E,M}^{NC,p(n)}$ of the nucleon [KM88]. Shortly after, McKeown and Beck proposed a feasible experimental probe, namely the parity violating (PV) elastic electron-proton scattering [Mck89, Bec89]. Their seminal proposal has been followed by more than a decade of experimental efforts on PV electron scattering. This thesis is devoted to one such experiment, known as G^0, and the remainder of the text is organized as follows. In Chap. 2, the theoretical formalism of the nucleon (vector) strangeness, and how one can measure it via parity violating electron scattering are presented. At the end of this chapter, various theoretical predictions will be given. In Chap. 3, a brief summary of the existing world data prior to the G^0 experiment will be given, followed by a discussion of the experimental aspects of G^0 in Chap. 4. The analysis of the G^0 data is separated into two parts: in Chap. 5, step-by-step corrections that bring the raw measured asymmetry to the physical elastic asymmetry of interest are detailed, followed by a discussion of the extraction of strange vector form factors in Chap. 6. We will end Chap. 6 by discussing the physics implications of the G^0 forward measurement, looking into the near future, and presenting our conclusions.

Chapter 2

Theory

2.1 Electroweak Currents in the Standard Model

In the Standard Model of particle physics, elementary fermions (leptons and quarks) interact by exchanging vector gauge bosons. The interaction Lagrangian can be formally written as fermion current operators coupling to gauge boson fields. The Standard Model contains a local symmetry group SU(2)×U(1), which leads to the unified electroweak theory. In this theory, there are three types of fermion currents, electromagnetic (EM), neutral current (NC) and charged current (CC), which couple to the gauge bosons γ (photon), Z^0 and $W^{\pm}$, respectively. Feynman diagrams representing these three types of interactions are depicted in Fig. 2.1.

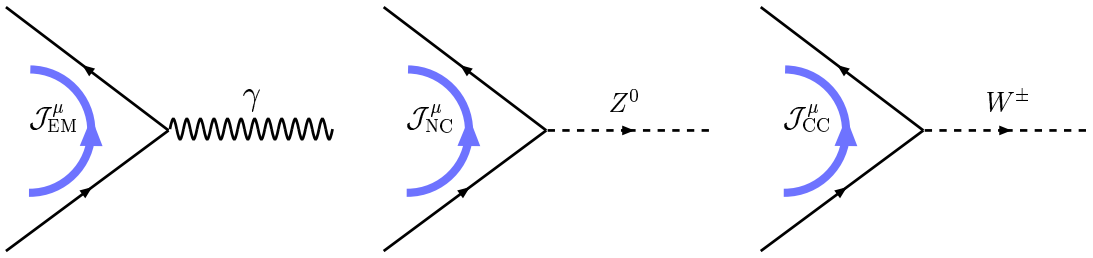

(a) *EM Current* (b) *Neutral Current* (c) *Charged Current*

Figure 2.1: *The Feynman diagrams of three types of electroweak currents and their couplings to the gauge bosons.*

The EM current operators can be expressed in terms of the field operators as

$$\hat{\mathcal{J}}^{\mu}_{\rm EM} = Q\bar{\psi}\gamma^{\mu}\psi\,, \tag{2.1}$$

in which ψ ($\bar{\psi}$) is the annihilation (creation) operator of the fermion field, γ^{μ} ($\mu = 0, 1, 2, 3$) are the Dirac matrices, and Q is the electric charge of the fermion (in units of the proton charge). The EM current is a pure Lorentz vector.

The neutral and charged currents both have a vector and an axial (V−A) component. The neutral current operator can be expressed as

$$\hat{\mathcal{J}}^{\mu}_{\rm NC} = \bar{\psi}\gamma^{\mu}(c_V + c_A\gamma_5)\psi\,, \tag{2.2}$$

in which $\gamma_5 = i\gamma^0\gamma^1\gamma^2\gamma^3$, and c_V and c_A are the so-called weak vector and axial charges of the fermion. In the electroweak theory, they are given by [‡]

$$\begin{aligned} c_V =& 2T^3 - 4\sin^2\theta_W Q\,, \\ c_A =& -2T^3\,, \end{aligned} \tag{2.3}$$

in which $T^3 = \pm\frac{1}{2}$ is the third isospin component of the (left-handed) fermion in the SU(2) weak isospin space, and θ_W is the Weinberg angle, which characterizes the mixing of the U(1) and SU(2) spaces. As an example, an electron has $T^3 = -\frac{1}{2}$ and $Q = -1$, therefore $c_V = -1 + 4\sin^2\theta_W$ and $c_A = 1$.

The charged current operator takes a similar form as

$$\hat{\mathcal{J}}^{\mu}_{CC} = \bar{\psi}'\gamma^{\mu}(1 - \gamma_5)\psi\,. \tag{2.4}$$

Unlike the electromagnetic and neutral currents, since $W^{\pm}$ carries one unit of charge, ψ' and ψ represent different particles with charges differing by one, e.g. ν and e, u and d quarks, etc. For completeness, we note that ψ' and ψ here are the so-called weak eigenstates of the fermions. For the quarks (and neutrinos), it has been discovered that their (measurable) mass eigenstates are mixtures of these weak eigenstates [HM84]. In parity violating electron scattering, the charged current is not involved and shall be ignored in the remainder of this work.

As a summary, the electric, weak vector and axial charges of different elementary fermions are listed in Table 2.1.

[‡]Here we are following the convention used in [Mus94]. In other places in the literature, the neutral and charged currents are also sometimes accompanied by factor of $\frac{1}{2}$, and c_V and c_A might also carry a factor $\frac{1}{4}$. To resolve the discrepancy, it is simply a matter of redefining the coupling constants when expressing the scattering amplitude.

Fermion	Q	T^3	c_V	c_A
ν_e, ν_μ, ν_τ	0	$\frac{1}{2}$	1	-1
e, μ, τ	-1	$-\frac{1}{2}$	$-1+4\sin^2\theta_W$	1
u, c, t	$\frac{2}{3}$	$\frac{1}{2}$	$1-\frac{8}{3}\sin^2\theta_W$	-1
d, s, b	$-\frac{1}{3}$	$-\frac{1}{2}$	$-1+\frac{4}{3}\sin^2\theta_W$	1

Table 2.1: *Electroweak charges of elementary fermions in the Standard Model.*

2.2 Nucleon Matrix Elements and the Form Factors

The experimental observables, such as the scattering cross section, are related to the matrix elements of the current operators in Sec. 2.1. For the elementary fermions, since they are assumed to be point-like particles, it is self-evident when writing the fermion matrix elements of these current operators. Using $|k\rangle$ and $|k'\rangle$ to denote the initial and final states of the fermion, Eqns. 2.1 and 2.2 become

$$\mathcal{J}^{\mu,f}_{\rm EM} \equiv \langle k'|\hat{\mathcal{J}}^{\mu}_{\rm EM}|k\rangle = Q\bar{\mathcal{U}}(k')\gamma^\mu\mathcal{U}(k)\,, \tag{2.5}$$

$$\mathcal{J}^{\mu,f}_{\rm NC} \equiv \langle k'|\hat{\mathcal{J}}^{\mu}_{\rm NC}|k\rangle = \bar{\mathcal{U}}(k')\gamma^\mu(c_V+c_A\gamma_5)\mathcal{U}(k) \equiv \mathcal{J}^{\mu,f}_{\rm NC,V} + \mathcal{J}^{\mu,f}_{\rm NC,A}\,, \tag{2.6}$$

in which $\mathcal{U}(k)$ and $\mathcal{U}(k')$ are now the Dirac spinors, and the "f" in the superscripts of $\mathcal{J}$ indicates it is the current of the elementary fermions. Note that the neutral current has been separated into its vector and axial components.

The nucleons are made up of point-like quarks. Therefore the nucleon current operator can be written as a sum of the underlying quark current operators. Using Eqns. 2.1 and 2.2, the nucleon electromagnetic and neutral currents can be expressed explicitly as

$$\mathcal{J}^{\mu,N}_{\rm EM} \equiv \langle N(p')|\hat{\mathcal{J}}^{\mu}_{\rm EM,N}|N(p)\rangle = \langle N(p')|\sum_{j=\rm quarks}\bar{q}_j Q^j\gamma^\mu q_j|N(p)\rangle \tag{2.7}$$

$$\mathcal{J}^{\mu,N}_{\rm NC} \equiv \langle N(p')|\hat{\mathcal{J}}^{\mu,N}_{\rm NC}|N(p)\rangle = \langle N(p')|\sum_{j=\rm quarks}\bar{q}_j\gamma^\mu(c^j_V+c^j_A\gamma_5)q_j|N(p)\rangle\,, \tag{2.8}$$

in which p and p' represent the initial and final four-momenta of the nucleon, j represents the quark species, q_j and $\bar{q_j}$ are the quark fields, and Q^j, c_V^j and c_A^j are the electric, weak vector and axial charges of quark flavor j, respectively.

Since the nucleon has extended structure, one cannot directly apply Eqns. 2.5 and 2.6 here. Instead, a set of form factors is defined to encapsulate the internal structure of the nucleon. Generally, from Lorentz invariance, it can be shown [HM84, TW00] that the hadronic vector and axial current of a spin $\frac{1}{2}$ particle can be expressed as

$$\mathcal{V}^\mu = \langle N(p')|\bar{\psi}\gamma^\mu\psi|N(p)\rangle = \bar{\mathcal{U}}(p')\left[F_1\gamma^\mu + F_2\frac{i\sigma^{\mu\nu}q_\nu}{2M}\right]\mathcal{U}(p)\,, \tag{2.9}$$

$$\mathcal{A}^\mu = \langle N(p')|\bar{\psi}\gamma^\mu\gamma_5\psi|N(p)\rangle = \bar{\mathcal{U}}(p')\left[G_A\gamma^\mu\gamma_5 + \frac{G_P}{2M}q^\mu\gamma_5\right]\mathcal{U}(p)\,, \tag{2.10}$$

in which $\sigma^{\mu\nu} = \frac{i}{2}[\gamma^\mu, \gamma^\nu]$, $q \equiv p' - p$ is the four-momentum transfer to the nucleon, M is the mass of the nucleon, and $\mathcal{U}$ and $\bar{\mathcal{U}}$ are the nucleon spinors. F_1, F_2 and G_A are the Dirac, Pauli and axial form factors, respectively; they are dimensionless quantities and are only functions of four-momentum transfer squared (q^2). In electron scattering, since $q^2 < 0$, it is conventional to use $Q^2 = -q^2 > 0$ instead of q^2. The pseudoscalar form factor, G_P, is introduced for completeness; we shall neglect it henceforth since it does not contribute to parity violating electron scattering.

Since the EM current is a pure Lorentz vector, we simply dress Equation 2.9 into

$$\mathcal{J}_{\rm EM}^{\mu,N} = \bar{\mathcal{U}}(p')[\gamma^\mu F_1^\gamma(Q^2) + \frac{i\sigma^{\mu\nu}q_\nu}{2M}F_2^\gamma(Q^2)]\mathcal{U}(p)\,. \tag{2.11}$$

F_1^γ and F_2^γ are the Dirac and Pauli EM form factors of the nucleon, and at $Q^2 = 0$ they are normalized as

$$F_1^\gamma(0) = Q_N, \quad F_2^\gamma(0) = \kappa_N\,, \tag{2.12}$$

in which Q_N is the electric charge of the nucleon (in units of $|e|$), and κ_N is the anomalous magnetic moment of the nucleon (in units of the Bohr magneton).

Another set of commonly used form factors are the Sachs form factors [ESW60],

G_E and G_M. They are related to F_1 and F_2 as

$$G_E = F_1 - \frac{Q^2}{4M^2} F_2 \,, \quad G_M = F_1 + F_2 \,. \tag{2.13}$$

G_E^γ and G_M^γ are usually called the electric and magnetic form factors of the nucleon, respectively. At $Q^2 = 0$, they are simply the charge and magnetic moments of the nucleon:

$$\begin{aligned} \text{proton:} \quad & G_E^\gamma(0) = 1, \quad G_M^\gamma(0) = 2.793 \,, \\ \text{neutron:} \quad & G_E^\gamma(0) = 0, \quad G_M^\gamma(0) = -1.931 \,. \end{aligned}$$

For each Q^2, there exists a reference frame such that the incident and recoiling nucleon momentum is $\vec{P} - \vec{q}/2$ and $\vec{P} + \vec{q}/2$, where $|\vec{q}| = \sqrt{Q^2}$. This is the so-called Breit frame, or in the context of elastic electron scattering, the center-of-mass frame of the electron-nucleon system. It can be shown that in the Breit frame, G_E^γ and G_M^γ are simply the Fourier transforms of the charge and magnetization densities of the nucleon [Sac62].

The neutral current has both the vector and axial components, and following Eqns. 2.9 and 2.10, it becomes

$$\mathcal{J}_{\rm NC}^{\mu,N} = \bar{\mathcal{U}}(p') \left[\gamma^\mu F_1^Z(Q^2) + \frac{i\sigma^{\mu\nu} q_\nu}{2M} F_2^Z(Q^2) + \gamma^\mu \gamma_5 G_A^Z(Q^2) \right] \mathcal{U}(p) \,, \tag{2.14}$$

of which F_1^Z and F_2^Z are now the weak (vector) Dirac and Pauli form factors, and G_A^Z is the axial form factor. A similar set of Sachs weak form factors, G_E^Z and G_M^Z, can be defined by Eqn. 2.13. The normalization of these form factors will be discussed in Sec. 2.3.

Finally, in terms of the Sachs form factors, the electromagnetic and neutral

currents of the nucleon, Eqn. 2.11 and 2.14, can be re-written as

$$\mathcal{J}^{\mu,N}_{\rm EM} = \bar{\mathcal{U}}(p') \left[\gamma^\mu G^\gamma_M - (p'+p)^\mu \frac{1}{2M} \frac{G^\gamma_M - G^\gamma_E}{1+\tau} \right] \mathcal{U}(p) \,, \tag{2.15}$$

$$\mathcal{J}^{\mu,N}_{\rm NC} = \bar{\mathcal{U}}(p') \left[\gamma^\mu G^Z_M - (p'+p)^\mu \frac{1}{2M} \frac{G^Z_M - G^Z_E}{1+\tau} + \gamma^\mu \gamma_5 G^Z_A \right] \mathcal{U}(p) \equiv \mathcal{J}^{\mu,N}_{\rm NC,V} + \mathcal{J}^{\mu,N}_{\rm NC,A} \,. \tag{2.16}$$

Again, we have separated the neutral current into the generic V−A form.

2.3 Flavor Decomposition

Using Eqns. 2.9 and 2.10, Eqns. 2.7 and 2.8 can now be rewritten as

$$\mathcal{J}^{\mu,N}_{\rm EM} = \bar{\mathcal{U}} \sum_{j=\text{quarks}} Q_j \left[\gamma^\mu F^j_1 + \frac{i\sigma^{\mu\nu} q_\nu}{2M} F^j_2 \right] \mathcal{U} \,, \tag{2.17}$$

$$\mathcal{J}^{\mu,N}_{\rm NC} = \bar{\mathcal{U}} \sum_{j=\text{quarks}} \left[c^j_V \left(\gamma^\mu F^j_1 + \frac{i\sigma^{\mu\nu} q_\nu}{2M} F^j_2 \right) + c^j_A G^j_A \gamma^\mu \gamma_5 \right] \mathcal{U} \,, \tag{2.18}$$

in which F^j_1, F^j_2 and G^j_A are the Dirac, Pauli and axial form factors of quark flavor j. Note that once the charges are factored out, the underlying *vector* currents of individual quarks are identical in the EM and neutral currents. Therefore F^j_1, F^j_2 are common to $\mathcal{J}^{\mu,N}_{\rm EM}$ and $\mathcal{J}^{\mu,N}_{\rm NC}$.

Comparing Eqns. 2.17 and 2.18 with Eqns. 2.11 and 2.14, one immediately writes

$$F^\gamma_{1,2} = \sum_{j=\text{quarks}} Q_j F^j_{1,2} \,, \tag{2.19}$$

$$F^Z_{1,2} = \sum_{j=\text{quarks}} c^j_V F^j_{1,2} \,, \tag{2.20}$$

$$G^Z_A = \sum_{j=\text{quarks}} c^j_A G^j_A \,. \tag{2.21}$$

2.3.1 Flavor Vector Form Factors

It has been argued that heavier quarks (c, t, b) have negligible contributions to the nucleon EM structure [KM88]. Therefore we shall only consider the three light quark flavors ($j = u, d, s$). Eqns. 2.19 and 2.20 can be written out explicitly as

$$F_{1,2}^{\gamma} = \frac{2}{3}F_{1,2}^{u} - \frac{1}{3}(F_{1,2}^{d} + F_{1,2}^{s})\,, \tag{2.22}$$

$$F_{1,2}^{Z} = \left(1 - \frac{8}{3}\sin^2\theta_W\right) F_{1,2}^{u} - \left(1 - \frac{4}{3}\sin^2\theta_W\right)(F_{1,2}^{d} + F_{1,2}^{s})\,, \tag{2.23}$$

or equivalently,

$$G_{E,M}^{\gamma} = \frac{2}{3}G_{E,M}^{u} - \frac{1}{3}(G_{E,M}^{d} + G_{E,M}^{s})\,, \tag{2.24}$$

$$G_{E,M}^{Z} = \left(1 - \frac{8}{3}\sin^2\theta_W\right) G_{E,M}^{u} - \left(1 - \frac{4}{3}\sin^2\theta_W\right)(G_{E,M}^{d} + G_{E,M}^{s})\,. \tag{2.25}$$

Note that Eqns. 2.22–2.25 are generic for the nucleons. To apply them to the proton or neutron, we shall add nucleon species superscripts (p or n) on the form factors. Similar to the nucleon Sachs form factors, the form factors of a given quark flavor, multiplied by the quark's electric charge, correspond to the Fourier transforms of the charge and magnetization densities (in the Breit frame) of this quark flavor inside the nucleon. One should note that each flavor form factor includes both the quark and anti-quark contributions. For nucleons, the u and d flavor form factors contain contributions from both the valence and sea quarks, whereas the s flavor form factors arise purely from the $s\bar{s}$ sea.

A good symmetry of the strong interaction is charge symmetry, which states that in exchanging the $u(\bar{u})$ and $d(\bar{d})$ quarks, a proton becomes a neutron, and vice versa [†]. In other words, the (u, d) quarks in the proton are in the same wave function as (d, u) quarks in the neutron, and the strange quark wave functions of the proton

[†]Note that this symmetry is less restrictive as compared to the isospin symmetry. The latter requires the invariance of interaction Lagrangian under any rotation in isospin space.

and neutron are identical [Mil98]. These imply

$$G_{E,M}^{u,p} = G_{E,M}^{d,n}\,, \quad G_{E,M}^{d,p} = G_{E,M}^{u,n}\,, \quad G_{E,M}^{s,p} = G_{E,M}^{s,n}\,. \tag{2.26}$$

The breaking of these equalities is generally at the level of 1% or less [Mil98]. Given the experimental precision at this stage, the charge symmetry violation can be generally neglected. Therefore Eqns. 2.24 and 2.25 can be rewritten into

$$G_{E,M}^{\gamma,p} = \frac{2}{3}G_{E,M}^{u} - \frac{1}{3}(G_{E,M}^{d} + G_{E,M}^{s})\,, \tag{2.27}$$

$$G_{E,M}^{\gamma,n} = \frac{2}{3}G_{E,M}^{d} - \frac{1}{3}(G_{E,M}^{u} + G_{E,M}^{s})\,, \tag{2.28}$$

$$G_{E,M}^{Z,p} = \left(1 - \frac{8}{3}\sin^2\theta_W\right)G_{E,M}^{u} - \left(1 - \frac{4}{3}\sin^2\theta_W\right)(G_{E,M}^{d} + G_{E,M}^{s})\,, \tag{2.29}$$

$$G_{E,M}^{Z,n} = \left(1 - \frac{8}{3}\sin^2\theta_W\right)G_{E,M}^{d} - \left(1 - \frac{4}{3}\sin^2\theta_W\right)(G_{E,M}^{u} + G_{E,M}^{s})\,, \tag{2.30}$$

with the superscript of "p" in the flavor form factors suppressed.

The electromagnetic form factors of the nucleons, $G_{E,M}^{\gamma,p}$ and $G_{E,M}^{\gamma,n}$, have been extensively measured for the past 50 years; here we shall treat them as known. If one could experimentally determine $G_{E,M}^{Z,p}$, then Eqns. 2.27, 2.28 and 2.29 would contain only three unknowns $(G_{E,M}^{u}, G_{E,M}^{d}, G_{E,M}^{s})$, which could be trivially solved.

The normalization of the flavor form factors at $Q^2 = 0$ follows the same prescription as the normal Sachs form factors. Since the charges of the quarks are factored out, the electric flavor form factors now represent the net numbers of the quarks. Therefore we have

$$G_E^u(0) = 2\,, \quad G_E^d(0) = 1, \quad G_E^s(0) = 0\,. \tag{2.31}$$

These lead to the weak charge of the proton and neutron:

$$Q_W^p \equiv G_E^{Z,p}(0) = 1 - 4\sin^2\theta_W\,, \tag{2.32}$$

$$Q_W^n \equiv G_E^{Z,n}(0) = -1\,. \tag{2.33}$$

On the other hand, the magnetic form factors at $Q^2 = 0$ do not have theoretically constrained values. Let us define

$$G_M^u(0) \equiv \mu_u\,, \quad G_M^d(0) \equiv \mu_d\,, \quad G_M^s(0) \equiv \mu_s\,, \tag{2.34}$$

Then Eqns. 2.27 and 2.28 become

$$\mu_p \equiv G_M^{\gamma,p}(0) = \frac{2}{3}\mu_u - \frac{1}{3}\mu_d - \frac{1}{3}\mu_s\,, \tag{2.35}$$

$$\mu_n \equiv G_M^{\gamma,n}(0) = \frac{2}{3}\mu_d - \frac{1}{3}\mu_u - \frac{1}{3}\mu_s\,. \tag{2.36}$$

One should note again here that for each quark flavor, $Q_q\mu_q$ gives its contribution to the magnetic moment of the nucleon in units of the Bohr magneton. Eqns. 2.35 and 2.36 can be rewritten into

$$\mu_u = 2\mu_p + \mu_n + \mu_s\,, \quad \mu_d = 2\mu_n + \mu_p + \mu_s\,. \tag{2.37}$$

Then the weak magnetic moments of the proton and neutron are

$$\mu_p^Z \equiv G_M^{Z,p}(0) = (1 - 4\sin^2\theta_W)\mu_p - \mu_n - \mu_s = 2.141 - \mu_s\,, \tag{2.38}$$

$$\mu_n^Z \equiv G_M^{Z,n}(0) = (1 - 4\sin^2\theta_W)\mu_n - \mu_p - \mu_s = -2.648 - \mu_s\,. \tag{2.39}$$

Sometimes the flavor decomposition is also made with respect to the SU(3) generators. For the vector current, we define SU(3) singlet, 3rd octet and 8th octet form factors as

$$\begin{aligned} G_{E,M}^{(0)} &= \frac{1}{3}(G_{E,M}^u + G_{E,M}^d + G_{E,M}^s)\,, \\ G_{E,M}^{(3)} &= \frac{1}{2}(G_{E,M}^u - G_{E,M}^d)\,, \\ G_{E,M}^{(8)} &= \frac{1}{2\sqrt{3}}(G_{E,M}^u + G_{E,M}^d - 2G_{E,M}^s)\,. \end{aligned} \tag{2.40}$$

Note that SU(3) decomposition does not assume SU(3) symmetry, such assumption would be imposed only if one tried to relate the three form factors.

Then $G_{E,M}^{\gamma,p}$ and $G_{E,M}^{Z,p}$ can be rewritten as

$$G_{E,M}^{\gamma,p} = G_{E,M}^{(3)} + \frac{1}{\sqrt{3}} G_{E,M}^{(8)} \tag{2.41}$$

$$\begin{aligned} G_{E,M}^{Z,p} &= -G_{E,M}^{(0)} + (2 - 4\sin^2\theta_W) G_{E,M}^{(3)} + \left(\frac{2}{\sqrt{3}} - \frac{4}{\sqrt{3}} \sin^2\theta_W \right) G_{E,M}^{(8)} \\ &= -G_{E,M}^{(0)} + (2 - 4\sin^2\theta_W) G_{E,M}^{\gamma,p} \,. \end{aligned} \tag{2.42}$$

This shows that without using charge symmetry, a measurement of $G_{E,M}^{Z,p}$, combined with the known electromagnetic form factors of the proton, leads to a determination of flavor singlet form factors of the proton, $G_{E,M}^{(0)}$. This is the origin of the name of the G^0 experiment.

To make connections with conventionally used notations of radiative corrections, we introduce another flavor decomposition of the neutral current form factors. If we define an SU(3) singlet weak charge $Q_W^{(0)}$ as

$$Q_W^{(0)} = c_V^u + c_V^d + c_V^s = -1 \,, \tag{2.43}$$

then using the three weak charges Q_W^p, Q_W^n and $Q_W^{(0)}$, and Eqns. 2.27 and 2.28, the neutral current form factors of the proton and neutron can be expressed as

$$G_{E,M}^{Z,p} = Q_W^p G_{E,M}^{\gamma,p} + Q_W^n G_{E,M}^{\gamma,n} + Q_W^{(0)} G_{E,M}^{s} \,, \tag{2.44}$$

$$G_{E,M}^{Z,n} = Q_W^n G_{E,M}^{\gamma,p} + Q_W^p G_{E,M}^{\gamma,n} + Q_W^{(0)} G_{E,M}^{s} \,. \tag{2.45}$$

Interestingly, $G_{E,M}^{Z,p}$ ($G_{E,M}^{Z,n}$) now contains contributions from EM form factors and weak charge of the neutron (proton), which is a direct consequence of charge symmetry.

2.3.2 Flavor Axial Form Factors

Taking the axial charge of u, d and s, and assuming the charge symmetry between the proton and neutron, Eqn. 2.21 leads to

$$G_A^{Z,p} = \sum_{j=\text{quarks}} c_A^j G_A^{j,p} = -(G_A^u - G_A^d) + G_A^s \,,$$
$$G_A^{Z,n} = \sum_{j=\text{quarks}} c_A^j G_A^{j,n} = (G_A^u - G_A^d) + G_A^s \,. \tag{2.46}$$

Again, the "p" superscripts in the flavor axial form factors are implicit. Eqn. 1.11 implies that at zero momentum transfer, the axial flavor form factor G_A^j of quark j is normalized to Δq_j, the contribution of quark j to the net spin of the proton, i.e.

$$G_A^j(0) = \Delta q_j \,. \tag{2.47}$$

The same SU(3) re-parameterization (Eqn. 2.40) can be made for the axial form factor G_A^Z. In the literature (see, e.g., [Mus94]), to emphasize the strange axial form factor, G_A^Z is usually decomposed in terms of an isovector form factor $G_A^{T=1}$, an SU(3) octet (isoscalar) form factor $G_A^{(8)}$, and G_A^s as

$$G_A^Z = \tau_3 Q_A^{T=1} G_A^{T=1} + Q_A^{T=0} G_A^{(8)} + Q_A^{(0)} G_A^s \,, \tag{2.48}$$

with $\tau_3 = +1(-1)$ for the proton(neutron), and $G_A^{T=1}$ and $G_A^{(8)}$ are defined as

$$G_A^{T=1} \equiv 2G_A^{(3)} = G_A^u - G_A^d \,, \tag{2.49}$$
$$G_A^{(8)} = \frac{1}{2\sqrt{3}}(G_A^u + G_A^d - 2G_A^s) \,. \tag{2.50}$$

The corresponding isovector, isoscalar and the flavor singlet charges are simply related to the axial charges of the quarks as

$$Q_A^{T=1} = \frac{1}{2}(c_A^u - c_A^d)\,, \tag{2.51}$$

$$Q_A^{T=0} = \sqrt{3}(c_A^u + c_A^d)\,, \tag{2.52}$$

$$Q_A^{(0)} = c_A^u + c_A^d + c_A^s\,. \tag{2.53}$$

At tree level, using the values in Table 2.1, we have $Q_A^{T=1} = -1\,, Q_A^{T=0} = 0\,, Q_A^s = 1$, therefore Eqn. 2.46 is simplified as

$$G_A^{Z,tree} = -\tau_3 G_A^{T=1} + G_A^s\,. \tag{2.54}$$

In neutrino-nucleon scattering, $G_A^{Z,tree}$ is a very good approximation of the axial form factor. In contrast, electroweak radiative corrections to the axial current is more significant in electron scattering. For clarity, we shall use the notation $G_A^e \equiv G_A^Z$ henceforward to denote the radiatively corrected axial form factor seen in electron scattering.

The Q^2 behavior of $G_A^{T=1}$ is generally parameterized with a dipole form as

$$G_A^{T=1}(Q^2) = \frac{G_A^{T=1}(0)}{(1+\frac{Q^2}{\Lambda_A^2})^2}\,, \tag{2.55}$$

with $\Lambda_A \sim 1.0$ GeV and

$$G_A^{T=1}(0) = \Delta u - \Delta d = -\frac{g_A}{g_V} = 1.2695 \pm 0.0029\,, \tag{2.56}$$

which is measured in neutron beta decay.

As mentioned in Sec. 1.2.3 and in Eqn. 2.47, at zero momentum transfer,

$$G_A^s(0) = \Delta s \sim -0.1 \tag{2.57}$$

Conventionally, the Q^2 evolution of G_A^s is assumed to be the same as $G_A^{T=1}$.

2.4 Experimental Observables: Parity Violating Asymmetry and the Neutral Weak Form Factors

As shown in Eqns. 2.27, 2.28 and 2.29, a measurement of the neutral weak form factor $G_{E,M}^{Z,p}$ would make the flavor separation possible. McKeown and Beck [Mck89, Bec89] proposed an experimental probe, namely the parity violating (PV) elastic electron-nucleon ($e-N$) scattering, to measured $G_{E,M}^{Z,p}$. The formalism of PV elastic $e-N$ scattering shall be discussed in this section.

Elastic $e-N$ scattering is dominated by the EM interaction, in which electron and nucleon exchange a photon γ. However, there is also a small contribution from the neutral current interaction, where a Z^0 boson is exchanged. The tree level Feynman diagrams describing these two processes are shown in Fig. 2.2.

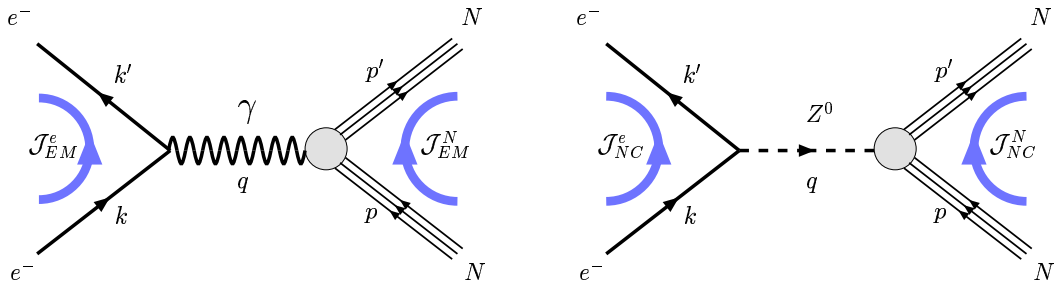

(a) γ *exchange.* (b) Z^0 *exchange*

Figure 2.2: *The tree level Feynman diagrams of the elastic electron-nucleon scattering via EM and neutral current interactions.*

The invariant amplitude of the scattering can be written using the standard Feynman rules: it is simply the gauge boson propagator, sandwiched between the electron and nucleon currents with coupling constant of the interaction. For the EM interaction in Fig. 2.2(a), the invariant amplitude is

$$\mathcal{M}_\gamma = 4\pi\alpha \mathcal{J}^{\mu,e}_{\rm EM} \frac{g_{\mu\nu}}{Q^2} \mathcal{J}^{\nu,N}_{\rm EM} \,, \tag{2.58}$$

in which $\alpha = 7.297 \times 10^{-3}$ is the fine structure constant, $Q^2 = -q^2 = (p' - p)^2 = (k' - k)^2 > 0$ is the four-momentum transfer squared. $\mathcal{J}^{\mu,e}_{\rm EM}$ is the electron EM

current, which takes the simple form for the point-like fermions given by Eqn. 2.5, and $\mathcal{J}_{\rm EM}^{\nu,N}$ is the nucleon EM current given by Eqn. 2.15.

The invariant amplitude of the neutral current diagram in Fig. 2.2(b) can be written out similarly:

$$\mathcal{M}_Z = \frac{g^2}{16\cos^2\theta_W}\mathcal{J}_{\rm NC}^{\mu,e}\frac{g_{\mu\nu} - q_\mu q_\nu/M_Z^2}{Q^2 - M_Z^2}\mathcal{J}_{\rm NC}^{\nu,N}\,, \tag{2.59}$$

where $g = 0.653$ is a dimensionless electroweak coupling constant [PDG04], θ_W is the Weinberg angle, $M_Z = 91.19$ GeV is the mass of the Z boson [PDG04], and $\mathcal{J}_{\rm NC}^{\mu,e}$ and $\mathcal{J}_{\rm NC}^{\nu,N}$ are the electron and nucleon neutral currents from Eqns. 2.6 and 2.16, respectively. At relatively low momentum transfer ($Q^2 < 1$ (GeV/c)^2), the Q^2 dependence of the propagator can be neglected, so the NC interaction can be simplified as a contact interaction with a coupling constant G_F, as first proposed by Fermi in the 1930's. So we have

$$\mathcal{M}_Z = -\frac{G_F g_{\mu\nu}}{2\sqrt{2}}\mathcal{J}_{\rm NC}^{\mu,e}\mathcal{J}_{\rm NC}^{\nu,N}\,, \tag{2.60}$$

$$G_F \equiv \frac{\sqrt{2}g^2}{8M_Z^2\cos^2\theta_W} = 1.16637\times10^{-5}{\rm GeV}^{-2}\,. \tag{2.61}$$

The total invariant amplitude of $e-N$ elastic scattering is a coherent sum of $\mathcal{M}_\gamma$ and $\mathcal{M}_Z$

$$\mathcal{M}_{tot} = \mathcal{M}_\gamma + \mathcal{M}_Z\,. \tag{2.62}$$

The scattering probability $d\sigma$ is proportional to the invariant amplitude squared:

$$d\sigma \propto |\mathcal{M}_{tot}|^2 = |\mathcal{M}_\gamma|^2 + 2\mathcal{M}_\gamma^*\mathcal{M}_Z + |\mathcal{M}_Z|^2\,, \tag{2.63}$$

in which the "*" on $\mathcal{M}_\gamma$ implies the complex conjugate.

Assuming the contributions of $\mathcal{J}$'s in Eqns. 2.58 and 2.60 are comparable, the orders of magnitude of the three terms in Eqn. 2.63 can be estimated. For example,

at $Q^2 \sim 1(\mathrm{GeV/c})^2$, one gets

$$|\mathcal{M}_\gamma|^2 : 2\mathcal{M}_\gamma^* \mathcal{M}_Z : |\mathcal{M}_Z|^2 \sim \left(\frac{4\pi\alpha}{Q^2}\right)^2 : 2\frac{4\pi\alpha}{Q^2}\frac{G_F}{2\sqrt{2}} : \left(\frac{G_F}{2\sqrt{2}}\right)^2 \sim 1 : 2\times10^{-4} : 9\times10^{-9}\,.$$

Clearly, the absolute cross section ($d\sigma \propto |\mathcal{M}_{tot}|^2$) is not a sensitive observable to measure the neutral current effect. On the other hand, since the weak interaction disrespects parity, the parity violation in $e-N$ elastic scattering solely arises from the interference term $2\mathcal{M}_\gamma^* \mathcal{M}_Z$. Therefore, a measurement of the parity violating asymmetry in elastic $e-N$ scattering will allow a determination of the neutral current contribution.

To make this discussion more self-contained, let us outline the experimental principle of parity violating electron scattering. In this type of experiment, a longitudinally polarized beam is used with an unpolarized target. The helicity of the electron is defined as the projection of the spin onto its momentum direction

$$\hat{h} = \frac{\vec{s}\cdot\vec{k}}{|\vec{s}||\vec{k}|}\,, \tag{2.64}$$

and $\hat{h}$ has two eigenvalues: $\lambda = +1$ or "right-handed" for spin and momentum aligned, and $\lambda = -1$ or "left-handed" for anti-aligned. With an unpolarized target, the only (parity violating) pseudoscalar one can construct is $\vec{s}\cdot\vec{k} \propto \lambda$. Therefore, a scattering process correlated with λ violates parity. Experimentally, the helicity of the electron is flipped back and forth, and the parity violating asymmetry is defined as the relative difference in the scattering cross section between the two helicity states of the electron

$$A_{PV} = \frac{d\sigma_R - d\sigma_L}{d\sigma_R + d\sigma_L}\,. \tag{2.65}$$

Notice that, since this is a measurement of the relative difference, to first order the luminosity of the beam and the spectrometer acceptance cancel out, which reduce the sensitivity to the experimental systematics significantly.

Now let us try to connect A_{PV} with physics. Using the V$-$A prescription in Eqns. 2.6 and 2.16, we can split $\mathcal{M}_Z$ into its V$-$V, A$-$A, V$-$A and A$-$V compo-

nents:

$$\begin{aligned}\mathcal{M}_Z &= -\frac{G_F}{2\sqrt{2}} g_{\mu\nu} \left[\mathcal{J}^{\mu,e}_{\mathrm{NC,V}} \mathcal{J}^{\nu,N}_{\mathrm{NC,V}} + \mathcal{J}^{\mu,e}_{\mathrm{NC,A}} \mathcal{J}^{\nu,N}_{\mathrm{NC,A}} + \mathcal{J}^{\mu,e}_{\mathrm{NC,V}} \mathcal{J}^{\nu,N}_{\mathrm{NC,A}} + \mathcal{J}^{\mu,e}_{\mathrm{NC,A}} \mathcal{J}^{\nu,N}_{\mathrm{NC,V}} \right] \\ &\equiv \mathcal{M}_{Z,VV} + \mathcal{M}_{Z,AA} + \mathcal{M}_{Z,VA} + \mathcal{M}_{Z,AV} \,, \end{aligned} \tag{2.66}$$

in which the the subscripts imply the couplings of Z^0 to the electron (first) and the nucleon (second), e.g., "VA" means the vector coupling of electron and axial coupling of nucleon to Z^0. A Lorentz vector conserves parity and an axial vector maximally violates parity [PS95], which implies that both $\mathcal{M}_{Z,VV}$ and $\mathcal{M}_{Z,AA}$ conserve parity, whereas $\mathcal{M}_{Z,VA}$ and $\mathcal{M}_{Z,AV}$ violate it. Mathematically, the PV terms are those containing odd numbers of γ_5. So we decompose $\mathcal{M}_Z$ into a parity conserving and a parity violating term as

$$\begin{aligned} \mathcal{M}_Z &= \mathcal{M}_Z^{PC} + \mathcal{M}_Z^{PV} \,, \\ \mathcal{M}_Z^{PC} &\equiv \mathcal{M}_{Z,VV} + \mathcal{M}_{Z,AA} \equiv -\frac{G_F}{2\sqrt{2}} g_{\mu\nu} \left[\mathcal{J}^{\mu,e}_{\mathrm{NC,V}} \mathcal{J}^{\nu,N}_{\mathrm{NC,V}} + \mathcal{J}^{\mu,e}_{\mathrm{NC,A}} \mathcal{J}^{\nu,N}_{\mathrm{NC,A}} \right] \,, \\ \mathcal{M}_Z^{PV} &\equiv \mathcal{M}_{Z,VA} + \mathcal{M}_{Z,AV} \equiv -\frac{G_F}{2\sqrt{2}} g_{\mu\nu} \left[\mathcal{J}^{\mu,e}_{\mathrm{NC,V}} \mathcal{J}^{\nu,N}_{\mathrm{NC,A}} + \mathcal{J}^{\mu,e}_{\mathrm{NC,A}} \mathcal{J}^{\nu,N}_{\mathrm{NC,V}} \right] \,. \end{aligned} \tag{2.67}$$

Ignoring the tiny third term in Eqn. 2.63, A_{PV} can be cast into

$$\begin{aligned} A_{PV} &= \frac{2\mathcal{M}_\gamma^* \mathcal{M}_Z^{PV}}{|\mathcal{M}_\gamma|^2 + 2\mathcal{M}_\gamma^* \mathcal{M}_Z} \sim \frac{2\mathcal{M}_\gamma^* \mathcal{M}_Z^{PV}}{|\mathcal{M}_\gamma|^2} \\ &= -\frac{G_F Q^2}{2\sqrt{2}\pi\alpha} \frac{2 g_{\mu\nu} (\mathcal{J}^{e,\mu}_{\mathrm{EM}} \mathcal{J}^{N,\nu}_{\mathrm{EM}})^* g_{\alpha\beta} \left(\mathcal{J}^{e,\alpha}_{\mathrm{NC,V}} \mathcal{J}^{N,\beta}_{\mathrm{NC,A}} + \mathcal{J}^{e,\alpha}_{\mathrm{NC,A}} \mathcal{J}^{N,\beta}_{\mathrm{NC,V}} \right)}{|g_{\mu\nu} \mathcal{J}^{e,\mu}_{\mathrm{EM}} \mathcal{J}^{N,\nu}_{\mathrm{EM}}|^2} \,, \end{aligned} \tag{2.68}$$

in which the EM and neutral currents of the electron and nucleon are written out explicitly in Eqns. 2.5,2.6, 2.15, and 2.16.

After a standard calculation [RS74], A_{PV} becomes

$$A_{PV} = -\frac{G_F Q^2}{4\sqrt{2}\pi\alpha} \frac{\epsilon G_E^\gamma G_E^Z + \tau G_M^\gamma G_M^Z - (1 - 4\sin^2\theta_W)\epsilon' G_M^\gamma G_A^e}{\epsilon (G_E^\gamma)^2 + \tau (G_M^\gamma)^2} \,, \tag{2.69}$$

with

$$\tau = \frac{Q^2}{4M_N^2}, \quad \epsilon = \left(1 + 2(1+\tau)\tan^2\frac{\theta_e}{2}\right)^{-1}, \quad \epsilon' = \sqrt{\tau(1+\tau)(1-\epsilon^2)}\,, \tag{2.70}$$

where θ_e is the lab angle of the scattered electron, and M_N is the mass of the nucleon. For elastic scattering, the kinematics is fixed once the beam energy and Q^2 are known. Two additional useful kinematic relations are

$$Q^2 = 4E_b E' \sin^2(\frac{\theta_e}{2})\,, \quad E' = E_b - \frac{Q^2}{2M_N}\,, \tag{2.71}$$

where E_b and E' are the incident the scattered electron energies. Several observations can be made at this point. First, in Eqn. 2.69, $\epsilon G_E^\gamma G_E^Z + \tau G_M^\gamma G_M^Z$ arises from $\mathcal{M}_{AV}$ (or $A(e) \times V(N)$) and $-(1-4\sin^2\theta_W)G_A^e$ arises from $\mathcal{M}_{VA}$ (or $V(e) \times A(N)$), of which $-(1-4\sin^2\theta_W)$ is the weak vector charge of the electron. Second, Eqn. 2.69 is a generic formula for elastic electron-nucleon scattering. To get the asymmetry of the proton or neutron, one simply feeds the corresponding form factors into the right-hand side of the equation. Third, if all but the neutral current form factors are known, a measurement of A_{PV} leads to a linear combination of G_E^Z and G_M^Z using Eqn. 2.69.

Substituting the proton weak form factor $G_{E,M}^{Z,p}$ by Eqn. 2.44, and G_A^e by Eqn. 2.48 (with $\tau_3 = 1$ for the proton), Eqn. 2.69 becomes

$$\begin{aligned} A_{PV} = & -\frac{G_F Q^2}{4\sqrt{2}\pi\alpha}\frac{1}{\epsilon(G_E^p)^2 + \tau(G_M^p)^2} \\ & \times\{(\epsilon(G_E^p)^2 + \tau(G_M^p)^2)Q_W^p + (\epsilon G_E^p G_E^n + \tau G_M^p G_M^n)Q_W^n \\ & + \epsilon G_E^p(G_E^s + \eta G_M^s)Q_W^{(0)} \\ & - \epsilon'(1-4\sin^2\theta_W)G_M^p(Q_A^{T=1}G_A^{T=1} + Q_A^{T=0}G_A^{(8)} + Q_A^s G_A^s)\}\,, \end{aligned} \tag{2.72}$$

in which $\eta = \frac{\tau G_M^p}{\epsilon G_E^p}$. Therefore, if one treats the nucleon EM and axial form factors as known, a measurement of the PV asymmetry leads to a linear combination of G_E^s and G_M^s. The parity violating asymmetry for the neutron can be obtained by

exchanging the "p" and "n" indices on nucleon form factors (but keep the indices of the weak charge unchanged), replacing the proton form factors by those of the neutron in the expression of η, and adding a negative sign to $G_A^{T=1}$ term in Eqn. 2.72. For later convenience, we define the isovector component of the axial form factor as

$$G_A^{e(T=1)} = Q_A^{T=1} G_A^{T=1} \,, \tag{2.73}$$

and we shall see in Sec. 2.5 that $Q_A^{T=1}$ is subject to significant electroweak radiative corrections.

At a given four-momentum transfer, two measurements with different kinematics are needed to separate G_E^s and G_M^s, just like the standard Rosenbluth separation in cross section measurements [Ros50]. To demonstrate the sensitivities of different observables to the kinematics, η, ϵ and ϵ' vs. electron scattering angle are shown in Fig. 2.3 for $Q^2 = 0.25$ (GeV/c)^2. For completeness the beam energy E_b as a function of the electron angle is also overlaid. One sees, first of all, that η starts from small values at the forward angle, then increases with θ_e (quite drastically at the backward angle). Therefore a forward (backward) angle experiment is more sensitive to G_E^s (G_M^s). One should note however, that ϵ' also increases with scattering angle, therefore the sensitivity to the axial form factor is also enhanced in backward angle experiment. Therefore, a better constrained electroweak radiative correction to the axial form factor is important for interpreting the result of the backward angle experiment. A measurement of the backward parity violating asymmetry of quasielastic scattering form deuterium will in this regard serve as a control experiment. Under the static approximation, the quasielastic asymmetry is

$$A_d = \frac{A_p \sigma_p + A_n \sigma_n}{\sigma_p + \sigma_n} \,, \tag{2.74}$$

in which A_p (A_n) and σ_p (σ_n) are the parity violating asymmetry and cross section for elastic scattering from proton (neutron). It can be shown that the relative sensitivity of A_d to $G_A^{e(T=1)}$ is further enhanced as compared to a backward proton measurement [Mus94]. Obviously one has to apply nuclear corrections to Eqn. 2.74,

but the above observation remains valid. Therefore by combining a proton forward and backward, as well as a deuterium backward measurement, one can make a model independent separation of G_E^s, G_M^s and $G_A^{e(T=1)}$. The full G^0 physics program is designed to perform these measurements at a few different values of four-momentum transfer.

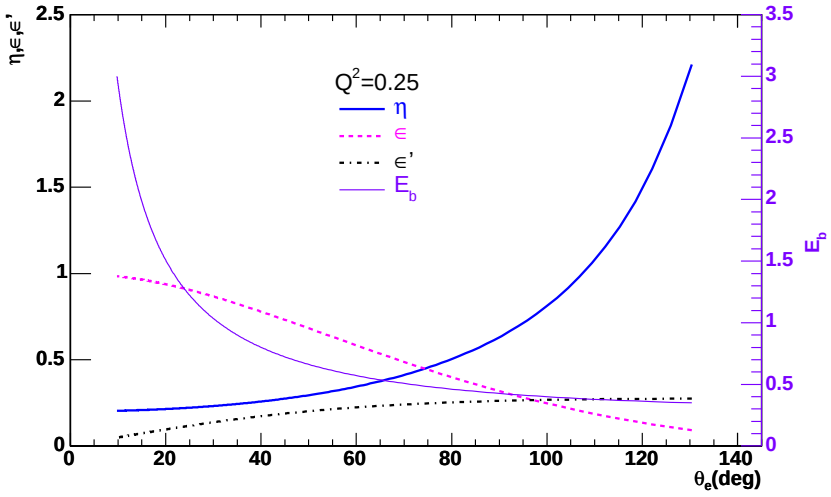

Figure 2.3: *The dependence of η (blue solid), ϵ (pink dashed) and ϵ' (black dot-dashed) on the electron scattering angle for $Q^2 = 0.25$ $(GeV/c)^2$. The required beam energy (solid purple) at different angle is also overlaid.*

2.5 Electroweak Radiative Corrections to the Neutral Current

So far Eqn. 2.72 only contains the lowest order (tree level) contributions in perturbation theory. The evaluation of higher order corrections is usually called the radiative correction. One has to redefine the theory in such a way to make higher order corrections finite — the prescription of this redefinition is called the "renormalization scheme". A widely used renormalization scheme is $\overline{\text{MS}}$ (or modified minimum subtraction) [PS95], in which the correction depends on a renormalization scale μ. In most applications of the standard model, μ is set to $M_z = 91.19$ GeV (the mass of the Z boson). All of the radiative corrections to A_{PV} in this work are evaluated in $\overline{\text{MS}}$. A detailed discussion of the electroweak radiative correction

for parity violating electron scattering can be found in [Arv05]. The procedure in [Arv05] will be recapped in this section for later reference.

As shown in Eqn. 2.60, the electroweak interaction has been reduced into a contact interaction. Higher order corrections modify the coupling constant at the interaction vertex. In effect, the weak vector and axial charges are modified. Taking the tree level formula, Eqn. 2.72, the following corrections are made to the six weak charges:

$$\begin{aligned}
&\text{Tree level} && \Longrightarrow && \text{Rad. Corr. Included} \\
&Q_W^p = 2c_V^u + c_V^d = 1 - 4\sin^2\theta_W && \Longrightarrow && Q_W^p = (1+R_V^p)(1-4\sin^2\theta_W)\,, \\
&Q_W^n = 2c_V^d + c_V^u = -1 && \Longrightarrow && Q_W^n = -(1+R_V^n)\,, \\
&Q_W^{(0)} = c_V^u + c_V^d + c_V^s = -1 && \Longrightarrow && Q_W^{(0)} = -(1+R_V^{(0)})\,, \\
&Q_A^{T=1} = \frac{1}{2}(c_A^u - c_A^d) = -1 && \Longrightarrow && Q_A^{T=1} = -(1+R_A^{T=1})\,, \\
&Q_A^{T=0} = \sqrt{3}(c_A^u + c_A^d) = 0 && \Longrightarrow && Q_A^{T=0} = \sqrt{3}R_A^{T=0}\,, \\
&Q_A^{(0)} = c_A^u + c_A^d + c_A^s = 1 && \Longrightarrow && Q_A^{(0)} = 1 + R_A^{(0)}\,.
\end{aligned} \tag{2.75}$$

The radiative correction of the PV asymmetry can be classified into three categories: heavier quark contributions, "one-quark" and "many-quark" electroweak radiative corrections, and generically the radiative correction factor R is broken down into three additive factors:

$$R = \Delta_{\text{heavy}} + R_{\text{one-quark}} + R_{\text{many-quark}}\,. \tag{2.76}$$

The modification of the hadronic NC coupling due to the heavy quark (c, b, t) renormalizations of the light quark current operator is called the heavy quark correction. This effect is estimated in [KM88] and found to be small: $\Delta_{\text{heavy}} \sim 10^{-4}$ for the vector term $(A(e) \times V(N))$ and $\sim 10^{-2}$ for the axial term $(V(e) \times A(N))$, and is therefore neglected in this work.

The "one-quark" correction collectively stands for the higher order corrections to the scattering, in which only a single quark is involved. Its contribution can be

evaluated rather reliably within the standard model, and there is a gentle dependence on Q^2 [Mus94, Zhu00]. Two representative higher order "one-quark" diagrams are shown in Fig. 2.4. Fig. 2.4(a) is the so-called $\gamma{-}Z^0$ mixing diagram, in which a Z^0 and γ couple to a $q\bar{q}$ loop. It is sometimes referred to as the vacuum polarization correction, analogous to a similar concept in QED. Fig. 2.4(b) is the so-called $\gamma{-}Z^0$ box diagram. It is assumed in this work that the "one-quark" correction has been performed reliably and has been reflected in the standard model parameters in the particle data book (PDG) [PDG04]. One should keep in mind, however, that there is still room for uncertainties. For example, the authors in [BH01] pointed out that the calculation of the $\gamma{-}Z^0$ box diagram involves excited hadronic states, which is not completely under control.

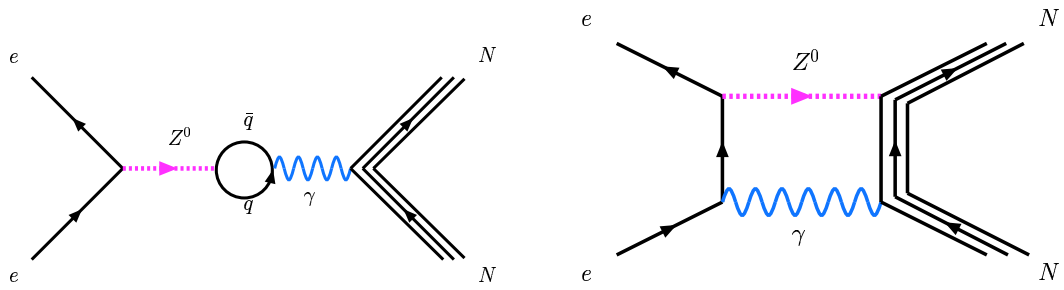

(a) $\gamma{-}Z^0$ *mixing diagram* (b) $\gamma{-}Z^0$ *box diagram*

Figure 2.4: *Two representative "one-quark" radiative correction diagrams.*

We shall next present the procedure of incorporating the PDG parameters into our formalism. For the PV electron scattering, PDG uses a set of constants, C_{1u}, C_{1d}, C_{2u} and C_{2d}, to describe the coupling of the electron current to the quark current. Specifically, C_{1u} and C_{1d} (C_{2u} and C_{2d}) are the parity violating coupling of $A(e) \times V(q)$ ($V(e) \times A(q)$) with "e" and "q" representing the electron and quark, respectively. Note that C_{1u} and C_{2u} (C_{1d} and C_{2d}) shall be applied to u, c, t (d, s, b). The C parameters, after the radiative corrections, are dressed into the following

forms [PDG04]

$$
\begin{aligned}
C_{1u} &= \rho_1(-\frac{1}{2} + \frac{4}{3}\kappa_1\hat{s}_Z^2) + \lambda_{1u}\,, \\
C_{1d} &= \rho_1(\frac{1}{2} - \frac{2}{3}\kappa_1\hat{s}_Z^2) + \lambda_{1d}\,, \\
C_{2u} &= \rho_2(-\frac{1}{2} + 2\kappa_2\hat{s}_Z^2) + \lambda_{2u}\,, \\
C_{2d} &= \rho_2(\frac{1}{2} - 2\kappa_2\hat{s}_Z^2) + \lambda_{2d}\,,
\end{aligned}
\tag{2.77}
$$

in which all quantities are evaluated in $\overline{MS}$, and $\hat{s}_Z^2 = 0.23120(15)$ is $\sin^2\theta_W$ with the renormalization scale at M_Z. At the tree level, $\rho_1 = \rho_2 = \kappa_1 = \kappa_2 = 1$ and $\lambda_{1u} = \lambda_{1d} = \lambda_{2u} = \lambda_{2d} = 0$. The connections between these set of C parameters and the c_V and c_A parameters in Eqn. 2.75 are

$$
\begin{aligned}
c_V^{u,c,t} &= -2C_{1u}\,, & c_V^{d,s,b} &= -2C_{1d}\,, \\
c_A^{u,c,t} &= \frac{2C_{2u}}{1 - 4\sin^2\theta_W}\,, & c_A^{d,s,b} &= \frac{2C_{2d}}{1 - 4\sin^2\theta_W}\,.
\end{aligned}
\tag{2.78}
$$

In Table 2.2, the ρ, κ, λ parameters in [PDG04], as well as our calculated values of the C and c parameters are listed. The standard model (SM) values of the weak charges of the nucleon, and the corresponding R factors, can then be computed by substituting the tree level c parameters by their SM values. The tree level and the SM weak charges, and their corresponding correction R factors are summarized in Table 2.3. Since [PDG04] does not provide uncertainties for the ρ, κ and λ parameters, we estimate their uncertainties based on a comparison with previous releases of the PDG. The resulting uncertainties of the weak charges (including the contribution due to $\hat{s}_Z^2$) are reflected in the uncertainties of the R factors summarized in parentheses in Table 2.3. Their effects are negligible compared to the "many-quark" correction to the axial charges, as will be discussed next.

The "many-quark" or anapole correction to the parity violating asymmetry involves an axial coupling of the photon to the nucleon, leading to the so-called anapole moment of the nucleon [BH01]. The underlying process is that during the

PDG ρ, κ, λ parameters

Parameter	Tree	SM
$\hat{s}_Z^2$		0.23120(15)
ρ_1	1	0.9881
ρ_2	1	1.0011
κ_1	1	1.0027
κ_2	1	1.0300
λ_{1u}	0	-1.85×10^{-5}
λ_{1d}	0	3.7×10^{-5}
λ_{2u}	0	-0.0121
λ_{2d}	0	0.0026

C and c parameters

Parameter	Tree	SM
C_{1u}	-0.191733	-0.188648
C_{1d}	0.345867	0.341377
C_{2u}	-0.0376	-0.0358541
C_{2d}	0.0376	0.0263541
$c_V^{u,c,t}$	0.383467	0.377296
$c_V^{d,s,b}$	-0.691733	-0.682753
$c_A^{u,c,t}$	-1	-0.953567
$c_A^{d,s,b}$	1	0.700907

Table 2.2: *The tree level and radiatively corrected ("one-quark") electroweak coupling parameters for electron-quark interactions. The table on the left contains the values from [PDG04]. The right table contains the C and c parameters calculated from Eqn. 2.77 and Eqn. 2.78.*

Quantity	Tree	SM	R Factor	Value
Q_W^p	0.0752	0.0718379	R_V^p	$-0.045(3)$
Q_W^n	-1	-0.988211	R_V^n	$-0.0118(2)$
$Q_W^{(0)}$	-1	-0.988211	$R_V^{(0)}$	$-0.0118(2)$
$Q_A^{T=1}$	-1	-0.827237	$R_A^{T=1}$	$-0.173(3)$
$Q_A^{T=0}$	0	-0.437619	$R_A^{T=0}$	$-0.253(2)$
$Q_A^{(0)}$	1	0.448247	$R_A^{(0)}$	$-0.552(5)$

Table 2.3: *The tree level and ("one-quark") radiatively corrected weak charges, and the radiative correction factors, defined in Eqn. 2.75. The uncertainties of the weak charges due to $\hat{s}_Z^2$ and the ρ, κ and λ parameters are reflected in the uncertainties of the R factors in parentheses.*

scattering, quarks inside the nucleon interact via exchanging a weak boson, which effectively induces a modification to the nucleon axial coupling. One such process

is depicted in Fig. 2.5, in which the weak interaction between quarks generates a parity violating pion emission (pink crossed circle), followed by a parity-conserving pion absorption (blue open circle) through the strong interaction. To date, there are still significant theoretical uncertainties to the "many-quark" corrections, since it is impossible to include all virtual hadronic states in the calculation. Nevertheless, it should be noted that the "many-quark" correction only affects the axial contribution.

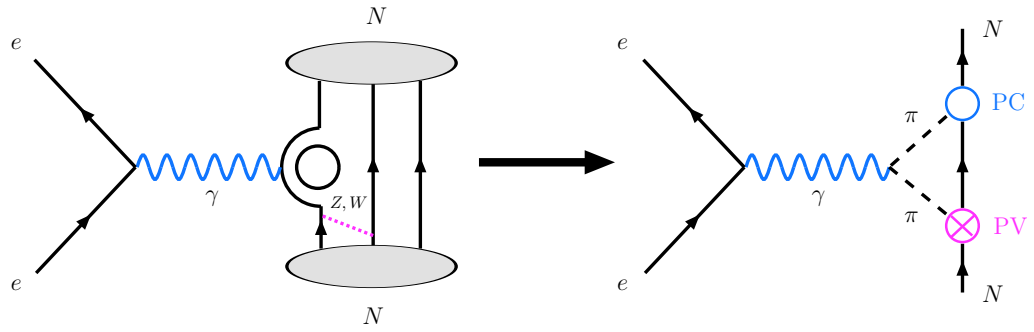

Figure 2.5: *One representative "many-quark" diagram.*

Recently, Zhu et al. made an evaluation of the anapole correction to the axial form factor [Zhu00]. Under the framework of HBχPT (see Sec. 2.6.1), the authors carried out a complete calculation of the "many-quark" diagrams, including Fig. 2.5, to the order of $\frac{p^2}{\Lambda_\chi^2}$ †. The authors expressed their results into two terms, $R_A^{T=1}$("many-quark") and $R_A^{T=0}$("many-quark"), in the on-shell renormalization (OSR) scheme. The prescription to cast R from OSR to $\overline{MS}$ involves a simple normalization [Zhu00]

$$\frac{R_{\bar{MS}}}{R_{OSR}} = \frac{1-4s_W^2}{1-4\hat{s}_Z^2} = 1.45\,, \tag{2.79}$$

in which $\hat{s}_Z^2 = 0.23120(15)$ is $\sin^2\theta_W$ in $\overline{MS}$, and $s_W^2 = 0.2228(4)$ is that in the OSR [PDG04]. After the normalization, the "many-quark" correction should be combined with the corresponding "one-quark" corrections from Table 2.3. This procedure is contained in Table 2.5. Since no evaluation of $R_A^{(0)}$(many-quark) has been made in the literature, we simply use the "one-quark" value for $R_A^{(0)}$ and assign

† p is a momentum of the order of pion mass and $\Lambda_\chi \sim 1$ GeV is scale of the chiral symmetry breaking.

100% fractional uncertainty to it.

	$R_A^{T=1}$	$R_A^{T=0}$	$R_A^{(0)}$
one-quark	$-0.173(3)$	$-0.253(2)$	$-0.552(5)$
many-quark	$-0.087(0.35)$	$0.015(0.20)$	N/A
total	$-0.26(0.35)$	$-0.24(0.20)$	$-0.55(0.55)$

Table 2.4: *The "one-quark" [PDG04] and "many-quark" [Zhu00] corrections to the axial charges, both in $\overline{MS}$, as well as the total corrections.*

To conclude this section, we combine Eqn. 2.72 with the radiatively corrected weak charges in Eqn. 2.75, and write out the full expression of parity violating asymmetry for the proton as

$$\begin{aligned} A_{PV} = & -\frac{G_F Q^2}{4\sqrt{2}\pi\alpha}\frac{1}{[\epsilon(G_E^p)^2+\tau(G_M^p)^2]} \\ & \times\{(\epsilon(G_E^p)^2+\tau(G_M^p)^2)(1-4\sin^2\theta_W)(1+R_V^p) \\ & -(\epsilon G_E^p G_E^n+\tau G_M^p G_M^n)(1+R_V^n) \\ & -\epsilon G_E^p(G_E^s+\eta G_M^s)(1+R_V^{(0)}) \\ & -\epsilon'(1-4\sin^2\theta_W)G_M^p G_A^e\}\,, \end{aligned} \tag{2.80}$$

in which

$$G_A^e = -(1+R_A^{T=1})G_A^{T=1}+\sqrt{3}R_A^{T=0}G_A^{(8)}+(1+R_A^{(0)})G_A^s\,. \tag{2.81}$$

and

$$\tau=\frac{Q^2}{4M_p^2}\,,\quad \epsilon=\left(1+2(1+\tau)\tan^2\frac{\theta}{2}\right)^{-1}\,,\quad \epsilon'=\sqrt{\tau(1+\tau)(1-\epsilon^2)}\,,\quad \eta=\frac{\tau G_M^p}{\epsilon G_E^p}\,.$$

2.6 Theoretical Predictions of G_E^s and G_M^s

In this section, a survey of various theoretical approaches to describe the strangeness of the nucleon and their predictions will be presented. An excellent review on this topic (from a more theoretical ground) can be found in [BH01].

Let us first define observables. In the literature, two quantities are commonly

used to capture the behavior of G_E^s and G_M^s at zero momentum transfer: $\langle r_s^2 \rangle_E$ and μ_s. The strange magnetic moment has already been defined in Eqn. 2.34 as $\mu_s \equiv G_M^s(Q^2 = 0)$. It has also been mentioned that $-\frac{1}{3}\mu_s$ gives the strange quark contribution to the nucleon magnetic moment (Eqns. 2.27 and 2.28) in units of Born nucleon magneton (n.m.). The strangeness mean square radius $\langle r_s^2 \rangle_E$ is defined as

$$\langle r_s^2 \rangle_E = -6 \frac{dG_E^s}{dQ^2}(Q^2 = 0)\,, \tag{2.82}$$

which is also often called the Sachs strangeness radius. Some authors define the strangeness radius $\langle r_s^2 \rangle$ as the slope of the Dirac form factor (F_1^s) instead:

$$\langle r_s^2 \rangle = -6 \frac{dF_1^s}{dQ^2}(Q^2 = 0)\,. \tag{2.83}$$

For clarification, we add the subscript "E" on the Sachs radius and note that it is the Sachs radius that gives the mean square radius of the strangeness "charge" distribution. A positive $\langle r_s^2 \rangle_E$ implies that the s quark is spatially further away from the center of the nucleon than $\bar{s}$ and vice versa [BH01]. According to Eqn. 2.13, the two radii are related by

$$\begin{aligned} \langle r_s^2 \rangle &= \langle r_s^2 \rangle_E - \frac{6}{4M^2}\mu_s \\ &= \langle r_s^2 \rangle_E - 0.066\mu_s\,. \end{aligned} \tag{2.84}$$

In the second expression, the nucleon mass M has been converted into the dimension of inverse length ($\sim$4.8 fm^{-1}) and the units of both sides of the equation are fm^2. Like μ_s, $-\frac{1}{3}\langle r_s^2 \rangle_E$ gives the contribution of the strange quark to the nucleon charge radius (see Eqns. 2.27 and 2.28). Although these two quantities do not contain the entire picture, we shall see that the predictions of them are already widely-spread enough to differentiate between models. Just to set the scale, the proton's magnetic moment is $\mu_p = 2.793$ n.m. and the neutron's charge radius [†] is $\langle r_n^2 \rangle_E = -0.12$ fm^2 [PDG04].

[†] The strangeness charge radius is more naturally to be compared to the neutron's, since neutron is an overall charge neutral object.

The calculation of static properties of the nucleon in QCD from first principle is one of the most difficult problems in hadronic physics. Unlike that of QED, the strong coupling constant (α_s) is of the order of unity at low energy. Therefore one cannot construct a natural perturbative expansion of the interaction in a power series of α_s. Instead, one has to seek other frameworks in which controlled approximations can be made based on general principles.

One of such general principles is the (broken) chiral symmetry in QCD. Let us consider the world with only the lightest three quark flavors, (u, d, s). In the limit that all these quarks are massless, the QCD Lagrangian possesses a global symmetry: it is invariant if the left-handed and right-handed quarks make independent rotations in the flavor space. This is the so-called chiral symmetry, which is represented by the symmetry group of $\mathrm{SU}(3)_L \times \mathrm{SU}(3)_R$. Since the physical masses of the three quarks (m_u, m_d and m_s) are much less than the typical hadronic scale (1 GeV), the massless approximation above is reasonably justified. The exact chiral symmetry leads to 16 conserved currents, 8 of them are vector currents ($L+R$) and the others are axial currents ($L-R$). In reality, $\mathrm{SU}(3)_L \times \mathrm{SU}(3)_R$ symmetry is *spontaneously* broken into a vector SU(3) flavor symmetry ($\mathrm{SU}(3)_V$), i.e., the ground state (vacuum) is asymmetric under the action of the axial charges. This implies that there are 8 *massless* Goldstone bosons (which are energetically degenerate with the vacuum), associated with the eight broken generators [TW00]. They are identified as the lightest pseudoscalar ($J^\pi = 0^-$) mesons, π's, K's and η. In a physical world, the non-zero masses of the quarks break the chiral symmetry *explicitly*. By this means, the pseudoscalar mesons acquire their physical masses. Nonetheless, due to the smallness of the light quark masses, the masses of pions, kaons and η (m_π, m_K and m_η) are considerably less than the mass of, say, the lightest non-Goldstone hadron, ρ. One should also note that $m_\pi \ll m_K \sim m_\eta$ reflects the mass hierarchy that $m_u, m_d \ll m_s$. At low energy, these pseudoscalar mesons can be treated as effective degrees of freedom that incorporate the symmetry of QCD. The quarks and gluons do not show up explicitly here, as a consequence of confinement. As was realized by Weinberg [Wei79], the Goldstone bosons interact weakly, and the loop

corrections are suppressed by orders of (p/Λ_χ), in which $\Lambda_\chi \sim 1$ GeV is the chiral symmetry breaking scale, and p collectively represents momentum or pseudoscalar meson masses that satisfy $p \ll \Lambda_\chi$. This suggests that at low energy, the effective interaction between Goldstone bosons can be treated perturbatively. In two seminal papers by Gasser and Leutwyler [Gas84, Gas85], this approach was systematically elaborated, which gave birth to the so-called chiral perturbation theory (χPT).

For the simplest two-flavor (u, d) case, the effective calculation in the meson sector only involves two parameters, the mass of the pion ($m_\pi \sim 135$ MeV) and the pion decay constant ($F_\pi \sim 92$ MeV). F_π effectively contains the transition amplitude of the Goldstone boson into the vacuum via the action of the broken axial charges; it therefore reflects the *spontaneously* broken chiral symmetry of the theory. m_π effectively captures the small quark masses, which *explicitly* break the chiral symmetry. When the loop corrections are included, however, one must insert counterterms into the effective Lagrangian to absorb infinities. These counterterms have unknown coefficients, called the low energy constants, which can only be fixed from experiments. This is a feature of χPT. SU(2) χPT has yielded enormous success in describing the interaction in the meson sector.

It is natural to extend this treatment to nucleons. However, the situation is complicated substantially since there now exist three parameters in the theory, m_π, F_π, and m_N, in which m_N is the mass of the nucleon. m_N does not vanish in the chiral limit ($m_u = m_d = m_s = 0$), and m_N is the same scale as the chiral symmetry breaking scale Λ_χ, which spoils the natural perturbative scheme. The problem was overcome by the proposal by Jenkins and Manohar [JM91], who suggested to treat the nucleons as *very* heavy, so that the dependence on m_N can be absorbed into a series of interaction vertices with increasing power of $1/m_N$. Then a consistent perturbative expansion of the theory emerges. This theoretical framework is the so-called heavy baryon chiral perturbation theory (HBχPT). Since most of the models that describe the nucleon strangeness are more-or-less related to it, we will present the application of HBχPT to the strange form factors first.

2.6.1 Heavy Baryon Chiral Perturbation Theory (HBχPT)

To include the strangeness in the calculation, one has to extend HBχPT from SU(2) to SU(3). The inclusion of the (kaon) loops introduces additional phenomenological counterterms. Some of these counterterms can be fixed by the experimental EM moments of the baryon octet, but two remaining singlet counterterms require knowledge of strangeness radius and magnetic moment, which are precisely the terms we seek to determine. Therefore HBχPT cannot predict nucleon strangeness [RMI97]. Despite this fact, Hemmert, Meissner and Steininger realized that to the order of p^3 ($\mathcal{O}(p^3)$) in the chiral expansion, the Q^2 behavior of G_M^s is dictated by the kaon loop diagram, which has an analytical and parameter free form [HMS98]. Shortly after, in [HKM99], Hemmert, Kubis and Meissner derived an expression of $G_E^s(Q^2)$ to $\mathcal{O}(p^3)$ in terms of the two unknown counterterms and argued that they could be fixed by the data from SAMPLE and HAPPEx [†]. From this treatment, the authors obtained strangeness radius of $\langle r_s^2 \rangle_E = 0.05 \pm 0.09$ fm^2 and a positive strangeness magnetic moment ($\mu_s \sim$0.18 n.m.). However, when the calculation was extended to $\mathcal{O}(p^4)$, Hammer et al. showed that there is a significant cancellation between the contributions from $\mathcal{O}(p^3)$ and $\mathcal{O}(p^4)$ [Ham03]. As a result, the Q^2 slope of the strange magnetic moment exhibits enhanced sensitivity to the unknown coefficient of an $\mathcal{O}(p^4)$ counterterm, b_r^s. According to their calculation, at small momentum transfer, μ_s takes the form

$$\mu_s = G_M^s(Q^2) - (0.17 + 1.3 b_s^r) Q^2 \,, \tag{2.85}$$

with $|b_s^r| \sim 1$ being the "reasonable" scale of this low energy constant. From this updated analysis, neither the magnitude nor the sign of μ_s is rigorously constrained.

The above discussions demonstrate the difficulties of using the chiral perturbation theory to calculate the strange vector matrix element, due to the presence of unconstrained counterterms. On the other hand, progress can be made by making model assumptions about the underlying physics. We shall discuss some of the

[†]These two experiments will be discussed in Chap. 3

models in dealing with the nucleon strangeness in the next few sections.

2.6.2 Vector Meson Dominance

Vector mesons are neutral, spin 1 and parity odd mesons. In many ways they share the characteristics of a space-like photon. Historically, vector meson dominance (VMD) played a crucial role in describing photo-hadron interactions [Sak69, Fey72]. The underlying idea is that a photon can fluctuate electromagnetically into an intermediate vector meson, which subsequently interacts strongly with the hadron. The process is depicted by the Feynman diagram in Fig. 2.6.

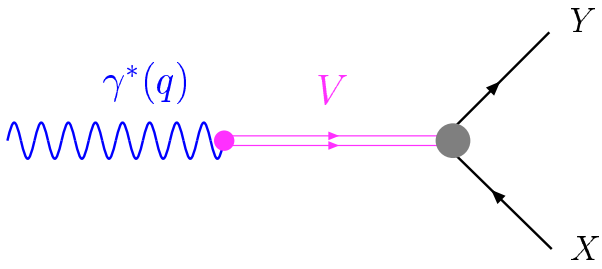

Figure 2.6: *The Feynman diagram of the vector dominance approximation. γ^* is a space-like photon, which fluctuates into an intermediate vector meson V. X and Y represent the initial and final states of the hadron.*

For the application to nucleon EM structure, VMD simply states that the nucleon matrix element $\langle N|\hat{\mathcal{J}}^{\mu}_{EM}|N\rangle$ can be written as a summation over intermediate vector states as [Fey72]

$$\langle N|\hat{\mathcal{J}}^{\mu}_{EM}|N\rangle = \sum_{V} f_V \frac{1}{m_V^2 - q^2}\langle N|V^{\mu}|N\rangle\,, \tag{2.86}$$

in which m_V is the mass of an intermediate meson V, and $q^2 < 0$ is the photon four-momentum-transfer squared, and f_V is the vector-meson-photon coupling constant. This expression can be understood diagrammatically from Fig. 2.6. f_V describes how much the physical state of the vector meson overlaps with the quark-antiquark

pairs created by the EM current operator:

$$\langle V|\hat{\mathcal{J}}^{\mu}_{EM}|0\rangle = f_V \epsilon^{\mu}\,, \tag{2.87}$$

in which $|0\rangle$ is the vacuum state and ϵ^{μ} is the polarization vector of the vector meson. The propagator of the vector meson, $\frac{1}{m_V^2-q^2}$, represents a pole (δ function) at $q^2 = m_V^2$ in the dispersive integral (see also Sec. 2.6.6). $\hat{V}^{\mu}$ is the field operator of the vector meson, and $\langle N|\hat{V}^{\mu}|N\rangle$ gives the strength of V coupling to the nucleon. An important underlying assertion of VMD is the so-called current field identity, which implies the equivalence between the field operator of the neutral vector meson and the quark current with the same quantum number [KLZ67]. Consequently, $\hat{V}^{\mu}$ is a conserved Lorentz vector current. So we can write $\langle N|\hat{V}^{\mu}|N\rangle$ in terms of two constant "form factors", g_1^{VNN} and g_2^{VNN}, similar to F_1 and F_2 defined in Eqn. 2.9.

The vector mesons with the lowest masses are ρ (770 MeV), ω (783 MeV) and ϕ (1020 MeV). The quark content of these vector mesons are

$$\rho = \frac{1}{\sqrt{2}}(u\bar{u} - d\bar{d})\,, \quad \omega_0 = \frac{1}{\sqrt{2}}(u\bar{u} + d\bar{d})\,, \quad \phi_0 = s\bar{s}\,. \tag{2.88}$$

The subscripts "0" on ω and ϕ imply that they are the flavor pure states. The small $\omega-\phi$ mixing will be taken into account a little later. One sees that ρ is an isovector meson, and ω and ϕ are isoscalars. In order to have a well-defined isospin quantum number for the vector-meson exchange, we consider the isoscalar (I=0) and isovector (I=1) nucleon form factors, defined in terms of the proton and neutron's form factors:

$$F_{1,2}^{I=0} = \frac{1}{2}(F_{1,2}^{p} + F_{1,2}^{n})\,, \quad F_{1,2}^{I=1} = \frac{1}{2}(F_{1,2}^{p} - F_{1,2}^{n})\,. \tag{2.89}$$

Let us use $F_i(q^2)$ as a generic symbol for these form factors. Based on Eqn. 2.86, $F_i(q^2)$ can be decomposed as

$$F_i(q^2) = \sum_V \frac{a_i^V}{m_V^2 - q^2}\,, \tag{2.90}$$

in which

$$a_i^V = f_V g_i^{VNN} \,. \tag{2.91}$$

Eqn. 2.90 suggests that the behavior of the form factor vs. q^2 can both be used to identify the dominating vector mesons, as well as to constrain the pole residual a_i^V. The most important vector mesons for the isovector and isoscalar channels are ρ and ω, respectively.

Höhler et al. made a global fit of the electron-nucleon elastic cross section data using a vector meson dominance model [Hoh76]. To get reasonable χ^2, the authors performed a three-pole fit to both the isovector and isoscalar form factor. The ρ pole in the isovector fit was fixed based on a $\pi-N$ scattering amplitude analysis, and the first pole in the isoscalar fit was fixed at ω. They identified the second isoscalar pole as ϕ, and used the third pole to mimic the contributions due to higher resonances [†]. The meson-nucleon coupling strengths, g_i^{VNN}, were also produced from their fits. Quite surprisingly, the ϕNN coupling was found to be large, which seems inconsistent with the approximate OZI rule of the strong interaction [OZI63] [‡]. We shall see that due to the large strangeness content of ϕ, Höhler's results imply significant nucleon strangeness, as argued later by Jaffe in [Jaf89]. Höhler's treatment was updated by Mergell et al. [MMD96]. In addition to a more recent data set, Mergell et al. imposed the constraints from perturbative QCD and unitarity. The results of this analysis support the identification of the 2nd pole in $F_{1,2}^{I=0}$ as the ϕ meson, as suggested by Höhler's fit, and identifies the 3rd pole as $\omega(1600)$.

We shall focus on the isoscalar form factors to make contact with the strangeness.

[†] To make contact with the later discussion of the form factor parameterization, we note here that the summation of two closely-lying monopoles with residuals of different signs mimics a dipole form given later in Eqn. 6.5 in Sec. 6.1.1.

[‡] To put into simple language, the OZI rule says that the process with disconnected quark lines is highly suppressed. Since ϕ is primarily made of $s\bar{s}$, which is disconnected from the u and d quarks in the nucleon, a large ϕNN implies the violation of OZI rule.

The forms of Höhler's three-pole fits are [§]

$$F_1^{I=0}(q^2) = \frac{1}{2} + \frac{q^2 a_1^{\omega,I=0}}{m_\omega^2 - q^2} + \frac{q^2 a_1^{\phi,I=0}}{m_\phi^2 - q^2} + \frac{q^2 a_1^{v,I=0}}{m_v^2 - q^2}\,, \tag{2.92}$$

$$F_2^{I=0}(q^2) = \frac{a_2^{\omega,I=0}}{m_\omega^2 - q^2} + \frac{a_2^{\phi,I=0}}{m_\phi^2 - q^2} + \frac{a_2^{v,I=0}}{m_v^2 - q^2}\,, \tag{2.93}$$

in which a_i^v and m_v correspond to the 3rd higher mass pole in Höhler's fits. In [Jaf89], Jaffe wrote the strange vector form factors into a very similar form:

$$F_1^s(q^2) = \frac{q^2 a_1^{\omega,s}}{m_\omega^2 - q^2} + \frac{q^2 a_1^{\phi,s}}{m_\phi^2 - q^2} + \frac{q^2 a_1^{v,s}}{m_v^2 - q^2}\,, \tag{2.94}$$

$$F_2^s(q^2) = \frac{a_2^{\omega,s}}{m_\omega^2 - q^2} + \frac{a_2^{\phi,s}}{m_\phi^2 - q^2} + \frac{a_2^{v,s}}{m_v^2 - q^2}\,. \tag{2.95}$$

Clearly, as implied from Eqns. 2.87 and 2.91, for each vector meson V,

$$\frac{a_i^{V,s}}{a_i^{V,I=0}} = \frac{\langle V|\hat{\mathcal{J}}_\mu^{I=0}|0\rangle}{\langle V|\hat{\mathcal{J}}_\mu^{s}|0\rangle}\,, \tag{2.96}$$

in which the subscript i can be either 1 or 2, and $\hat{\mathcal{J}}_\mu^{I=0} = \frac{1}{6}(\bar{u}\gamma_\mu u + \bar{d}\gamma_\mu d) - \frac{1}{3}(\bar{s}\gamma_\mu s)$ and $\hat{\mathcal{J}}_\mu^{s} = \bar{s}\gamma_\mu s$ are the isoscalar and strange vector currents, respectively. By further assuming that the quark current of flavor k couples exclusively with a universal strength to the component of the vector-meson wave function $\bar{q_k}q_k$ with the same flavor [†], the ratio of the matrix elements above is simply determined by the quark content of V. For instance, $\dfrac{\langle V|\hat{\mathcal{J}}_\mu^{I=0}|0\rangle}{\langle V|\hat{\mathcal{J}}_\mu^{s}|0\rangle}$ is 0 and -3 for ω_0 and ϕ_0, respectively. In reality, there is a small mixing between ω and ϕ, parameterized by the mixing angle $\epsilon = 0.053 \pm 0.005$ [Jaf89], so that the physical state of ω and ϕ are

$$\omega = \cos\epsilon\ \omega_0 - \sin\epsilon\ \phi_0\,, \quad \phi = \sin\epsilon\ \omega_0 + \cos\epsilon\ \phi_0\,. \tag{2.97}$$

[§]Note that Eqn. 2.93 is the same as Eqn. 2.90, which represents the so-called unsubtracted dispersion relation. Eqn. 2.92, on the other hand, has utilized the a subtracted dispersion relation to enforce the constraint that $F_1^{I=0}(0) = \frac{1}{2}$.

[†]This flavor counting rule that Jaffe used is in excellent agreement with experiment [Mei88].

Having taken this into account, from Eqn. 2.96 Jaffe derived

$$\frac{a_i^{\omega,s}}{a_i^{\omega,I=0}} = -\frac{\sqrt{6}\sin\epsilon}{\sin(\epsilon+\theta_0)} \simeq -0.2\,, \quad \frac{a_i^{\phi,s}}{a_i^{\phi,I=0}} = -\frac{\sqrt{6}\cos\epsilon}{\cos(\epsilon+\theta_0)} \simeq -3\,, \tag{2.98}$$

in which $\theta_0 = \tan^{-1}\frac{1}{\sqrt{2}}$, the "magic" angle of octet-singlet mixing that yields flavor pure states ω_0 and ϕ_0. For the third higher mass pole, Jaffe used the asymptotic constraints that F_1 vanishes as $1/q^2$ and F_2 as $1/q^4$. Then by applying the pole residuals from the Höhler's fits, he obtained the expressions of $F_1^s(q^2)$ and $F_2^s(q^2)$, from which he concluded that $\mu_s = -0.31 \pm 0.09$ and $\langle r_s^2\rangle_E \sim 0.14 \pm 0.09$ fm^2. Hammer, Meissner and Drechsel made an updated analysis based on the Mergell fit and obtained $\mu_s = -0.25 \pm 0.03$ and $\langle r_s^2\rangle_E = 0.22 \pm 0.03$ fm^2 [HMD96], in good agreement with Jaffe's estimate, as well as a similar analysis by Forkel [For97].

Despite the consistent results from various VMD analyses, the common model dependence in them should not be neglected. First, the values of μ_s and $\langle r_s^2\rangle_E$ crucially depend on the identification of the 2nd pole as ϕ (which has a large strangeness content). The results are also quite sensitive to $\omega-\phi$ mixing angle ϵ. Second, the asymptotic constraints imposed to determine $a_i^{v,s}$, as a matter of fact, requires more poles with unknown masses and residuals. Therefore the three-pole treatment is ambiguous at best [RMI97]. Furthermore, one should also be concerned about mimicking the high energy continuum as a zero-width pole [BH01]. Along this line, Forkel has shown that replacing Jaffe's asymptotic ansatz with the QCD asymptotics would reduce the magnitude of the three-pole results up to a factor of 2.5 [For97].

The connection between Jaffe's VMD analysis and χPT was made in a paper by Ramsey-Musolf and Ito [RMI97]. As was mentioned earlier, in HBχPT, the experimental μ_s and $\langle r_s^2\rangle_E$ contain the contributions from both loops *and* the counterterms. In [RMI97], it was elucidated that using the VMD model to calculate $a_i^{V,s}$ is equivalent to evaluating the counterterms. However, in a pure pole fit like Jaffe's, the loop (or multi-meson continuum) is not well-represented. As an attempt to remedy this, these authors took the pole residuals of ω and ϕ from Höhler's isoscalar fit [Hoh76] to fix the counterterms, and *calculated* the leading,

nonanalytic loop contribution based on χPT. They called this treatment the resonance saturation model. The results from this treatment were $\langle r_s^2 \rangle_E \sim 0.36$ fm^2 and $\mu_s = 1.85$. The strangeness radius result is larger than the findings in the three-pole fits [Jaf89, HMD96], due to the fact that the cancellation between the ϕ pole and continuum in this analysis is not as drastic as that between ϕ and the 3rd higher mass poles in [Jaf89, HMD96]. The surprisingly large and positive μ_s arises from a very large kaon loop contribution to the isoscalar anomalous magnetic moment (a factor of 20 higher than the experimental value). As these authors pointed out, this kaon loop contribution requires large counterterms to balance it. However the Höhler fit is a pure resonance fit with no continuum. So using Höhler's pole residuals to fix the counterterms of the isoscalar form factors in this procedure is conceptually inconsistent with the kaon loop continuum calculation.

2.6.3 Kaon Loop

A different and intuitively appealing model of the nucleon strangeness is that the nucleon can fluctuate into a kaon (K) and a hyperon (Y), with strangeness -1 and 1, respectively. The photon can vector-couple to either K or Y. The process is depicted as the Feynman diagrams in Fig. 2.7. The kaon is much lighter than a hyperon, therefore is more likely to be located further away from the center of the nucleon. For this reason, this picture is also often referred to as the kaon cloud model. Due to the negative strangeness of $\bar{s}$ in the kaon, naively one expects that strangeness radius $\langle r_s^2 \rangle_E$ should be negative, if the recoiling effect is ignored [For94]. The expectation of μ_s is not so obvious under the same "cloudy" picture. Nonetheless, according to a simple non-relativistic argument in [HRG00], μ_s due to the $K-\Lambda$ fluctuation is expected to be negative as well. Both arguments are clearly over-simplistic. Nevertheless, the results from various calculations bear these features.

One should be concerned about the kaon loop picture, since the loop integral includes both the long and short distance physics. This is not a problem in general, since the short distance (or high energy) physics, e.g. ultra-violet divergence, should

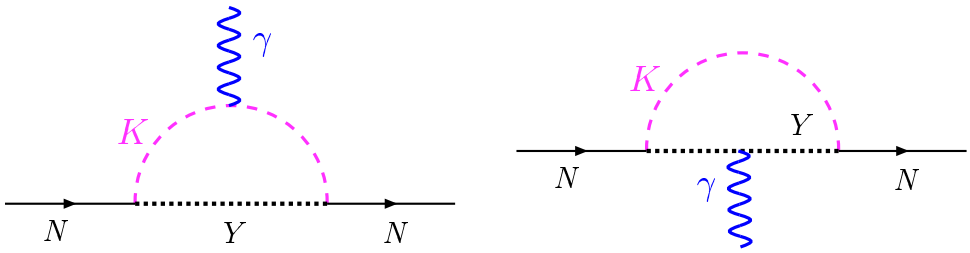

(a) γ *couples to* K. (b) γ *couples to* Y.

Figure 2.7: *The kaon loop diagrams with* γ *coupling to either the kaon or the hyperon.*

be absorbed into the renormalized parameters of the low energy effective theory, which is fully correct at low energy. However, a subtlety arises when the residual short distance effects remain large *after* the renormalization. As pointed out by Donoghue and Holstein, this is precisely the situation in HBχPT — the residual short distance component of the loop diagram is responsible for the poor convergence of the chiral loop [DH98]. They suggested to reformulate the theory by introducing a form-factor-like regulator into the chiral loop as

$$F(q^2) = \left(\frac{\Lambda^2}{\Lambda^2 - q^2}\right)^2 , \tag{2.99}$$

in which q is the loop momentum, and Λ is a cutoff scale (typically from 300 to 600 MeV), with which the short distance physics is largely eliminated from the loop integral. This regulator maintains the chiral symmetry of the theory, while improving the convergence of the chiral expansion significantly. In many ways, this prescription provides justification to similar regularization procedures which had been adopted by some kaon loop practitioners. On the other hand, one should note the subtleties arising from this procedure. First, the additional cutoff scale breaks the consistency of the chiral expansion, which is not desirable from the theoretical point of view. Second, for finite value of Λ, to satisfy Ward-Takahashi identity [PS95] [†], "seagull" or contact terms at the meson-nucleon vertices have to be introduced,

[†] A general identity for a two point correlation function in a field theory to satisfy in order to maintain the gauge invariance.

of which the choice is not unique. As an example, the authors in [RMB94] noted $\sim$30% difference in μ_s and $\langle r_s^2 \rangle_E$ in two different treatments of these contact terms. Third, some dependence on the cutoff scale Λ is an inevitable consequence of this procedure.

Bearing these in mind, let us focus now on some representative calculations. In a paper by Ramsey-Musolf and Burkardt [RMB94], the nucleon strangeness arising from the $K-\Lambda$ loop was computed. At the meson-nucleon vertices, they inserted the form factor from the Bonn-Jülich potential [BJ89] obtained from the fits of baryon-baryon scattering, $F(k^2) = \dfrac{m^2 - \Lambda^2}{k^2 - \Lambda^2}$. Here, m and k are the mass and the momentum of the meson, respectively, and the cutoff scale Λ, has a typical range from 1 to 2 GeV. Ad hoc "seagull" vertices were introduced to ensure gauge invariance. The strange magnetic moment and radius obtained from this calculation were $\mu_s = -0.31 \pm 0.05$ n.m. and $\langle r_s^2 \rangle_E = -0.03 \pm 0.003$ fm^2, with the uncertainties corresponding to the the variation of Λ within the "nominal" range in the Born-Jülich potential, from 1.2 to 1.4 GeV. To test the predictive power of this simple kaon loop model, the authors also calculated the contribution of $\pi-N$ loop to the neutron EM form factors using the same procedure and the cutoff parameter. They found that the neutron's Sachs charge radius was over-predicted by more than a factor of two (the situation was even worse for the Dirac radius). This, at the very least, implies that the picture with only the lightest meson-loop is far from complete.

An alternative implementation of the kaon loop is through the so-called cloudy bag model. The original MIT bag model [Cho74] separates the short and long distance physics via a three dimensional "bag". The surface of the bag has a δ function potential, outside which no free quarks are allowed. In contrast, the quarks confined inside the bag interact very weakly. This simple construction reflects important characteristics of QCD: the short distance asymptotic freedom and the long distance confinement. The inverse of the bag dimension (radius if one considers a spherical bag) serves as a natural cutoff scale. However, the bag surface breaks the chiral symmetry. The so-called cloudy bag model introduces the pion field, whose coupling to the confined quarks restores the broken chiral symmetry at the bag surface [TTM80].

To calculate the strangeness of the nucleons, Koepf, Henley and Pollock extended the pionic cloudy bag to the full pseudoscalar octet, kaons in particular [KHP92]. The radius of the bag was determined to be ~ 1.1 fm by fitting with the experimental nucleon EM form factors. The strangeness moments from their calculation were $\mu_s = -0.026$ and $\langle r_s^2 \rangle_E = -0.012$ fm^2, which agree in signs with those in [RMB94], but with less magnitude.

Cohen, Forkel and Nielsen proposed a hybrid model to combine the vector-meson-dominance model with the kaon loop [CFN93, For94]. Their treatment was not a simple addition of the results from the two. Rather, the calculation started by computing the intrinsic strangeness form factors of the nucleons with the assumption of $K-\Lambda$ dominance, similar to the treatment in [RMB94]. Effectively, in the framework of VMD, the intrinsic kaon loop renders strangeness to the matrix element $\langle N|\hat{V}^\mu|N\rangle$ in Eqn. 2.86, which was ignored in the pure VMD treatment [†]. The intrinsic isoscalar (I=0) form factors were also computed, on the other hand, based on Höhler's empirical fits, instead of using a pion loop model. The intrinsic isoscalar and strangeness form factors were then mixed with the "external" contribution under the VMD assumption with only ω and ϕ poles. Due to the $\omega-\phi$ mixing, both the intrinsic isoscalar and strange form factors contribute to the full strange form factors. The resulting strangeness moments are $\mu_s \sim -0.28$ n.m. and $\langle r_s^2 \rangle_E \sim -0.042$ fm^2, in reasonable agreement with those in [RMB94]. Along the same line, Meissner et al. also made the calculation by combining the kaon loop and the VMD [Mei97]. The authors looked into the OZI-allowed ϕ meson coupling to the kaon loop. In addition to the simple $K-\Lambda$ loop, they also considered the excited intermediate states with K^* and Σ. However, no $\omega-\phi$ mixing was considered in their treatment. Their treatment gave very small and positive μ_s and $\langle r_s^2 \rangle_E$.

The assumptions made in simple kaon loop calculations had been challenged by later authors. One concern raised by Malheiro and Melnitchouk was that the one-meson current (or impulse approximation) used in the naive kaon cloud calculation

[†] We reiterate that according to the current field identity $\hat{V}^\mu$ is equivalent to a EM current with the same flavor quantum number. In the pole fits discussed in Sec. 2.6.2, the matrix element of $\langle N|V^\mu|N\rangle$ was simply parameterized with g_i^{VNN} with no flavor separation.

violates Lorentz covariance [MM97]. These authors calculated the spurious contributions arising from this violation and observed that, once subtracted, the resulting μ_s became quite small and slightly positive (+0.01 n.m.). Geiger and Isgur made a quark level calculation to include the complete set of OZI allowed intermediate loops of K^*-Y^* [GI97]. They assumed simple harmonic oscillator wave functions (with empirical "tension" parameters) for the baryons and mesons. In contrast to the simple $K-\Lambda$ loop, the authors arrived at a small and positive μ_s ($\sim$+0.035 n.m.), although $\langle r_s^2 \rangle_E$ stayed negative (~ -0.04 fm^2). They noted that the resulting signs of these two quantities are accidental, since they arise from delicate cancellations between large contributions from a tower of intermediate states. Prompted by this paper, Barz et al. made the complementary hadronic calculation of the contribution from K^*, employing both the one-loop calculation, as well as the dispersion analysis [Bar98]. They confirmed the findings in [GI97], that the contribution from K^* can be as important as K. In view of all these complications, any kaon loop prediction should at best serve as a qualitative estimate of the strangeness effect that one might expect.

2.6.4 Constituent Quark Model

In the non-relativistic version of the constituent quark model, the nucleon is made up of the point-like constituent U and D quarks [†]. This intuitive model has been very successful in describing the properties and the spectroscopy of the hadrons. However, this simple picture is apparently inconsistent with the existence of a non-trivial QCD sea. Kaplan and Manohar had argued some time ago that the constituent quarks are the QCD quarks surrounded by a non-perturbative cloud of $q\bar{q}$ and gluons [KM88]. Under this picture, even U and D quarks can have a strangeness distribution. The nucleon strangeness is then simply the quark model average of the strangeness of individual constituent quarks. Spontaneously broken chiral symmetry is reflected in this model by the interaction between the pseudoscalar mesons and the constituent quarks, which can be formulated in the framework of χPT. This is

[†] We have capitalized U and D to distinguish them from the u and d quark in QCD.

the so-called chiral quark model. Due to the fact that the mass of the constituent quark ($\sim$ 300 MeV) is significantly lighter than the chiral symmetry breaking scale (Λ_χ $\sim$1 GeV), and that the coupling between the meson and constituent quark is weak, the convergence of the chiral loops in this model is much faster than the conventional baryon χPT. Moreover, the quark model approach automatically takes into account the intermediate baryonic states [RMI97, HRG00].

There are different approaches to implement the strange quark effects into the constituent quarks. One of them is by employing the Nambu Jona-Lasinio model (NJL) [NJL61]. In application to modern QCD, the NJL model replaced the short range interaction between quark currents with an effective local four fermion term, which respects chiral symmetry [TW00]. Under this construction, if a massless quark is exposed to a nonzero $\langle q\bar{q}\rangle$ condensate (mean field), it becomes a massive pseudo-particle (constituent quark). Consequently, chiral symmetry is spontaneously broken. The generalization of the NJL model to $N_f \geq 3$ (N_f is the number of flavors) is given in [BJM88], in which a $2N_f$-quark term was included to break the axial $U(1)$ symmetry. In the mean field approximation, this is precisely the term that generates flavor mixing, which renders strangeness to constituent U and D quarks. The coupling constant in this model can be fixed by the known η–η' and ρ–ω mixings, but a cutoff has to be introduced to regularize the point-like interaction. In [For94], Forkel et al. presented a calculation of the nucleon strangeness under this framework and obtained a small and positive $\langle r_s^2\rangle_E$ (+0.017 fm^2).

Ramsey-Musolf and Ito took an alternative approach by estimating the effect of constituent U and D quarks fluctuating into a kaon and a constituent S quark [RMI97], illustrated by the Feynman diagrams in Fig. 2.8. The axial coupling of the constituent quark to the kaon was determined via fitting the constituent quark calculation of the nucleon's axial charge g_A with its experimental value (1.27). Similar to their kaon cloud calculation, the hadronic form factor with a cutoff scale $\Lambda = \Lambda_\chi$ was introduced at kaon-constituent-quark vertices, along with additional seagull terms to preserve gauge invariance. Their results of μ_s and $\langle r_s^2\rangle_E$ are both small and negative. This treatment was extended by Hannelius, Riska and Gloz-

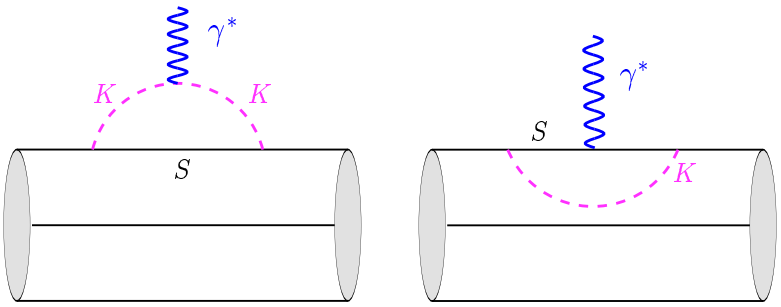

(a) *Meson cloud* (b) *Vertex correction*

Figure 2.8: *The Feynman diagrams contributing to the nucleon strangeness form factors in the $K-S$ version of the chiral quark model.*

man, who included contributions due to pseudovector K^* loop (replacing K by K^* in Fig. 2.8), and kaon loop with $K-K^*$ radiative transition (which only contribute to the Pauli form factor F_2^s) [HRG00, HR00]. None of the loops create significant strangeness, and the resulting strangeness moments are $\mu_s = -0.05$ n.m. and $\langle r_s^2 \rangle_E = 0.02$ fm^2. Lyuboviskij et al. made another estimate based on the perturbative chiral quark model [Lyu02]. In their model the valence quarks are viewed as moving in a perturbative Goldstone meson cloud. The effective confinement potential that quarks feel has a cutoff scale, which is determined via a fit to the charge radius of the proton; the underlying idea is quite similar to the cutoff scale used in previous calculations. The perturbative calculation is carried out at one-loop, and the values of both μ_s and $\langle r_s^2 \rangle_E$ obtained by these authors are small and negative, in reasonable agreement with the conclusions in [RMI97]. However, as stressed in [RMI97], besides the usual model dependence involved in a meson loop calculation mentioned in Sec. 2.6.3, a conceptual concern associated with the chiral quark model is the issue of double-counting, i.e. it is unclear whether the $Q\bar{Q}$ bound states presented in the chiral quark effective theory should be separated from the pseudoscalar Goldstone bosons or not.

2.6.5 Skyrme and Soliton Models

Long before the birth of QCD or χPT, Skyrme constructed a non-linear field theory based on the isovector meson fields, and conjectured that baryons are the solitons of the meson fields [Sky61]. The theory was revitalized by Witten, who made contact between the Skyrme model and QCD at the limit of a large number colors (large N_c QCD) [Wit79, Wit83]. Shortly after, Adkins et al. successfully calculated the static nucleon properties under the Skyrme model [ANW83]. In its simplest SU(2) framework, the starting point of Skyrme model is a 2×2 unitary field U defined as

$$U(x) = \exp\left[i\vec{\tau} \cdot \pi(\vec{x})/F_\pi\right] \tag{2.100}$$

in which $\vec{\tau}$ is the vector made by Pauli matrices and $\vec{\pi}$ is a vector representing the pion fields (π_1, π_2, π_3). The so-called Skyrme Lagrangian is constructed as [†]

$$\mathcal{L} = \frac{F_\pi^2}{8} Tr\left[\partial^\mu U \partial_\mu U^\dagger\right] + \mathcal{L}_s\,, \tag{2.101}$$

in which $\mathcal{L}_s$ is a phenomenological term in fourth-order of U and its derivative in order to stabilize the solution of the field [HS86]. This construction satisfies $SU(2)_L \times SU(2)_R$ chiral symmetry. To minimize the static energy of the system, one takes the *hedgehog ansatz* that the *time-independent* solution of the Lagrangian should satisfy $U_0 = exp\,[i\vec{\tau} \cdot \hat{r}\theta(r)/F_\pi]$, in which $\hat{r}$ is the radial direction, and imposed the boundary conditions that $\theta(0) = \pi$ and $\theta(\infty) = 0$. This results in a stable soliton solution, with a conserved topological quantum number, which is identified as the baryon number. Interestingly, baryons arise from this theory without any quarks present. However, the soliton is the eigenstate of the vector-sum of isospin and angular momentum, $\vec{I} + \vec{J}$, because U_0 ties the isospin with the coordinate. Hence it does not represent a single hadronic state with spin and isospin quantum numbers. Therefore, one has to quantize the soliton in some way and seek time-dependent solution of the Skyrme Lagrangian. As an example, practitioners sometimes take

[†] We only keep the relevant terms for this discussion.

a collective rotation of the soliton in the coordinate space, quantize the rotation, and then obtain the solution using the variational principle [HS86, BH01]. For application to real hadronic problems, one has to add terms in the Lagrangian to mimic the effect of explicit chiral symmetry breaking due to the quark masses. Despite the technical difficulties associated with a non-linear field theory, the SU(2) Skyrme model has been a successful picture describing nucleon structure [HS86].

In order to make an estimate of the strangeness effect in nucleons, obviously one has to extend the SU(2) Skyrme model to SU(3). However, similar to the situation of χPT, this is not at all trivial, since one can not simply "map" the SU(3) flavor space into a 3-D coordinate space. Various treatments in this respect inevitably contain ambiguities [WSP91]. Furthermore, SU(3) flavor symmetry breaking has to be carefully taken into account. In a paper by Weigel, Schechter and Park, the authors addressed the flavor symmetry breaking by introducing nonminimal derivative terms in the Lagrangian [WSP91]. Only pseudoscalar mesons were considered in this calculation. After the quantization of the collective perturbations, they diagonalized the Hamiltonian, with the symmetry breaking term treated exactly (in numerical sense). The strangeness radius and magnetic moment they obtained were $\langle r_s^2 \rangle_E = -0.11$ fm^2 and $\mu_s = -0.13$ n.m.. In a follow-up study [PW92], vector mesons were added into the model. The magnitudes of both quantities dropped by a factor of two, and the sign of strangeness radius changed. This indicates the uncertainty of Skyrme model predictions.

The concept of the Skyrme model is intimately related to an alternative model — the chiral soliton-quark model. The prototype of the latter, in SU(2), describes the interaction of quarks with the chiral fields with a so-called linear sigma Lagrangian as [TW00, Rip97]

$$\mathcal{L} = \bar{\psi} \left[i\gamma_\mu \partial^\mu - g(\sigma - i\gamma_5 \vec{\tau} \cdot \vec{\phi}) \right] \psi \,, \tag{2.102}$$

in which the fermion field ψ is a doublet of the Dirac u and d quark, and σ and $\vec{\phi}$ are a scalar-isoscalar and pseudoscalar-isovector field, respectively. It is noteworthy

that $U(x)$ in Eqn. 2.100 can be cast in the terms of an isoscalar and isovector field as well. Therefore from an "impressionistic" perspective the two approaches are not dissimilar. The Lagrangian in Eqn. 2.102 respects chiral symmetry, and the "hedgehog" ansatz again leads to a stable soliton solution for the meson fields. Similar to the Skyrme model, the soliton solution is identified as a baryon. An equivalent treatment starts from the NJL model, which contains only the quark degree-of-freedom (see Sec. 2.6.4) [TW00, Rip97]. The four-quark point interaction can be "bosonized" into the Yukawa type couplings between the quark and the collective scalar-isoscalar and pseudoscalar-isovector fields, σ and $\vec{\pi}$, which gives rise to a linear sigma Lagrangian as in Eqn. 2.102. Once again one has to extend the model to SU(3) in order to tackle the strangeness. A recent treatment of nucleon strangeness under the chiral soliton-quark model was made by Silva, Kim and Goeke [SKG02]. They obtained a positive strange magnetic moment ($\mu_s \sim 0.12$ n.m.) and a negative strangeness radius ($\langle r_s^2 \rangle_E \sim -0.1$ fm^2).

The main difference between the Skyrme and chiral soliton-quark models is that the quarks are explicit in the latter, so the soliton (baryon) can be more intuitively pictured as a localized object which binds quarks together. However, the prediction of strangeness from either framework can be challenged from several grounds. First of all, there are ambiguities in extending the model from SU(2) to SU(3) in both models. Second, since the Skyrme model does not contain quark degrees of freedom, the strangeness effect is calculated based on the difference between the matrix elements of the baryon and hypercharge currents. The prediction of the strangeness matrix element is then plagued by taking the (small) difference between the two large and uncertain terms [For94, BH01]. This uncertainty is not present in the chiral soliton-quark models. Third, both models are regarded as justified in the large N_c limit of QCD; therefore one should be concerned about their reliability of making predictions in the physical world with $N_c = 3$.

2.6.6 Dispersion Relations

Like χPT, the dispersion relation is another approach to derive observables of interest from experimental data based on general principles. The underlying principles of a dispersion relation are causality and analyticity, instead of chiral symmetry in case of χPT. The vector meson dominance model presented in Sec. 2.6.2 is a special application of a dispersion relation. In this section, we will discuss the latter from more general grounds.

The Dirac and Pauli form factors measured in electron scattering, $F_{1,2}(q^2)$, are associated with a *space-like* virtual photon, i.e., the four-momentum transfer squared q^2 is negative. One can extend q^2 to a complex variable z. The key point of the dispersion relation is that, as a consequence of causality and analyticity, $F_{1,2}(z)$ have certain analytic properties, which imply integral relations based on Cauchy's theorem [TW00]. Specifically, one writes

$$F_1(t) = F_1(0) + \frac{t}{\pi}\int_{t_0}^{\infty} \frac{\mathrm{Im}\left[F_1(t')\right]}{t'(t'-t)}dt' \,, \tag{2.103}$$

$$F_2(t) = \frac{1}{\pi}\int_{t_0}^{\infty} \frac{\mathrm{Im}\left[F_2(t')\right]}{t'-t}dt' \,, \tag{2.104}$$

with conventional variable substitution of $t = q^2 < 0$, and t' is a complex variable infinitesimally close to the real axis. As mentioned in Sec. 2.6.2, Eqn. 2.103 and Eqn. 2.104 are subtracted and unsubtracted dispersion relations, respectively; the former was applied to F_1 so that the physical bound of $F_1(0)$ can be imposed. The integral $\int_{t_0}^{\infty} dt'$ is along the *positive* real axis, corresponding to a *time-like* photon. In this region, $F_{1,2}(t' > 0)$ captures $\langle N\bar{N}|\hat{\mathcal{J}}^{\mu}_{EM}|0\rangle$, the matrix element of the EM current in electron-positron annihilation ($e^+e^- \to N\bar{N}$), the crossed-channel of the electron scattering. The integral can be replaced by a sum over all possible intermediate states, which carry the same quantum numbers, $\left[I^G J_{PC}\right]$, as the EM current. This decomposition with respect to various intermediate states is illustrated in Fig. 2.9. The lower limit of the integral, t_0, represents the production threshold of the lowest possible intermediate state. For the isovector(isoscalar) form factors,

it is $4(9)m_\pi^2$, corresponding to $\pi\pi(\pi\pi\pi)$ thresholds [TW00]. To the extent that the scattering amplitudes of the intermediate states are experimentally determined in the time-like region, the space-like form factors can be derived *model-independently*. $\mathrm{Im}\,[F_{1,2}(t')]$ are commonly referred to as the spectral functions, since they imply dynamical contributions from the intermediate states to the form factors. In this regard, VMD relations in Eqns. 2.92 and 2.93 simply represent the approximation that the spectral functions are dominated by a few zero-width vector meson resonances: $\mathrm{Im}\,[F_{1,2}(t')] = \pi \sum_V a_{1,2}^V \delta(t' - m_V^2)$. Unlike VMD, which only includes a few *off-shell* vector meson resonance [HRM99b], a general dispersion relation includes all possible *on-shell* intermediate states (continuum). For the isoscalar and strangeness form factors, the allowed continuum are 3π, 5π, 7π, $K\bar{K}$, $K\bar{K}\pi$, $N\bar{N}$, $\cdots$. The *virtual* vector meson resonances, such as ω, are already included in the *on-shell* continuum contributions, such as that from 3π.

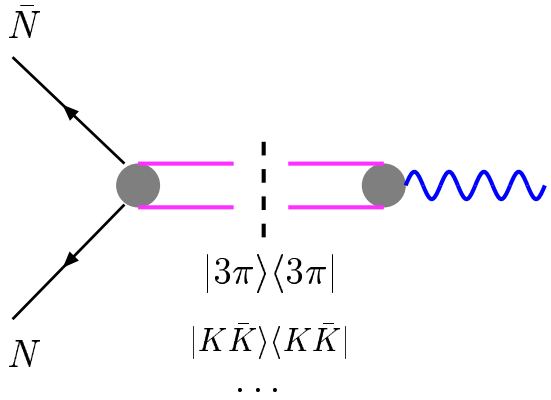

Figure 2.9: *Diagrammatic representation of the decomposition of the spectral functions into individual intermediate states.*

In applying the dispersion relation to nucleon strangeness, it is quite natural to focus on the $K\bar{K}$ continuum, since it is the lowest intermediate state containing strangeness explicitly (no OZI suppression), and it is closely related to the kaon cloud picture. This evaluation was first carried out by Ramsey-Musolf, Hammer and Drechsel [MHD97]. Like in the VMD model, the contribution of $K\bar{K}$ to the strangeness spectral function can be written in terms of a product of the amplitudes

of $\gamma \to K\bar{K}$ and $K\bar{K} \to N\bar{N}$:

$$\mathrm{Im}\left[F_1^{(a)}(t)\right] = \mathrm{Re}\left\{A_1(b_1^{\frac{1}{2},\frac{1}{2}}(t), b_1^{\frac{1}{2},-\frac{1}{2}}(t)) \times F_K^{(a)}(t)^*\right\}, \tag{2.105}$$

$$\mathrm{Im}\left[F_2^{(a)}(t)\right] = \mathrm{Re}\left\{A_2(b_1^{\frac{1}{2},\frac{1}{2}}(t), b_1^{\frac{1}{2},-\frac{1}{2}}(t)) \times F_K^{(a)}(t)^*\right\}, \tag{2.106}$$

with the superscript "*" denoting complex conjugate. In these two relations, $F_K^{(a)}(t)$ is an effective kaon form factor defined by

$$\langle K(k)\bar{K}(k')|\hat{\mathcal{J}}_\mu^{(a)}|0\rangle = (k-k')_\mu F_K^{(a)}(t=k+k'), \tag{2.107}$$

analogous to Eqn. 2.87. The superscript "(a)" implies that $\hat{\mathcal{J}}_\mu^{(a)}$ is either an EM or strangeness current, and at $t=0$, $F_K^{(a)}$ is normalized to its corresponding charge, e.g. $F_K^s(t=0) = -1$. $b_1^{\frac{1}{2},\pm\frac{1}{2}}(t)$ are the $J=1$ partial wave amplitudes of $K\bar{K} \to N\bar{N}$, analogous to the VNN coupling in Fig. 2.6, and A_1 and A_2 are two different linear combinations of them. The dispersive integrals in Eqns. 2.103 and 2.104 go from $4m_K^2$ to ∞. However, the data of $K\bar{K} \to N\bar{N}$ only exist in the physical region of $t > 4m_N^2$. Therefore some modeling/extrapolation is needed. In [MHD97], the authors calculated the scattering amplitudes of $K\bar{K} \to N\bar{N}$ in both the physical and unphysical regions under the Born approximation. They showed that (a) the Born approximation of $K\bar{K} \to N\bar{N}$ with point-like kaon strangeness form factors ($F_K^s(t) \equiv -1$) is equivalent to the lowest order kaon loop calculation (Sec. 2.6.3), and (b) the Born amplitudes in the physical region ($t > 4m_N^2$) violate unitarity substantially. Based on these, they argued that the rescattering (multi-loop) effects have to be included to restore the unitarity, and any calculation based on the one-loop (in χPT framework) or Born approximation (in dispersion relation) is problematic. In addition, they showed that a realistic kaon strangeness form factor could have major impact on the prediction of the nucleon strangeness.

Ramsey-Musolf and Hammer refined this analysis in a series of papers [RMH98, HRM99a, HRM99b]. Due to the low quality of $K\bar{K} \to N\bar{N}$ data, they simply set $b_1^{\frac{1}{2},\pm\frac{1}{2}}(t)$ in the physical region ($t > 4m_N^2$) at their unitarity bounds. This turns out

to have negligible contribution to the dispersive integral. In the unphysical region ($4m_K^2 < t < 4m_N^2$), instead of using the erroneous Born approximation, $b_1^{\frac{1}{2},\pm\frac{1}{2}}(t)$ were determined by making an analytical continuation of the experimental $K-N$ scattering amplitudes. The determination of the kaon strangeness form factor F_s^K follows a similar procedure as in [Jaf89]. The authors started from the fact that the time-like EM kaon form factor F_K^{EM} measured in $e^+e^- \to K\bar{K}$ is well described by a VMD parameterization with three poles at ρ, ω and ϕ. Assuming the same ω and ϕ pole structure in F_s^K, one can derive the pole residual based on Jaffe's "flavor rotation" relations in Eqn. 2.98. Numerically, the ω pole is of little consequence compared with the ϕ pole. Once the spectral functions were determined via Eqns. 2.105 and 2.106, they completed the dispersive integral (Eqns. 2.103 and 2.104) to determine the space-like Dirac and Pauli strange form factors arising from the $K\bar{K}$ continuum. The strangeness magnetic moment obtained in this analysis is $\mu_s = -0.42$, in reasonable agreement with the one loop kaon cloud calculation [RMB94]. The strangeness radius, on the other hand, is enhanced by more than a factor of two ($\langle r_s^2 \rangle_E = -0.07$ fm^2), as compared with that in [RMB94], due to the implicit inclusion of multi-loop effects in the dispersion analysis. In [HRM99a], Ramsey-Musolf and Hammer reanalyzed the nucleon isoscalar form factors by combining the $K\bar{K}$ continuum contribution with the three-pole fits. They realized that the ϕ pole strength in the Höhler and Mergell fits [Hoh76, MMD96] can be accounted for by the $K\bar{K}$ continuum in the Pauli form factor $F_2^{I=0}$, whereas additional ϕ resonance strength is required for $F_1^{I=0}$. The resulting strangeness moments (by combining the three-pole with the $K\bar{K}$ continuum) are $\langle r_s^2 \rangle_E \sim 0.42$ fm^2 and $\mu_s \sim -0.28$ n.m.. The charge radius from this analysis is large and positive, due to the dominating contribution from the ϕ resonance. However, as these authors noted, one can also obtain a reasonable fit by replacing the ϕ pole by a "fictitious" ω' pole with a mass of 1.12 MeV to mock up a $\rho\pi$ continuum. Under this treatment, $\langle r_s^2 \rangle_E$ becomes ~ -0.15 fm^2 instead. In addition, the 3rd high mass pole again introduces some ambiguity. In general terms, unlike χPT, dispersion relations do not provide a scheme with a systematically controlled approximation. For example,

the treatment presented above assumed that the lowest OZI-allowed state $K\bar{K}$ has dominating contribution to the continuum, which is not that obvious. The contributions from light multi-meson intermediate states can also be important, despite the fact that naively these processes are OZI violating. In this regard, the same authors showed in [HRM98] that the effects of $3\pi \to \omega$ or $3\pi \to \rho\pi \to \phi$ can enhance the 3π contribution up to the same scale as the $K\bar{K}$ continuum.

2.6.7 Lattice QCD

Like QED, the QCD Lagrangian is constructed based on the Yang-Mills local gauge invariance principle [YM54]. The only parameters of theory are the coupling constant of the quark and gauge field, and the Dirac masses of the quarks [PS95]. However, analytic solution to such a seemingly simple and almost parameter-free theory is formidable, due to its non-perturbative nature in the low energy regime. The effective theories discussed in the previous sections contain certain characteristics of QCD, e.g. the chiral symmetry. However, none of them provides a complete physical picture. Lattice QCD is a unique theoretical approach, which formulates QCD on discrete space-time lattice, and which has the potential of solving QCD from first principles numerically [Wal95].

Lattice field theory is developed based on the concept of Feynman's path integral [PS95]. For any Lagrangian $\mathcal{L}(\Phi(x), \partial^\mu \Phi(x))$ of field $\Phi(x)$, the action $S[\Phi]$ is defined as

$$S[\Phi] = \int d^4x \mathcal{L}(\Phi(x), \partial^\mu \Phi(x)) \,. \tag{2.108}$$

The n-point Green's function of the theory can then be formulated as

$$\mathcal{G}^{(n)}(x_1, x_2, \cdots, x_n) = \frac{\int [\mathcal{D}\Phi] \Phi(x_1)\Phi(x_2)\cdots\Phi(x_n) e^{iS[\Phi]}}{\int [\mathcal{D}\Phi] e^{iS[\Phi]}} \,, \tag{2.109}$$

in which $\int [\mathcal{D}\Phi]$ represents a *functional integral* over all possible configurations of the field Φ, and the "differential volume" $\mathcal{D}\Phi$ is commonly referred to as the *measure* of the path integral. All physical observables can be derived from the Green's

function [Wal95, TW00].

To introduce a discrete lattice in space-time has two purposes. First, any renormalizable quantum field theory requires ultra-violet regularization in order to eliminate unphysical infinities. Using spaced lattice to replace the continuum, the inverse of the lattice spacing provides a natural momentum cutoff. Second, the finite number of lattice sites makes numerical computation possible. In this regard, the lattice must also have a finite volume. The cell associated with each lattice site is called a *plaquette*, and the space-time integral in the action S can be replaced by a sum of the action of each plaquette. The functional integral in the Green's function, on the other hand, is replaced by a multi-integral over the values of the field at each plaquette [Wal95].

A gauge theory on a lattice has to satisfy gauge invariance. Therefore one has to make special constructions of both the action S, as well as the measure $\mathcal{D}\Phi$ for each plaquette, to ensure that they are both invariant under gauge transformations [Wal95]. Afterwards, it is just a matter of carrying out a numerical integration to solve the Green's function.

In QCD, the Lagrangian contains both the quark (fermion) and the gluon (gauge boson) fields. Due to the anticommutation relation, the functional integral of the fermion fields leads to the so-called fermion determinant term, which is extremely time-consuming to calculate. Enormous simplification can be achieved if one makes the so-called *quenched approximation*, which replaces the fermion determinant with a constant. However, it turns out that the quark determinant generates quark loops [TW00]. Therefore, any quenched lattice calculation of the QCD sea effects, such as the nucleon strangeness, inevitably contains some theoretical uncertainties.

Despite its phenomenological nature, χPT plays a very crucial role alongside lattice QCD. One important feature of lattice QCD is that the convergence improves with increasing quark masses. Therefore, lattice calculations are usually made at several different unphysically large quark (or equivalently pion) masses. Then, with the guidance from χPT, one extrapolates the results to masses of physical quarks. This procedure is called chiral extrapolation. However, for a quenched lattice theory,

the corresponding effective theory needs to be modified from the full χPT to the so-called quenched χPT. The construction of the SU(3) quenched χPT for baryons is discussed, e.g., in [LS96].

With these somewhat lengthy preliminaries, we now focus on lattice QCD predictions of the nucleon strangeness content. The evaluation of the strangeness EM matrix elements in lattice QCD involves a three-point Green's function, which can be separated into two topologically distinct processes, as illustrated by the connected and disconnected diagrams in Fig. 2.10. To a certain extent, the connected and disconnected diagrams correspond to the "valence" and "sea" contributions. However, both diagrams can be dressed by an arbitrary number of gluons. This, at the very least, has indicated that the "valence" and "sea" diagrams in the lattice framework are different from the conventional experimental jargon in, e.g., deep inelastic scattering. This point will be further elucidated later. In any event, the strangeness of the nucleon entirely arises from the disconnected diagram in Fig. 2.10(b).

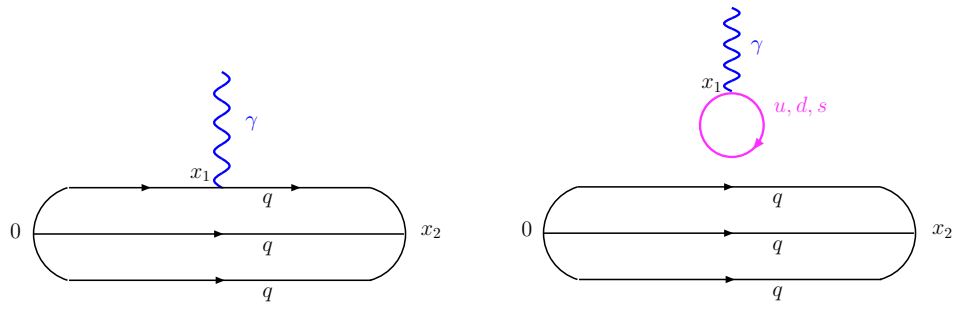

(a) *Connected "valence" diagram.* (b) *Disconnected "loop" diagram.*

Figure 2.10: *The lattice diagrams illustrating two different insertions (connected and disconnected) of the EM current. Both diagrams make a three-point Green's function to correlate* $(0, x_1, x_2)$.

Dong, Liu and Williams made the first quenched lattice calculation of G_E^s and G_M^s [DLW98]. With a simple extrapolation to physical valence masses, they obtained a negative μ_s (-0.36 ± 0.20 n.m.) and a small and negative strangeness Sachs radius. After a refinement of the Monte Carlo technique, their μ_s was updated to -0.28 ± 0.10 n.m. [MD01].

Like in full χPT, the strangeness form factors in quenched χPT can be expressed explicitly in terms of the four-momentum transfer and the valence and the strange quark masses, apart from a few low energy constants. A more elaborate quenched chiral extrapolation was made in a paper by Lewis, Wilcox and Woloshyn [LWW03]. These authors obtained the low energy constants by fitting the lattice data, from which they deduced the quenched strangeness form factors. The strangeness magnetic moment μ_s, according to their calculation, is slightly positive (+0.05 n.m.), and the strangeness Sachs radius is small and negative ($\langle r_s^2 \rangle_E \sim -0.02$ fm^2). However, as these authors pointed out, one should be aware of the "quenched" nature of their calculation, as well as the omission of higher order terms in the chiral expansion, which could introduce non-trivial theoretical uncertainty to their results.

Leinweber proposed to attack the problem from a different perspective. Starting from the symmetry of the QCD path integral and the Green's functions, with additional *charge symmetry* considerations, he derived a set of equalities among the quark sector contributions [Lei96]. Let us recap the principle of Leinweber's QCD equalities in a more "mundane" language. The magnetic moments of baryon octet can be flavor-decomposed into the following form: †

$$
\begin{aligned}
p &= \frac{2}{3}u^p - \frac{1}{3}d^p + O_p\,, & n &= -\frac{1}{3}d^n + \frac{2}{3}u^n + O_n\,,\\
\Sigma^+ &= \frac{2}{3}u^{\Sigma^+} - \frac{1}{3}s^{\Sigma^+} + O_{\Sigma^+}\,, & \Sigma^- &= -\frac{1}{3}d^{\Sigma^-} + \frac{2}{3}s^{\Sigma^-} + O_{\Sigma^-}\,,\\
\Xi^0 &= \frac{2}{3}u^{\Xi^0} - \frac{1}{3}s^{\Xi^0} + O_{\Xi^0}\,, & \Xi^- &= -\frac{1}{3}d^{\Xi^-} + \frac{2}{3}s^{\Xi^-} + O_{\Xi^-}\,.
\end{aligned}
\tag{2.110}
$$

$p, n, \cdots$ on the left hand sides of these equations represent magnetic moments of corresponding baryons. u^p, d^p, etc. are the contributions of different "valence" flavors from the *connected* diagram in Fig. 2.10(a). O_n, O_p, etc. represent the "loop" contributions from the *disconnected* diagram in Fig. 2.10(b). Standard SU(3) flavor

†Recall that the valence quark content of these baryons are: $p = uud, n = udd, \Sigma^+ = uus, \Sigma^- = dds, \Xi^0 = uss, \Xi^- = dss$.

decomposition can be made for the loop contributions, e.g.,

$$O_p = \frac{2}{3}{}^l G_M^{u,p} - \frac{1}{3}{}^l G_M^{d,p} - \frac{1}{3} G_M^{s,p}\,, \quad O_n = \frac{2}{3}{}^l G_M^{u,n} - \frac{1}{3}{}^l G_M^{d,n} - \frac{1}{3} G_M^{s,n}\,, \tag{2.111}$$

in which the superscripts "l" on the left of the u and d flavor form factors indicate that they arise from the disconnected loops. "l" on the strange form factors are suppressed since they solely arise from the disconnected loops. In this context, all these flavor form factors are short-hands of their values at zero momentum transfer. A similar decomposition can be made for the Σ and Ξ baryons.

Now let us generalize *charge symmetry*, which has been used in Eqn. 2.26 to relate the flavor form factors of the proton and neutron. Charge symmetry states that if one neglects the mass difference between the u and d quarks and ignores the electromagnetic effects, the QCD Lagrangian that governs hadronic physics would be invariant under the interchange of u and d quarks [Mil98]. The charge symmetry assumption leads to

$$\begin{aligned} &d^n = u^p\,, \quad u^n = d^p\,, \quad d^{\Sigma^-} = u^{\Sigma^+} \equiv u^\Sigma\,, \quad d^{\Xi^-} = u^{\Xi^0} \equiv u^\Xi\,, \\ &s^{\Sigma^+} = s^{\Sigma^-} \equiv s^\Sigma\,, \quad s^{\Xi^0} = s^{\Xi^-} \equiv s^\Xi\,, \end{aligned} \tag{2.112}$$

and

$${}^l G_M^{u,n} = {}^l G_M^{d,p}\,, \quad {}^l G_M^{d,n} = {}^l G_M^{u,p}\,, \quad G_M^{s,p} = G_M^{s,n} \equiv G_M^s \quad \text{and} \quad {}^l G_M^{u,p} = {}^l G_M^{d,p}\,. \tag{2.113}$$

Similar "loop" relations hold for Σ's and Ξ's. Naively, the fourth relation in Eqn. 2.113 seems to imply an additional assumption of an iso-symmetric sea in a given baryon, which is known to be significantly violated [Haw98]. This is a misunderstanding. As pointed out in [Lei96], the connected "valence" diagram simply describes the quark whose flow line propagates continuously from $0 \to x_2$. These lines can flow backwards as well as forwards in time, therefore have a sea contribution associated with them. For disconnected loops depicted in Fig. 2.10(b), the correlator associated with u and d are strictly identical under $u \leftrightarrow d$ if $m_u = m_d$. Therefore

${}^{l}G_M^{u,p} = {}^{l}G_M^{d,p}$ is "unconditionally" satisfied under charge asymmetry. The experimental iso-asymmetric quark sea effect measured in deep inelastic scattering arises purely from the connected diagram in Fig. 2.10(a). Eqns. 2.111 and 2.113 lead to relations

$$O_p = O_n \equiv O_N\,, \quad O_{\Sigma^+} = O_{\Sigma^-} \equiv O_\Sigma\,, \quad O_{\Xi^0} = O_{\Xi^-} \equiv O_\Xi\,. \tag{2.114}$$

In other words, the disconnected loop contributions between the isospin doublets are identical. Now with Eqns. 2.112 and 2.114, Eqn. 2.110 can be rewritten into

$$\begin{aligned}
p &= \frac{2}{3}u^p - \frac{1}{3}d^p + O_N\,, & n &= -\frac{1}{3}u^p + \frac{2}{3}d^p + O_N\,,\\
\Sigma^+ &= \frac{2}{3}u^\Sigma - \frac{1}{3}s^\Sigma + O_\Sigma\,, & \Sigma^- &= -\frac{1}{3}u^\Sigma + \frac{2}{3}s^\Sigma + O_\Sigma\,,\\
\Xi^0 &= \frac{2}{3}u^\Xi - \frac{1}{3}s^\Xi + O_\Xi\,, & \Xi^- &= -\frac{1}{3}u^\Xi + \frac{2}{3}s^\Xi + O_\Xi\,.
\end{aligned} \tag{2.115}$$

This set of relations are the QCD equalities Leinweber derived for baryons [Lei96]. They are direct consequences of QCD under charge symmetry. Defining ${}^{l}R_d^s \equiv G_M^s/{}^{l}G_M^d$ to be the ratio of the s quark contribution to that of the "sea" d quark, Eqn. 2.115 leads to two *independent* constraints of G_M^s [LT00]:

$$G_M^s = \frac{{}^{l}R_d^s}{1 - {}^{l}R_d^s}\left[2p + n - \frac{u^p}{u^\Sigma}(\Sigma^+ - \Sigma^-)\right]\,, \tag{2.116}$$

$$G_M^s = \frac{{}^{l}R_d^s}{1 - {}^{l}R_d^s}\left[p + 2n - \frac{u^n}{u^\Xi}(\Xi^0 - \Xi^-)\right]\,. \tag{2.117}$$

$\frac{u^p}{u^\Sigma}$ and $\frac{u^n}{u^\Xi}$ imply the environmental sensitivity of the "valence" u quark in the medium of different baryons; in the naive quark model both of them are unity. Since the magnetic moments of the baryon octets are well measured, a determination of $\frac{u^p}{u^\Sigma}$ (or $\frac{u^n}{u^\Xi}$) and ${}^{l}R_d^s$ leads to G_M^s.

A recent calculation in this framework is made by Leinweber and collaborators [Lei05]. The environmental ratios $\frac{u^p}{u^\Sigma}$ and $\frac{u^n}{u^\Xi}$ are determined from the lattice. Similar to the treatment of Lewis et al. [LWW03], quenched lattice data were fit

to yield the chiral expansion coefficients in quenched χPT. A correction from the quenched χPT to full χPT was made, followed by an extrapolation of the pion mass to its physical value. The extracted $\frac{u^p}{u^\Sigma}$ and $\frac{u^n}{u^\Xi}$ yielded excellent agreement between the bracketed term in Eqns. 2.116 and 2.117, both ~ -0.3 n.m.. These authors thus argue that their chiral extrapolation is very precise. To calculate ${}^lR_d^s$, these authors started from the full χPT obtained from the previous step, and inserted a dipole regulator (Eqn. 2.99) suggested by Donoghue and Holstein [DH98] into the loop integrals, which vastly improved the convergence properties. They concluded that ${}^lR_d^s = 0.14 \pm 0.04$, with the uncertainty estimated by varying the cutoff scale of the regulator. Combining ${}^lR_d^s$ with the environmental ratios, their treatment led to a small negative strangeness magnetic moment ($\mu_s = -0.05 \pm 0.02$ n.m.). However, one should be aware of the potential uncertainties not included in this evaluation, particularly in the determination of ${}^lR_d^s$. The loop integration procedure with the dipole regulator, apart from the uncertainty of the cutoff, contains similar model dependent uncertainties, as was stressed in Sec. 2.6.3. As an indication, we note that ${}^lR_d^s = 0.55$ was taken in [LT00] instead. Second, in [Lei05], it was argued that ${}^lR_d^s$ has to lie between 0 and 1, corresponding to $m_s = \infty$ and $m_s = m_u = m_d$. However it is not obvious that ${}^lR_d^s$ is required to stay within the limits when m_s takes its physical value, nor could one even make a convincing case about its sign. As a side note, the value of μ_s crucially depends on the value of ${}^lR_d^s$, e.g., if ${}^lR_d^s < 0$ or ${}^lR_d^s > 1$, μ_s would become positive. Third, the charge symmetry assumption is generally regarded as satisfied at the level of 1%. Leinweber's derivation not only assumed the charge asymmetry between proton and neutron, but also between $\Sigma^+(\Xi^0)$ and $\Sigma^-(\Xi^-)$. Therefore, were μ_s indeed as small as -0.05 n.m., one might have to more carefully evaluate the impact of the charge symmetry breaking. This was not presented in [Lei05]. Lastly, the non-trivial chiral extrapolation leading to the environmental ratios might also have a larger uncertainty than assigned. In this regard, the large theoretical uncertainty of the chiral extrapolation that Lewis et al. assigned to their results is suggestive [LWW03].

2.6.8 Summary

So far we have made a survey of various theoretical approaches in evaluating the nucleon strangeness. This survey is not meant to cover all existing calculations, but rather to give the flavor of the wide spread of various physical pictures, as well as the outcomes of the predictions. We have emphasized the non-trivial theoretical uncertainties associated with individual approaches. It is perhaps fair to say that none of the treatments so far give unambiguous predictions. Lattice QCD is constructed from first principles of QCD, and therefore has the potential of making model-independent predictions. However credible predictions still await the development of powerful computers, as well as a firmer theoretical framework of making numerical simplifications. The χPT and the dispersion relations are based on well-grounded general principles and are closely connected to experimental data. In dealing with the strangeness EM matrix elements, however, χPT is non-predictive, therefore one has to make model assumptions. The dispersion relations seem more secure, but the dispersion analysis does not contain a systematically controlled approximation procedure: one has no choice but to analyze a limited number of intermediate states. It is also somewhat frustrating that both χPT and dispersion relations do not provide simple physical pictures. For the model predictions, on the other hand, there is no obvious way to make judgment from physical grounds, and by definition none of the model contains the complete picture. In any case, one could hope, that the experimental data will eventually tell which model is more "true" than the others, or prompt model builders to come up with new ideas.

To conclude this section, listed in Table 2.5 are the predictions of μ_s and $\langle r_s^2 \rangle_E$ from different theoretical approaches. The predictions can be compared, for example, with the proton's magnetic moment ($\mu_p = 2.793$ n.m.), and the neutron's charge radius ($\langle r_n^2 \rangle_E = -0.12$ fm^2) [PDG04]. For each approach, only one representative prediction is selected. Once again, this table is not meant to cover the entire spectrum but to give a flavor of the outcomes. For clarity we choose to not to quote the uncertainties from the literature, but to stress that any value in the table could have

100% or even larger uncertainty. In any event, one sees that most of the theoretical predictions of μ_s are negative. The predictions of $\langle r_s^2 \rangle_E$ are either small or negative, except for the dispersion relation, which predicts a large and positive value.

Model	Reference	μ_s (n.m.)	$\langle r_s^2 \rangle_E$ (fm^2)
HBχPT	[HKM99]	0.18	0.05
VMD	[HMD96]	-0.25	0.02
Kaon Loop	[RMB94]	-0.31	-0.03
Cloudy Bag	[KHP92]	-0.026	-0.012
Hybrid	[CFN93]	-0.28	-0.04
Chiral Quark	[HR00]	-0.05	0.02
Dispersion	[HRM99a]	-0.28	0.42
Skyrme	[WSP91]	-0.13	-0.11
Chiral Soliton	[SKG02]	0.12	-0.1
Lattice	[LWW03]	0.05	-0.02

Table 2.5: *A summary of different theoretical predictions of strangeness magnetic moment and Sachs radius. μ_s is in units of Bohr nucleon magneton, and $\langle r_s^2 \rangle_E$ is in fm^2. Only one representative prediction is chosen for each theoretical approach.*

Chapter 3

Summary of Existing Measurements

Several parity violating electron scattering experiments have attempted to access the strange vector form factors prior to the G^0 experiment. The kinematics of these measurements vary, so they have different sensitivity to G_E^s and G_M^s. In this section, a brief summary of these measurements will be presented.

3.1 SAMPLE

The SAMPLE experiments were performed at the MIT-BATES laboratory [Spa00, Has00, Ito04, Spa04, Bei05]. The experimental setup is shown in Fig. 3.1. The detector was a set of air Čerenkov modules designed to detect electrons scattered from a hydrogen or deuterium target at backward angle ($\theta_e \sim 145^\circ$). An array of ten ellipsoidal mirrors focused the Čerenkov light cones onto an array of ten 8" PMTs. The beam was pulsed at 600 Hz, with the duration of each pulse $\sim$25 μs, and a helicity which was selected pseudo-randomly. For each beam pulse, the signals (anode currents) from the phototubes were integrated for a period of 60 μs and then digitized by the ADCs, which were then read out by the data acquisition system.

With a beam energy of 200 MeV, measurements were performed on liquid hydrogen (SAMPLE-I) and deuterium (SAMPLE-II) targets. Detecting backward-scattered electrons, these measurements were sensitive to the nucleon strange magnetic and axial form factors, but much less so to the strange electric form factor. The measured asymmetries with hydrogen and deuterium targets were [Bei05]

$$A_p(Q^2 = 0.1) = -5.61 \pm 0.67_{(\text{stat})} \pm 0.88_{(\text{sys})} = -5.56 + 3.37 G_M^s + 1.54 G_A^{e(T=1)} \,\text{ppm}\,, \tag{3.1}$$

$$A_d(Q^2 = 0.1) = -7.77 \pm 0.73_{(\text{stat})} \pm 0.72_{(\text{sys})} = -7.06 + 0.72 G_M^s + 1.66 G_A^{e(T=1)} \,\text{ppm}\,. \tag{3.2}$$

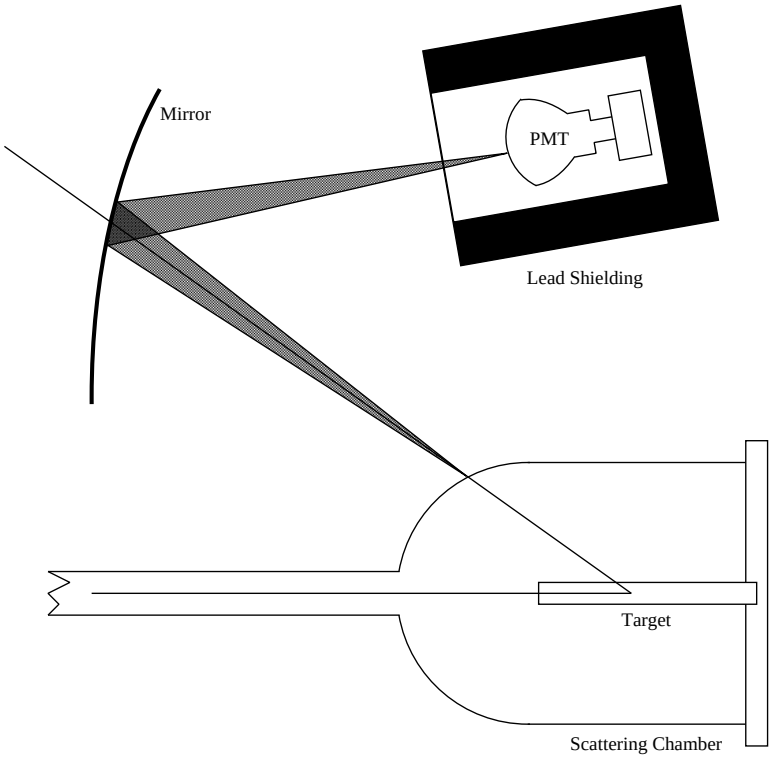

Figure 3.1: *The schematic setup of the SAMPLE experiment. The Čerenkov photons from backward-scattered electrons were reflected and focused by the mirrors onto the phototubes. Figure taken from [Spa01].*

In these two results, $G_A^{e(T=1)}$ is the isovector component of the axial form factor defined in Eqn. 2.73. In Fig. 3.2 the two results are plotted in the space of G_M^s vs. $G_A^{e(T=1)}$. The dark pink ellipse is the 1σ error ellipse obtained from combining the two experimental results. Also overlaid is the theoretical prediction of $G_A^{e(T=1)} = -0.83 \pm 0.26$ (the vertical band) by Zhu et al. [Zhu00], which is in agreement with the experimental result. The light yellow ellipse in Fig. 3.2 is the 1σ contour obtained by combining the hydrogen result with the theoretical $G_A^{e(T=1)}$. The value of G_M^s using this approach is

$$G_M^s(Q^2 = 0.1) = 0.37 \pm 0.20_{(\text{stat})} \pm 0.26_{(\text{sys})} \pm 0.07_{(\text{model})} \,, \tag{3.3}$$

in which the last model uncertainty includes those due to the nucleon electromagnetic and axial form factors.

To further test the theoretical calculation of $G_A^{e(T=1)}$, a third SAMPLE deu-

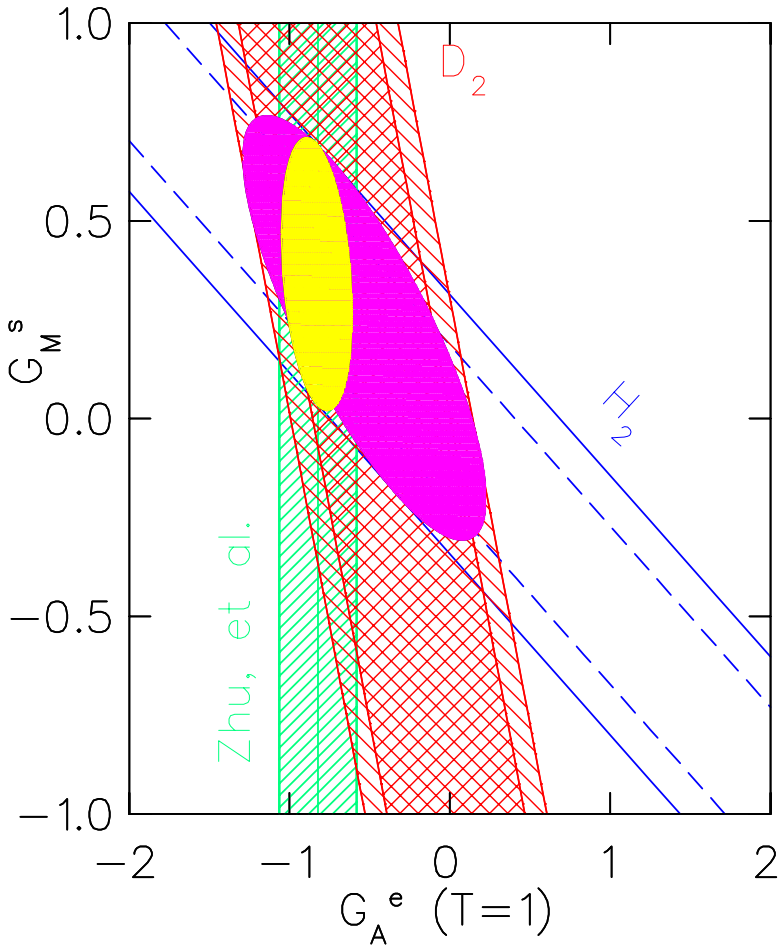

Figure 3.2: *The SAMPLE hydrogen (blue diagonal band) and deuterium (red band in crossed hatch) results plotted in the G_M^s vs. $G_A^{e(T=1)}$ plane. The inner and outer error bands represent the statistical and total uncertainties. The dark pink ellipse is the 1σ error ellipse from combining the two measurements. The light green vertical band is the theoretical calculation of $G_A^{e(T=1)} = -0.83 \pm 0.26$ from [Zhu00]. The light yellow ellipse is the 1σ error ellipse by combining the SAMPLE hydrogen results with the theoretical prediction of $G_A^{e(T=1)}$. Figure taken from [Bei05].*

terium measurement was performed at $Q^2 = 0.038$ (GeV/c)^2 with a beam energy of 125 MeV. The measured value of $G_A^{e(T=1)}$ in this experiment is in agreement with the theoretical calculation [Ito04].

3.2 HAPPEx

The HAPPEx is a parity violating electron scattering program in Hall A of the Jefferson Lab. The experimental setup is shown in Fig. 3.3. The incoming

electron beam energy is 3.2 GeV. Forward-scattered electrons from a hydrogen or ^{4}He target are focused by the two high resolution spectrometers. There have been three HAPPEx measurements so far. The first one was performed in 1998 with a liquid hydrogen target at $Q^2 = 0.477$ (GeV/c)^2 (HAPPEx-H-I) [Ani04]. Two other measurements were recently performed on hydrogen (HAPPEx-H-II) [Ani05] and ^{4}He (HAPPEx-He) [Ani05b] targets in 2004 at $Q^2 \sim 0.1$ (GeV/c)^2. The HAPPEx detectors are Čerenkov calorimeters, with lead-lucite used in the first experiment, and alternating layers of brass and quartz in the later two, and Čerenkov photons from the scattered electrons were collected by the phototubes. Similar to SAMPLE, the phototube signals were integrated for each helicity state (1/30 s) and read out by the DAQ.

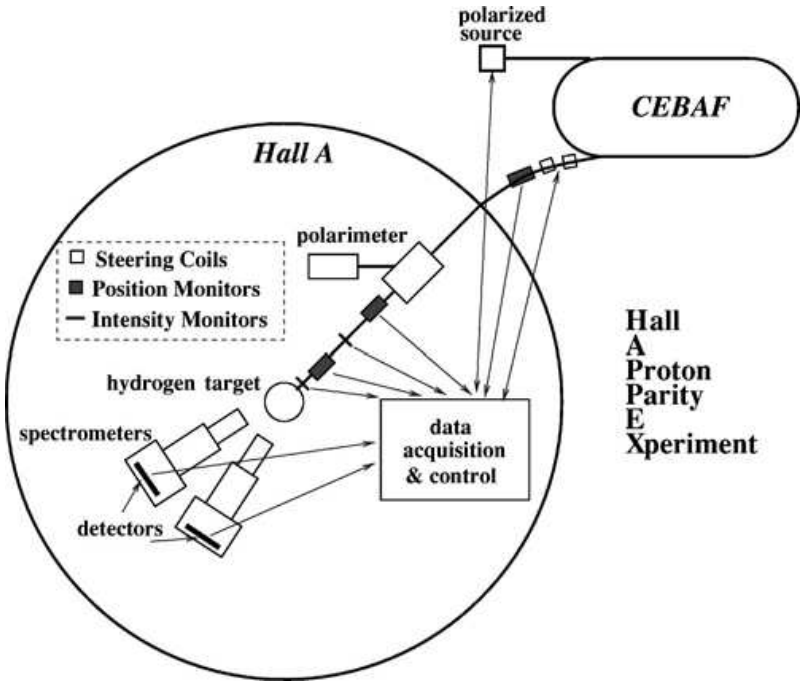

Figure 3.3: *The setup of the HAPPEx experiment. The forward-scattered electrons are detected by the high-resolution spectrometers. Figure taken from [Ani04].*

The measurements with hydrogen are sensitive to a linear combination of G_E^s and G_M^s, whereas the measurement on ^{4}He is only sensitive to G_E^s. The first

HAPPEx measurement at $Q^2 = 0.477$ (GeV/c)^2 yielded [Ani04]

$$A_p(Q^2 = 0.477) = -15.05 \pm 0.98_{(\text{stat})} \pm 0.56_{(\text{sys})}\,\text{ppm}\,, \tag{3.4}$$

which led to

$$(G_E^s + 0.39 G_M^s)(Q^2 = 0.477) = 0.014 \pm 0.020 \pm 0.010\,, \tag{3.5}$$

with the first uncertainty being experimental, and the second uncertainty arising from the uncertainties of the nucleon EM form factors. The other two measurements at $Q^2 \sim 0.1$ (GeV/c)^2 resulted in [Ani05, Ani05b]

$$A_p(Q^2 = 0.099) = -1.14 \pm 0.21_{(\text{stat})} \pm 0.06_{(\text{sys})}\,\text{ppm}\,, \tag{3.6}$$

$$(G_E^s + 0.080 G_M^s)(Q^2 = 0.099) = 0.030 \pm 0.025_{(\text{stat})} \pm 0.008_{(\text{sys})} \pm 0.012_{(\text{model})}\,, \tag{3.7}$$

and

$$A_{He}(Q^2 = 0.091) = -1.14 \pm 0.21_{(\text{stat})} \pm 0.06_{(\text{sys})}\,\text{ppm}\,, \tag{3.8}$$

$$G_E^s(Q^2 = 0.091) = -0.038 \pm 0.042_{(\text{stat})} \pm 0.010_{(\text{sys})}\,. \tag{3.9}$$

When these results were published in 2005, both these two low Q^2 measurements had only collected 10% of the proposed statistics. The programs resumed in 2005 and data taking has recently been completed. Another forward angle measurement at $Q^2 = 0.63$ (GeV/c)^2 is in preparation (see Sec. 6.3.4).

3.3 PVA4

The PVA4 experiment is being carried out at the MAMI accelerator facility in Mainz, Germany. A schematic drawing of its forward angle setup is shown in Fig. 3.4. The electron beam helicity is flipped at 25 Hz. A liquid hydrogen target was used in the forward angle experiment, and there is no magnetic spectrometer. Forward-

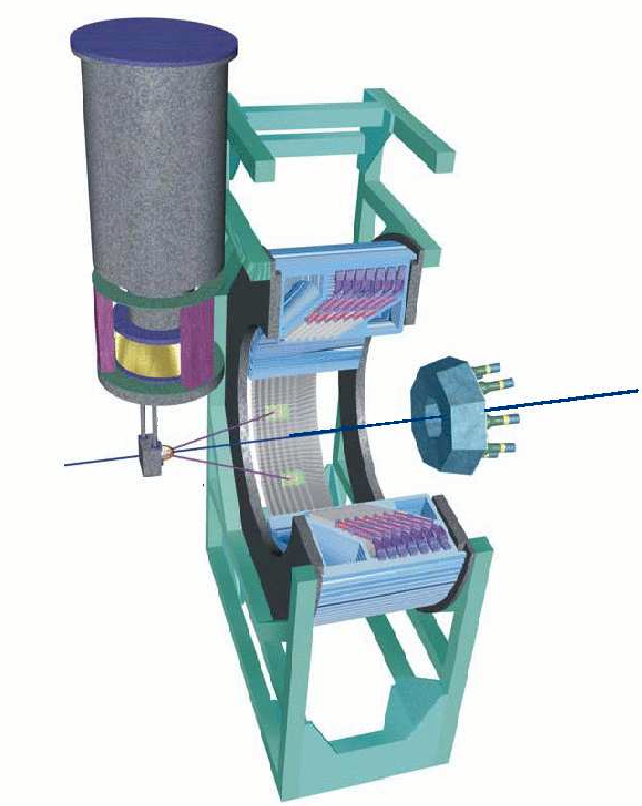

Figure 3.4: *The setup of the PVA4 forward angle experiment. The forward-scattered electrons were detected by an array of PbF_2 Čerenkov detectors. Eight water Čerenkov luminosity detectors were placed at very small angle. Figure taken from [Bat04].*

scattered electrons were detected by an array of PbF_2 Čerenkov total-absorptive calorimeters, which covered elastically scattered electrons between 30° to 40°. In addition, eight auxiliary water Čerenkov luminosity detectors were placed at very small angle.

The Čerenkov photons in the PbF_2 crystals resulting from scattered electrons are collected by phototubes. Inelastic electrons and photons from π^0 decays are also detected. The separation of the elastic signals and the inelastic background is made based on their differing energy loss in the PbF_2 crystals. The electronics of this experiment works like a very fast ADC: the pulses from the phototubes are integrated over 20 ns, digitized by a fast digitizer with a threshold trigger, and stored in a first-in-first-out (FIFO) pipeline chip. By this means, the individual

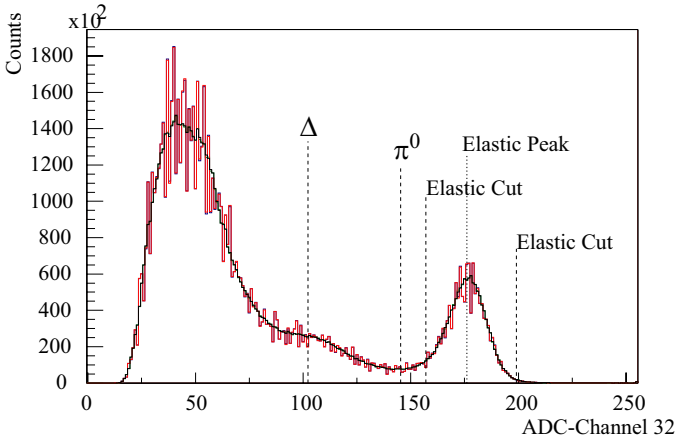

Figure 3.5: *A typical energy spectrum of detected particles in PVA4. The red histogram is the raw spectrum and the smooth black histogram has been corrected for the non-uniform energy bin width of the ADC. The energy losses of inelastic electrons from the Δ excitation and decay photons from the threshold π^0, and the cuts on elastic electrons are also indicated in the plot. Figure taken from [Maa04].*

particles are counted, and histograms of the deposited energy of these particles are read out by the DAQ. A typical energy spectrum of the particles striking the crystals is plotted in Fig. 3.5.

Two forward angle measurements have been performed by PVA4, at $Q^2 = 0.230$ (PVA4-I) and 0.108 GeV/c^2 (PVA4-II), respectively. The results of the two measurements were [Maa04, Maa05]

$$A_p(Q^2 = 0.230) = -5.44 \pm 0.54_{(\text{stat})} \pm 0.26_{(\text{sys})}\,\text{ppm}\,, \tag{3.10}$$

$$(G_E^s + 0.225 G_M^s)(Q^2 = 0.230) = 0.039 \pm 0.034\,, \tag{3.11}$$

and

$$A_p(Q^2 = 0.108) = -1.36 \pm 0.29_{(\text{stat})} \pm 0.13_{(\text{sys})}\,\text{ppm}\,, \tag{3.12}$$

$$(G_E^s + 0.106 G_M^s)(Q^2 = 0.108) = 0.071 \pm 0.036\,. \tag{3.13}$$

The uncertainties of the linear combination of G_E^s and G_M^s have combined the statistical, systematic and the nucleon form factor uncertainties.

Currently, the backward angle experiment of PVA4 is ongoing, which will be

discussed briefly in Sec. 6.3.4.

3.4 Summary

A summary of the world data prior to G^0 is contained in Table 3.1. The table includes average kinematics, measured asymmetries, linear combination coefficients (η) between G_E^s and G_M^s, and published results of $G_E^s + \eta G_M^s$ from [Bei05, Ani04, Ani05, Ani05b, Maa04, Maa05]. The results of SAMPLE-II and SAMPLE-III have been neglected, since they are insensitive to G_E^s. To make the result more compatible with the world data, the SAMPLE-I result in [Bei05] has been cast into $G_E^s + \eta G_M^s$, with G_A^e taken from the theoretical calculation [Bei05p].

Reference	Q^2 $(\mathrm{GeV/c})^2$	θ_{lab} (deg)	A_{phys} (ppm)	η	$G_E^s + \eta G_M^s$
[Bei05]	0.098	144.8	$-5.61 \pm 0.67 \pm 0.88$	1.67	0.56 ± 0.55
[Ani05]	0.099	6.0	$-1.14 \pm 0.24 \pm 0.06$	0.080	0.030 ± 0.029
[Ani05b]	0.091	5.7	$6.72 \pm 0.84 \pm 0.21$	0	-0.038 ± 0.043
[Maa05]	0.108	35.0	$-1.36 \pm 0.29 \pm 0.13$	0.225	0.039 ± 0.034
[Maa04]	0.230	35.0	$-5.44 \pm 0.54 \pm 0.26$	0.106	0.071 ± 0.036
[Ani04]	0.477	12.3	$-15.05 \pm 0.98 \pm 0.56$	0.39	0.014 ± 0.022

Table 3.1: *A summary of the available world data prior to G^0, including the average kinematics, measured asymmetries, η, and $G_E^s + \eta G_M^s$ from the publications. Rows listed in order of SAMPLE-I, HAPPEx-H-II, HAPPEx-He, PVA4-II, PVA4-I and HAPPEx-H-I. The first and the second uncertainties of the measured asymmetries are statistical and systematic, respectively. The central kinematics of the two PVA4 measurements and the SAMPLE measurement are obtained from [AM05p] and [Bei05p] respectively. Both experiments have rather large kinematical acceptance, so a determination of the central kinematics requires a Monte Carlo acceptance averaging. However, the SAMPLE central kinematics can be determined accurately by taking $Q^2 = 0.1$ $(GeV/c)^2$ and $E_b = 193.5$ MeV.*

One should note that in extracting $G_E^s + \eta G_M^s$, different experiments have used different parameterizations of the nucleon EM form factors and electroweak radiative correction parameters in their published results. A global analysis requires taking the measured asymmetries, applying a common set of theoretical and form factor

parameters, calculating $G_E^s+\eta G_M^s$, and then combining them to make the separation of G_E^s and G_M^s. The details of such a global analysis will be presented in Sec. 6.3.2.

As a prelude to the coming sections, a combined analysis of the SAMPLE-I, PVA4-II, HAPPEx-II and HAPPEx-He measurements at $Q^2 = 0.1$ (GeV/c)^2 from [Ani05] is shown in Fig. 3.6. The bands in G_E^s vs. G_M^s space are the experimental results, and the ellipse represents the 95% confidence contour of a joint determination of G_E^s and G_M^s. The light blue point in the figure represents $G_E^s = G_M^s = 0$, which is clearly disfavored by the data at the ~95% confidence level. The vertical pink band represents the lattice calculation by Leinweber et al. [Lei05] discussed in Sec. 2.6.7, which is also disfavored by the data. The black point in the figure is the best fit of (G_E^s, G_M^s) by combining the four measurements. The resulting G_E^s and G_M^s are

$$G_E^s(Q^2 = 0.1\ (\mathrm{GeV/c})^2) = -0.01 \pm 0.03\,, \tag{3.14}$$

$$G_M^s(Q^2 = 0.1\ (\mathrm{GeV/c})^2) = 0.55 \pm 0.28\,. \tag{3.15}$$

One sees that, according to this analysis, G_M^s is large and positive at the 2σ level, which is contradictory to most of the theoretical predictions (see discussions in Sec. 2.6 and Table 2.5).

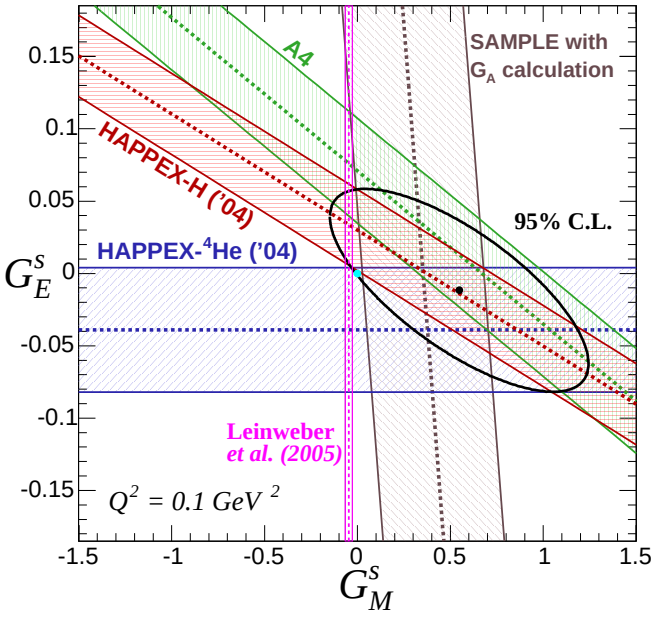

Figure 3.6: *The G_E^s vs. G_M^s space at Q^2=0.1 $(GeV/c)^2$ constrained by the HAPPEx-I(red band), HAPPEx-He (blue band), SAMPLE-I (black band), and PVA4-II (green band) measurements. The black point is the solution of (G_E^s, G_M^s) with the maximum likelihood by combining the four measurements. The ellipse represents the 95% confidence contour for a joint determination of G_E^s and G_M^s at this Q^2. The vertical pink band represents the calculation in [Lei05]. Figure taken from [Ani05]. For clarity, other theoretical calculations in the same figure in [Ani05] have been removed.*

Chapter 4

The G^0 Experiment

The G^0 experiment is being carried out in Hall C of the Thomas Jefferson National Accelerator Facility (TJNAF or JLab) in Newport News, Virginia. G^0 is designed to measure both the forward parity violating asymmetries on the proton, as well as the backward parity violating asymmetries on proton and deuterium targets at various values of momentum transfer, thereby allowing a model independent separation of G_E^s, G_M^s and $G_A^{e(T=1)}$. In this section, experimental aspects of the forward angle measurement will be discussed in detail.

4.1 Principle

The first measurement of parity violation was made by C. S. Wu et al. in 1957 [Wu57]. It was a β decay experiment with ^{60}Co nuclei: $^{60}\mathrm{Co} \rightarrow ^{60}\mathrm{Ni}^* + \mathrm{e}^- + \bar{\nu}_\mathrm{e}$. A simplified setup of the experiment is shown in Fig. 4.1. The ^{60}Co atoms were polarized in a magnetic field. The decay electrons were detected by a β detector. The magnetic field was flipped back and forth, reversing the polarization of ^{60}Co. The relative difference in electron rates between the two polarization states (labeled as $+$ and $-$), $A \equiv \dfrac{R^+ - R^-}{R^+ + R^-}$, is proportional to $\vec{\sigma}\cdot\vec{p}$, where $\vec{\sigma}$ and $\vec{p}$ are the net spin of ^{60}Co and the momentum of the outgoing electron. $\vec{\sigma}\cdot\vec{p}$ is a pseudo-scalar, therefore A is the parity violating asymmetry of the decay. This measurement showed that A was of the order of unity, which gave the very first evidence that parity is maximally violated in the weak interaction.

The measurement of parity violation in electron scattering employs the same idea. A schematic diagram of the experiment is drawn in Fig. 4.2. The incident electron can be polarized either parallel or anti-parallel to its momentum, corresponding to positive (right-handed) and negative (left-handed) electron helicity, respectively (Eqn. 2.64). The target is unpolarized, and the outgoing particles are detected. The

relative difference of the detected rates between the two incoming electron helicity states, $A \equiv \dfrac{R^+ - R^-}{R^+ + R^-}$, is then the parity violating asymmetry of the scattering (Eqn. 2.65). The size of the asymmetry, due to the dominance of the parity conserving electromagnetic interaction, is only of the order of $10^{-4}Q^2$ (see Sec. 2.4), in which Q^2 is the four-momentum transfer squared in units of $(\mathrm{GeV/c})^2$. Therefore, parts-per-million (ppm) is conventionally used as the unit for these asymmetries.

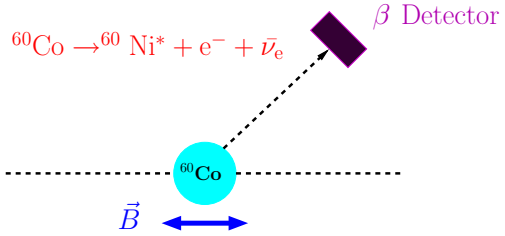

Figure 4.1: *A simplified setup of Wu's experiment to measure parity violation in ^{60}Co's β decay.*

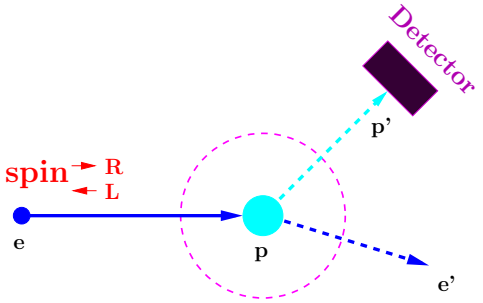

Figure 4.2: *A schematic diagram of the experimental technique to measure parity violation in electron scattering.*

4.2 Experimental Setup

The setup of the forward angle G^0 experiment is illustrated in Fig. 4.3. The polarized electrons were incident upon a liquid hydrogen target, and the recoiling protons were bent by a toroidal magnetic field in the superconducting magnet system (SMS), and focused onto scintillating detectors (FPDs) located along the focal plane of the spectrometer. The magnetic field was set to select positively charged particles, and particle time of flight was used to identify elastic and inelastic protons, and positively charge pions.

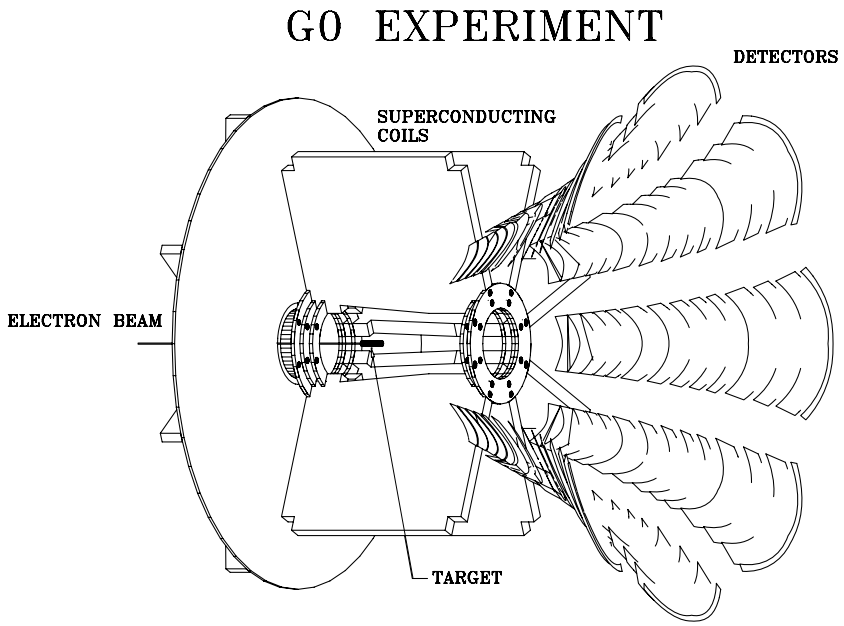

(a) *An overview of the G^0 forward angle setup.*

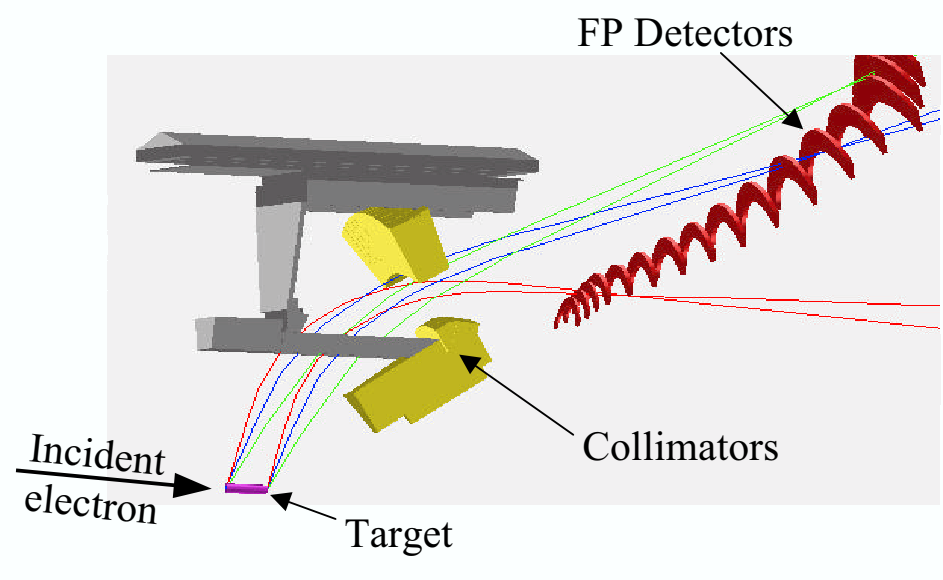

(b) *An inside view on one segment of G^0 spectrometer.*

Figure 4.3: *G^0 forward angle setup. The full setup is illustrated in (a). The beam is incident on the target from the left. Recoiling protons are focused by the magnetic field onto segmented detectors. An inside view of one segment of the spectrometer is depicted in (b). There are eight such segments in total. The trajectories of protons are defined by two collimators (yellow blocks) inside the magnet. Each arc is a pair of scintillating detectors.*

4.2.1 Beam

4.2.1.1 CEBAF Accelerator

The electron beam at JLab is provided by the CEBAF (continuous electron beam accelerator facility) accelerator, which allows for the delivery of *continuous* electron beams of different energies (from 1 to 6 GeV) simultaneously to the three experimental areas, Halls A, B and C. The word "continuous" is only approximate, in that all three beams are in fact pulsed with very high repetition rate [†]. The accelerator can be divided into two major components: the injector and the recirculating linear accelerators (LINACs). The layout of the electron injector is depicted in Fig. 4.4. Three individual lasers, one for each hall, all pulsed at 499 MHz but

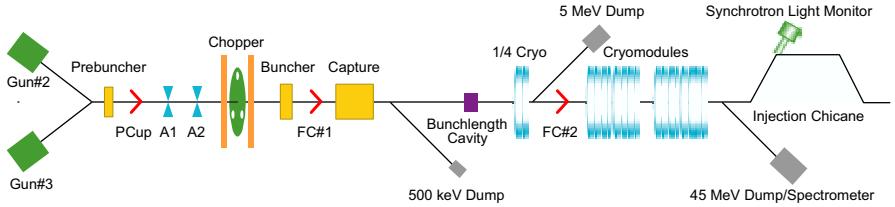

Figure 4.4: *The layout of the CEBAF injector. Figure taken from [Kaz04]*

offset in phase by 120°, illuminate a common photo-cathode, from which electrons are created by the photo-electric effect. The electrons are accelerated by a cathode gun to ∼100 keV. The electrons first go through a pre-buncher cavity and a few apertures, followed by a chopper cavity, which operates at 499 MHz. As the name "chopper" suggests, the cavity provides three variable RF "slits" for the three individual beams with the full width of the phase acceptance from 0 to 110 ps. The pre-buncher and the chopper ensure the timing and the longitudinal spread of the three beams. These are followed by the main beam buncher and a capture cavity, which accelerates the beam to ∼500 keV. Two superconducting radio frequency (SRF) cavities provide further bunching and accelerate the beam to ∼5 MeV. At the

[†]During normal running, all three beams are pulsed at 499 MHz. During the G^0 running period, the Hall C beam had a repetition rate of 31.1875 MHz to allow a clean measurement of particle flight time.

end of the injector, there are two modules, each containing 8 SRF cavities, which accelerate the electrons to the 45 MeV region [‡] [Hov96, Kaz04]. The beam passes through a chicane before entering the main machine.

A layout of the CEBAF accelerator is shown in Fig. 4.5. It is arranged in a

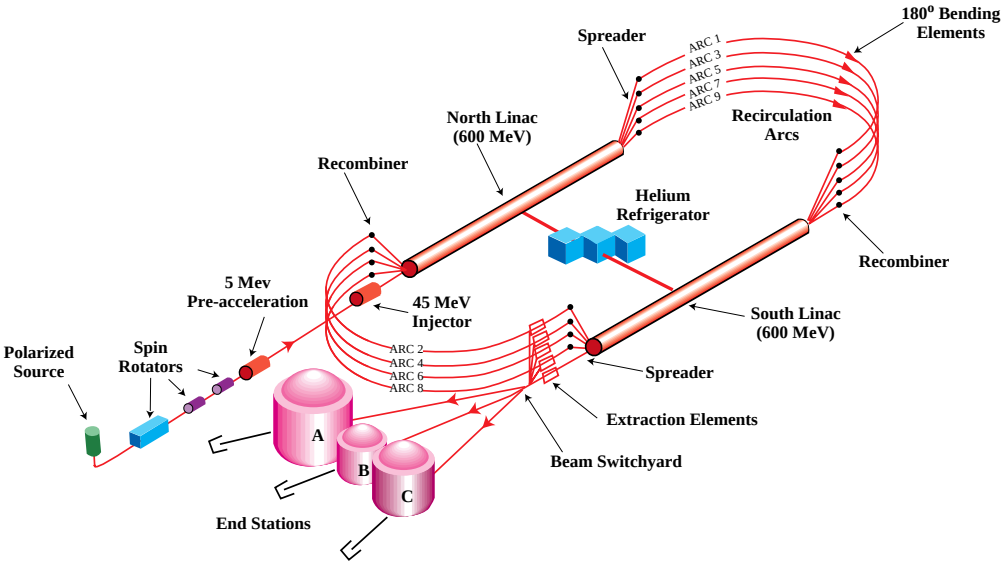

Figure 4.5: *The CEBAF accelerator. Figure taken from [Gra00].*

five-pass racetrack configuration. There are two SRF LINACs, the south and north LINACs, joined by two 180° bending arcs. The fundamental operation frequency of the machine is 1497 MHz. There are in total 20 SRF cavities in each LINAC. In each pass, the electron gains a maximal energy of 600 MeV in each LINAC [Kee01]. Inside each bending arc, the beams from different passes have different energies, therefore they require different bending fields and have to follow different orbits. To accommodate this, beams of different passes are deflected vertically into different beam lines by the *spreader* made up of a series of magnets. At the exit of each arc, the reverse of the above happens — the beams are recombined vertically by the *recombiners* for the subsequent acceleration by the LINAC. To allow for the extraction of the beams with different passes into different experimental halls, there are RF separators (time-domain beam deflector) located at the exit of the south

[‡]In fact, the electrons can have a variable exit energy from 23 to 68 MeV.

LINAC (see Fig. 4.5). Each separator cavity operates at 499 MHz, therefore can be tuned to extract the beam bunches for any one hall with the desired pass without interfering with the acceleration of the remaining bunches [Gra00]. The extracted beams enter the beam switch yard, and are deflected into Halls A, B and C according to their different timing.

The timing of the three beams is determined by the timing of the pulses of the three lasers. In reality, the beam into hall X can have a small mixture of the beam from the other two lasers due to the fact that those lasers are not turned off completely when laser X fires. This is the so-called leakage beam. Since the leakage beam originates from different lasers, it can have very different characteristics compared with the main beam. For the G^0 forward running, this turned out to be a nontrivial contamination because of the fact that the G^0 beam had a different time structure. The impact of the leakage and the systematic studies carried out to quantify its effect are presented in detail in Appendix A.

4.2.1.2 Polarized Beam for the G^0 Experiment

As mentioned in Sec. 4.1, a polarized electron beam is required for the parity violation measurement. The polarized electrons are produced with the widely-used technique of optical pumping of a gallium arsenide (GaAs) semi-conductor with a circularly polarized light [Pre95]. With appropriate energy, the photon field can excite the electrons from the valence band ($\mathbf{J} = \frac{\mathbf{3}}{\mathbf{2}}$) to the conduction band ($\mathbf{J} = \frac{\mathbf{1}}{\mathbf{2}}$) with $\Delta m_J = \pm 1$. A mono-layer of cesium (Cs) is coated onto the crystal to lower the potential barrier to help the electrons to escape into the vacuum. Quantum mechanically, the electrons favor carrying the same handedness as the photons. With 100% polarized light, the electrons excited to the conduction band could carry up to 50% of the polarization [Pre95]. The polarization can be further enhanced by applying strain to the crystal in such a way that the degenerate valence band structure is broken at the gap minimum [Pre95]. During the G^0 running period, the average electron polarization was $\sim$73.7%.

Careful tuning is required to maintain the highest possible longitudinal polar-

ization of the electron beam in the experimental hall [Gra00]. The G^0 run can be broken down into two periods, with a 3-pass electron beam for one and a 4-pass for the other (with the same final beam energy). The electron spins in the hall for these two periods were opposite to each other, which can be understood as follows. To first order, the precession of the spin of the electron with horizontal momentum in a vertical dipole magnetic field is [Gra00]

$$\Delta\theta_{pre} = \frac{g-2}{2}\gamma\Delta\theta_{bend}\,, \tag{4.1}$$

in which $\Delta\theta_{bend}$ and $\Delta\theta_{pre}$ are the rotation of the momentum and spin of the electron, respectively. The dipole magnets in each arc rotate the electron momentum by π. For the 3-pass beam, the electrons go through 5 arcs in the machine. To get a final electron energy of 3.03 GeV, the electron gains 505 MeV in each LINAC (neglecting the small pre-acceleration in the injector). For the 4-pass beam, the electron goes through 7 arcs instead, and the energy gain of the electron in each LINAC is 379 MeV. Summing the spin precession angles $\Delta\theta_{pre}$ in all arcs, the electron spin rotates approximately by 17π and 24π in the 3-pass and 4-pass configurations, respectively. Therefore, if the source and injector conditions are kept the same, the spins of the electrons in the hall are opposite for these two configurations.

A simplified diagram of the G^0 laser and its control devices is shown in Fig. 4.6. The G^0 laser is a commercial mode-locked AOM (acousto-optic loss modulator) Ti:Sapphire laser, also known as a "Tiger" laser, from Time-Bandwidth Products [TBWP]. It is capable of delivering $>$ 400 mW power, with the wavelengths selectable from 780 to 860 nm. The laser was pulsed at 31.1875 MHz instead of the JLab nominal 499 MHz, with the duration of each pulse $\sim$70 ps and an output wave-length of 840 nm to match the width of the band gap of the cathode [Bay02]. Circularly polarized light is generated from linear polarized light with a helicity Pockels cell (HPC), a crystal which exhibits an induced birefringence upon the application of the electric field [Het97]. The high voltage applied on the HPC was reversed back and forth, which led to an alternating circularly polarized light.

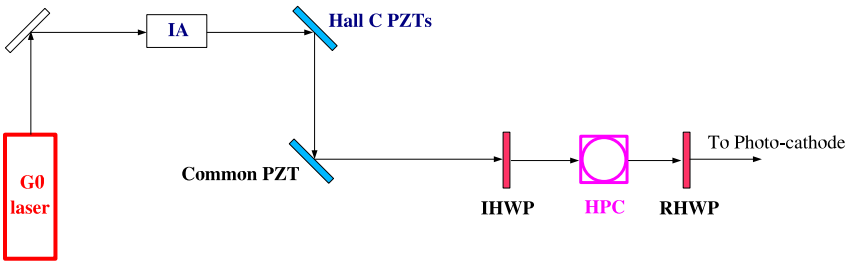

Figure 4.6: *A simplified layout of the laser table for G^0.*

The reversal frequency of the Pockels cell high voltage was chosen to be 30 Hz in order to cancel any potential 60 Hz noise due to the cycle of the power line. Each 1/30 s window is a basic unit of the G^0 measurement, which will be referred to as a macro-pulse (MPS). The electron helicity of a given MPS is defined by the polarity of the electric field on the Pockels cell. The helicity flip sequence was generated in a quartet pattern, such as $+--+$ or $-++-$, in order to minimize the effect of potential long term drifts. The asymmetry of the detector yield was computed for each of these quartets. The helicity bit of the first MPS within a quartet was decided by a software pseudo-random bit generator [Sta01]. In between MPSs, there was a $\sim$500 μs period, during which the data taking was inhibited, to allow the high voltage on the HPC to settle.

To further eliminate the potential cross-talk of the helicity bit with the detector electronics, the actual bit that was reported to the G^0 data acquisition was delayed by 8 MPSs, i.e., the helicity bit in the data of a given MPS was the actual helicity 8 MPSs ago. In the analyzer, the true helicity was recovered in software based on the delayed helicity and the algorithm of the pseudo-random bit generator [Sta01]. With this implementation, even if there were cross-talk between the detector signals and the reported helicity, it would be totally uncorrelated with the true helicity of the beam, therefore would not contaminate the measured asymmetries.

Before discussing the control components on the laser table, let us elaborate on the potential systematic effect of the beam. For parity violating experiments, any helicity-correlated beam property (the beam intensity, position, etc.) would result in a false asymmetry in the detector (see detailed discussion in Sec. 5.3.3).

Ideally, one wants to understand the origin of any helicity-correlated property, as well as to minimize it. The helicity-correlated beam intensity asymmetry, or charge asymmetry, can result from a helicity-correlated change in the quantum efficiency of the photo-cathode. As mentioned before, the GaAs crystal at CEBAF is strained, which typically has an analyzing axis; the absorption of the linear polarization along or orthogonal to it could have an anisotropy of the order of 10%. It is also known that light emerging from the HPC always contains some small linear admixture, therefore is elliptically polarized. When the handedness of the light is flipped, usually the major axis of the ellipse also rotates [Cat05]. So if the major axes of the ellipses for the two helicity states are not symmetric with respect to the analyzing axis of the crystal, a helicity correlated change in the quantum efficiency of the cathode will be created, which leads to a charge asymmetry of the electron beam.

The helicity-correlated position difference is a more subtle issue. One mechanism is that the alternating electric field on the helicity Pockels cell could alter the shape of the cell (since the birefringent crystals are usually piezoelectric as well), which results in a helicity-correlated steering or lensing of the laser. Another possibility is a helicity-correlated change of the profile of the electron beam from the cathode, either due to a non-uniformly distributed ellipticity of the laser (the so-called phase gradient) or a gradient of the analyzing power of the photo-cathode within the laser spot (typically mm$\times$mm) on the cathode [Cat05].

Two halfwave plates sandwich the HPC (Fig. 4.6). The upstream one is called the Insertable Halfwave Plate (IHWP). If inserted, it results in a reversal of the handedness of the polarized light, which will ultimately lead to a flip of the helicity of the electron beam. The helicity bit that is decoded by the analysis software, however, is simply the polarity of the electric field applied on the HPC, which knows nothing about the halfwave plate. Therefore, if the measured asymmetries are truly due to physics, the corresponding values of the "IN" and "OUT" states of the IHWP should be the same but *opposite* in sign. On the other hand, some of the false asymmetries, e.g., due to the Pockels cell steering or a cross-talk between the electronics and the "telegraphed" true helicity bit from the source, will stay intact.

Therefore using the IHWP enables us to study the impact of such a class of false asymmetries. During the run, the IHWP was inserted or retracted about once every three days.

The HPC might have a residual birefringence even without the external electric field. Under this circumstance, to achieve circular polarization, one has to apply asymmetric electric fields for the two helicity states. The adjustment of the voltages on the HPC is the first line of defense against the charge asymmetry.

As mentioned earlier, the charge asymmetry will be minimized if the major axes of the polarization ellipse of the laser light for the two helicity states are symmetric with respect to the analyzing axis of the cathode. The halfwave plate downstream of the HPC is the so-called Rotating Halfwave Plate (RHWP). By rotating the RHWP, one can symmetrize the residual linear polarizations of the two states of laser light. This technique is another powerful means of minimizing the charge asymmetry.

The two methods described above are "static" adjustments — the adjustment of the HPC voltage was only performed once every few weeks, and the RHWP tuning was performed about once every three days (right after the insertion/retraction of the IHWP). Besides these, there were two types of active feedback devices located upstream of the HPC, which modulated the property of the laser to make real-time adjustment of the charge asymmetry and the position difference. We shall discuss these two feedbacks in turn.

The IA (Intensity Attenuator) Cell (see Fig. 4.6) is a feedback device to minimize the charge asymmetry of the beam [Cat05]. It is made up of an upstream linear polarizer, a wave plate ($\lambda/4$ or $\lambda/10$), a Pockels cell, and a downstream linear polarizer. The laser light is first elliptically polarized by the wave plate. An alternating voltage is applied onto the Pockels cell for different helicity states, which changes the ellipticity of the laser. By this means, the transmission of the light through the downstream linear polarizer can be modulated in a helicity-correlated way.

The helicity-correlated position differences in the x and y directions were actively controlled by two PZT mirrors (see Fig. 4.6). The PZT is a piezo-electric

crystal whose dimension changes with the applied electric field [Kit95]. Two reflection mirrors are mounted onto these PZT transducers on the path of the laser [†]. If the voltages on these transducers are altered in a *helicity-correlated* manner, one can achieve a helicity-correlated steering of the laser to compensate for the observed helicity-correlated position difference of the beam. The two mirrors are commonly referred as PZTx and PZTy. However, each mirror steers the beam in both the x and y directions.

The IA and PZTs were calibrated and implemented in active feedback systems. The error signals of these feedback systems were the charge asymmetry or position differences measured in the experimental hall. The implementations and the performance of these feedback systems are discussed in detail in [Nak05a, Nak06]. With these feedback systems, the helicity-correlated beam properties were controlled at very low level. The average helicity-correlated parameters over the entire run are summarized in Table 4.1. We will translate these values in terms of the false asymmetry in the detectors in Sec. 5.3.3: they had virtually no impact on the measured asymmetries.

Parameter	value
Δx (nm)	3 ± 4
Δy (nm)	4 ± 4
$\Delta\theta_x$ (nrad)	1 ± 1
$\Delta\theta_y$ (nrad)	1.5 ± 1
ΔE (eV)	29 ± 4
A_Q (ppm)	-0.14 ± 0.32

Table 4.1: *Summary table of the helicity-correlated beam parameters throughout the entire run. The quantities in the first 5 rows are defined as the helicity-correlated differences:* $\Delta Q = Q^+ - Q^-$. *The last row is the charge asymmetry, defined as* $A_Q = \frac{Q^+ - Q^-}{Q^+ + Q^-}$. *The values are taken from [Nak05a], corrected for a mistaken factor of 2 [Nak05p].*

It is also important to note a few features of the G^0 beam. Despite the mod-

[†]There is also a common PZT mirror on the paths of all three lasers. Since this device affects all three beams, we had no control over it.

erate beam current (40 μA), the G^0 beam bunch charge was $\sim$1.6 pC/bunch, as compared to $\sim$0.2 pC/bunch for the 100 μA standard 499 MHz beam, due to the unusual 31.1875 MHz time structure. This imposed a challenge to the beam transport. A number of modifications to the injector setup had to be made to ensure the quality of the beam [Kaz04].

For each beam bunch, the measurement of the time of flight (ToF) of the detected particle required the beam arrival time on target as the reference. This "$T = 0$" reference signal (also known as the Y_0) is conceptually simple. However, special attention had to be paid since any helicity correlated timing shift of Y_0 would lead to a false asymmetry in the detector, because a timing shift leads to a change in the rate in a fixed ToF window. The maximally tolerable helicity-correlated timing shift for G^0 was of the order of a few femto-seconds (averaged over the entire run) [Liu01]. One of the first options of Y_0 being considered was the start signal from the 31.1875 MHz master oscillator of the laser. However, due to the potential helicity-correlated orbit difference, Y_0 produced from the laser was likely to introduce a helicity-correlated offset to the actual time of flight of the scattered particle from the target to the detector. Therefore, instead we chose to use a beam pick-off signal right upstream of the target. This signal was generated by a custom piece of electronics that derived Y_0 and another 499 MHz clock signal (CLK) from the 1497 MHz RF cavity signal of the CEBAF machine, in conjunction with the signal from a 31.1875 MHz stripline beam position monitor (BPM) [Qui03a, G0Cer04] For monitoring purposes, the Y_0 signals were also sampled by a VME TDC. The sensitivity of the Y_0 signal to the beam charge and position had been studied and shown to be negligible [G0Cer04]. Furthermore, *no* helicity correlated Y_0 timing shift was observed up to a statistical precision of $\sim$ 1 femto-second, averaged over the entire running period [Bis05].

4.2.1.3 Beam Polarimetry

The beam polarization P_b is a dilution factor to the parity violating asymmetry. To correct for this dilution, one has to measure P_b precisely. The polarization

of the G^0 beam was measured periodically with the standard Hall C Møller [†] polarimeter [Hau01], whose working principle is as follows. Consider the situation that both the incident beam and the target atomic electrons are polarized longitudinally with a polarization P_b and P_t. Then the asymmetry of the scattering cross section between the beam-target spin parallel and anti-parallel configurations is [Hau01]

$$A_{mol} = \frac{\frac{d\sigma^{\uparrow\uparrow}}{d\Omega} - \frac{d\sigma^{\uparrow\downarrow}}{d\Omega}}{\frac{d\sigma^{\uparrow\uparrow}}{d\Omega} + \frac{d\sigma^{\uparrow\downarrow}}{d\Omega}} = P_b P_t A_{zz}\,, \quad A_{zz}(\theta) = -\frac{\sin^2\theta(8-\sin^2\theta)}{(4-\sin^2\theta)^2}\,, \tag{4.2}$$

where the superscripts of $\dfrac{d\sigma}{d\Omega}$ indicate the beam-target spin alignment, $A_{zz}(\theta)$ is the physical analyzing power of the Møller scattering, and θ is the center-of-mass scattering angle. The above expression of $A_{zz}(\theta)$ is a very good approximation for high energy electrons ($\gamma \gg 1$), and higher order QED corrections have virtually no contribution. Therefore, if one knows the target polarization P_t, a measurement of the scattering asymmetry A_{mol} will determine the beam polarization. We further note that the analyzing power A_{zz} peaks at $\theta = 90^\circ$ with $A_{zz} = -\frac{7}{9}$. Therefore it is preferable to design the polarimeter to focus the scattered and recoiling electrons close to these kinematics.

The Hall C Møller polarimeter is located 40 m upstream of the Hall C pivot. The layout of the polarimeter is shown in Fig. 4.7. The Møller target is made from a

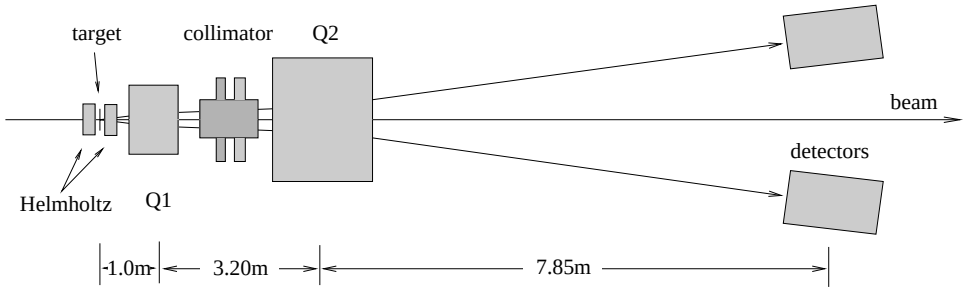

Figure 4.7: *The layout of the Hall C Møller polarimeter. Figure taken from [Gra00].*

thin Fe foil with its normal parallel with the incoming beam direction. A 4 μm thick

[†]The Møller scattering is the elastic scattering of two electrons.

target is the default target used by G^0. The target is polarized with an out-of-plane 4 T magnetic field provided by a pair of superconducting Helmholtz coils. Under such a high field, the foil is polarized to saturation; for pure iron the polarization under this circumstance is known to very high precision: $P_t = 8.00\% \pm 0.02\%$ [Hau01]. The spectrometers are made up of two quadrapole magnets, Q_1 and Q_2, separated by 3.2 m, with a collimator in between. This design helps to separate the small angle and high energy scattered electrons from the elastic electron-nucleus scattering, and focus only the Møller electrons with $\sim 90^\circ$ center-of-mass angles onto the detectors. Two left-right symmetric detectors are located 7.85 m downstream of Q_2. There are lead slits in front of both of them to further define the angular acceptance. In front of the main detectors, there are two hodoscopes, each made up of 14 vertical scintillator bars, which provides information about the actual scattering angle. The main detectors are made up of lead glass total-absorptive shower counters, with a 5" phototube (PMT) attached to each of them. The PMT signals are discriminated, providing further energy selection. The left-right detector coincidence is required such that the Møller pairs are detected with essentially no background. The coincident hits are counted by scalers, which are then read out by the DAQ for each beam helicity state. The asymmetry between the two beam helicity states is measured, which leads to a determination of the beam polarization (Eqn. 4.2).

If the beam current is too high, it will heat up and demagnetize the Møller target. Therefore, the normal Møller measurements were restricted to a beam current of < 2 μA. Some higher beam current measurements were also performed. First, a much thinner Møller (1 μm) target was used, which could tolerate beam currents up to 10 μA. Second, a new kicker magnet and a 25 μm wire target system was commissioned. The kicked beam had a much lower duty factor, therefore the target wire could endure a much higher beam current. The system was tested with a beam current up to 20 μA. In both measurements, no current dependent polarization change was observed [G0Cer04], which gave us confidence that the routine polarization measurement at the low beam current could be applied to our normal high current data runs.

4.2.2 Target

The target for the G^0 forward angle experiment was an unpolarized cryogenic liquid hydrogen target. The design of the target was driven by the need to measure tiny parity violating asymmetries. First of all, it is desirable to have a long target to ensure high luminosity and good statistical precision. Second, the target conditions need to be kept stable. This requires not only a large flow of coolant and a powerful pump to recirculate the liquid hydrogen, but also a feedback system to maintain the target temperature. Third, the target density fluctuations due to the beam heating need to be minimized. Such fluctuations would increase the otherwise purely statistical fluctuations of the measurements (see Sec. 5.2.2) and thus deteriorate the measurement precision.

A detailed description of the G^0 target system and its performance during the forward angle running is presented in [Cov04, Cov05]. Only the main features will be recapped here. A schematic view of the target loop is shown in Fig. 4.8. Due to

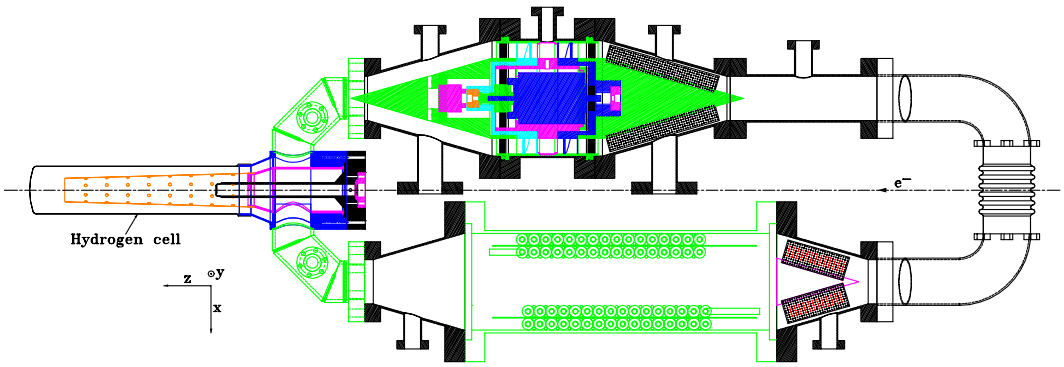

Figure 4.8: *A schematic view of the G^0 target loop. The electron beam comes from the right. Figure taken from [Cov05].*

the space constraints, the loop is placed horizontally inside the magnetic vacuum enclosure with a loop volume of 6.5 l. The beam came from the right of Fig. 4.8. The cell that contained the liquid hydrogen was located at the downstream end of the target loop inside a target manifold structure. A high torque cryogenic pump (upper side in Fig. 4.8) circulates the target liquid rapidly ($\sim$ 0.2 l liquid dislodged per revolution) with a nominal operation frequency of 31 Hz. The liquid hydrogen,

driven by the pump and guided by the flow diverters inside the loop, flows in a clockwise direction in Fig. 4.8.

A heat exchanger (the two layers of tightly-packed tubes at the bottom of Fig. 4.8) is located at the other leg of the target loop. Gaseous He coolant (15 K, 12 atm) provided by the end station refrigerator was circulated through the heat exchanger, with a typical flow rate of 6 g/s. On average, the heat removal rate of the exchanger was 50 W per g/s coolant flow.

A zoomed-in view of the target manifold is shown in Fig. 4.9. It is connected

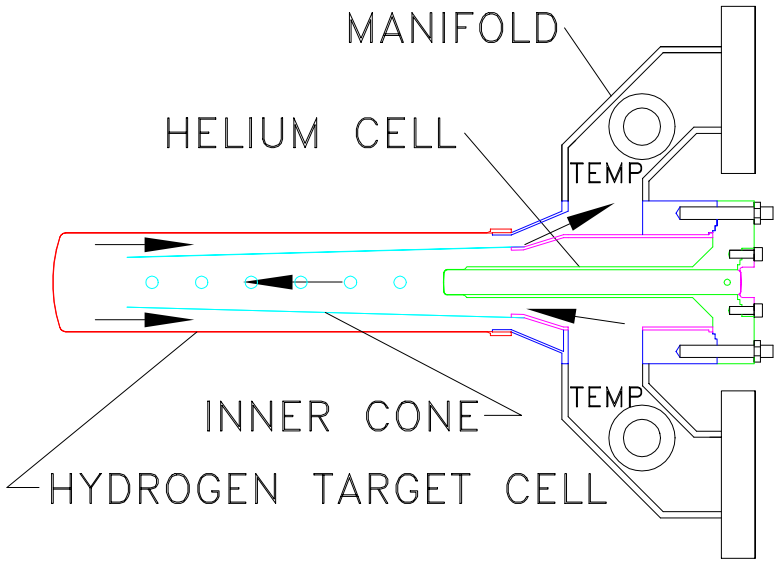

Figure 4.9: *A detailed view of the G^0 target manifold which houses the primary hydrogen cell and the secondary helium cell. Figure taken from [Cov05].*

with the target loop through two aluminum conflat flanges. The manifold contains two cylindrical aluminum cells: a primary hydrogen cell and a secondary helium cell, both are placed parallel to the beam direction. The hydrogen cell was machined in one piece with a total length of 23 cm, a wall of the thickness 0.178 mm, and an inner diameter of 5 cm. The downstream wall of the hydrogen cell functioned as the *exit window* of the target. The center of it was machined down to a thickness of 0.0762 mm within a diameter of 8 mm to reduce inelastic proton and deuteron background from the interaction in the aluminum. The remainder of the exit window had a uniform thickness of 0.178 mm. The helium cell was a 16 cm long cylinder

placed upstream of the hydrogen cell with an inner diameter of 1.27 cm. The downstream window of the He cell, with a thickness of 0.228 mm, was also the *entrance window* of the hydrogen cell. The distance between entrance and the exit window of the hydrogen cell was 20 cm, defining the length of the liquid hydrogen target. The upstream end of the helium cell was protected against the vacuum with another aluminum window (the so-called He window) of 0.178 mm thick. The helium cell was filled with He gas, which was maintained at the same pressure and temperature as the hydrogen cell. Under this circumstance, both the entrance and the exit windows of the hydrogen cell had a spherical convex shape with a curvature radius of 7.6 cm, which helps to reduce any helicity correlated change in target length due to potential helicity correlated parallel beam position shifts. Another advantage of having a long He cell is that the entrance window of the hydrogen cell naturally becomes azimuthally symmetric — the asymmetric joints/elbows of the vacuum window of the manifold have been pushed further upstream, outside of the detector acceptance.

As indicated by the arrows in Fig. 4.9, the liquid hydrogen flows into the target cell from the heat exchanger side. There is a thin-walled (0.0762 mm) conical aluminum tube (the light blue tube in Fig. 4.9) in the hydrogen cell, which guides the liquid down the center of the cell. There are holes on the wall of the conic tube to help remove heated liquid from the interaction region. The conical tube and the flow diverters inside the loop also increase turbulence in the liquid, which enhances the heat transfer and removal.

The nominal running conditions for liquid hydrogen target was 19 K (2 degrees below the boiling point) with a loop pressure of 1.7 atm. During normal running, the target loop was connected to a 2500 gallon ballast tank filled with hydrogen gas, which served as a pressure buffer to maintain a constant loop pressure. There are temperature sensors located at various places inside the loop, and a high power heater is located upstream of the cryopump. The loop temperature was maintained by a Proportional-Integral-Differential (PID) feedback system. The feedback tracked the beam current incident on the target, and regulated the output of the heater to

maintain the total power from the beam and heater at $\sim$ 300 W and to keep one of the temperature sensors constant. By this means, the temperature excursion after changes in beam current (e.g., beam trips) was maintained to be less than 0.2 K.

The electron beam creates local heating, hence some boiling and/or density fluctuation of the liquid is expected. As mentioned before, these fluctuations would increase the width of the measured asymmetry beyond that expected from Poisson statistics. In addition, boiling might reduce the target density globally. The boiling effect can be studied systematically by adjusting three variables: the beam current, the raster size and the pump speed. The raster was a two-magnet system which steered the beam with high frequency in a uniform square pattern on the target (2 mm$\times$2 mm was the nominal size for G^0) [Yan05]. By varying the size of the raster, the power density (per unit area of the beam) can be controlled. Varying the pump speed affects the heat removal and liquid mixing, therefore indirectly affects the boiling.

There were two sets of auxiliary luminosity detectors (or LUMIs) instrumented downstream of the G^0 main detectors, with a scattering angle of $\sim$2° and 1.3°, respectively. Each set was made up of four quartz Čerenkov detectors, which were placed in thin-walled (1.59 mm) aluminum cups intruding into the beam pipe in an azimuthally symmetric manner. With a nominal 40 μA of beam, the primary scattering rate per detector was $\sim$1 GHz, much higher than the rates in the main focal-plane detectors ($\sim$1 MHz per detector). The high scattering rate in the lumis led to good statistical precision, beyond which one could easily observe the effect of target density fluctuations. Furthermore, the electronics of the lumis were integrating instead of counting, so the non-linearity due to the electronic deadtime was not present in these detectors. This allows a precise determination of the global target density reduction. A detailed description of the lumi detectors and the target density related analysis are given in Appendix C. Here, we simply quote the published values in [Cov05]. Under the normal running conditions, i.e., 40 μA beam current, 2 mm$\times$2 mm rastered beam size and 31 Hz pump speed, the global density reduction was less than 1.5%, as compared to that with no beam on target. The

target density fluctuation contributes 238 ± 65 ppm to the measured asymmetry width, typically about 1200 ppm in a Q^2 bin in the main detector.

The target loop can also be filled with gaseous hydrogen (GH2) to allow studies of the background contribution arising from the aluminum cell windows. During the experiment, measurements were made on the GH2 target under two conditions, one at 28 K and the other at 35 K, both with the loop pressure maintained at 2.2 atm. In addition, two dummy Al targets were instrumented for G^0 forward configuration: the so-called "aluminum frame" and "flyswatter", designed to mock up the entrance and exit windows of the hydrogen cell, respectively. The frame target was located 1.7 cm upstream of the entrance window, with a thickness of 0.307 cm, and the flyswatter target was located 1.0 cm downstream of the exit window, with a thickness 0.076 cm. A tungsten (W) radiator of 0.0085 cm thick was located 38.5 cm upstream of the flyswatter. The flyswatter could be used with or without the W radiator in order to study the contribution of inelastic protons due to the photo- or electro-production from the exit window.

4.2.3 Spectrometer: the Magnet and Detectors

The G^0 spectrometer consists of a superconducting toroidal magnet (SMS) and an array of scintillating detectors. The details of the design and the performance of the spectrometer are given in [G0NIM]. What shall be highlighted here is how the spectrometer achieves the physical requirements of this experiment.

The toroidal magnet has the features of large acceptance due to its unobstructing structure, intrinsic azimuthal symmetry, iron-free construction [†], and zero magnetic field at the target location which avoids beam steering. To accommodate a long target, the magnet by design has so-called "zero-magnification" optics, with which the particles from different z locations in the target of the same momentum and angle are focused onto the same location on the focal plane.

As shown in Fig. 2.3, at a given four-momentum transfer, the linear com-

[†] The rescattering of recoiled protons with the magnetized iron has a large analyzing power, which could create a false asymmetry in the detectors.

bination coefficient between G_E^s and G_M^s, η, increases with electron angle θ_e. To optimize the experimental separation of G_E^s and G_M^s, it is therefore desirable to run the forward and a later backward experiment at a small and large electron angle, respectively. For the forward angle measurement, given the requirements of high luminosity and solid angle, detecting scattered electrons at very forward angles would be difficult. Therefore the experiment was designed to measure recoil protons instead. Since the four-momentum transfer varies rapidly with proton angle θ_p, a coverage of four-momentum transfer from 0.1 to 1.0 $(\mathrm{GeV/c})^2$ is made possible with a single beam energy at the forward angle configuration. For the G^0 forward angle electron beam energy (3.03 GeV), $0.1 < Q^2 < 1.0$ $(\mathrm{GeV/c})^2$ corresponds to $77.4^\circ > \theta_p > 52.0^\circ$ and $6.0^\circ < \theta_e < 20.9^\circ$. It is noteworthy that the elastic proton angle has an inverse correlation with the four-momentum transfer and the proton momentum, i.e., an elastic proton with larger angle has a smaller four-momentum transfer and momentum.

The G^0 magnet consists of 8 superconducting coils (SMS). The coils supply the toroidal fields, with a nominal coil current of 5000 A and a field integral of 1.6 T·m. The layout of the coils (labeled from A to H) is shown on the left side of Fig. 4.10, with the field direction indicated by the green arrows. The bending of

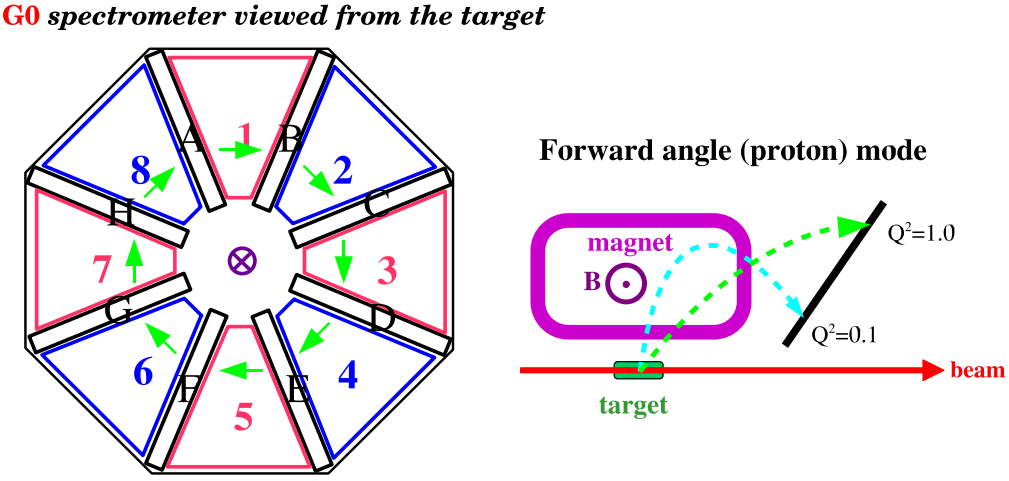

Figure 4.10: *Left side: the layout of the eight superconducting coils viewed from upstream. The magnetic field direction, in the forward angle mode, is shown as the green arrows. The placement of the 8 detector octants is also indicated (1-8). Right side: an illustration of the bending of elastic protons with different* Q^2.

elastic protons under such a field is illustrated on the right side of Fig. 4.10. The lower the Q^2 of the elastic proton, the lower momentum it has, and the stronger bending it experiences in the magnetic field.

There are two sets of collimators made from lead-alloy inside the magnet: the upstream azimuthal collimators and the downstream primary collimators. Both are arranged in 8 azimuthally symmetric segments, corresponding to the 8 detector octants, which will be described later. A drawing of one segment of the collimators is displayed in Fig. 4.11. Each pair of (upstream) azimuthal collimators has a $\pm 10^\circ$ azimuthal opening, cutting off the acceptance close to the coils to maintain a uniform field within the Φ acceptance of the detectors, in order to achieve a good Q^2 resolution. The lower jaws of the primary collimators (LPC) shield the focal plane detectors from direct view of the target. They also cut off protons with high momenta but low recoil angles, whereas the higher jaws of the primary collimators (HPCs) eliminate the slow protons with large recoil angles.

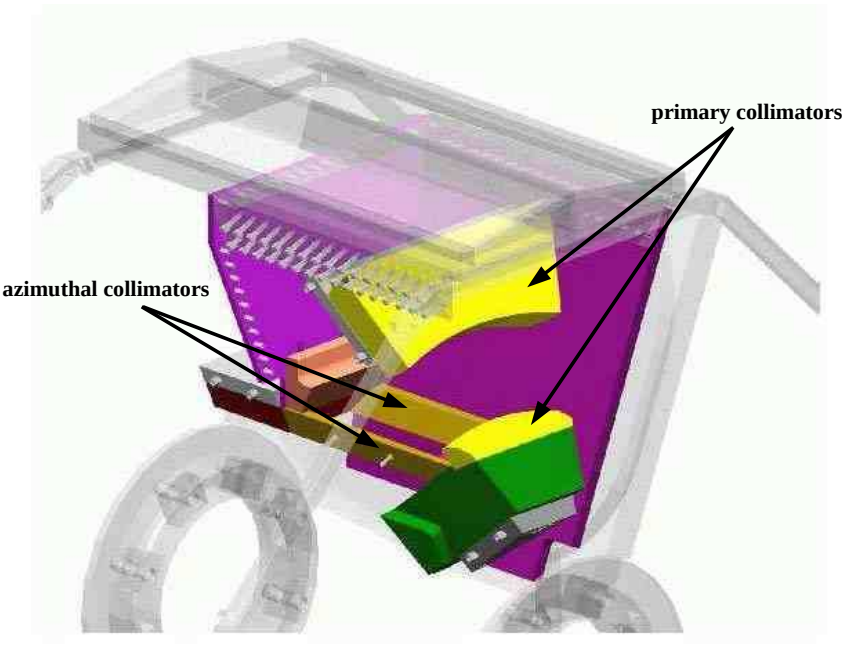

Figure 4.11: *One of the eight segments of the azimuthal and primary collimators inside the SMS. Figure taken from [Bat04].*

Thin Titanium windows (0.51 mm) on the downstream vacuum end cap of the magnet allowed the protons to pass through and be collected by an array of plastic

scintillation detectors located on the focal plane of the magnet. The layout of the detector package relative to the magnet is shown in Fig. 4.3(a). It was made up of 8 azimuthally symmetric octants (Fig. 4.10), labeled 1 through 8 in clockwise order if viewed from upstream. The azimuthal acceptance ($\pm 10°$) of each octant was defined by the upstream collimators. A 3-D rendered drawing of a single octant is displayed in Fig. 4.12. In each octant, there are in total 16 detectors (FPDs) with arc-like shape dispersed on the focal-plane, with FPD 1 located closest to the beam axis.

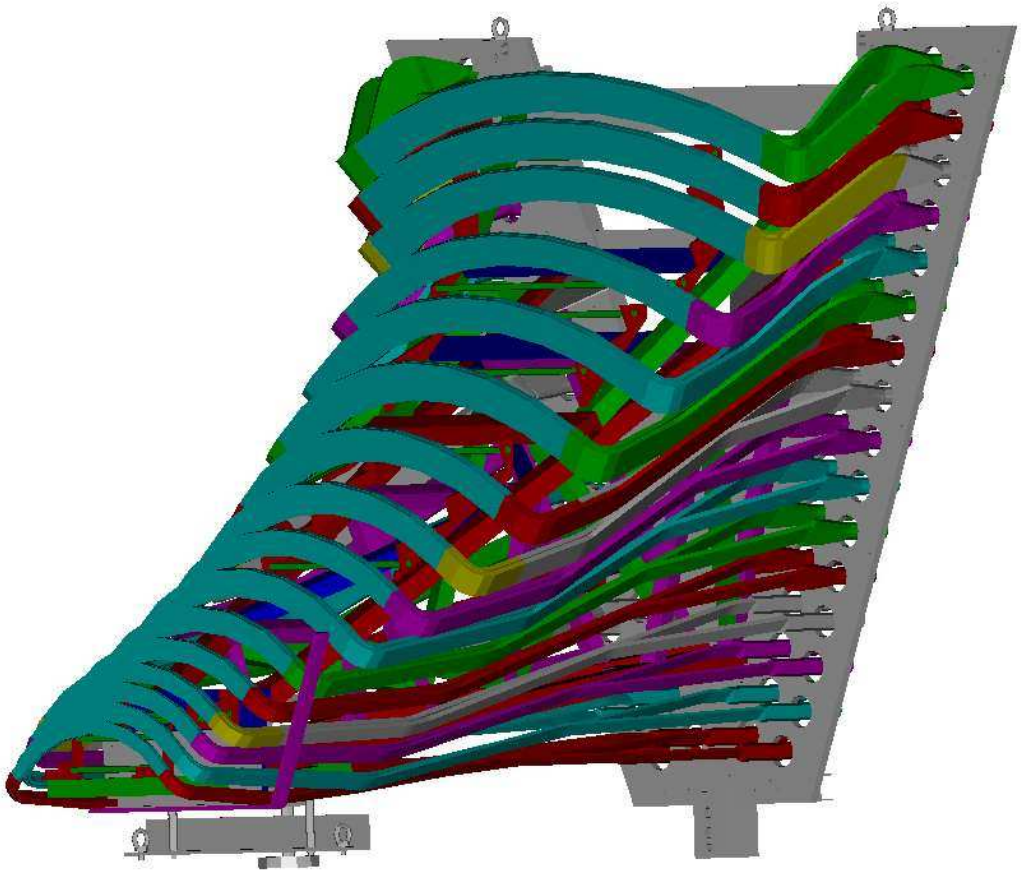

Figure 4.12: *A 3-D rendered picture of a French octant. There are 16 arc-like detectors. Each detector consists of two layers of plastic scintillators. Light guides are attached to both ends of the scintillator, which transmit the lights into phototubes (not shown) located behind the back plate.*

Let us revisit the elastic optics shown on the right side of Fig. 4.10, with the detector configuration (Fig. 4.12) taken into account. Elastic protons with the lowest Q^2 start off at the target with the largest θ_p, however they experience

the strongest bending by the magnetic field and thus strike the lowest detectors. The Q^2 of the elastic protons increases with detector number up to 0.55 $(\mathrm{GeV/c})^2$, which correspond to the late time of flight region in detector 15 (see Sec. 5.3.6.2). Beyond this point the decrease of the θ_p becomes faster than the decrease in the bending angle, so the locus of the elastics on the focal-plane moves slightly backwards with increasing Q^2. As a consequence, detector 15 covers a broad range of four-momentum transfer from 0.44 to 0.88 $(\mathrm{GeV/c})^2$ (see Sec. 5.3.6.2), and there is a secondary elastic peak on detector 14 with a four-momentum transfer $\sim$1.0 $(\mathrm{GeV/c})^2$ (see Sec. 5.3.6.3).

Now let us consider all types of protons without the elastic kinematic constraint. A given location on the focal plane corresponds to a range of (p, θ_p) at the target. The (p, θ_p) phase space covered by individual FPDs is shown as the 2-D map in Fig. 4.13. Each colored band on the figure corresponds to the acceptance of a single detector, with lower numbered FPD covering lower momentum. The left and the right edges of the acceptance, highlighted in thick black lines, are defined by the lower and higher jaws of the primary collimators, as mentioned earlier. The diagonal dashed line represents the constraint of the elastic kinematics with $E_b = 3.03$ GeV, and the intercepts between the horizontal lines and the elastic line indicate the (p, θ_p) of the elastic proton at given values of Q^2. As discussed earlier, detector 15 (second highest band in cyan) covers $0.44 < Q^2 < 0.88$ $(\mathrm{GeV/c})^2$, and detector 14 (third highest band in pink) has two foci, the main $Q^2 \sim 0.41$ $(\mathrm{GeV/c})^2$ and a "folding-over" $Q^2 \sim 1.0$ $(\mathrm{GeV/c})^2$. The separation of the elastic and inelastic protons in a given detector can be made via additional time of flight information. The majority of the inelastic protons are located in the phase space below the elastic line. For a given FPD, these protons have higher momentum and lower angle than the elastics, therefore have shorter flight time. The emerald band above the elastic line corresponds to the acceptance of detector 16. In principle inelastic protons from electron-proton scattering are kinematically prohibited in detector 16, but some do reach it due to the resolution of the spectrometer, protons from interactions in the Al target cells, as well as re-scattering. For all other detectors, the regions to the

right of the elastic line correspond to the protons with longer flight time than the elastics in the same detector. The rates there share the same "super-elastic" origins as those in detector 16.

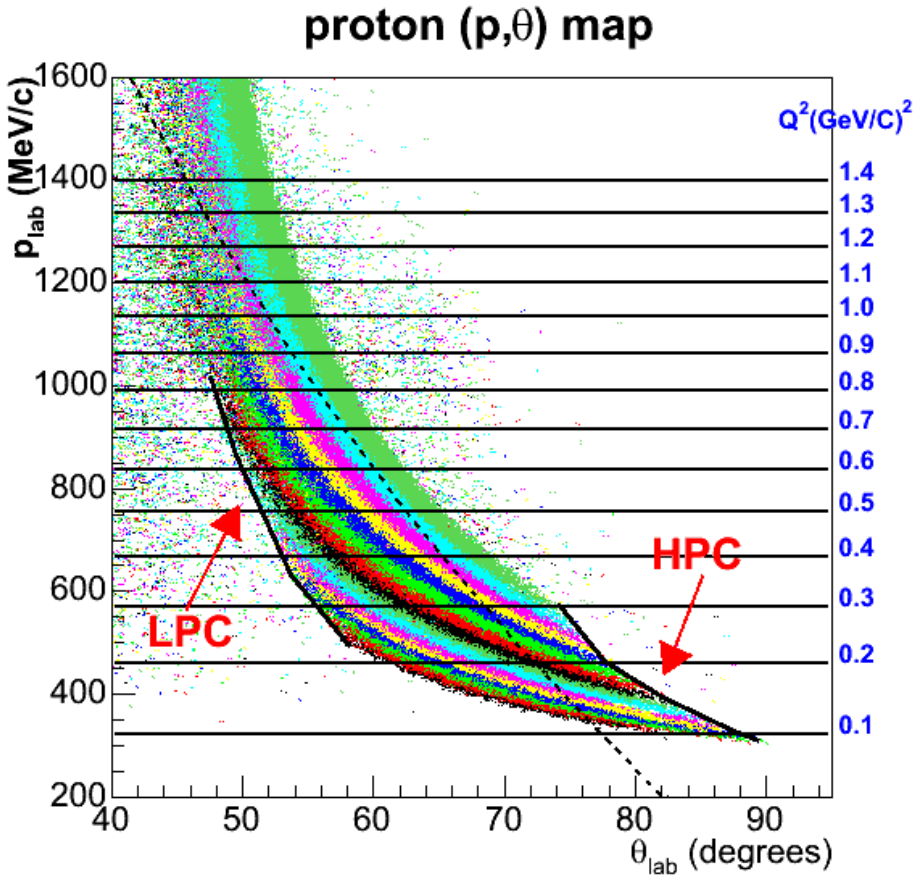

Figure 4.13: *The proton acceptance of the G^0 spectrometer in the space of proton lab momentum and angle (p, θ_p) at the reaction vertex. These protons are not constrained by the elastic kinematics. Each colored band corresponds to a given FPD, with lower numbered ring covering lower momentum: [black = FPDs 1 and 9, red = FPDs 2 and 10, green = FPDs 3 and 11, blue = FPDs 4 and 12, yellow = FPDs 5 and 13, pink = FPDs 6 and 14, cyan = FPDs 7 and 15, emerald = FPDs 8 and 16]. The cutoffs defined by the HPC and LPC are represented by the two thick black lines. The elastic proton is represented by the diagonal dashed line in the figure. The intercepts between the horizontal lines and the elastic line indicates the (p, θ_p) of an elastic proton at a given Q^2. The diffusive dots outside the colored bands correspond to the protons that penetrate the collimators or that are rescattered.*

The lengths of the detectors were defined by the protons originating from the target with a $\Phi = \pm 10.5^\circ$ about the center of each octant, slightly larger than the

opening of the azimuthal collimators to take into account multiple scattering and the potential misalignment. The width of the detectors were determined such that elastic proton rates for detectors 1 through 11 are roughly the same ($\sim$500 kHz). For higher numbered detectors, the elastic rates were smaller and the widths were chosen based on the momentum resolution. Typically the scintillators are 60$-$120 cm in length and 5$-$10 cm in width.

Octants 1, 3, 5 and 7 were constructed in North America (NA) and the others were constructed in France. As illustrated in Fig. 4.12, each detector consists of a pair of scintillators (with identical shapes and areas), made from Bicron BC-408, with lucite light guides attached to both ends. The scintillators were polished and wrapped in aluminized mylar (NA) or aluminum foil (French). Neutral background events are strongly suppressed by requiring a coincidence between the pair. To further reduce the low energy charged particle background entering the back scintillator created by neutrals in the front scintillator, a layer of absorber was inserted between the two scintillators. For the NA detectors, it was a layer of 3 mm black plastic (polycarbonate) [Roc02b]. The French detectors used a 3 mm thick aluminum plates instead, which at the same time served as a support structure [Bat04].

Scintillation light was collected by the phototubes attached to the end of the light guides. The NA octants used 12-stage Phillips XP-2262B photomultiplier tubes with custom-built bases. Modified commercial Phillips amplifiers ($\times$25) were installed so that the gain of the tubes could be kept low. The French octants used 8-stage Phillips XP2282B tubes with an on-board amplifier of a gain of $\sim$20 in the bases. Furthermore, a base-line restorer was also included in the French base to avoid a shift of the base-line due to changes in counting rate.

4.2.4 Electronics

A conceptual diagram of the G^0 forward angle electronics is shown in Fig. 4.14. The electronics contained two components, the time-encoding and the monitoring (Fastbus) electronics. Due to the high counting rates, the event-by-event recording with conventional electronics was not practical, so the experiment used custom-built

time-encoding electronics to store histograms of the particle ToF spectra for each MPS (1/30 s).

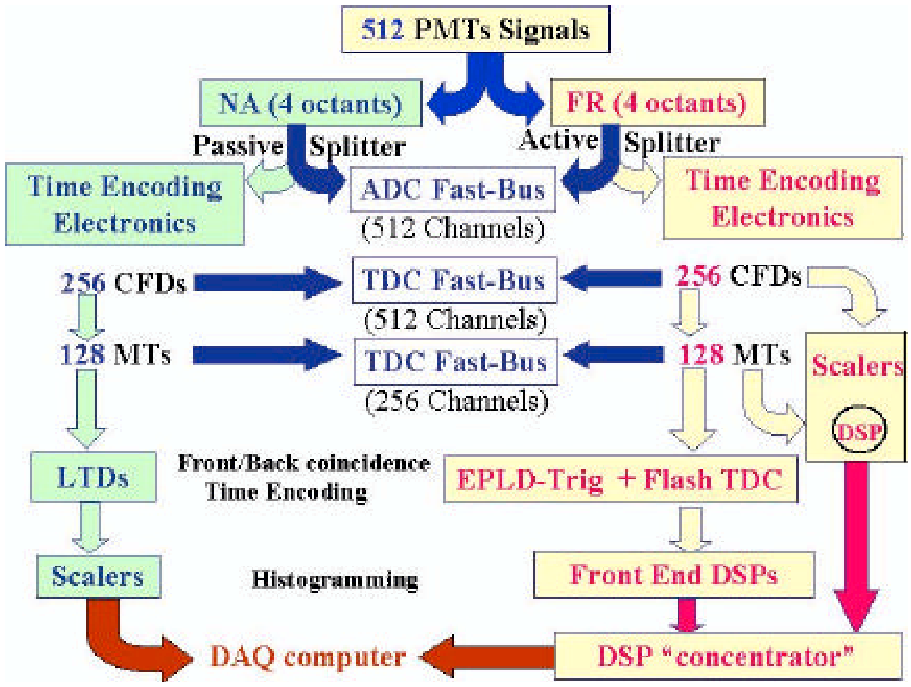

Figure 4.14: *A block diagram of the G^0 electronics. Figure taken from [MK02].*

Different time-encoding electronics were instrumented for the NA and French octants. Both sets used the coincidence counting technique. The pulses from each phototube were sent to a constant-fraction-discriminator (CFD), and an average timing signal was produced between each pair of CFDs of a given scintillator by a meantimer (MT). For later reference, let us define some useful nomenclature here. The four CFDs for a given detector are labeled according to the location of the corresponding phototube as viewed from upstream: front-left (FL), front-right (FR), back-left (BL) and back-right (BR). The meantimers are named in a similar fashion as either the front or back meantimer. A coincidence between the front and back MTs were required with a window of ~10 ns, and the timing was encoded in the custom built electronics. The high counting rate inevitably leads to deadtime losses (~10%). Both sets of electronics implemented a technique called "next-pulse-neutralization" (NPN), which would disable the electronics for a given detector during the remainder of the micropulse (32 ns) and the one following it after a given

hit. The result of this technique is slightly higher, but more deterministic deadtime (see Sec. 5.3.1).

For monitoring purposes, a small sample of the hits were also recorded with Fastbus ADCs (LeCroy 1875) and TDCs (LeCroy 1885). There is one ADC channel associated with each phototube, and one TDC channel associated with each CFD and MT.

We will describe the NA and French custom time-encoding electronics in turn in the next two sections.

4.2.4.1 North American Electronics

A detailed description of the NA custom-built electronics is given in [Cla03]. Shown in Fig. 4.15 is the chain of the NA electronics, including both the time-encoding and Fastbus. Only the essential components of the time-encoding electronics will be recapped here.

The analog signal from a phototube was first split by a passive splitter: 33% of the signal went into the Fastbus ADC, and remaing 67% triggered the CFD. Commercial CFDs (LeCroy 3420) were used in the NA electronics. Careful tuning of the CFD parameters was carried out to minimize the pileup and deadtime effects [Fur03, Qui03].

The NA meantimers were custom-built based on an Application Specific Integrated Circuit (ASIC) developed at IPSC-Grenoble. The outputs of the CFDs of a given scintillator propagate in opposite directions along two separate delay lines. A meantime signal was generated when a coincidence occurred between these two signals [Cla03]. The timing resolution of the meantimer was determined to be $\sim$200 ps [Roc02].

The main component of the NA time-encoding electronics is the Latching Time Digitizer (LTD). There were two reference signals for timing, the 31.1875 MHz beam pick-off signal at the target (Y_0) and a syncronized 499 MHz clock (CLK) signals, as discussed at the end of Sec. 4.2.1.2. A gated clock signal was externally generated by turning off 8 ns of the 499 MHz clock signal, which served as the basic clock train

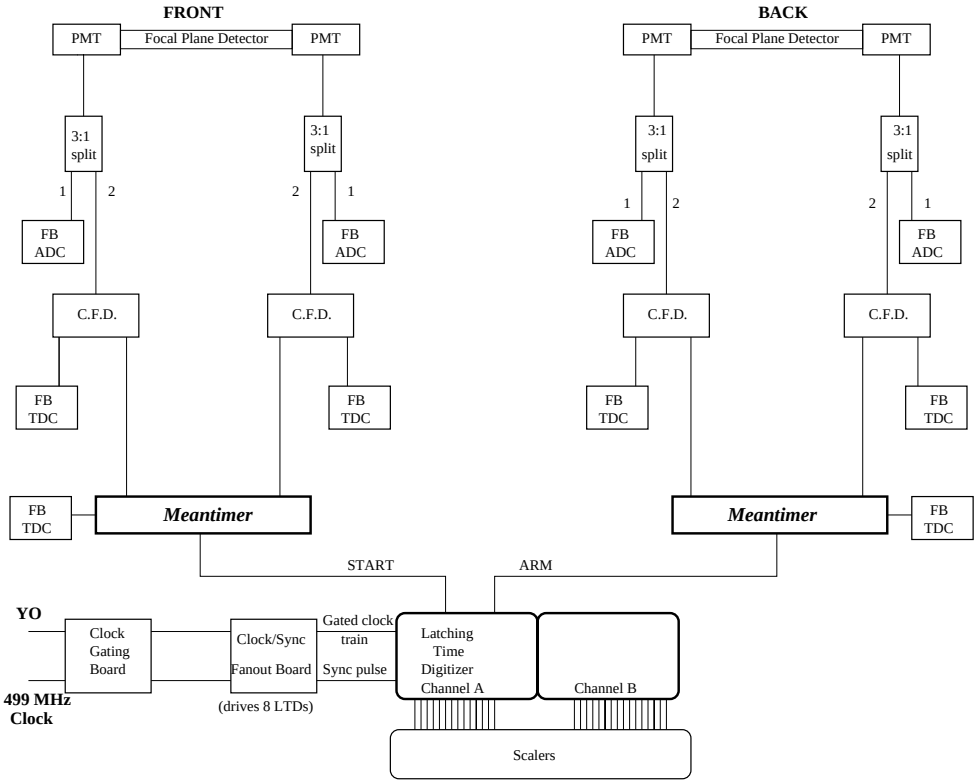

Figure 4.15: *The chain of the NA electronics corresponding to a pair of the scintillators, including both the time-encoding electronics and the Fastbus. The label "FB" in the figure stands for Fastbus. Figure taken from [Cov04].*

for the ToF measurement. The relation among the three timing signals is illustrated in Fig. 4.16.

The concept of the operation of the LTD is quite simple. The back and (few ns delayed) front meantimer signal of a given detector were fed into the signal input and the clock input of a latch, respectively. When a front-back coincidence occurred, the output of the latch was held high upon seeing the rising edge of the clock input (delayed front signal). The back MT output has a width of 10 ns, which defines the width of the coincidence window [Qui06], and the timing of the coincidence trigger is determined by the front hit. The NPN was enforced by waiting until the end of a following beam pulse before resetting the latch. The output of the latch was connected to the signal input of a 16-bit serial-in parallel-out shift register. The gated clock signal was connected to the clock input of the shift register. At the

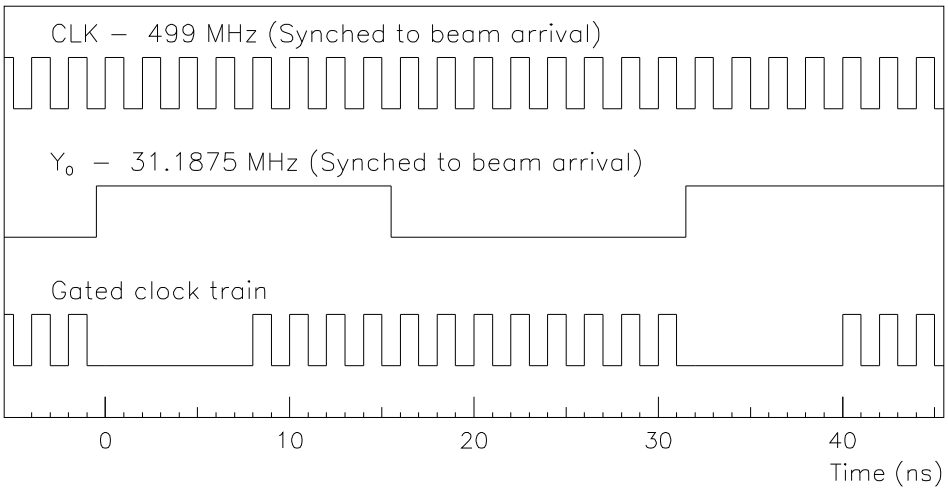

Figure 4.16: *An illustration of the three timing reference signals: Y_0, CLK and the gated clock, used by the NA electronics. Figure taken from [G0NIM].*

rising edge of each clock pulse, the shift register recorded the data input state to its lowest bit, and shifted the previous states of the bits to their adjacent higher bits. Therefore, the penetration depth of the input "high" into the shift register encoded the ToF of the hit.

The gated clock signals were 2 ns apart, therefore using the above method one could only achieve 2 ns timing resolution. The resolution was improved to 1 ns by feeding the inverse of the clock signal ($\overline{\text{CLK}}$) into another 16-bit shift-register and combining the two clock trains. For each channel there were in total 24 bits which encode the ToF. After the last pulse of the gated clock train, the bit patterns of the shift-registers were copied to registers, which subsequently incremented the scalers associated with individual bits. The scalers used by the NA electronics were custom-built VME latching scalers, designed by LPSC-Grenoble. During the interval between macropules (1/30 s), the scaler data were read out and cleared to get ready for the next macropulse. The encoded bit pattern collected by the scalers represented an integrated ToF spectrum. To reconstruct the normal spectra, one has to take the difference of the raw data associated with adjacent bits.

4.2.4.2 French Electronics

The French electronics used active (1:1) splitters, so that the sizes of the signals going into the Fastbus ADCs and the CFDs were identical to the original PMT signal. A diagram of the French time-encoding electronics is displayed in Fig. 4.17. The electronics were integrated onto the DMCH boards (Discriminator, Meantimer, Time-to-Digital-Convertor and Histogramming) developed at IPN-Orsay. Each board contained 32 CFDs and 16 MTs by custom design. The front-back MT coincidence logic (EPLD-Trig) was also built on board and programmable, with nominal configuration as the front-back coincidence with NPN. The coincidence window was selectable with 7 ns (default) and 11 ns.

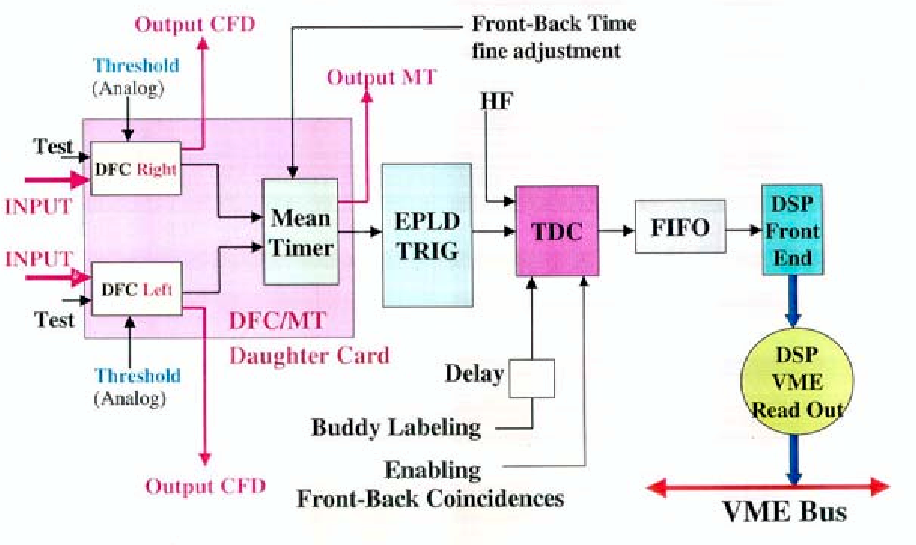

Figure 4.17: *A block diagram of the French time-encoding electronics. Figure taken from [Bim02]. Different components are explained in the text.*

In contrast to the NA system, the French electronics used flash TDCs to encode the time, with a reference high frequency signal (HF) derived from the Y_0. The TDCs were readout by the Digital Signal Processors (DSPs, Model 2106 by Analog Devices Inc.), in which the ToF histograms with 250 ps timing resolution were constructed. The DSPs were processed by the VME bus. Each DMCH board also contained a daughter SDMCH board, which recorded the number of hits for

each CFD and MT with scalers. These data will be important later on when we consider the deadtime loss due to the single hits in Sec. 5.3.1.

Each DMCH board processed signals for 8 detectors. There are 9 such boards in total, with the first 8 covering all 4×16 French detectors. The 9th board imported the signals from detectors 14 and 15 of the NA octants, in order to record their ToF spectra with better timing-resolution. This implementation was essential for the Q^2 binning and background correction in these NA detectors (see Secs. 5.3.6.2 and Sec. 5.3.6.3). The data from the 9th DMCH board shall be later referred to as the hybrid data.

All DMCH boards were housed in a single VXI crate. Similar to the NA electronics, the data in the VXI CPU were read out by the DAQ for each MPS.

4.2.5 Data Acquisition

The G^0 data acquisition (DAQ) was built upon the CODA system [Hey94] developed at JLab, and ran on a linux computer in the counting house. In Fig. 4.18, a conceptual diagram of the DAQ system is shown. Different crates contained the electronics modules for different sub-systems. The DAQ computer sent the trigger command to a "command module", called the Trigger-Supervisor (TS), which then passed the signals to the readout controller (ROC) of each crate. The acquisition software on each ROC then read the data from individual modules according to the trigger types and parameters. The data from the ROCs were shipped to the DAQ computer through Ethernet.

For the G^0 forward angle experiment, there were in total 5 crates. ROC0 was in the crate containing the trigger supervisor (TS0), the scalers which read out the beam monitors, and the VME TDC module which samples signals of Y_0. The beam helicity bit was stored in the input register of the trigger supervisor. ROC1, 2 and 4 corresponded to the VME crates housing the scalers (32 channels/module) for the NA detectors. ROC3 was in the French VXI crates reading the data from all 9 DMCH boards. ROC5 was in the Fastbus crate, which contained all the monitoring ADCs and TDCs modules.

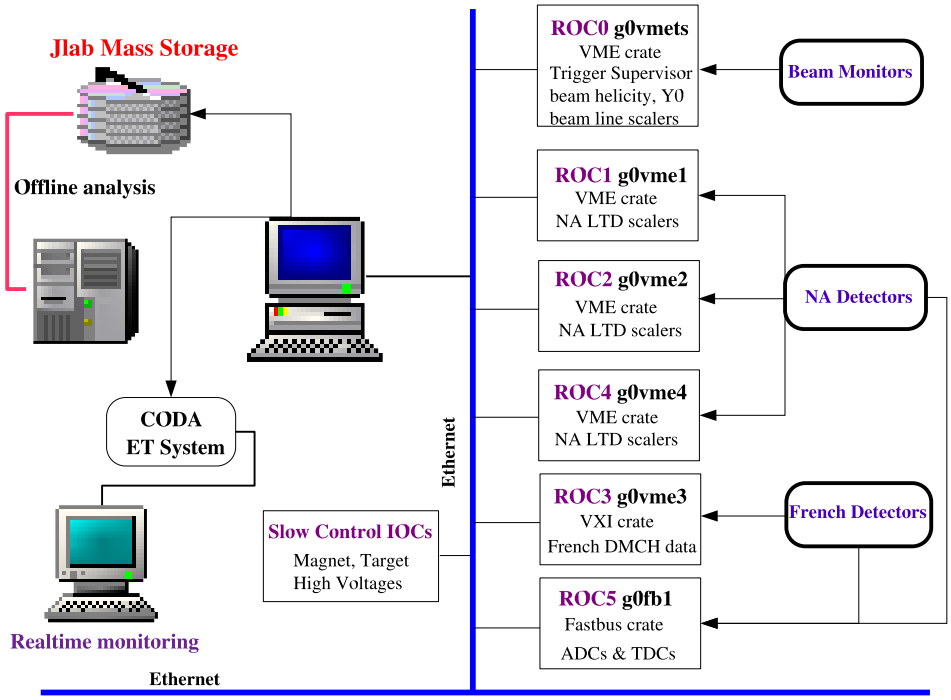

Figure 4.18: *A block diagram of the G^0 DAQ system including the read-out controllers, the DAQ computer, the slow control IOCs, and the analysis computer.*

There were three general types of triggers: 30 Hz, Fastbus and 120 Hz. For the regular 30 Hz trigger (type 1), ROC0, ROCs 1,2 and 4, and ROC3 were read out at the end of each MPS. This formed the basic data stream for asymmetry computation. The Fastbus triggers (type 4) were invoked by a prescaled Y_0 signal, so that only a small sample of the beam pulses were taken. To improve the trigger efficiency, a fast clear was implemented, which cleared all channels unless there was at least one good front-back coincidence hit in all 8×16 detectors. The time required to read out all Fastbus modules was ∼1 ms, which limited the trigger rate to a few hundred Hz. In order to measure the 60 Hz noise in the electronics [Pat99], a special 120 Hz trigger mode (type 2) was implemented. In this mode, each MPS was split into 4 equally spaced periods, during which the NA and the beam monitor scalers were read out [G0NIM]. The 60 Hz noise extracted from the 120 Hz data had been verified to be negligible [Arv05b].

The data were stored in the standard CODA format onto a disk drive in a "bank" structure: the data from a given ROC were written into a bank, with the

ROC number and the length of the data encoded in the band header. The slow control data (target and magnet conditions, high voltages, etc.) were sampled every half a minute or so and written into the data stream as well. Data were collected in one-hour runs, after which each was analyzed by a replay engine running on a dedicated analysis computer in the counting house. The details of the replay engine will be presented in Sec. 5.1.

To facilitate the realtime monitoring during data taking, the DAQ also wrote the data into a shared memory buffer, called the event-transfer (ET) buffer. A consumer program running on the same analysis machine read the data from ET in realtime and produced diagnostic plots (detector rates, beam qualities, etc).

Chapter 5

From Raw Asymmetries to Physics Asymmetries

The details of the data analysis will be presented in this chapter. The mechanics of the replay engine will be introduced in Sec. 5.1, followed by a short overview of the G^0 raw data in Sec. 5.2. The main focus of this chapter is the correction procedure that brings the raw asymmetries to the physics asymmetries; it will be presented step by step in Sec. 5.3.

5.1 Data Reduction Procedure

The raw data collected by the data acquisition system (DAQ) are processed by the replay engine, which decodes the raw data into physical quantities event by event, and reduces the data set. A simplified flow diagram of the data processing is shown in Fig. 5.1. The analysis of the asymmetries involves only the 30 Hz events (MPSs); which will be the focus of this section.

A MySQL database [MySQL] harbors all the input data for the replay, including the calibration data and the cuts, which are loaded at the beginning of the replay. The standard I/O functions of the CODA libraries are invoked to read out the CODA banks. The data are decoded into physical quantities, e.g., the coincidence rate measured in each time bin, and the beam current and position.

Cuts are imposed MPS by MPS to ensure the data quality. The first cut is applied on the beam current to remove the events with beam current < 4 μA (the nominal beam current is ~ 40 μA). Furthermore, the first 500 MPSs ($\sim$17 s) after a beam trip recovery are also removed in order to give the liquid hydrogen target some time to thermally stabilize. In addition to the beam cuts, more stringent cuts are imposed onto individual detectors. Both sets of the electronics have error indicators in the data stream. For each LTD board of the NA electronics, if it happens to "see" too many or too few beam micro-pulses in a given MPS, the error counter associated

with it will increment. For the French electronics, an error occurs whenever a data word overflows 16 bits ($\sim$2 MHz instantaneous rate). In the analyzer, the detectors are tagged as bad in an event whenever the associated counter reads non-zero. To detect an instability in the electronics, which occasionally results in some non-statistical "jumps" in the detector yield (current normalized), the code sacrifices the first 100 *good* MPSs which pass the above cuts in each run to compute the mean and width of the yield distribution of each time bin, and applies a $\pm 10\,\sigma$ cut around the 100 MPS mean on each time bin henceforth. A detector is tagged as bad if any time bin fails the cut subsequently during the run.

If all of the above cuts are satisfied, the beam parameters and the raw detector rates for each time bin are kept. The electronic deadtime correction (see details in Sec. 5.3.1) is then made detector by detector to compute the true rate bin by bin, which is then normalized to the beam current to give the detector yield.

As mentioned in Sec. 4.2.1, the helicity of the beam is flipped in a quartet-wise pattern ($+--+$ or $-++-$). If all the four MPSs of a quartet pass the cuts, the asymmetry of the detector yield in each time bin will be computed as

$$A_{QRT} = \mathcal{H}\frac{Y_1 + Y_4 - (Y_2 + Y_3)}{Y_1 + Y_4 + Y_2 + Y_3}\,, \tag{5.1}$$

in which Y_i is the yield measured in the ith MPS in a quartet, and $\mathcal{H} = 1(-1)$ if the helicity bit of the first MPS of the quartet is $+(-)$. Note that $\mathcal{H}$ is determined by the helicity bit which sets the polarity of the helicity Pockels cell. The charge asymmetry of the beam can be computed the same way. For the beam positions, angles, and energy, conventionally we calculate the helicity correlated difference instead, such that

$$\Delta p = \mathcal{H}\frac{p_1 + p_4 - (p_2 + p_3)}{2}\,, \tag{5.2}$$

in which p_i is a generic symbol for any of these beam parameters measured in an MPS. For all these quantities, the helicity uncorrelated (straight) averages within a quartet are computed as well.

The libraries of the ROOT package (an object-oriented analysis framework) [Bru97],

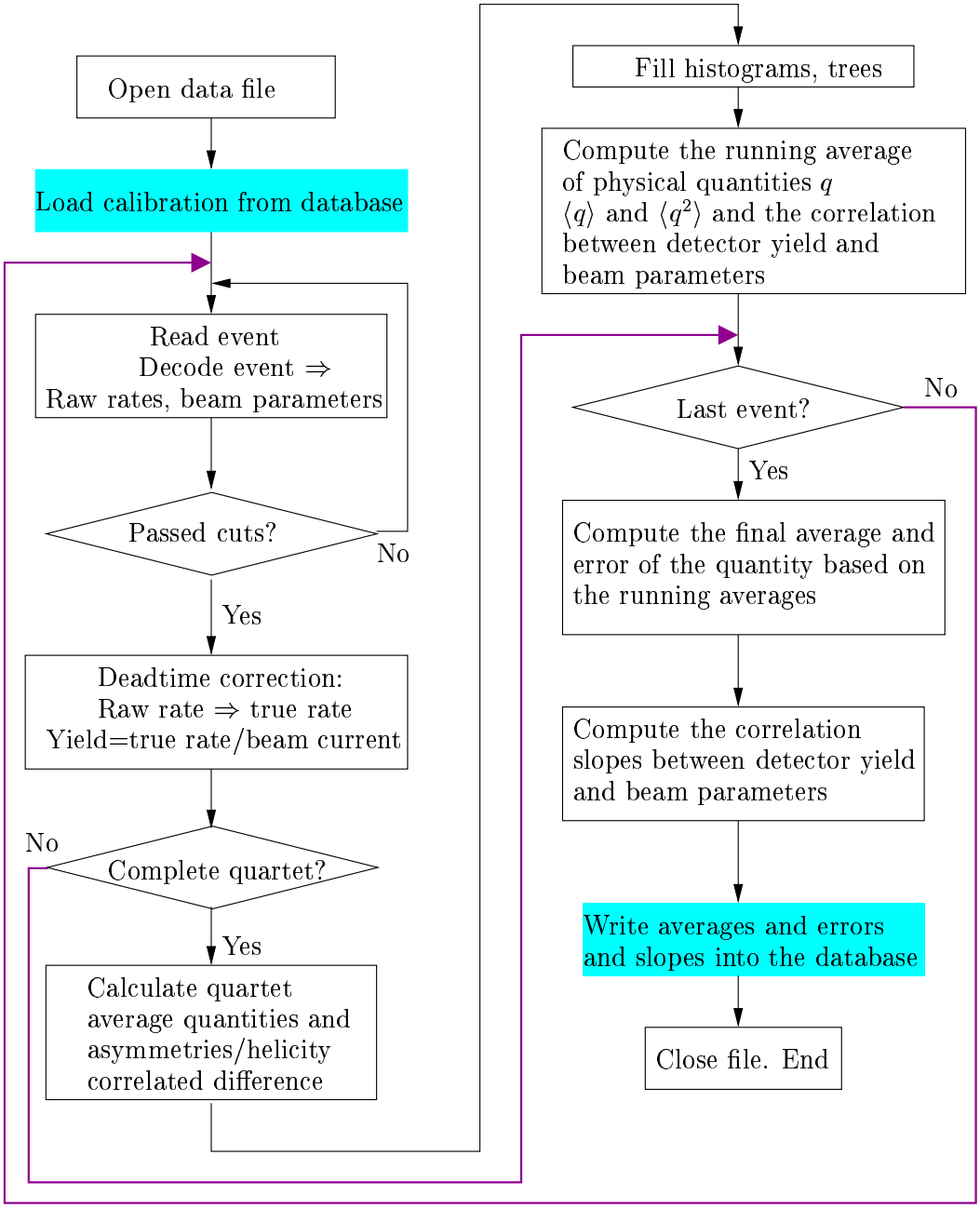

Figure 5.1: *The data flow diagram of the G^0 replay engine.*

developed at CERN, are dynamically linked to the analyzer, so that the data can be stored in the form of histograms and "trees" for further analysis. For each quartet, the detector yields, asymmetries, and the helicity uncorrelated and correlated beam parameters are filled into the histograms and "trees".

The ROOT histograms and trees provide a convenient means for diagnosis.

However, they take significant disk space, and further data extraction is rather inefficient from the computation point of view. Therefore, for each quartet, the running averages of a quantity q and q^2, $\langle q \rangle$ and $\langle q^2 \rangle$, up to this quartet are computed. This is performed on the detector yield and asymmetry of each time bin, as well as the beam parameters (helicity-correlated and uncorrelated).

At the end of the run, the mean of q is simply the running average $\langle q \rangle$, and the uncertainty of the mean (assuming a normal distribution) is calculated as

$$\sigma(q) = \frac{\langle q^2 \rangle - \langle q \rangle^2}{N_{QRT}}, \tag{5.3}$$

in which N_{QRT} is the total number of good quartets of this run. Note that we have assumed equal statistical significance of the measurements in individual quartets. This assumption can be justified by noting that during a given run, the beam current typically is maintained at a constant level to less than 2%, and the low current events due to the beam trips are removed by the beam current cut and the "trip recovery" cut. We will elaborate further on the statistical property of the data in Sec. 5.2.2.

The correlation slope, $\frac{\partial Y}{\partial p}$, between the detector yield Y and a given beam parameter p, is also computed by keeping the running average $\langle Y \times p \rangle$. The detailed procedure of calculating the slope will be discussed in Sec. 5.3.3.

At the end of the replay of each run, the means and uncertainties of the yields, asymmetries, beam parameters, as well as the correlation slopes of this run are written into the MySQL database, which serves as a reduced data set for further analysis.

5.2 Overview of the G^0 Data

Before a detailed discussion of the physics analysis, it is appropriate to present an overview of the data and their quality. In the next two sections, some representative raw data of G^0 will be shown, followed by a discussion of the statistical properties of the data.

5.2.1 G^0 Data: Time-of-Flight Histograms of Yield and Asymmetry

As mentioned, the raw data of G^0 primarily consist of the time of flight spectra of the yield and asymmetry. The physics analysis will be focusing on extracting the elastic asymmetries from the raw measurements. For future reference, let us take a snapshot of the raw data. In Fig. 5.2, typical time of flight histograms of the yields and asymmetries measured by the French and NA electronics are displayed. The pion and elastic proton peaks are located at about 12 ns and 23 ns in the plots, respectively. The inelastic proton bump is located between the pion and elastic peaks, with a tail that extends underneath the elastics. The following particle ID cuts are made along the time of flight spectra as shown in the figures:

- proton cut: a window around the elastic proton peak — detectors 1 through 14: 4.25 ns (17 bins) for the French and 5 ns (5 bins) for the NA, detector 15: 6.25 ns (25 bins) for the French and 7 ns (7 bins) for the NA;
- pion cut: a window around the pion peak — 4.25 ns (French), 5 ns (NA);
- inelastic cut [†]: the region in between the pion and proton cuts;
- cut1/2: regions inside the inelastic cut. Cut2 is a 2.25 ns (French) or 3 ns (NA) window preceding the proton cut, and cut1 is another window preceding cut2 with the same size;
- cut3: a window right behind the elastic proton peak, with the same size as the proton cut;
- total: the entire 32 ns spectrum.

Due to different timing resolutions, these cuts are not 100% consistent between the two sets of electronics. They are used primarily as nomenclatures for qualitative discussions.

[†]The inelastic cut, cut1, and cut2 are undefined for detector 15, where the pion peak is very close to the elastic proton peak.

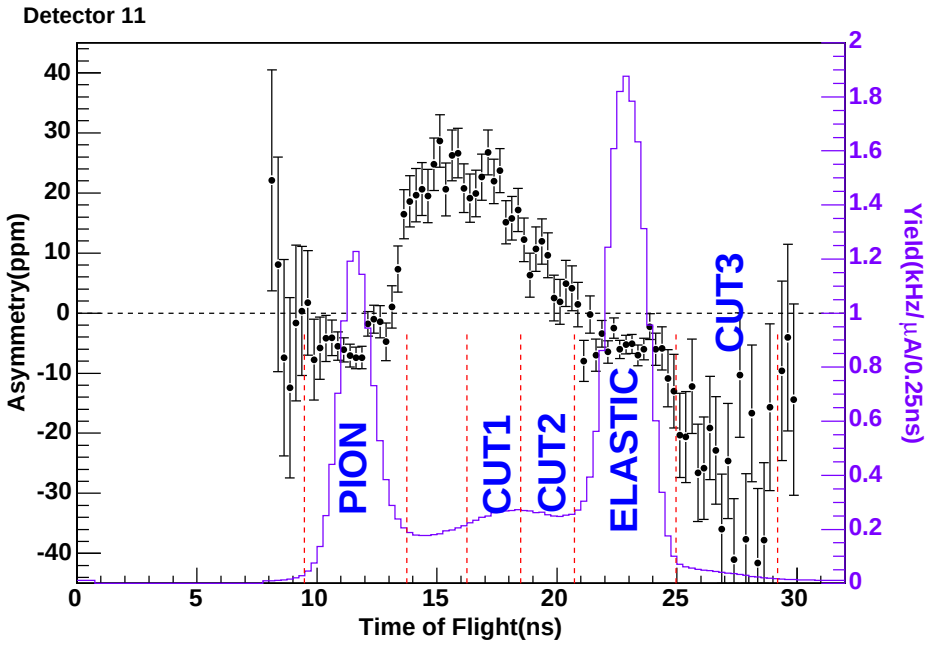

(a) *French data.*

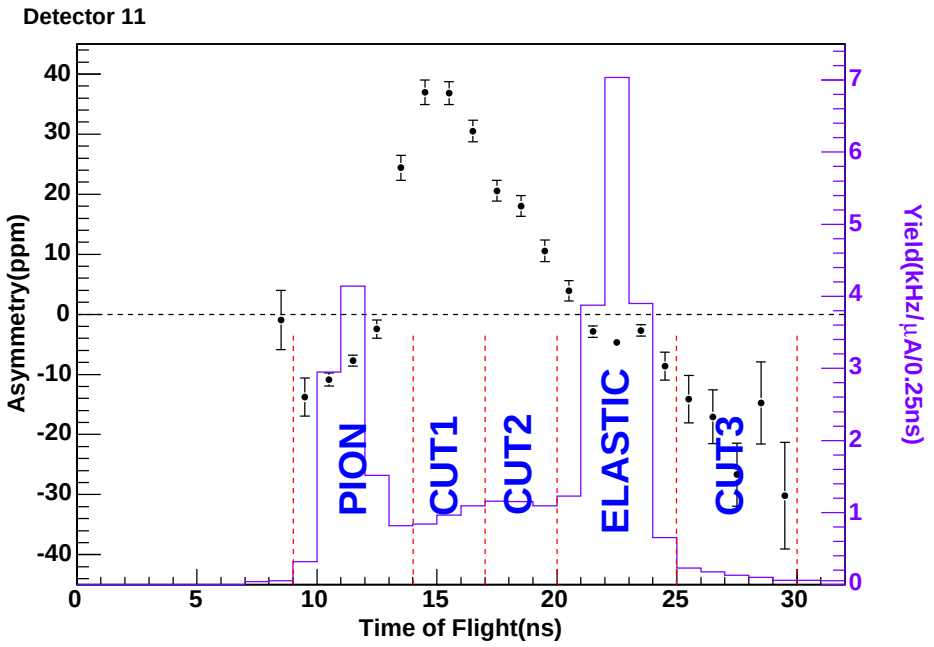

(b) *NA data.*

Figure 5.2: *An example of the raw data collected by the French (a) and NA (b) electronics (detector 11). The yield (solid line) and asymmetry (data points with error bars) histograms are overlaid, and various PID cuts are indicated in the plots. The asymmetries are corrected for the beam polarization (∼0.737), but are blinded by a factor of 0.8056 (see the beginning of Sec. 5.3).*

5.2.2 Statistical Properties of the Data

If the asymmetry measured in each individual quartet has the same statistical weight, the distribution of the asymmetries should behave as a pure random distribution with a perfect Gaussian shape. In Fig. 5.3, the quartet-by-quartet asymmetry of the proton peak in octant 7 detector 8 throughout the entire experiment is histogrammed. One sees that the asymmetry is distributed cleanly with no side tails.

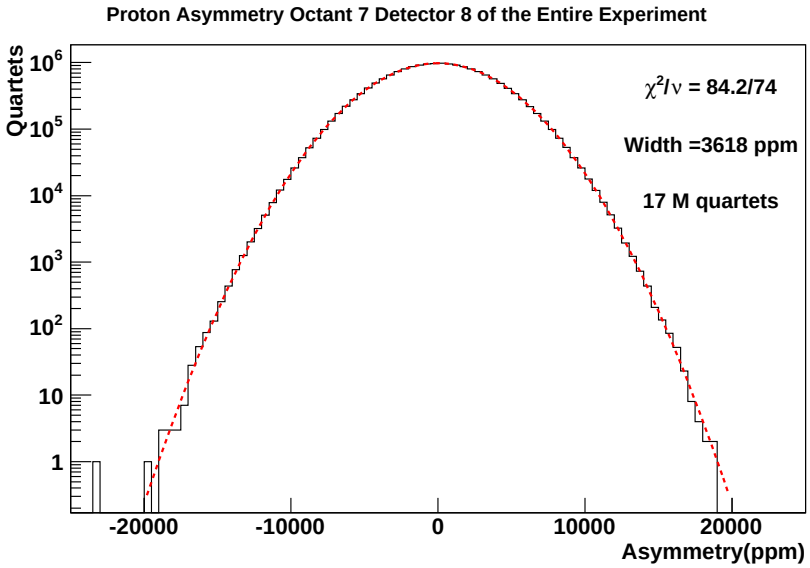

Figure 5.3: *The distribution of the measured quatet-by-quartet proton asymmetries of octant 7 detector 8 during the entire experiment and the Gaussian fit.*

Let us assume the beam current is a constant and neglect the small helicity correlated asymmetry so that the physical scattering rate is the same for both helicity states. For each measurement period (1/30 s), the measured particle counts should be Poisson-distributed. For large numbers of counts, the Poisson distribution with average N counts is equivalent to a Gaussian distribution with a standard deviation of $\sqrt{N}$. In other words, the width of the measured counts in each helicity state satisfies [†]

$$\mathcal{W}(N^+) = \mathcal{W}(N^-) = \sqrt{N}\,, \tag{5.4}$$

[†]For clarity, we have used the $\mathcal{W}(x)$ to denote the *width or standard deviation* of a distribution, and reserved $\sigma(x)$ as the *uncertainty of the mean* of a distribution.

The asymmetry in each quartet is

$$A = \frac{N_1^+ + N_2^+ - N_1^- - N_2^-}{N_1^+ + N_2^+ + N_1^- + N_2^-}\,, \tag{5.5}$$

in which N_1^+ (N_1^-), N_2^+ (N_2^-) are the particle counts measured in first and second positive (negative) helicity states in a quartet, respectively. Since each MPS is an independent measurement, one can simply propagate $\mathcal{W}(N^+)$ and $\mathcal{W}(N^-)$ to get

$$\mathcal{W}(A^0_{expected}) = \frac{1}{\sqrt{4N}}\,. \tag{5.6}$$

In principle, one could compare the width of the measured asymmetry with $\mathcal{W}(A^0_{expected})$. However, the deadtime loss introduces more complications. If a measurement is made with a deadtime loss factor f_{dead}, such that the measured counts N_m is related to the true count N as

$$N_m = (1 - f_{dead})N\,, \tag{5.7}$$

in which f_{dead} will be shown to be $\propto N$ in Sec. 5.3.1. Even if one makes a perfect correction to the deadtime loss such that

$$N_c = \frac{N_m}{1 - f_{dead}} = N\,, \tag{5.8}$$

it is still apparent that the uncertainty of N_c will be larger than $\sqrt{N_c}$, since one has to pay the price of accuracy for the loss of information due to deadtime. The calculation of $\mathcal{W}(N_c)$ can be found in [Coa92], which gives an approximate relation for small f_{dead} that

$$\mathcal{W}(N_c) \simeq \sqrt{N_c}\sqrt{1 + f_{dead}}\,. \tag{5.9}$$

This leads to an expected width of the deadtime corrected asymmetry

$$\mathcal{W}(A^c_{expected}) = \frac{\sqrt{1 + f_{dead}}}{\sqrt{4N}}\,. \tag{5.10}$$

In our analysis, the distribution of the proton asymmetry of each detector is fitted

with a Gaussian as shown in Fig. 5.3, and the observed width, $\mathcal{W}(A_{obs})$, is compared with $\mathcal{W}(A^c_{expected})$ given by Eqn. 5.10, using values of f_{dead} as determined in Sec. 5.3.1.3. In Fig. 5.4, $\frac{\mathcal{W}(A_{obs})}{\mathcal{W}(A^c_{expected})}$ is plotted for all detectors. One sees that the observed and expected widths agree well, which demonstrates that the measured uncertainty of the asymmetry is dominated by the statistical fluctuation of the scattering events.

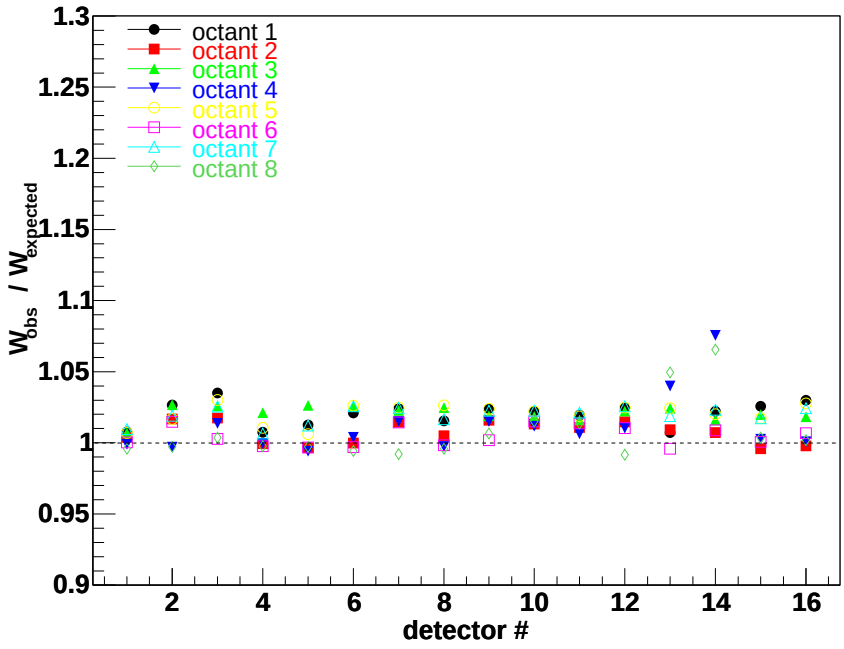

Figure 5.4: *The ratio of the observed and statistically expected proton asymmetry widths of all detectors. Different colored markers represent the measurements in different octants, with the code given in the legend. Figure courtesy of B. Guillon [Gui05].*

Despite the nice results shown above, one problem was discovered in the French electronics. As discussed in Sec. 5.2, the proton cut there contains 17 time bins (0.25 ns/bin). The mean and width of the asymmetry in the proton cut can be computed in two different ways, and they are found to disagree. First, one can integrate the yield in all 17 bins to get the proton yield, compute the proton asymmetry quartet by quartet of this yield, and find its mean and width (method A). Alternatively, one can compute the asymmetry and find its measured width bin by bin, and then make a weighted average to get the expected proton asymmetry and

width as

$$A_p = \frac{\sum_{i=1}^{17} \frac{A_i}{\mathcal{W}(A_i)^2}}{\sum_{i=1}^{17} \frac{1}{\mathcal{W}(A_i)^2}}, \quad \mathcal{W}(A_p) = \frac{1}{\sqrt{\sum_{i=1}^{17} \frac{1}{\mathcal{W}(A_i)^2}}}, \tag{5.11}$$

in which A_i and $\mathcal{W}(A_i)$ are the measured asymmetry and its width in time bin i (method B).

If the measurement of each time bin i is independent, the widths of the proton asymmetries obtained using the two methods should agree. However, as mentioned earlier, $\mathcal{W}(A_p)$ calculated using method B is found to be $\sim$20% larger than that given by method A in the French electronics. Also there are strong correlations of the yields and asymmetries among different time bins within the proton peak [Han05]. The origin of this is not completely understood, but it has been strongly suspected that the electronic noise present in the French time-encoding TDCs can cause a modulated jitter to the widths of the time bins. A simulation of the French electronics has identified that the resulting intrinsic jitter of the TDC is of the order 100 ps [Mar05p]. Since the total width of the 128 bins of a given spectrum is fixed at 32 ns, a jitter of the width of any bin will introduce correlations among all time bins. In [Cov04], the author presented a dedicated simulation to look into the impact of this type of timing jitter. The study indicates that if there was a periodic timing jitter of $\sim$50 ps, with a modulation frequency between 1-10 kHz, it would reproduce the observed correlation.

Consequently, the uncertainties of bin-by-bin asymmetries in the French electronics cannot be treated as independent uncertainties. On the other hand, the uncertainty of the proton peak (obtained using method A) is insensitive to the internal TDC jitter, as substantiated by the simulation in [Cov04]. This can be understood from the fact that the proton cut encloses more than $\sim \pm 3$ half-widths of the elastic peak, hence the variation of the yield inside the cut is negligible if cut boundaries jitter by $\sim$50 ps. The uncertainty of the proton peak calculated using method A will also be referred to as the "proton peak uncertainty". It will be used

in Sec. 5.3.6 to evaluate the statistical uncertainty of the elastic asymmetry.

To estimate the systematic uncertainty due to this bin correlation effect, we compare the values of the proton asymmetries (averaged over the entire experiment and over all French detectors) calculated using methods A and B; the results given by the two methods differ by 0.14 ppm. The same comparison made on the NA data leads to a tiny difference of 0.0005 ppm. The differences of methods A and B in the NA and French data are averaged, and $\frac{1}{2}$ of that is assigned as the systematic uncertainty due to this effect, which leads to

$$\sigma(A_{bin-correlation}) = 0.035 \text{ ppm}\,. \tag{5.12}$$

This is a global uncertainty assigned to final asymmetries of the entire data set. It has been corrected for the beam polarization (see Sec. 5.3.4), but is blinded by a blinding factor of 0.8056 (see the beginning of Sec. 5.3) to be consistent with the discussions in the remainder of this chapter.

To investigate whether there exists a long term systematic drift in the asymmetries, the data are broken down into different sets, according to the state of the insertable halfwave plate (see Sec. 4.2.1.2). Plotted in Fig. 5.5 are the average asymmetries of the proton cut of detector 9 from different data sets during the entire experiment. The corrections to the deadtime (Sec. 5.3.1) and the leakage effects (Sec. 5.3.2) have been made on these data. The error bar on each data point is the measured "proton peak uncertainty" described for method A above. The data sets are arranged in chronological order. As one can see, the average asymmetry clearly flips sign when the state of the halfwave plate changes. The statistical agreement of the asymmetries from different sets is excellent.

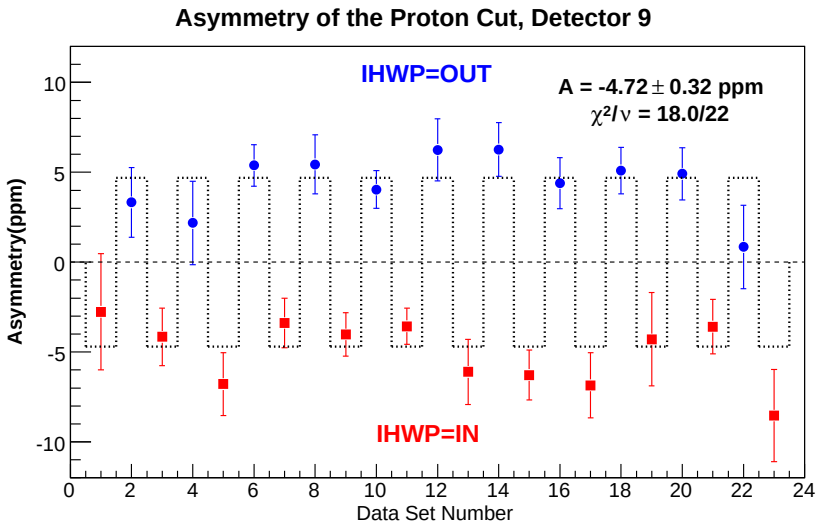

Figure 5.5: *Asymmetries of the proton cut of detector 9, in ppm, divided into data sets. The blue circles (red squares) are the data with the insertable halfwave plate (IHWP) inserted (retracted). For data sets before 22, each represents a continuous period with a given IHWP state. In order to have comparable statistical precision on each data point, the last 3(4) short running periods with IHWP inserted (retracted) are grouped to form data set 22(23). The stepwise pattern of the data reflects the alternating insertion/retraction of the IHWP (about once every three days). The average asymmetry over the entire run is indicated by the amplitude of the dashed step. Data are corrected for the beam polarization (~ 0.737), but are blinded by a factor of 0.8056 (see the beginning of Sec. 5.3).*

5.3 Corrections to the Raw Asymmetries

In Fig. 5.6, a flow diagram of the analysis procedure is shown. The data correction procedure will be presented in the order in which the corrections were applied [†]. To avoid human bias, the raw asymmetry A_{raw} and the helicity correlated beam parameters are first multiplied by a global blinding factor [‡] $f_{blind} \equiv 0.8056$, followed by a series of instrumental corrections, for the electronics deadtime, the leakage asymmetry in the beam, that due to the helicity correlated beam properties, and the beam polarization. A correction is subsequently made to remove the background contamination underneath the elastic peak, followed by a small electromagnetic radiative correction to the elastic asymmetry A_e. The corrected asymmetry is then

[†] Two exceptions are the corrections for the helicity correlated beam properties and the *residual* deadtime, which are applied after the background correction.

[‡] This blinding factor had been encrypted until the end of the analysis.

unblinded, which gives the physics asymmetry. The procedure to extract the strange form factors from the physics asymmetry will be presented in Chapter 6.

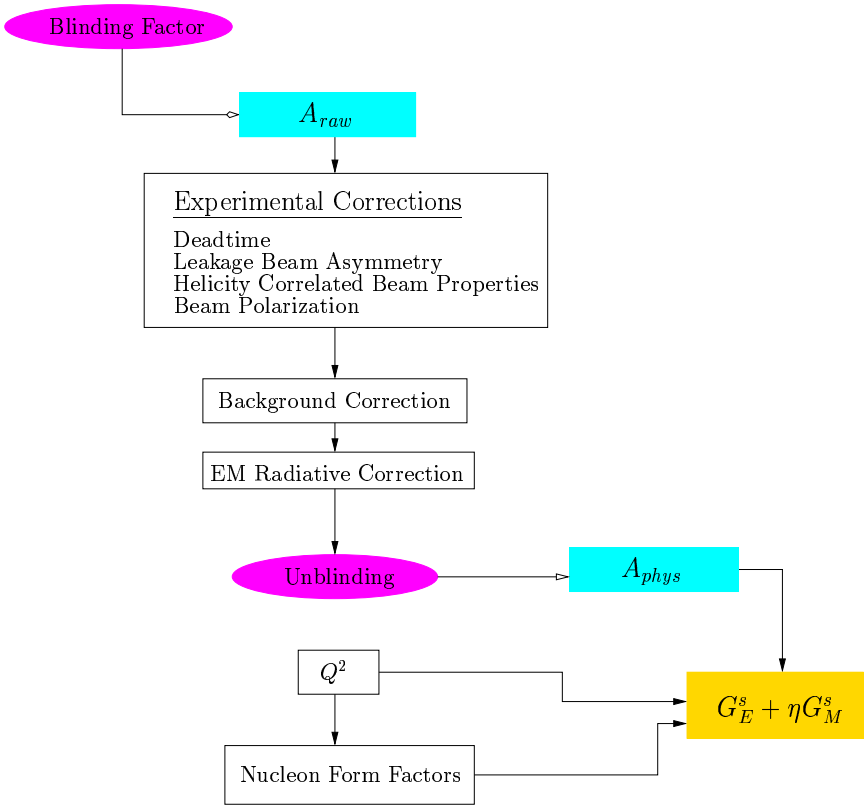

Figure 5.6: *The flow diagram of the analysis procedure. See text for details.*

Unless otherwise specified, all asymmetries in the remaining part of this chapter are blinded by $f_{blind} \equiv 0.8056$.

5.3.1 Deadtime Correction

All counting electronics have some degree of deadtime. The electronics will not respond during a time period τ following a hit that triggers the electronics, where τ is a characteristic deadtime of the electronics. For a flat and Poisson distributed rate R, the average probability of at least one hit occurring during the window τ is $1 - e^{-R\tau}$, which is precisely the average "dead" probability of the electronics f_{dead}. Therefore one writes

$$f_{dead} = 1 - e^{-R\tau} \,, \tag{5.13}$$

and the measured rate r can be expressed as

$$r = (1 - f_{dead})R\,. \tag{5.14}$$

At the limit that $R\tau \ll 1$, f_{dead} is simply

$$f_{dead} \simeq R\tau\,. \tag{5.15}$$

If the true rate carries helicity correlated asymmetry, Eqn. 5.14 becomes

$$r^{\pm} = (1 - f^{\pm}_{dead})R^{\pm}\,, \quad f^{\pm}_{dead} \simeq R^{\pm}\tau\,, \tag{5.16}$$

resulting in

$$A_r \simeq (1 - \frac{f_{dead}}{1 - f_{dead}}) \times A_R \tag{5.17}$$

in which A_r and A_R are the asymmetries carried by the measured (uncorrected) rate r and the true rate R. The false asymmetry thus introduced, $-f_{dead} \times A_R$, is a directly consequence of the fact that f_{dead} is helicity correlated. For G^0, a typical value of f_{dead} ~10%. Therefore, understanding the deadtime and making corrections for it is an essential step in understanding the systematics of the G^0 experiment. It is important to note that the correction needs to reflect the helicity correlation of f_{dead}. Thus in our analysis, the correction is made on the measured rate MPS by MPS.

In this section, the deadtime correction of the NA electronics will be discussed in detail. The principle of the deadtime correction for the French electronics is very similar, therefore only the differences will be highlighted.

5.3.1.1 North American Deadtime Correction

Only the front-back detector coincidences are collected by the time-encoding electronics (see Sec. 4.2.4.1). However, both the CFDs and MTs have an intrinsic deadtime, therefore not only the coincidences but also the singles contribute to

the deadtime loss. The situation is further complicated by the 32 ns pulsed beam structure, which results in a non-uniformly distributed rate in time.

In general, measuring a coincident hit in time bin i, requires that at least one true hit occurs in time bin i, and the electronics is alive. Therefore the probability of measuring a hit , P_m^i, can be written as

$$P_m^i = (1 - P_{dead}^{coin} - P_{dead}^{sing}) P_t^i \,, \tag{5.18}$$

in which P_{dead}^{coin} and P_{dead}^{sing} are the "dead" probability of the electronics due to coincidences and to singles, respectively, and P_t^i is the probability of at lease one true hit in bin i. The true hits should be Poisson distributed, therefore we expect

$$P_t^i = 1 - e^{-R_i \tau_i} \,, \tag{5.19}$$

in which R_i and τ_i are the true rate and the width of time bin i. On the other hand, P_m^i is related to the measured rate in bin i, r_i, with

$$P_m^i = r_i \tau_i \,. \tag{5.20}$$

The intrinsic deadtimes of the CFDs and MTs are roughly 30−40 ns. For a 1 MHz of rate, this corresponds to a ∼3.5% loss. Taking into account the G^0 beam structure, one realizes that after a hit, the meantimer is recovered in the middle of the next pulse, as illustrated in Fig. 5.7. In principle this effect can be corrected if the deadtime of each meantimer is known accurately. However, with 256 channels this is impractical. As discussed in Sec. 4.2.4, the so-called next-pulse-neutralization (NPN) is implemented into the electronics as a remedy, whose scheme is illustrated also in Fig. 5.7.

Based on the design of the NPN, let us consider P_{dead}^{coin} first. Ignoring the singles, the electronics is dead in bin i if there is at least one hit in the previous pulse, or there is a hit measured within one of the earlier $i-1$ bins of the same pulse.

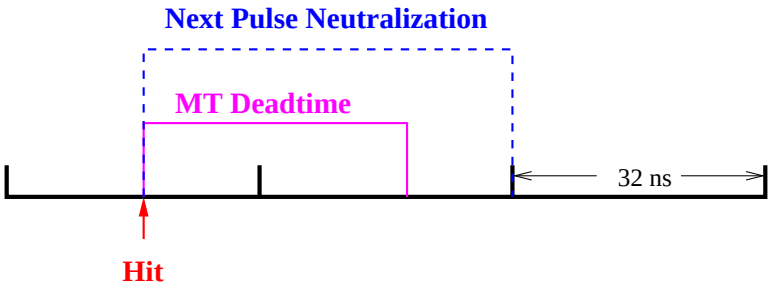

Figure 5.7: *The scheme of the next-pulse-neutralization (NPN). Once a hit occurs, the encoding electronics is disabled in the remaining period of the same pulse, as well as the next pulse.*

The probabilities of these two cases are denoted as P_{pre} and P^i_{ear}, respectively, and

$$P^{coin}_{dead} = P_{pre} + P^i_{ear} \,. \tag{5.21}$$

Note that P_{pre} and P^i_{ear} are additive, because they are not independent probabilities, i.e., a measured hit in an earlier bin in the current pulse requires that there was no hit in the previous pulse. One should also note that the NPN is implemented in such a way that P_{pre} is determined by the occurrence of the true hits and P^i_{ear} is determined by the measured hits. For example, consider three consecutive pulses. If the busy latch of the second pulse is set due to a hit in the first pulse, then no hits can be measured in the second pulse. But the busy latch of the 3rd pulse can still be set if there is a true hit in the 2nd pulse, even though we do not measure it. On the other hand, if the current pulse is not dead and a hit is measured anywhere between bin 1 and bin $i-1$, bin i of the same pulse is dead [Cla02p]. With this precaution, we can write

$$P_{pre} = 1 - e^{-\sum R_k \tau_k} \tag{5.22}$$

$$P^i_{ear} = \sum_{k=1}^{i-1} P^k_m = \sum_{k=1}^{i-1} r_k \tau_k \,. \tag{5.23}$$

Again, the probabilities P^k_m here are additive since they are not independent.

Besides the NPN, additional deadtime is introduced by the single hits — low energy hits which do not fire both MTs. The NA electronics does not have dedicated

scalers to count these hits, but they can be determined by analyzing the Fastbus data. Naively, one can sort the single hits into

- CFD singles, a CFD fires but the corresponding MT does not;
- MT singles, one of the MT fires, but the other one of the same detector does not.

However, this simple sorting leads to double counting. For example, a hit that fires the front-left CFD and both back CFDs would be counted as both a CFD single, as well as a back MT single [†] . To avoid this, one has to sort the hits into all possible single/coincidence combinations. There are in total 15 different combinations, which can be represented "geometrically" by a 4×4 table shown in Table 5.1. "FL", "FR", "BL" and "BR" in the table are the abbreviations for front-left, front-right, back-left and back-right CFDs, respectively. The (1,1) cell of the table corresponds to no hits in any of the CFDs, therefore should be ignored. For the rest of the cells, each represents a unique type of hit. The four-fold coincidence rates of "FL/BL/FR/BR" has

FL/BL	FL/BL/FR	FL/BL/BR	FL/BL/FR/BR
BL	BL/FR	BL/BR	BL/FR/BR
FL	FL/FR	FL/BR	FL/FR/BR
n/a	FR	BR	FR/BR

Table 5.1: *The 4×4 table which sorts the hits in terms of "geometry". See text for details.*

been dealt with in the time-encoding and NPN. Now let us sort the remaining 14 cells into three categories: the rates in "FL/FR", "FL/BL/FR" and "FL/FR/BR" (blue cells) are sorted into a front meantimer singles rate, R_{f}, and similarly "BL/BR", "FL/BL/BR" and "BL/FR/BR" (pink cells) are summed into a back meantimer singles rate R_{b}. The rates in the rest of the slots are treated as the CFD single rates R_{s}. Therefore for a given point in time t, the "dead" probability is simply the

[†]See nomenclature of the CFDs and MTs in Sec. 4.2.4.

sum of the three probabilities of having at least one hit within the deadtime window preceding t [†]:

$$P_{dead}^{sing} = (1 - e^{-R_{\rm f}\tau_{\rm f}}) + (1 - e^{-R_{\rm b}\tau_{\rm b}}) + (1 - e^{-R_{\rm s}\tau_{\rm s}})\,, \tag{5.24}$$

in which $\tau_{\rm f}$, $\tau_{\rm b}$ and $\tau_{\rm s}$ are the deadtimes of the front meantimer, back meantimer and CFD single hits, respectively. Eqn. 5.24 would contain no subtlety if the single rates are distributed flat in time. In reality this is untrue — singles are mostly pions and photons, which have shorter flight time than the protons. Therefore a single hit would "shadow" the proton in the same micropulse. Hence, although the intrinsic deadtime of the CFDs and MTs are roughly 30-40 ns, the effective deadtime due to the singles that the proton "feels" is the length of the micropulse, 32 ns [‡]. Moreover, in the NA electronics, the front meantimer single hits also trigger the NPN, therefore on average, the front meantimer causes a deadtime of ∼48 ns. These two values of the singles deadtime have been substantiated by a detailed simulation of the electronics chain [Bis04]. Therefore we have

$$\tau_{\rm b} = \tau_{\rm s} = 32 \text{ ns}, \quad \tau_{\rm f} = 48 \text{ ns}\,. \tag{5.25}$$

In principle, for each given run, one could replay the Fastbus data first to obtain the singles rates, then make another replay to apply these singles rates to correct for the deadtime loss of the coincidence rates. In practice, the singles rates exhibit stable and almost linear relations with the beam current. These relations are calibrated using a few runs at different beam current. Then during the normal replay, the singles rates are simply calculated MPS by MPS based on the calibration and the measured beam current.

[†] In principle, the single rates appeared on the right-hand side of Eqn. 5.24 should be the true single rates, whereas those in the 4×4 table measured by Fastbus contained deadtime losses due to the CFDs, MTs and Fastbus TDCs. This second order inconsistency was omitted in our treatment nevertheless.

[‡] Strictly speaking, this statement is valid only to the proton regions, however it is applied throughout the whole spectrum as an approximation.

Applying Eqns. 5.21-5.24, Eqn. 5.18 can be written out explicitly as

$$r_i\tau_i = \left[1 - \left(1 - e^{-\sum R_k\tau_k}\right) - \sum_{k=1}^{i-1} r_k\tau_k - P_{dead}^{sing}\right] \times \left(1 - e^{-R_i\tau_i}\right) , \tag{5.26}$$

in which P_{dead}^{sing} is given by Eqn. 5.24. This equation relates the true rates R_i with the measured rates r_i and the singles rates. To avoid confusion with the later defined first order expansion, let us define a full deadtime factor F_{dead} such that

$$r_i = (1 - F_{dead})R_i , \tag{5.27}$$

and note that F_{dead} is a complicated function of the true, raw and the singles rates as implied by Eqn. 5.26.

It is useful to cast Eqn. 5.26 into a more intuitive first order relation. Using $e^{-x} \to 1 - x$, Eqn. 5.26 becomes

$$r_i = \left(1 - f_{dead}^c - f_{dead}^m - f_{dead}^s\right) R_i , \tag{5.28}$$

$$f_{dead}^c = \sum R_i\tau_i + \sum_{k=1}^{i-1} r_k\tau_k , \tag{5.29}$$

$$f_{dead}^m = R_{\rm f}\tau_{\rm f} + R_{\rm b}\tau_{\rm f} , \tag{5.30}$$

$$f_{dead}^s = R_{\rm s}\tau_{\rm s} , \tag{5.31}$$

and f_{dead}^c, f_{dead}^m and f_{dead}^s are the first order fractional deadtime loss due to the coincidences, the MT singles and the CFD singles.

Were the true spectrum R_i known, it would be straightforward to use Eqn. 5.26 to compute the measured spectrum r_i. Going the other way is much more difficult; generally there is no analytical solution. However, R_i can be solved numerically via an iterative procedure for which a flow diagram is shown in Fig. 5.8. In the first iteration, $f^0 = 5\%$ and $R_i^1 = \dfrac{1}{1 - f^0} r_i$ are taken as a guess of the deadtime loss and the true rate, respectively. Eqn. 5.26 is applied to this spectrum to calculate the measured spectrum, r_i^1 (the superscript is the index of the iteration). The deadtime

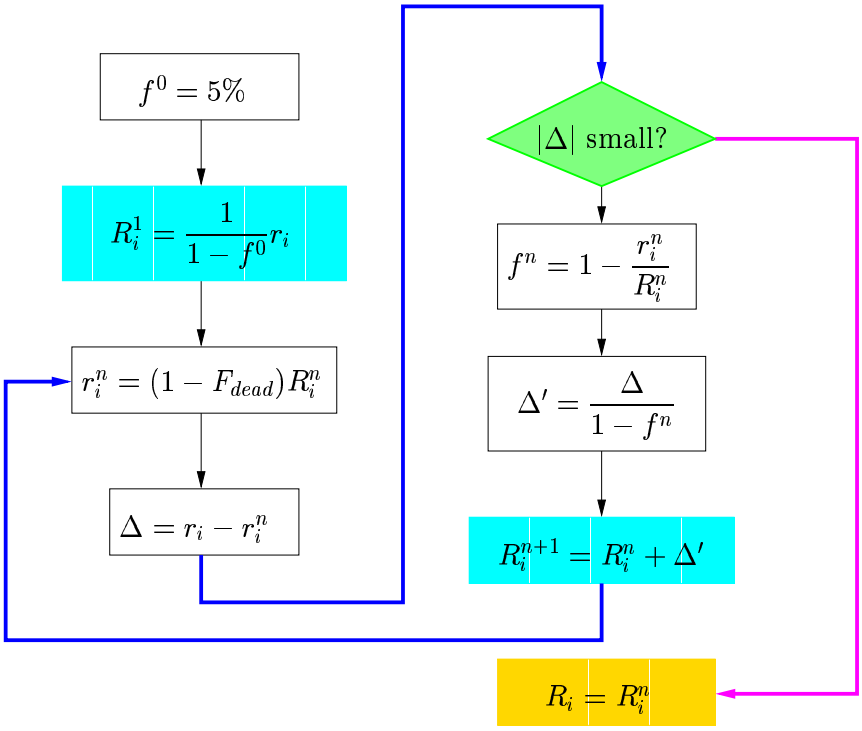

Figure 5.8: *The flow diagram of the iteration used in the NA deadtime correction to calculate the true rate. See text for details.*

loss is then updated in this iteration as $f^1 = 1 - \frac{r_i^1}{R_i^1}$. Then r_i^1 is compared with the measured spectrum r_i, and the difference between them, Δ, divided by the lifetime $1 - f^1$ [†], is then applied to correct the "true" spectrum R_i^1, which goes into the next iteration. This procedure is performed recursively until the nth iteration, in which the difference between r_i^n and the r_i becomes "negligible". R_i^n is then taken as the the corrected true spectrum.

Let us elaborate on the exit condition of the iteration — how small should $|\Delta|$ be? Eqns. 5.14 and 5.17 imply that if a correction is made on the rate to a precision of ϵ [‡], such that

$$R_{corr} = (1 - \epsilon f_{dead}) R \,, \tag{5.32}$$

[†] Δ is the difference between r_i and r_i^n, and the difference between R_i and R_i^n is expected to be larger by a lifetime correction.

[‡] Note that this implies that the correction is made on the two helicity states separately with equal precision.

then the corrected asymmetry would be

$$A_{corr} = (1 - \epsilon f_{dead})A\,. \tag{5.33}$$

In other words, if the rate is corrected to one percent, the corrected asymmetry is good to one percent, which is satisfactory. In reality, however, the corrected asymmetry in a certain time bin is also correlated with the correction of the rate in other bins, due to the complicated entanglement in Eqn. 5.26. The realistic situation is studied with a simulation [Liu02], in which a typical G^0 rate spectrum (with typical asymmetry) was used as the "true" spectrum, which was then corrupted by Eqn. 5.26. Then the corrections were made iteratively and different exit conditions were tested. It was found that the corrected asymmetry of each time bin was good to 1% if

$$\frac{\langle|\Delta|\rangle}{\langle r_i\rangle} < 0.1\%\,, \tag{5.34}$$

in which $\langle\rangle$ denotes a time-average over the entire spectrum. This is therefore adopted as the convergence condition in the analyzer. For a typical G^0 spectrum, this convergence condition is met in three iterations. The corrected rate spectra are then used to compute the asymmetries.

5.3.1.2 French Deadtime Correction

The French deadtime correction uses the same principle as that in the NA electronics. In the French electronics, however, P_{pre} (Eqn. 5.22) depends only on the measured rates [Arv01], therefore

$$P_{pre} = \sum r_i\tau_i\,. \tag{5.35}$$

This simplifies the correction considerably, i.e., R_i can be directly solved as

$$R_i = -ln\left(1 - \frac{r_i}{1 - \sum r_k\tau_k + \sum_{k=1}^{i-1} r_k\tau_k - P^s_{dead,i}}\right)\,. \tag{5.36}$$

Note that in the French case, the deadtime loss due to the singles, $P^s_{dead,i}$ is evaluated bin by bin, which we will elaborate on a bit later. There are two additional technical subtleties associated with the French NPN deadtime. First, the French NPN is not naturally ended at the end of the spectrum (32 ns or the 128th bin); typically it is at the 110th bin and is different for each board. This is the so-called "upstream cutoff". Second, each DMCH board also has a "downstream cutoff" located early in the spectrum, typically the 20th bin. If a hit is made between the upstream and downstream cutoffs, two subsequent pulses will be disabled. The two cutoffs are calibrated for each DMCH board and loaded into the analyzer, which are taken into account when computing the NPN deadtime.

The French electronics has scalers associated with each CFD and MT, therefore the CFD singles and MT singles can be approximately determined by

$$\begin{aligned} R_{\mathrm{s,CFD}} &= \sum R_{\mathrm{CFD}} - 2 \times \sum R_{\mathrm{MT}} \,, \\ R_{\mathrm{s,MT}} &= \sum R_{\mathrm{MT}} - 2 \times R_{\mathrm{DMCH}} \,, \end{aligned} \tag{5.37}$$

in which R_{CFD}, R_{MT} and R_{DMCH} are the total rates measured in CFDs, MTs and time-encoding electronics, respectively. However as discussed in the previous section, this naive evaluation leads to double counting. Therefore a more sophisticated Fastbus analysis is made. This analysis takes into account the shape of the ToF spectrum of the singles, as well as possible double counting. The analysis culminated into two effective deadtimes as a function of bin number i [†], $\tau_{\mathrm{CFD,i}}$ and $\tau_{\mathrm{MT,i}}$, which contain the effect of the time of flight shape of the singles, as well as a scaling to remove the double counting. $\tau_{\mathrm{CFD,i}}$ and $\tau_{\mathrm{MT,i}}$ are loaded at the beginning of the

[†]In fact this analysis computes another tiny loss corresponding to the MT single hits during the NPN period [Bat04]. Its discussion will be omitted here.

replay. Then at each bin i, $P^s_{dead,i}$ is computed as [Bat04]

$$P^s_{dead,i} = P_{\mathrm{CFD,i}} + P_{\mathrm{MT,i}}\,, \tag{5.38}$$

$$P_{\mathrm{CFD,i}} = \tau_{\mathrm{CFD,i}} \times R_{\mathrm{s,CFD}}\,, \tag{5.39}$$

$$P_{\mathrm{MT,i}} = \tau_{\mathrm{MT,i}} \times R_{\mathrm{s,MT}}\,, \tag{5.40}$$

MPS by MPS. The French correction is then performed using Eqn. 5.36.

5.3.1.3 Results of the Deadtime Correction

Simplified relations between the raw and the true rates/asymmetries are given at the beginning of Sec. 5.3.1 in Eqns. 5.14 and 5.17. Since $R \propto \dfrac{d\sigma}{d\Omega} I_b$, where I_b is the beam current, the measured asymmetry A_R is a sum of the physics asymmetry A_{phys} and the charge asymmetry A_Q. It is always desirable to take out the effect of the fluctuation of the beam current to first order. Normalizing both the measured and true rates in Eqn. 5.14 by the beam current, we have

$$Y_m = (1 - f_{dead})Y_t\,, \quad f_{dead} = R\tau\,, \tag{5.41}$$

where $Y_m = \dfrac{r}{I_b}$ and $Y_t = \dfrac{R}{I_b}$ are the normalized raw and true detector yields, respectively.

Since the true scattering rate R scales with the beam current, the measured normalized yield falls off linearly with beam current. This is perhaps the most obvious effect of the deadtime, and f_{dead} can be "measured" as a (dimensionless) slope:

$$f_{dead} = -\frac{dY}{dI_b} \times \frac{40\ \mu\mathrm{A}}{Y(I_b = 0)}\,. \tag{5.42}$$

The average four-fold coincidence and the single rates (summed over the single rates in the 4×4 table (Table 5.1) that contribute to f_{dead} are listed in Table 5.2. If one takes $\tau \sim 50$ ns for the coincidences and $\tau \sim 30$ ns for the singles, f_{dead} is estimated to be $\sim$10%, and the coincidences and singles contributed roughly 40% and 60% of it.

	NA		French	
Detector	4-fold (MHz)	singles (MHz)	4-fold (MHz)	singles (MHz)
1	0.69	1.1	0.65	1.6
2	0.90	1.3	0.86	1.8
3	0.93	1.2	0.91	1.9
4	0.84	1.2	0.76	1.2
5	0.90	1.1	0.83	1.7
6	0.97	1.4	0.90	1.8
7	1.0	1.2	0.99	1.6
8	0.90	1.6	0.87	1.5
9	1.0	1.5	0.98	1.7
10	1.0	2.0	1.0	2.0
11	1.1	1.7	1.0	2.1
12	0.90	2.5	0.84	2.3
13	0.76	1.7	0.70	2.8
14	0.80	2.6	0.73	2.9
15	0.85	2.2	0.77	3.7
hybrid 14			0.86	5.8
hybrid 15			0.92	7.4

Table 5.2: *The average rates of the four-fold coincidences and singles per detector. The four NA and French octants are averaged separately.*

As an example, the normalized proton yields of North American detector 8 measured at a few different beam currents are plotted against the beam current in Fig. 5.9(a). The black open circles represent the raw measured yield. The pink solid squares and the blue open squares represent the yield corrected with the coincidences only, and that corrected by both the coincidences and the singles, respectively. One sees that coincidences and singles contribute comparably to the deadtime loss, and after the full correction, the dependence of the normalized yield on the beam current is largely removed. We will elaborate on the systematic uncertainty due to the residual slope in Sec. 5.3.1.4.

Although the correction has reduced the yield slope, one should not stop at this point. As illustrated by Eqn. 5.17, the real issue of the deadtime is that it introduces a helicity correlated loss, which is not reflected in the average yield.

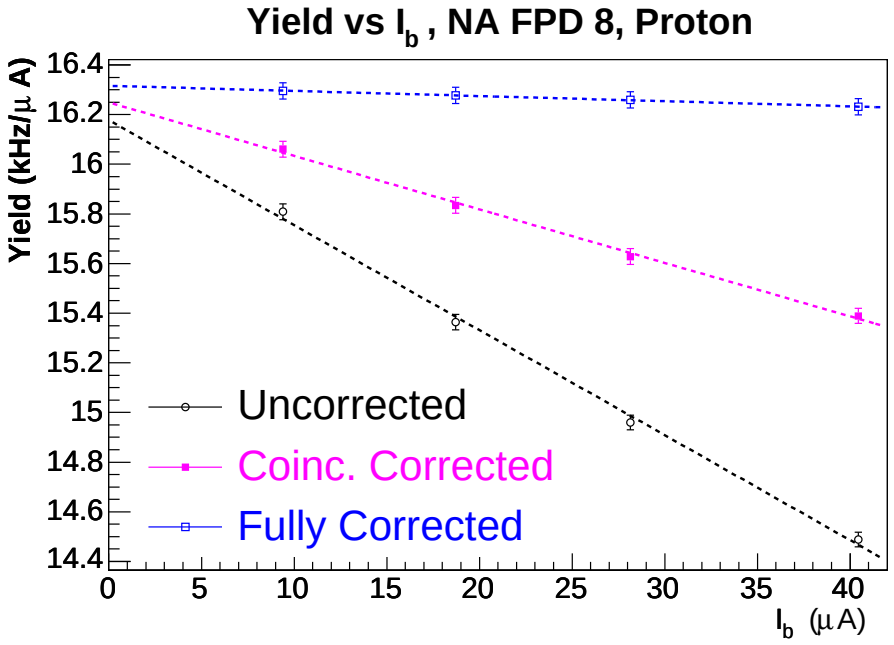

(a) *Yield vs. beam current.*

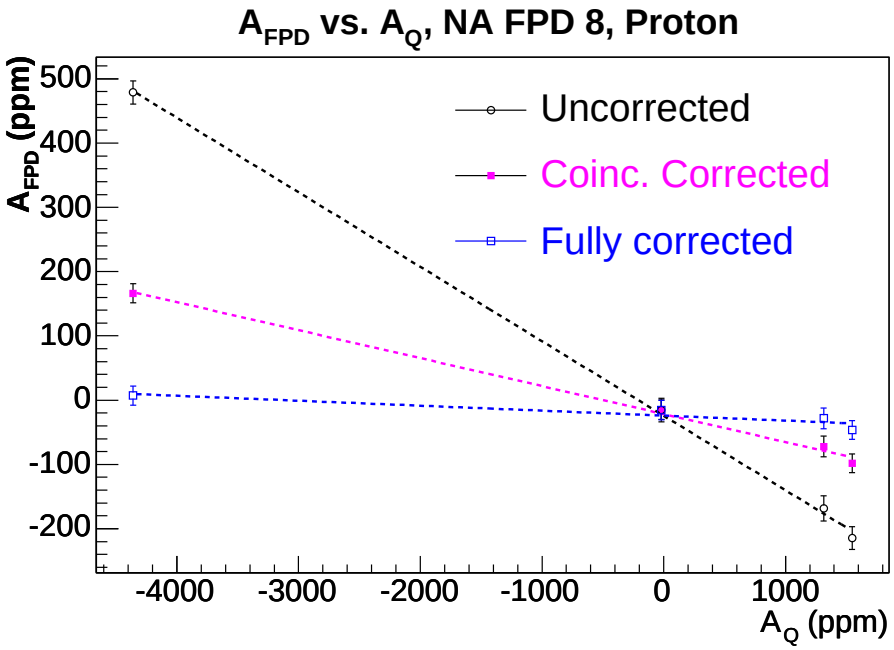

(b) *Asymmetry vs. charge asymmetry.*

Figure 5.9: *The proton yield vs. beam current (a) and asymmetry vs. charge asymmetry (b) for NA detector 8. The black open circles, pink solid squares, and the blue open squares are the raw yields, yields corrected for the deadtime due to the coincidences, and the yields corrected for both the coincidences and singles deadtime, respectively.*

Similar to Eqn. 5.17, Eqn. 5.41 can be cast into asymmetries as

$$A_m = A_{phys} - \frac{f_{dead}}{1 - f_{dead}}(A_{phys} + A_Q)\,, \tag{5.43}$$

of which A_m and A_{phys} are the asymmetries carried by Y_m and Y_t. One should note, first of all, that both the charge asymmetry and the physics asymmetry contribute to the false asymmetry through the deadtime. Secondly, this equation suggests that we can measure f_{dead} by measuring the correlation between A_m and A_Q, i.e.,

$$\frac{\partial A_m}{\partial A_Q} = -\frac{f_{dead}}{1 - f_{dead}}\,. \tag{5.44}$$

In Fig. 5.9(b), a correlation plot of A_m and A_Q for North American detector 8 is shown, with the same color code as that of Fig. 5.9(a). In these measurements, the charge asymmetry of the beam was adjusted by the rotatable halfwave plate (see Sec. 4.2.1.2) to introduce large enough variation of the charge asymmetry. One clearly sees that the large correlation between A_m and A_Q disappears after one applies the full deadtime correction.

f_{dead} measured through the yield slope and the asymmetry slope are in good agreement. Table 5.3 shows the raw and deadtime-corrected asymmetry slopes for the proton cuts for the NA, French and hybrid (see Sec. 4.2.4.2) detectors. After the correction, the asymmetry slope of the NA detectors is negligible, and the French detectors have a $\sim -2.5\%$ residual slope remaining.

5.3.1.4 Residual Deadtime and the Systematic Uncertainty of the Correction

To examine the residual false asymmetry for the proton peak due to the residual asymmetry slope, let us consider the following simplified version of the NA/French deadtime model (NPN + singles).

To measure an elastic hit at time t in the proton peak, it is required that there are

	NA		French	
Detector	raw (%)	corrected (%)	raw (%)	corrected (%)
1	−8.4(0.4)	−0.5(0.3)	−10.1(0.4)	−2.2(0.3)
2	−9.3(0.3)	0.3(0.3)	−11.6(0.3)	−2.2(0.3)
3	−9.9(0.3)	0.2(0.3)	−12.8(0.3)	−2.5(0.3)
4	−9.3(0.4)	0.1(0.3)	−10.2(0.4)	−2.3(0.3)
5	−9.8(0.3)	−0.3(0.3)	−11.1(0.4)	−2.4(0.3)
6	−9.9(0.3)	0.6(0.3)	−12.0(0.4)	−2.4(0.3)
7	−10.9(0.3)	−0.1(0.3)	−13.0(0.3)	−2.5(0.3)
8	−11.5(0.4)	−0.8(0.3)	−11.6(0.4)	−1.9(0.3)
9	−11.0(0.4)	−0.1(0.3)	−13.3(0.4)	−2.5(0.3)
10	−11.6(0.4)	0.1(0.3)	−14.1(0.4)	−2.6(0.3)
11	−12.1(0.4)	−0.2(0.4)	−15.0(0.4)	−3.0(0.3)
12	−10.5(0.4)	1.6(0.4)	−13.4(0.4)	−2.5(0.4)
13	−10.2(0.5)	0.4(0.4)	−13.9(0.5)	−3.2(0.4)
14	−13.1(0.5)	0.4(0.4)	−16.8(0.5)	−3.8(0.4)
15	−12.8(0.4)	1.9(0.3)	−19.6(0.4)	−4.2(0.4)
hybrid 14			−34.7(0.5)	−5.3(0.5)
hybrid 15			−37.7(0.5)	6.3(0.4)

Table 5.3: *The raw and deadtime-corrected asymmetry slopes, $\frac{dA_{FPD}}{dA_Q}$, for the proton cuts of different detectors. All slopes are in %, and the values in parentheses are their statistical uncertainties.*

- no coincidence pion hits in this and previous beam pulses ($\tau_\pi = 64$ ns);
- no coincidence inelastic proton hits in this and previous beam pulses ($\tau_{in} = 64$ ns);
- no coincidence elastic proton hits in the previous beam pulse ($\tau_p = 32$ ns);
- no single hits occur in a 32 ns window preceding t ($\tau_s = 32$ ns) .

The regions before the pion peak and after the elastic peak have small rates, and are therefore neglected. To first order, this leads to

$$Y_{m,p} = (1 - f_{dead})Y_p = (1 - f_\pi - f_{in} - f_p - f_s)Y_p \,, \tag{5.45}$$

$$f_\pi = R_\pi \tau_\pi \,, \quad f_{in} = R_{in}\tau_{in} \,, \quad f_p = R_p \tau_p \,, \quad f_s = R_s \tau_s \,, \tag{5.46}$$

in which $Y_{m,p}$ and Y_p are the raw and the deadtime-free yields in the elastic peak, and R_π, R_{in}, R_p and R_s (f_π, f_{in}, f_p and f_s) are the rates (fractional yield losses) due to the pion, inelastic, elastic and single hits, respectively.

Similar to Eqn. 5.43, Eqn. 5.45 easily leads to a relation in terms of the asymmetries:

$$A_{m,p} = A_p - \frac{f_\pi(A_\pi + A_Q) + f_{in}(A_{in} + A_Q) + f_p(A_p + A_Q) + f_s(A_s + A_Q)}{1 - f_\pi - f_{in} - f_p - f_s} . \quad (5.47)$$

One realizes that the deadtime correlates the measured asymmetry in the proton peak with the physics asymmetries along the entire time of flight spectrum. Without the correction, the slope for the measured asymmetry is

$$\frac{\partial A_{m,p}}{\partial A_Q} = -\frac{f_\pi + f_{in} + f_p + f_s}{1 - (f_\pi + f_{in} + f_p + f_s)} . \quad (5.48)$$

For the corrected asymmetry, we define a multiplicative "precision" coefficient ϵ, such that ϵ =0 and 1 corresponds to a perfect correction and no correction, respectively. Then the corrected asymmetry can be expressed as

$$A_{c,p} = A_p - \epsilon\frac{f_\pi(A_\pi + A_Q) + f_{in}(A_{in} + A_Q) + f_p(A_p + A_Q) + f_s(A_s + A_Q)}{1 - \epsilon(f_\pi - f_{in} - f_p - f_s)} , \quad (5.49)$$

Note that here we choose a global ϵ for simplicity, although it could be different for different types of hits. Under this assumption, the corrected slope can be expressed as

$$\frac{\partial A_{c,p}}{\partial A_Q} = -\frac{\epsilon(f_\pi + f_{in} + f_p + f_s)}{1 - \epsilon(f_\pi + f_{in} + f_p + f_s)} \sim -\epsilon(f_\pi + f_{in} + f_p + f_s) . \quad (5.50)$$

Therefore, based on the corrected slope in Table 5.3, ϵ can be computed for each detector.

Eqn. 5.49 shows explicitly the consequence of an imperfect deadtime correction: the corrected asymmetry has a residual false asymmetry due to the charge asymmetry, as well as the physics asymmetry along the time of flight spectrum. The linear regression correction (which will be discussed in Sec. 5.3.3) on the he-

licity correlated beam properties will further remove the piece due to the charge asymmetry, so we will ignore A_Q in the remainder of this discussion. What remains is a false asymmetry due to the physics asymmetries

$$A_{false} = A_{c,p} - A_p = -\epsilon \frac{f_\pi A_\pi + f_{in} A_{in} + f_p A_p + f_s A_s}{1 - \epsilon(f_\pi - f_{in} - f_p - f_s)}$$
$$\sim -\epsilon(f_\pi A_\pi + f_{in} A_{in} + f_p A_p + f_s A_s)\,. \tag{5.51}$$

In Table 5.4, the residual false asymmetries of the French detectors are summarized. For the coincidence hits, the values of A listed in the table are the deadtime corrected asymmetries, and those of f's are computed based on the corrected rates in individual PID cuts. The total singles rates are evaluated by the summed single rates from the 4×4 table (Table 5.1), from which we calculate f_s. The asymmetries of the singles are evaluated with the SDMCH scaler data — the rates of the CFD and MT singles are computed for each helicity state using Eqn. 5.37 (despite the ambiguity of the double-counting), after which the asymmetries are computed. In Fig. 5.10 the asymmetries of CFD and MT singles are shown. The MT singles asymmetry vs. the detector number shows a similar trend as the coincidence pion asymmetry. On the other hand, the CFD singles exhibit $\sim$+5 ppm asymmetry for detectors below 6, which might be threshold related. The weighted average of the asymmetries of the CFD and MT singles is taken as A_s in Table 5.4.

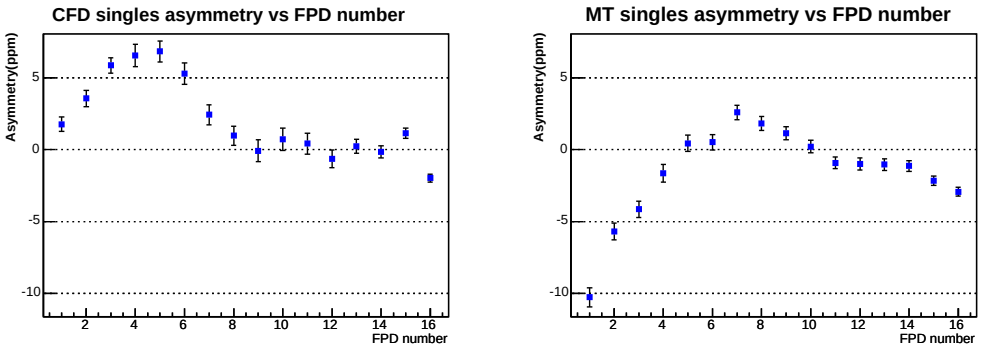

Figure 5.10: *The asymmetries of the CFD and MT singles calculated from the SDMCH scaler data vs. the detector number. The asymmetries are corrected for the beam polarization, but blinded by a factor of* $f_{blind} \equiv 0.8056$.

Detector	f_π	f_{in}	f_p	f_s	A_π	A_{in}	A_p	A_s	ϵ	A_{false}
1	0.00	0.01	0.02	0.05	−53.1	−12.5	−1.8	−2.9	0.26	0.13(0.08)
2	0.01	0.02	0.03	0.06	−28.1	−10.6	−1.5	−1.0	0.20	0.09(0.08)
3	0.01	0.02	0.02	0.06	−25.1	−10.0	−2.7	0.9	0.22	0.09(0.12)
4	0.00	0.02	0.02	0.04	−21.7	−11.5	−2.3	0.9	0.28	0.08(0.10)
5	0.01	0.02	0.02	0.06	−12.1	−8.8	−2.7	2.9	0.24	0.03(0.11)
6	0.01	0.02	0.02	0.06	−8.1	−6.1	−3.3	2.0	0.21	0.04(0.09)
7	0.02	0.02	0.03	0.05	−4.9	−3.9	−3.4	2.5	0.22	0.02(0.08)
8	0.02	0.02	0.02	0.05	−3.3	−0.1	−4.7	1.5	0.18	0.02(0.04)
9	0.03	0.02	0.02	0.06	−3.8	6.2	−5.0	0.9	0.20	0.01(0.03)
10	0.03	0.02	0.02	0.06	−3.9	12.2	−6.4	0.4	0.20	0.00(0.01)
11	0.03	0.02	0.02	0.07	−4.1	16.3	−5.2	−0.6	0.23	−0.00(0.02)
12	0.03	0.01	0.02	0.07	−4.9	17.9	−4.9	−0.9	0.20	0.01(0.02)
13	0.02	0.01	0.01	0.09	−7.6	19.0	−4.2	−0.6	0.24	0.03(0.01)
14	0.02	0.01	0.01	0.09	−9.6	7.5	−3.4	−0.6	0.28	0.07(0.07)
15	0.02	0.01	0.02	0.12	−12.5	−4.7	−8.0	−1.2	0.25	0.13(0.17)
hybrid 14	0.03	0.01	0.01	0.18	−9.9	14.9	−1.1	−0.6	0.22	0.06(0.06)
hybrid 15	0.02	0.01	0.02	0.24	−13.3	−1.8	−5.7	−1.2	−0.22	−0.16(0.25)

Table 5.4: *The French deadtime losses and the asymmetries of various types of hits, the residual slope factors ϵ, and the resulting false asymmetries A_{false} calculated using Eqn. 5.51. Columns f_π, f_{in}, f_p and f_s (A_π, A_{in}, A_p and A_s) represent the measured deadtime losses (asymmetries) of the pions, inelastic and elastic protons, and the singles. The uncertainties of A_{false} are in parentheses in the last column. All asymmetries are in ppm, corrected for the beam polarization, but blinded by a factor of $f_{blind} \equiv 0.8056$.*

The statistical uncertainty of A_{false} contains 3 components:

- the uncertainty of the measured asymmetries of individual types of hits;
- the uncertainty of the deadtime fraction (f). We estimated this as the difference between Eqn. 5.48 and the measured asymmetry slope without the correction. The difference is found to be less than 10% of f for most of the detectors;
- the uncertainty of ϵ based on the the statistical uncertainty of the corrected asymmetry slope, as shown in Table 5.3.

The combined uncertainty is $\sim$0.01 ppm, and is dominated by the statistical uncertainty of the measured asymmetries of individual types of hits. However, as hinted earlier, there is a caveat in the above evaluation: we have made the assumption that the deadtime losses due to individual types of hits are equally under- or over-corrected (by a global ϵ). This could be untrue in reality, and the impact can be estimated by assuming that either the singles or the coincidences are 100% responsible for the residual slope. The resulting half differences of the two evaluations is of the order of $\sim$100% of A_{false}, and are listed in parentheses of the last column in Table 5.4. Clearly they dominate the systematic uncertainty of the residual correction.

The last two rows in Table 5.4 deal with the hybrid data (NA detectors 14 and 15 plugging into the French electronics, see the end of Sec. 4.2.4.2). There is no Fastbus information available for these channels. But based on the raw asymmetry slope in Table 5.3 and the measured coincidence rates, we estimate according to Eqn. 5.48 that their values of the singles loss fraction f_s are roughly twice as high as their French counterparts (due to the difference in thresholds). We further assume that their singles asymmetries are the same as measured by the SDMCH scalers. Then the evaluation of A_{false} and δA_{false} follows the exact same procedure as above.

The residual NA asymmetry slopes are very close to zero; naively one would expect the residual A_{false} to be also very small. The reality is more subtle. As mentioned earlier, the singles rates in a given MPS are calculated according to the beam current based on an empirical parameterization, and the correction is applied to each helicity state. This implementation ensures that A_{false} due to A_Q will be corrected, but the contamination due to the physics asymmetry of the singles remains [†].

Therefore, the residual uncorrected false asymmetry of the NA detectors should be calculated as

$$A_{false} \sim -\epsilon(f_\pi A_\pi + f_{in} A_{in} + f_p A_p) - f_s \times A_s \sim -f_s \times A_s \,. \qquad (5.52)$$

[†]This is unlike the French case, in which we have shown that $(1-\epsilon)$ of this effect has been corrected by using the singles rates measured simultaneously with the coincidence data.

In Table 5.5 the false asymmetries of the NA detectors are summarized. The asymmetries of the singles measured by the French SDMCH are taken as the singles asymmetries for the NA detectors (A_s). The uncertainty of this assignment is estimated by using the relative difference of the pion asymmetries between the NA and French detectors, since the pions and the singles both are low pulse-height events. The singles loss fraction, f_s, is again computed using the summed single rates from the 4×4 table (Table 5.1). For completeness, we computed A_{false} using the full expression of Eqn. 5.52, although the terms due to the coincidences are small. Finally, the uncertainty of A_{false} are computed by propagating the uncertainties of the measured asymmetries, and those of f's and ϵ. Attributing the residual slopes solely to either the coincidences or the singles does not make too much variations to A_{false}, since the residual slopes are small for the NA; the systematic uncertainty due to this variation is therefore neglected. The uncertainties of A_{false} are listed in parenthesis in the last column in Table 5.5; they are dominated by the uncertainty due to the assignment of the NA singles asymmetry mentioned above. One realizes that the uncertainty of A_{false} is again of the order of $\sim$100% of A_{false}.

As a note of caution, the above estimate of the false asymmetry is made on the measured asymmetry in the proton cut, but not on the background corrected elastic asymmetry. On the other hand, the elastic events should have exactly the same deadtime loss as the background events inside the proton cut, since the electronics can not tell whether a hit is elastic inside the same cut. Therefore it follows that the residual false asymmetries of the elastic asymmetries are exactly the same as those in Tables 5.4 and 5.5. The correction to residual A_{false} is therefore made after the background correction (Sec. 5.3.6), and for simplicity we assigned 100% of the correction as the systematic uncertainty of this residual correction. It shall be treated as a point-point (uncorrelated from Q^2 bin to Q^2 bin) systematic uncertainty in the final uncertainty budget.

Detector	f_π	f_{in}	f_p	f_s	A_π	A_{in}	A_p	A_s	ϵ	A_{false}
1	0.00	0.01	0.02	0.03	−32.3	−7.9	−1.1	−2.9	0.14	0.12(0.04)
2	0.01	0.02	0.03	0.04	−24.4	−6.4	−0.4	−1.0	−0.06	0.03(0.02)
3	0.01	0.02	0.02	0.04	−21.7	−6.6	−0.1	0.9	−0.04	−0.04(0.02)
4	0.01	0.02	0.02	0.04	−16.4	−8.0	−2.4	0.9	−0.00	−0.04(0.02)
5	0.01	0.02	0.02	0.04	0.8	−6.0	−1.8	2.9	0.06	−0.10(0.11)
6	0.01	0.02	0.02	0.04	0.1	−1.4	−2.7	2.0	−0.11	−0.10(0.10)
7	0.01	0.02	0.03	0.04	−2.0	4.6	−4.2	2.5	0.02	−0.10(0.06)
8	0.01	0.02	0.02	0.05	−6.0	10.6	−3.9	1.5	0.16	−0.08(0.07)
9	0.02	0.02	0.02	0.05	−2.6	14.2	−4.3	0.9	0.02	−0.04(0.02)
10	0.02	0.02	0.02	0.06	−5.6	22.3	−3.5	0.4	−0.02	−0.02(0.03)
11	0.02	0.02	0.02	0.05	−6.0	25.0	−3.4	−0.6	0.03	0.03(0.03)
12	0.03	0.01	0.02	0.08	−5.7	27.8	−3.4	−0.9	−0.28	0.08(0.05)
13	0.02	0.01	0.01	0.05	−8.1	29.3	−1.2	−0.6	−0.09	0.04(0.02)
14	0.02	0.01	0.01	0.08	−11.3	18.9	−0.1	−0.6	−0.09	0.05(0.03)
15	0.02	0.00	0.02	0.09	−14.2	1.4	−5.8	−1.2	−0.41	0.04(0.03)

Table 5.5: *NA deadtime losses and the asymmetries of various types of hits, the residual slope factor ϵ, and the resulting false asymmetries A_{false} calculated using Eqn. 5.52. The arrangement of the columns is the same as that of Table 5.4. All asymmetries are in ppm, corrected for the beam polarization, but blinded by a factor of $f_{blind} \equiv 0.8056$.*

5.3.2 Leakage Correction

The G^0 beam bunches are separated by 32 ns to facilitate the time-of-flight measurements. On the other hand, the electron beams to Halls A and B are pulsed with 2 ns separation between bunches. In Fig. 5.11, the time structures of the beams to the three halls are illustrated. During the experiment, it was realized that there was ∼50 nA of the 499 MHz beam leaking into Hall C. Although small in current, the charge asymmetry of the leakage beam turned out to be quite significant (∼600 ppm), and it was not stable over time. The beam charge monitors in the hall measured the integrated beam charge every 1/30 s, so they were only sensitive to the combined average current of the G^0 and leakage beams. This resulted in a significant time-of-flight dependent false asymmetry, which needed to be corrected.

The correction of the leakage effect was carried out using the rate and the

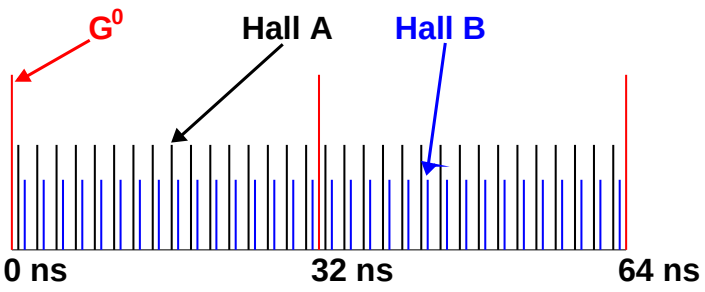

Figure 5.11: *An illustration of the JLab beam structure delivered to Halls A, B and C during the G^0 running period. The beams of Halls A and B are pulsed with a repetition rate of 499 MHz, whereas the G^0 beam is pulsed at 31.25 MHz.*

asymmetry measured in the "forbidden" regions (the so-called "cut0"): very early and late regions on the time-of-flight spectrum. A detailed description of the leakage problem as well as the correction procedure is given in Appendix A. Here, only the final results will be presented. The correction to the elastic A_e of all Q^2 bins is

$$\Delta_{leak} = A_{e,corr} - A_{e,raw} = 0.57 \pm 0.11 \text{ ppm}\,, \tag{5.53}$$

with 0.11 ppm being the global systematic uncertainty. Note these values have been corrected for the beam polarization, but they are still blinded by the blinding factor (0.8056).

5.3.3 Correction to Helicity Correlated Beam Properties

The detector yield is proportional to the scattering cross section and the acceptance; both have dependence on the beam properties, e.g. the incident beam positions, angles, and the energy. Generally, we can write the change of the yield δY, as the product of the detector sensitivities and the change of n different beam parameters, i.e.

$$\delta Y = \sum_{m=1}^{m=n} \frac{\partial Y}{\partial P_m} \delta P_m\,, \tag{5.54}$$

with $\delta Y \equiv Y - \langle Y \rangle$ and $\delta P_m \equiv P_m - \langle P_m \rangle$ being the change of the yield and the beam parameter P_m away from their means. Therefore, if the beam parameter is

helicity correlated with a difference

$$\Delta P_m \equiv P_m^+ - P_m^- \,, \tag{5.55}$$

it leads to a false asymmetry

$$A_{false} = \sum_{m=1}^{m=n} \frac{1}{2Y} \frac{\partial Y}{\partial P_m} \Delta P_m \,. \tag{5.56}$$

In the experiment, ΔP_m were monitored continuously with the beam monitors. Therefore, the key to remove the false asymmetry is to determine the correlation slopes, $\dfrac{\partial Y}{\partial P_m}$. One should note that a given parameter might be correlated with the others. A standard multi-dimensional linear regression technique was thus used to evaluate the slopes by taking into account the correlations.

Let us consider that we make large number of measurements N, and in each measurement the detector yield and the beam parameters are denoted as Y^i and P_m^i, where the superscript i is the index of the measurements. To simplify the notation, we rewrite the correlation slope as $\dfrac{\partial Y}{\partial P_m} \equiv C_m$. The goal of this analysis is to determine C_m based on these N measurements, with the assumption that the parent distribution is

$$\delta Y = \sum_m C_m \delta P_m \,. \tag{5.57}$$

C_m can be determined via the least-squares method, with χ^2 defined as

$$\chi^2 = \sum_i \frac{\left(\delta Y^i - \sum_m C_m \delta P_m^i \right)^2}{(\sigma^i)^2} \,, \tag{5.58}$$

in which σ^i is the uncertainty of $\delta Y - \sum_m C_m \delta P_m$ in measurement i. The best values of C_m are those that minimize χ^2. Therefore, C_m is determined with the constraint that

$$\frac{\partial \chi^2}{\partial C_m} = 0 \,, \tag{5.59}$$

which leads to a set of n equations:

$$\sum_i \frac{\delta P_k^i}{(\sigma^i)^2} \left(\delta Y^i - \sum_m C_m \delta P_m^i \right) = 0 \,. \tag{5.60}$$

If one further assumes that all N measurements share the same statistical weight, i.e., $\sigma^i = \sigma$, then Eqn. 5.60 can be simplified to

$$\langle \delta P_k \delta Y \rangle = \sum_m C_m \langle \delta P_k \delta P_m \rangle \,, \tag{5.61}$$

in which we have replaced $\sum_i$ with $\langle\rangle$, the straight average of N measurements. Let us define

$$\overrightarrow{\xi} \equiv \begin{pmatrix} \langle \delta P_1 \delta Y \rangle \\ \langle \delta P_2 \delta Y \rangle \\ \cdot \\ \cdot \\ \cdot \\ \langle \delta P_n \delta Y \rangle \end{pmatrix}, \overleftrightarrow{\mathcal{M}} \equiv \begin{bmatrix} \langle \delta P_1 \delta P_1 \rangle & \langle \delta P_1 \delta P_2 \rangle & \cdot & \cdot & \cdot \\ \langle \delta P_2 \delta P_1 \rangle & \langle \delta P_2 \delta P_2 \rangle & \cdot & \cdot & \cdot \\ \cdot & \cdot & \cdot & & \\ \cdot & \cdot & \cdot & & \\ \cdot & \cdot & \cdot & & \\ \langle \delta P_n \delta P_1 \rangle & \langle \delta P_n \delta P_2 \rangle & \cdot & \cdot & \cdot \end{bmatrix}, \overrightarrow{\mathcal{C}} \equiv \begin{pmatrix} C_1 \\ C_2 \\ \cdot \\ \cdot \\ \cdot \\ C_n \end{pmatrix} . \tag{5.62}$$

Then Eqn. 5.61 can be cast into a compact matrix form

$$\overrightarrow{\xi} = \overleftrightarrow{\mathcal{M}} \, \overrightarrow{\mathcal{C}} \,. \tag{5.63}$$

Clearly it is a set of n linear equations with n unknowns (C_m), therefore C_m can simply be solved by inverting $\overleftrightarrow{\mathcal{M}}$:

$$\overrightarrow{\mathcal{C}} = \overleftrightarrow{\mathcal{M}}^{-1} \, \overrightarrow{\xi} \,. \tag{5.64}$$

The slopes thus obtained are independent in the sense that they characterize how fast the yield changes with a given parameter, if we keep all the other parameters fixed at their means.

As a side note, a common trick used to compute the average product of the deviations of any two independent quantities x and y is the following:

$$\begin{aligned}\langle \delta x \delta y \rangle &\equiv \langle (x - \overline{x})(y - \overline{y}) \rangle \\ &= \langle xy - x\overline{y} - \overline{x}y + \overline{x}\ \overline{y} \rangle = \langle xy \rangle - \langle x \rangle \langle y \rangle \,. \end{aligned} \tag{5.65}$$

During the event by event processing, the running averages of x, y and xy are kept track of, and $\langle \delta x \delta y \rangle$ is computed at the end of the replay. The elements in $\overrightarrow{\xi}$ and $\overleftrightarrow{\mathcal{M}}$ are both obtained this way.

For completeness, let us discuss the statistical precision of the slopes. The statistical uncertainty of C_m is calculated based on the curvature matrix of χ^2 [Bev92]. The curvature matrix, $\overleftrightarrow{\alpha}$, is computed in this context as

$$\alpha_{lk} \equiv \frac{1}{2}\frac{\partial^2 \chi^2}{\partial C_l \partial C_k} = \sum_m \sum_i \frac{\delta P_l^i \delta P_k^i}{(\sigma^i)^2} = \frac{1}{\sigma^2/N}\langle \delta P_l \delta P_k \rangle = \frac{1}{\sigma^2/N}\mathcal{M}_{lk} \,, \tag{5.66}$$

in which we have again used the assumption that $\sigma^i = \sigma$. The error matrix, $\overleftrightarrow{\epsilon}$, is the inverse of the curvature matrix,

$$\overleftrightarrow{\epsilon} \equiv \overleftrightarrow{\alpha}^{-1} = \frac{\sigma^2}{N}\ \overleftrightarrow{\mathcal{M}}^{-1} \,, \tag{5.67}$$

and the diagonal elements of the error matrix are the squares of the uncertainties of the individual free parameters C_m, including the correlations among C_m [Bev92, Jam94], and the off-diagonal elements are the covariance among the parameters. Since $\overleftrightarrow{\mathcal{M}}$ is known, an evaluation of σ would yield $\overleftrightarrow{\epsilon}$. σ is the average uncertainty of $\delta Y - \sum_m C_m \delta P_m$ in each measurement, therefore it is natural to take it as the standard deviation of $\delta Y - \sum_m C_m \delta P_m$. Therefore we have

$$\sigma^2 = \frac{1}{N-n}\sum_i \left(\delta Y^i - \sum_m C_m \delta P_m^i \right)^2 \sim \frac{1}{N}\sum_i \left(\delta Y^i - \sum_m C_m \delta P_m^i \right)^2 \,. \tag{5.68}$$

After a bit algebra, this leads to

$$\begin{aligned}\sigma^2 &= \langle \delta Y^2 \rangle - 2 \sum_m C_m \langle \delta P_m \delta Y \rangle + \sum_l \sum_k C_l C_k \langle \delta P_l \delta P_k \rangle \\ &= \langle \delta Y^2 \rangle - 2 \sum_m C_m \xi_m + \sum_l \sum_k C_l C_k \mathcal{M}_{lk} \,, \end{aligned} \tag{5.69}$$

which, combined with Eqn. 5.67, will give the error matrix.

The calculation of the slopes and their uncertainties discussed above are implemented in the replay engine. The set of the beam parameters are chosen to be $(x, y, \theta_x, \theta_y, E_b, Q)$, the horizontal and vertical beam positions and angles, and the beam energy and charge. The beam charge is included here, since an imperfect deadtime correction or an offset of the pedestal of the charge monitor would lead to a residual dependence of the yield on the beam current. The beam position and angle on the target are projected based on the two strip-line beam position monitors ("G0B" and "G0"), roughly 5 meters upstream of the target, separated by ~2.5 meters. The change of the beam energy is estimated using the x position of the beam measured by a beam position monitor ("3C12") at the dispersion point in the Hall C arc, with a calibration of 1%/4 mm [Yan03]. The linear regression is made with each set of PID cuts (protons, pions, cut1/2/3, etc) for each individual detector. At the end of the replay of each run, the slopes and their uncertainties are computed, which then are written into the database. In principle, one could make a second pass replay, by taking the slopes computed in the previous pass, and correcting the yield (MPS by MPS) as

$$Y_c^i = Y_m^i - \sum_m \frac{\partial Y}{\partial P_m} (P_m^i - \langle P_m \rangle) \,, \tag{5.70}$$

with the superscript i being the index of the MPS, after which the false asymmetry should be removed. In practice, the actual correction to the beam parameters is made after the background corrections (see Sec. 5.3.6) — the average slopes of the proton cuts and ΔP_m are taken to compute A_{false} using Eqn. 5.56, which then gets applied to the background-corrected elastic asymmetry.

One should note that in the extreme case where two of the beam parameters are 100% correlated, $\overleftrightarrow{\mathcal{M}}$ would become a singular matrix, which could not be inverted. In reality, due to the noise of the device this is never the case. However, if the two parameters are too strongly correlated one should consider eliminating one. A correlation matrix among the six beam parameters measured in a typical run is shown in Table 5.6. We note that the correlations between these parameters change with time, since they are very sensitive to how the beam is tuned. In this particular run, one observes a strong correlation between x and θ_x (they are both computed using the beam x positions on "G0B" and "G0"), which is no surprise. Similarly since the beam energy change is estimated based on the beam x positions in the arc, one also expects that it is correlated with the x position on the target. However, the y and θ_y measured by the same two monitors are not strongly coupled, implying that they are controlled independently. Despite the correlations, this matrix is non-singular enough to be inverted, and we are able to get six independent correlation slopes.

	x	y	θ_x	θ_y	E_b	Q
x	1	0.12	0.90	−0.38	0.51	0.01
y	0.12	1	0.25	0.26	−0.07	0.02
θ_x	0.90	0.25	1	−0.23	0.61	0.01
θ_y	−0.38	0.26	−0.23	1	−0.22	−0.07
E_b	0.51	−0.07	0.61	−0.22	1	−0.20
Q	0.01	0.02	0.01	−0.07	−0.20	1

Table 5.6: *The correlation matrix of the six beam parameters in a typical run.*

In Fig. 5.12, the raw and corrected (Eqn. 5.70) proton yield of octant 2 detector 3 vs. the six beam parameters in a typical run are shown. One sees that the linear regression analysis determines the yield slope quite accurately; the dependence of the corrected yield on the beam parameters are largely removed.

The statistical uncertainties of the slopes are usually very small, since in an hour-long run there are large number of independent measurements (∼100,000).

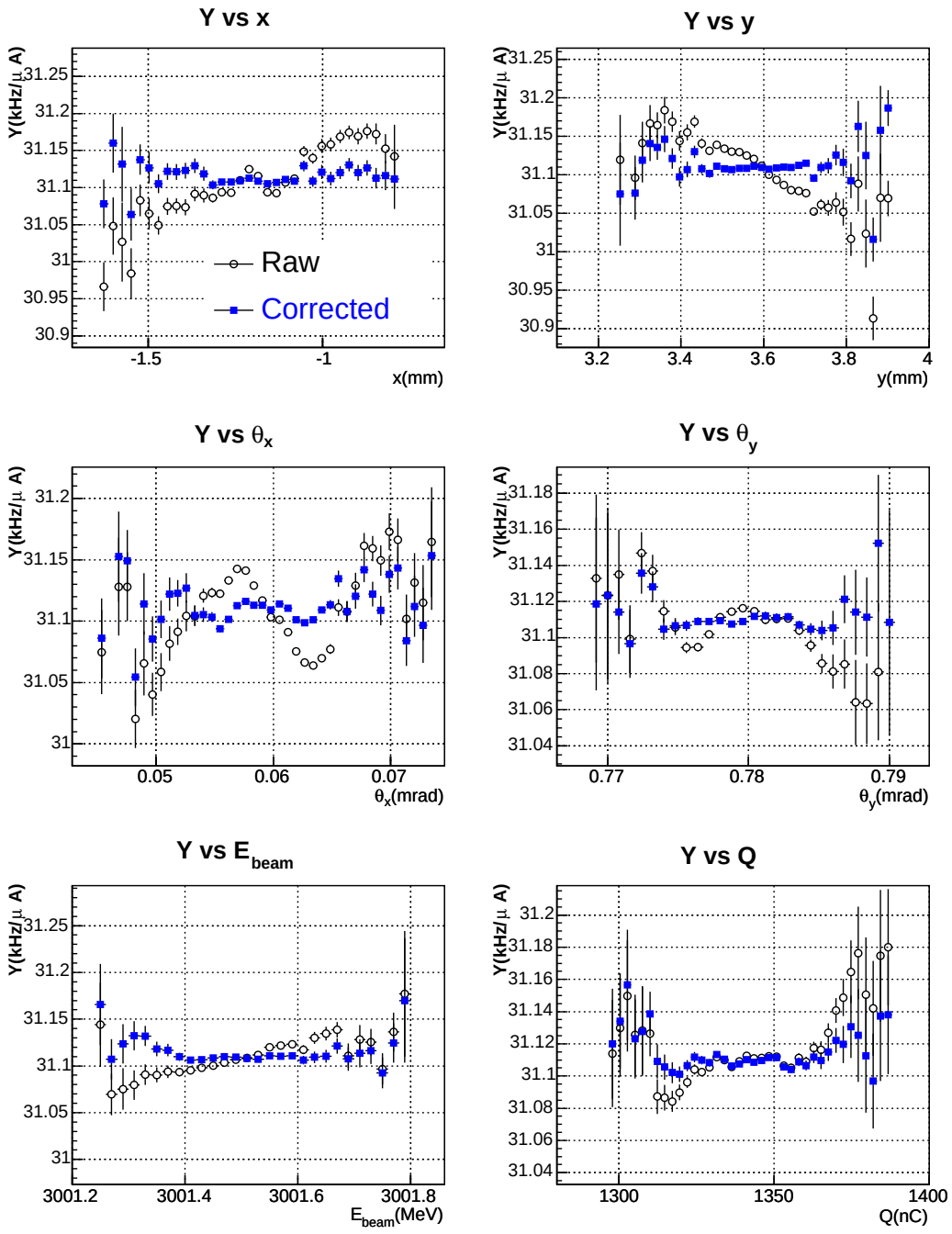

Figure 5.12: *The raw (black open circles) and slope-corrected (blue solid squares) proton yields vs. beam parameters* $(x, y, \theta_x, \theta_y, E_b, Q)$ *for octant 2 detector 3 in run 19870.*

However, the run-by-run fluctuations of the slopes (especially those associated with the positions and angles) are much larger than their corresponding statistical uncertainties, implying that the systematic effects, such as the beam halos, change the

sensitivities of the detectors. Nevertheless, if one averages the slopes over a long enough period to suppress the short term systematic fluctuations, the expected sensitivity of the spectrometer is observed. In Fig. 5.13, the proton yield sensitivities of all eight octants on detector 8 to the beam y position are plotted against the run number during the entire production run. Each data point on the figure is an

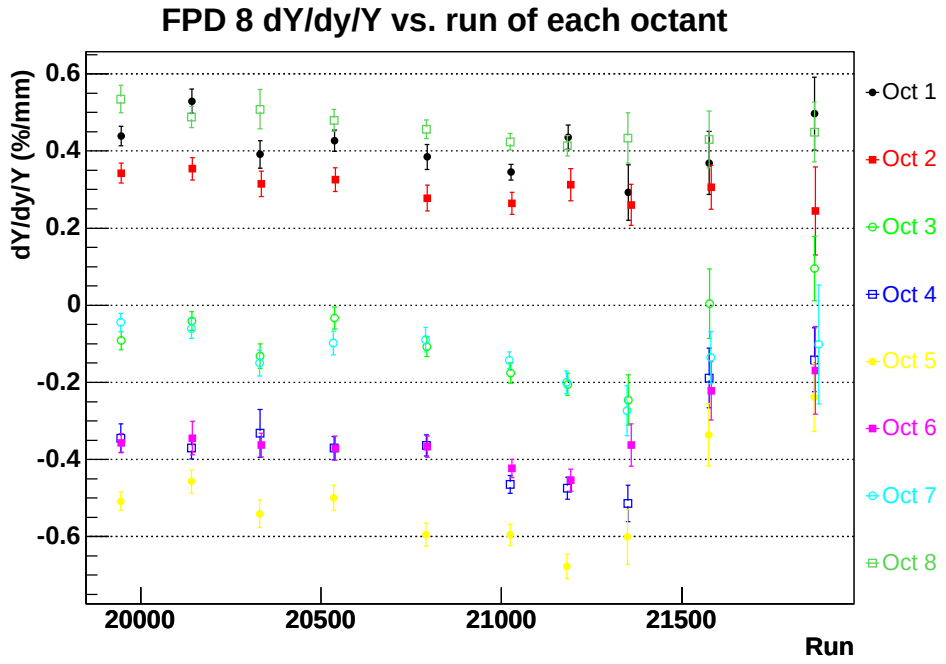

Figure 5.13: $\frac{1}{Y}\frac{\partial Y}{\partial y}$ *[Y = yield, y = vertical beam position] in %/mm for the proton peak in all eight octants of detector 8 vs. the run number during the entire production run period, with each data point being an average value over 100 runs: [black solid circles = octant 1, red solid square = octant 2, green open circles = octant 3, blue open squares = octant 4, yellow solid circles = octant 5, pink solid squares = octant 6, light blue open circles = octant 7, emerald open squares = octant 8].*

average slope over 100 runs (~100 hours), with the uncertainty being the standard deviation of the distribution of the run-by-run slopes divided by $\sqrt{100}$. Clearly, different octants exhibit different sensitivities, which is expected from their geometrical placement. For example, among all octants, $\frac{1}{Y}\frac{\partial Y}{\partial y}$ of octant 1 and octant 5 are the largest but opposite in sign, which is consistent with the fact that octant 1 and 5 are the very top and bottom octants. Furthermore, the longer term stability of the slopes appears to be reasonably good. For example, the variation of octant 5

is $\sim \pm$ 0.1%/mm, roughly $\pm$20% of the average slope of this octant.

To demonstrate the (geometrical) sensitivity of individual octant to the beam positions more explicitly, the average $\frac{1}{Y}\frac{\partial Y}{\partial y}$ during the production run period is plotted against the average Φ angle of the acceptance of each octant (with $\Phi = 0$ being the x or horizontal direction) in Fig. 5.14. The uncertainty of each data point is

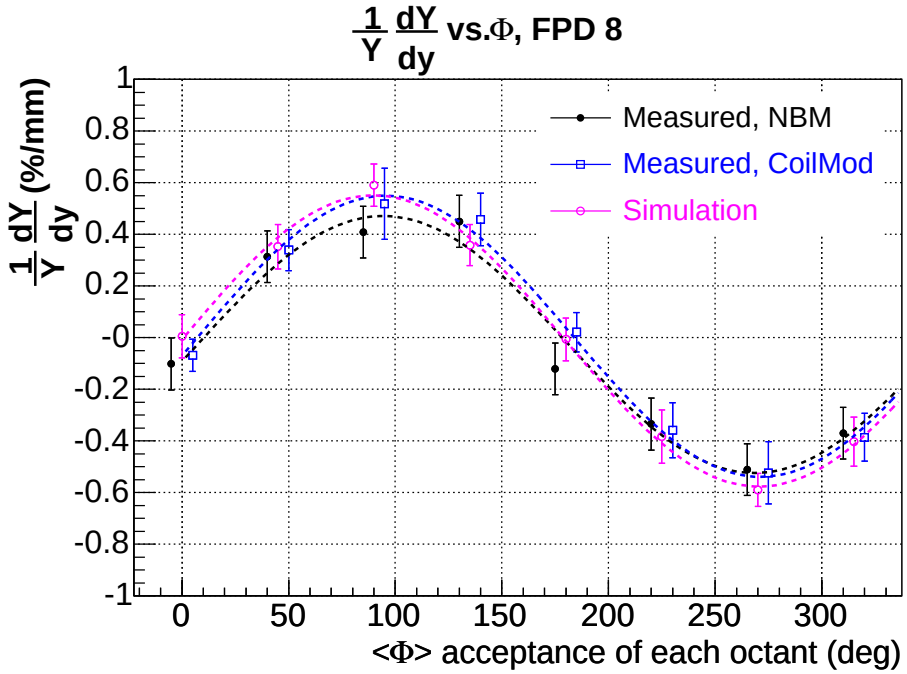

Figure 5.14: $\frac{1}{Y}\frac{\partial Y}{\partial y}$ *[Y = yield, y = vertical beam position] in %/mm of detector 8 vs. the average Φ of each octant from different data sets and their sinusoidal fit. The black solid circles and the blue open squares are the experimental slopes determined using the natural beam motion (NBM) and the coil modulation (CoilMod). The pink open circles are the same slopes determined from a G0GEANT simulation.*

chosen to be 0.1%/mm, based on the fluctuation of the slopes seen in Fig. 5.13. One sees that the slopes sit nicely on a sinusoidal curve, and if one averages over all the eight octants, the slopes of different octants will largely cancel. This demonstrates the advantage of having an azimuthally symmetric spectrometer. One should note that the slopes are computed using the "natural beam motion", with a typical range of motion of $\sim$ 0.1 mm. In another so-called "coil-modulation" running mode, the beam positions were steered in a grid-like pattern, with a range of the beam position motion of $\sim$ 1 mm, which has a larger lever arm to determine the correlation slopes

with respect to the beam positions and angles. The slopes determined during the coil-modulation are overlaid in Fig. 5.14. The detector sensitivities have also been studied with the G0GEANT simulation [G0GEA99, Han04], of which the results are also overlaid. The agreement among the three sets of results is excellent. The octant-by-octant yield slopes to other beam position and angle parameters can be found in [Nak05a, Nak05]. They also agree with the geometrical expectation.

In Table 5.7, the slopes (averaged over all 8 octants and all detectors) are listed. For each detector, the uncertainties of the slopes are conservatively taken

Slope	Value	Uncertainty
$\frac{1}{Y}\frac{\partial Y}{\partial x}$(%/mm)	0.12	0.05
$\frac{1}{Y}\frac{\partial Y}{\partial y}$(%/mm)	-0.02	0.04
$\frac{1}{Y}\frac{\partial Y}{\partial \theta_x}$(%/mrad)	-1.6	0.9
$\frac{1}{Y}\frac{\partial Y}{\partial \theta_y}$(%/mrad)	0.08	0.4
$\frac{1}{Y}\frac{\partial Y}{\partial E}$(%/MeV)	-0.002	0.02
$\frac{1}{Y}\frac{\partial Y}{\partial Q}$(%/nC)	2.3×10^{-4}(NA) -1.5×10^{-3}(FR)	8×10^{-5}

Parameter	value
Δx (nm)	3 ± 4
Δy (nm)	4 ± 4
$\Delta\theta_x$ (nrad)	1 ± 1
$\Delta\theta_y$ (nrad)	1.5 ± 1
ΔE (eV)	29 ± 4
A_Q (ppm)	-0.14 ± 0.32

Table 5.7: *Left table: the average slope for all octants and detectors. The last row, the charge slope* $\frac{1}{Y}\frac{\partial Y}{\partial Q}$*, have been separated into the NA and French octants to reflect their different residual deadtimes. Right table: helicity correlated differences/asymmetries of individual parameters defined in Eqn. 5.55 (calculated quartet by quartet and averaged over the entire run).*

as the standard deviation of the slopes over all runs, the inverse square of which is used as the weight when computing the grand averages and uncertainties over all detectors. For $\frac{1}{Y}\frac{\partial Y}{\partial Q}$, the NA and French octants are averaged separately. To make contact with Sec. 5.3.1, we note that

$$\frac{1}{Y}\frac{\partial Y}{\partial Q} \times (40\ \mu\text{A} \times \frac{1}{30}\ \text{s}) = \frac{\partial A}{\partial A_Q}\,, \tag{5.71}$$

and $\frac{1}{Y}\frac{\partial Y}{\partial Q}$ in the table are in good agreement with the residual asymmetry slopes of 0% (NA) and -2.5% (French) (see Table 5.3). For reference, the average helicity correlated beam parameters and uncertainties of the entire experiment are also listed in the right part of Table 5.7.

Using Eqn. 5.56 and the values in Table 5.7, the overall false asymmetry is

$$A_{false} = -0.005 \pm 0.011 \text{ ppm}\,. \tag{5.72}$$

In the actual analysis, A_{false} is computed detector by detector, and the correction of the residual A_{false} is also made detector by detector, after the background correction [Nak05].

Lastly, one should note the conceptual similarity of correction of the beam properties and the deadtime correction. To first order, the deadtime correction is equivalent to making a linear regression correction on the yield with one beam parameter (beam charge). However, in the deadtime correction, the correlation slope $\frac{\partial Y}{\partial Q}$ is calculated *a priori* based on a model of the electronics, whereas here the correlation slopes are determined empirically with a linear regression analysis. Furthermore, a distinct feature of the deadtime is that it correlates the measured asymmetry with the physical asymmetry itself, whereas the false asymmetry discussed in this section is correlated with the asymmetry of the beam parameters only.

5.3.4 Beam Polarization Correction

The correction of the raw asymmetry due to the beam polarization is simply

$$A_{corr} = \frac{A_{raw}}{P_b} \tag{5.73}$$

where A_{raw} and A_{corr} are the raw and corrected asymmetries, respectively, and P_b is the polarization of the beam.

The longitudinal polarization of the electron beam was measured with a Møller

polarimeter in Hall C. The setup of the polarimeter and the principles of the beam polarization measurement have been described in Sec. 4.2.1. The measurements typically occurred about once every three days before and after the change of the state of the insertable halfwave plate.

The beam polarization as measured over the entire production run is summarized in chronological order in Fig. 5.15. The top (bottom) plot shows the polariza-

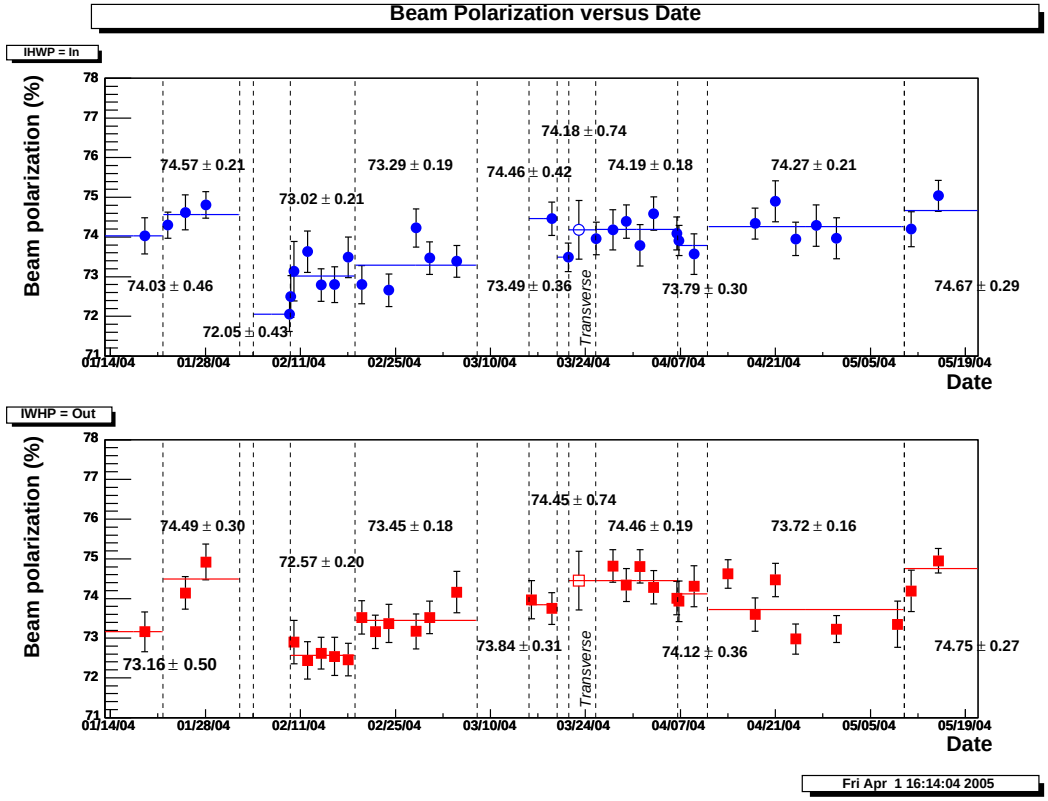

Figure 5.15: *The beam polarization versus date, broken down into data sets according to the state of the insertable halfwave plate: "in" (top) and "out" (bottom). In each data set, the measured values are subgrouped according to the configuration of the injector and the polarized source, and constant fit is made on each group. The open data points in the plots represent the polarization when beam was transversely polarized. The value near the top of each plot is the grand average of all polarization measurements for this given state of the insertable halfwave plate. Figure taken from [Phi05].*

tion measured with the insertable halfwave plate inserted (retracted). One can see that the polarization is fairly stable and on average is ∼74% [Phi05]. The measured values of the polarization are broken down into subsets according to the configura-

tion change of the polarized source and the injector, and the average polarization in each set is assigned to the corresponding range of G^0 data runs. The average polarization during the entire experiment, weighted by the G^0 production data collection, is 73.73%, slightly different from the straight averages shown in Fig. 5.15. The asymmetries and their uncertainties measured by the G^0 detectors are corrected with Eqn. 5.73 run by run.

One noteworthy point is that the raw asymmetries were computed based on the helicity bit (the polarity of the Pockels cell). To determine the true helicity of the beam on target, the state of the insertable halfwave plate and the beam transport need to be taken into account. The sign of the true beam helicity relative to the helicity bit was determined via the Møller measurement, and is reflected by the sign of P_b in Eqn. 5.73.

The evaluation of the systematic uncertainty of the beam polarization has been summarized in [Phi05]. The overall systematic uncertainty is 1.32% (fractional), which is dominated by the uncertainty (1% fractional) when extrapolating the polarization measured at 2 μA to the nominal running current at 40 μA. The statistical uncertainty of each beam polarization measurement is typically 0.3%, which is negligible compared with the systematic uncertainty. This 1.32% (fraction) uncertainty is assigned as a global systematic uncertainty to the final physics asymmetries.

5.3.5 Physics Background

Unless otherwise specified, the asymmetries in the remainder of Chapter 5 are corrected for the leakage and the beam polarization, but are still "blinded" by the encryption factor ($f_{blind} \equiv 0.8056$).

In this section (Sec. 5.3.5), we shall discuss the behaviors of the background in various aspects and explore its physics nature. Although it is an important ingredient to understand our measurement, this discussion is not directly used in the asymmetry analysis and correction procedure. For clarity, the correction procedure for the background will be presented separately in Sec. 5.3.6.

5.3.5.1 Decomposition of the Background Yield

The G^0 spectrometer separates π^+ and elastic protons by their different time of flight from the target to the detector. Particle identification, used for diagnostics, can be made by combining the information of the time of flight (measured by TDCs) and the energy loss in the scintillators (measured by ADCs) in the Fastbus data. In Fig. 5.16(a), a typical two dimensional plot of events as a function of pulse-height (in ADC channels) and flight time for a given detector is shown. A four-fold coincidence

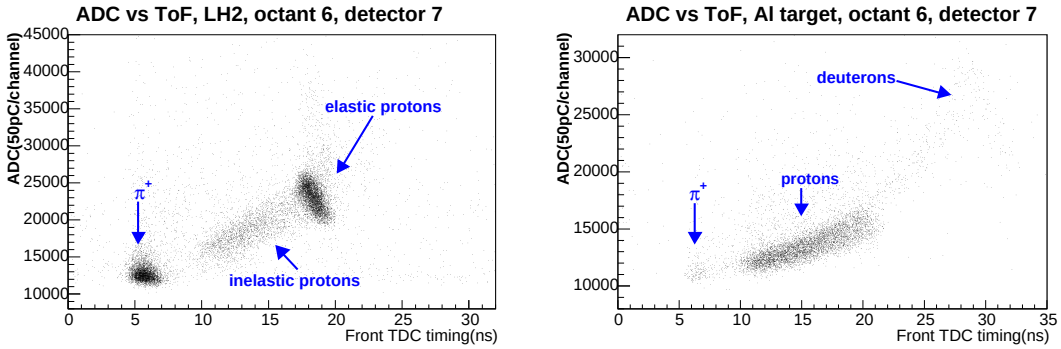

(a) *Full LH2 target.* (b) *Dummy Al target.*

Figure 5.16: *Energy loss (in ADC channel) vs. time of flight for four-fold coincidence events with LH2 target (a), and the aluminum frame target (b). The particle identification is explained in the text.*

between four phototubes of a front-back scintillator pair is required for the hits in the plot and the y axis is the sum of the ADCs of all four tubes of the same detector. The energy loss of the π^+ in the scintillator is given by the minimum ionizing energy. In Fig. 5.16(a), these hits correspond to the cluster at early time of flight (< 10 ns) with low ADC amplitude ($<$ channel 15000). The protons, whose ionization energy loss scales with $1/\beta^2$, deposit much more energy than the pions. The thick cluster in Fig. 5.16(a) centered around 19 ns and ADC channel 21000 corresponds to the elastic protons hits. The fading vertical band above it corresponds to pileup (more than one hit occurred in the ADC integration gate). The inelastic protons are (counter-intuitively) faster than elastic protons of the same detector due to the optics of the spectrometer (see Sec. 4.2.3), therefore they have shorter flight time and deposit less

energy, corresponding to the continuous band between the pions and elastic protons.

To illustrate the particles produced by the target aluminum cell walls, a similar pulse-height vs. time of flight plot is shown in Fig. 5.16(b), for a run with the dummy Al frame target (see Sec. 4.2.2). One observes a faint band after the band of the inelastic and quasi-elastic protons. As substantiated by a GEANT simulation [HF04, Bre04], this corresponds to deuterons knocked out from the aluminum target. The "kink" around 29 ns corresponds to the minimum kinetic energy required to penetrate both the front and back scintillators; deuterons slower than that are stopped in the back scintillator. One should note that for the regular liquid hydrogen target, the rate of the deuterons from the thin Al target windows is very low and can be practically neglected in the data.

We have taken two independent approaches to determine the background (or the "non-elastic") component underneath the elastic peak. They shall be discussed in turn next.

Background Yield Determination I: Empirical Approach

The first approach is an empirical determination. The background contains the inelastic protons from the target vessels (aluminum cells and helium gas) and the inelastic protons from the hydrogen. It is desirable to separate the two. Naively, the empty target measurement would give the inelastic yield from the target vessels. The situation is complicated by two facts: 1) there exists non-negligible gaseous hydrogen (GH2) in the empty target (the target thickness of GH2:Al in g/cm^2 is $\sim$ 1:2); 2) the contribution of the aluminum cell windows in the full target is enhanced due to the additional photon radiation from LH2. The yields from the LH2 ("full") target (19 K, 1.7 atm) and the GH2 ("empty") target (28 K, 2.2 atm) can be decomposed as:

$$\begin{aligned} Y_{\rm full} &= Y_{\rm up} + Y_{\rm lh} + Y_{\rm exit,full} \\ Y_{\rm empty} &= Y_{\rm up} + Y_{\rm gh} + Y_{\rm exit,empty} \, . \end{aligned} \tag{5.74}$$

In these two relations, $Y_{\rm up}$ represents the yield arising from the target components upstream of the hydrogen volume, i.e., the helium cell entrance window, the helium gas, and the hydrogen cell entrance window; it is common to both the full and empty targets [†]. $Y_{\rm lh}$ and the $Y_{\rm gh}$ are the elastic and inelastic rates arising from the liquid and gaseous hydrogen, respectively, and should scale with their densities as

$$\frac{Y_{\rm lh}}{Y_{\rm gh}} = \frac{\rho_{\rm lh}}{\rho_{\rm gh}}\,. \tag{5.75}$$

For static LH2 and GH2 at 28 K, this ratio is $\sim$33. However, gaseous hydrogen in the loop is circulating rapidly and can not be treated as static gas, hence its density can not be simply predicted from the ambient temperature and pressure. Therefore $\rho_{\rm gh}$ is empirically determined by taking the ratio of the yields of the (background subtracted) elastic peak with LH2 and GH2 (at 28 K) targets, and it is $\sim \frac{1}{21}$ of $\rho_{\rm lh}$.

The inelastic yields (from He gas, hydrogen and aluminum) arise from both the photo-nuclear and electro-nuclear (or virtual photon) reactions. The probability of the photo-nuclear reaction scales with the real photon flux and the photo-production cross section. The (real) Bremsstrahlung photon flux created in different materials is characterized by the radiation length X_0, the mean distance a (high-energy) electron travels in the material for losing all but $1/e$ of its energy due to Bremsstrahlung radiation [PDG04]. For this reason, the real photon flux Φ_γ is usually expressed as the thickness of the radiator in the unit of X_0. Note that for the same type of material, X_0 scales with the inverse of density. For an electron beam incident directly on a target, on average one half of the target can be regarded as the radiator [Tsa74]. The reaction probability of the electro-nucleus reaction can be treated similarly; under the equivalent photon approximation (EPA), it scales with Φ_e, the equivalent virtual photon flux, and the photo-production cross section. With a beam of $\sim$1 GeV, Φ_e is on average $\sim$2.9% [Kos02] [‡]. Therefore, the measured inelastic yield

[†] The helium gas will have some slight density change from the LH2 temperature ($\sim$19 K) to the GH2 ($\sim$28 K); we shall neglect this small difference here.

[‡] As a matter of fact, Φ_e can be estimated from our data [Roc04] by comparing the inelastic yield from the aluminum dummy target (the flyswatter) with and without the tungsten radiator. The results agrees very well with 2.9%.

can be written as [§]

$$Y = \mathcal{Y}(\Phi_\gamma + \Phi_e) \times t_{\rm tgt}\,, \tag{5.76}$$

in which $\mathcal{Y}$ is some constant proportional to the photo-production cross sections and the acceptance, and $t_{\rm tgt}$ is the thickness of the target.

The yields coming from the 3 mil exit window in the full and empty targets are denoted as $Y_{\rm exit,full}$ and $Y_{\rm exit,empty}$, respectively. As mentioned earlier, real photon fluxes from the liquid and gaseous hydrogen volumes scale inversely with their densities. Therefore, we write $Y_{\rm exit,full}$ and $Y_{\rm exit,empty}$ as

$$\begin{aligned} Y_{\rm exit,full} &= \mathcal{Y}(\Phi_{\rm up} + \Phi_{\rm lh} + \Phi_{\rm exit/2} + \Phi_e) \times t_{\rm exit} \\ Y_{\rm exit,empty} &= \mathcal{Y}(\Phi_{\rm up} + \frac{\rho_{\rm gh}}{\rho_{\rm lh}}\Phi_{\rm lh} + \Phi_{\rm exit/2} + \Phi_e) \times t_{\rm exit}\,, \end{aligned} \tag{5.77}$$

in which $\Phi_{\rm up}$ and $\Phi_{\rm lh}$ are the real photon flux from the upstream target components and liquid hydrogen, respectively. $\Phi_{\rm exit/2}$ is the flux from half of the aluminum exit window. Combining Eqns. 5.74, 5.75 and 5.77, we have

$$Y_{\rm full} - Y_{\rm empty} = \left(1 - \frac{\rho_{\rm gh}}{\rho_{\rm lh}}\right) Y_{\rm lh} + \mathcal{Y}\left(1 - \frac{\rho_{\rm gh}}{\rho_{\rm lh}}\right) \Phi_{\rm lh} \times t_{\rm exit}\,. \tag{5.78}$$

Another constraint comes from the measurement made on the flyswatter target (see Sec. 4.2.2). The tungsten (W) radiator was used to enhance the photon flux [†] (see also Sec. 4.2.2). As in Eqn. 5.77, the measured yield with the flyswatter and with W can be written as

$$Y_{\rm fs+w} = \mathcal{Y}(\Phi_{\rm W} + \Phi_{\rm fs/2} + \Phi_e) \times t_{\rm fs} \tag{5.79}$$

in which $\Phi_{\rm W}$ and $\Phi_{\rm fs/2}$ are the real photon flux from the tungsten and one half of the flyswatter, and $t_{\rm fs}$ is the thickness of the flyswatter. Combining Eqns. 5.78 and

[§]Note that this relation holds for thin target, i.e. for $t_{\rm tgt}$ much less than the radiation length of the target material.

[†]The direct events from the tungsten were mostly outside the acceptance and are therefore neglected.

5.79, we get

$$Y_{\rm lh} = \frac{1}{\beta}\left(Y_{\rm full} - Y_{\rm empty} - \alpha Y_{\rm fs+w}\right) \tag{5.80}$$

with

$$\beta = 1 - \frac{\rho_{\rm gh}}{\rho_{\rm lh}}, \quad \alpha = \frac{t_{\rm exit}}{t_{\rm fs}} \frac{\beta\Phi_{lh}}{\Phi_{\rm W} + \Phi_{\rm fs/2} + \Phi_e}. \tag{5.81}$$

The thicknesses of different target components have been described in Sec. 4.2.2. For reference, their values and the corresponding real photon flux (in units of radiation length) are summarized in Table 5.8.

	He window	GHe	entrance window	LH2	exit window	FS	W
t (cm)	0.018	16	0.023	20	0.008	0.076	0.0085
Φ_γ (%)	0.20	0.08	0.26	2.31	0.09	0.86	2.43

Table 5.8: *The thickness of different target components and the real photon flux in units of radiation length.*

Using Eqn. 5.80, the yield (elastic and inelastic) purely from the liquid hydrogen can be extracted. Clearly the contributions from the aluminum cells and the GHe, $Y_{\rm non-hyd}$, can be extracted as

$$Y_{\rm non-hyd} = Y_{\rm full} - Y_{\rm lh}. \tag{5.82}$$

In Fig. 5.17, the measured $Y_{\rm full}$ and the extracted $Y_{\rm lh}$ and $Y_{\rm non-hyd}$ are overlaid for four different detectors.

Since $Y_{\rm non-hyd}$ is determined by subtracting two "large" values, the uncertainty is treated with care. We assigned an 1% (fractional) uncertainty to $Y_{\rm full}$, $Y_{\rm empty}$ and $Y_{\rm fs}$ due to time bin width variation, spectra misalignment, deadtime and charge normalization, a 10% (fractional) uncertainty to α due to the precision of the thickness of the exit windows and the flyswatter, and the photon flux, and $0.4\% \sim \frac{22}{23} - \frac{20}{21}$ as the uncertainty for β. Despite the relatively large uncertainty underneath the elastic peak, $Y_{\rm non-hyd}$ appears to contribute less than 40% of the inelastic background, and the remaining more than 60% background arises from the inelastics from hydrogen.

Besides the approach presented above, there are other experimental approaches

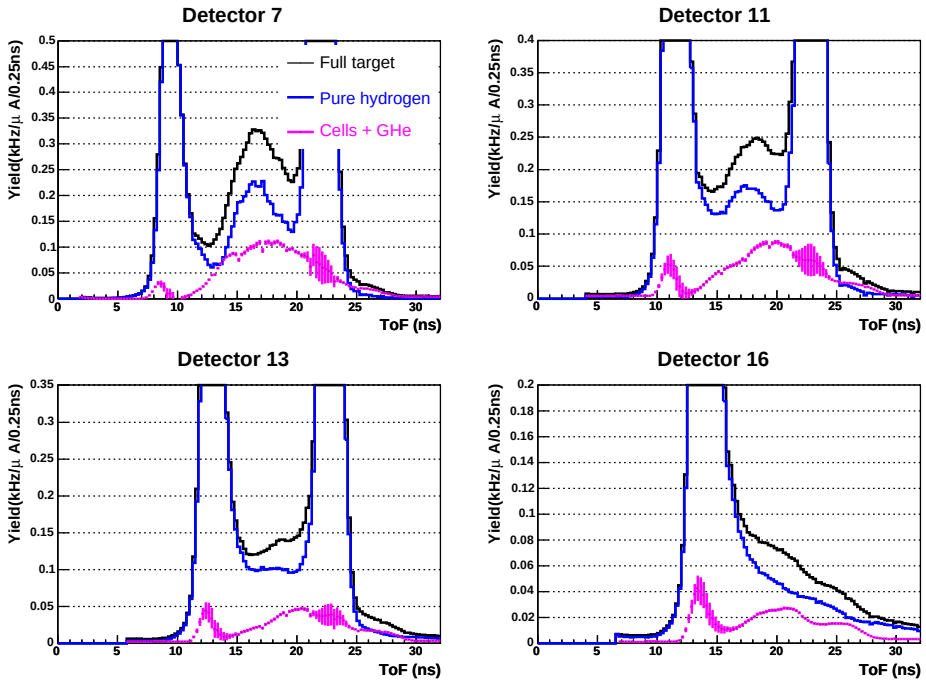

Figure 5.17: *The total measured yield of the full target (black), the yield purely from the hydrogen (blue), and the inelastic yield from the aluminum target windows and gaseous helium (pink) for four typical detectors.*

to determine the contribution from the target windows. For example, the contribution of electro-production from the three windows can be obtained cleanly with the empty target measurements performed at two temperatures: the difference between the two measurements gives the combined contribution from GH2 and GHe, from which one can extract the contribution from the three windows (mostly through electro-production). Also, the thickness of the exit window was 11 mil during the engineering run and was thinned to 3 mil in the production run; the difference implies the contribution from the exit windows. A detailed analysis of the decomposition of the contributions from the cell windows, and separation of the photo- and electro-productions is documented in [Gui04]. Nevertheless, one should note, that using the experimental data would not allow a separation of the elastic and inelastic yields from the hydrogen itself.

Determination of Background Yield II: Monte Carlo Simulation

Another approach to decompose the yield is to use a GEANT-based simulation [GEA94]. The G0GEANT package is a customized GEANT Monte Carlo simulation program with the G^0 spectrometer geometry and magnetic field map [G0GEA99]. Particle generation is made with a uniform sampling in the initial phase space at the reaction vertex. The inelastic reaction probability, multiplied by the volume of the phase space for particle generation, is stored as the weight of the event. The tracking of the particles is handled by GEANT and once a good hit is recorded by a detector, the information of the hit, e.g., the event weight, initial momentum and angle at the vertex, and the particle flight time are stored. Since the detector rate is proportional to the integral of the cross section over the acceptance, it can be calculated as

$$R = \mathcal{L}\frac{\sum^i \text{weight}^i}{N_{thrown}}, \tag{5.83}$$

in which $\mathcal{L}$ is the luminosity factor, N_{thrown} is the total number of generated events, and $\sum^i \text{weight}^i$ is a summation of the event weight over all detected hits.

The inelastic protons arise from photo- and electro-production processes. As mentioned earlier, their reaction probabilities can be computed with the real or virtual photon flux, folded with photo-production cross section. More details of the rate computation are given in Appendix B.2, where the hyperon Monte Carlo is discussed. Here we will limit ourselves only to the general methodology. As an example, for the inelastic process of $\gamma + p \to p + \pi^0$, the energy of the photon E_γ and the outgoing angles of the proton θ_p and ϕ_p are uniformly sampled. Then the event weight can be calculated as

$$\text{weight} = \Gamma_{real}(E_\gamma)\frac{d\sigma_\gamma}{d\Omega_p}(E_\gamma, \theta_p)\sin(\theta_p)\Delta_{phase}, \tag{5.84}$$

in which $\Gamma_{real}(E_\gamma)$ is the Bremsstrahlung photon flux, $\frac{d\sigma_\gamma}{d\Omega_p}(E_\gamma, \theta_p)$ is the photo-production cross section, Δ_{phase} is the volume of the phase space in which the events are generated, and $\sin(\theta_p)$ is the Jacobian between $d\Omega_p$ and $d\theta_p d\phi_p$.

The Bremsstrahlung photon flux, $\Gamma_{real}(E_\gamma)$, defined as the number of photons per incident electron per unit photon energy and material length, can be computed with the formulation in [Mat73]. Under the forward peaking approximation, the virtual photon flux is given in [WT82], which can be treated in exactly the same way as the real photon flux. A slightly different version of the virtual photon spectrum as a function of E_γ and Q^2 is given in [Dre92], in which case the photon is no longer along the direction of the incident beam, and vector rotations are needed in computing the lab kinematics of the outgoing particles.

The photo-production cross section $\frac{d\sigma_\gamma}{d\Omega_p}(E_\gamma, \theta_p)$ from the aluminum windows and GHe is calculated from the model by Lightbody and O'Connell [LOC88]. This model decomposes the inelastic γ-nucleus scattering into quasi-free knock-out, quasi-deuteron scattering, and Δ resonance. In Fig. 5.18, the measured spectra purely from the target cells [†] are overlaid with those from the electro-production simulation (inelastic protons only). Note that these are the rates computed from the simulation directly with no additional empirical scaling factors. The agreement between the MC and data is good for lower numbered detectors. For detectors above 10, the simulation under-predicts the rate. As a side note, the flat and low rate background observed above detector 7 are from deuteron knockout from the aluminum, a process which is not included in the event generator; they "wrap-around" and make a flat background also at the early time-of-flight region.

For the inelastic protons and pions from the hydrogen, three different models are implemented: MAID [MAID03], Δ-resonance in LB&OC [LOC88] and a generator developed at Orsay [Mor01, Arv03]. MAID is a unitary isobar model for single pion photo- and electro-production on the nucleon developed at Mainz [MAID03]. It is applicable for photon energies below 1 GeV, corresponding to a maximum invariant mass (W) of $\sim$1.7 GeV of the $\gamma - p$ system. Therefore, we extrapolated with a constant cross section for $W > 1.7$ GeV in our MC. However, the G^0 acceptance, especially that of the higher numbered detectors, favors the inelastic protons with

[†]From the empty target measurement, the contribution from GH2 and GHe is obtained by taking the difference of the spectrum with two different temperatures, from which one could deduce the contribution (mostly electro-production) from the three aluminum cells.

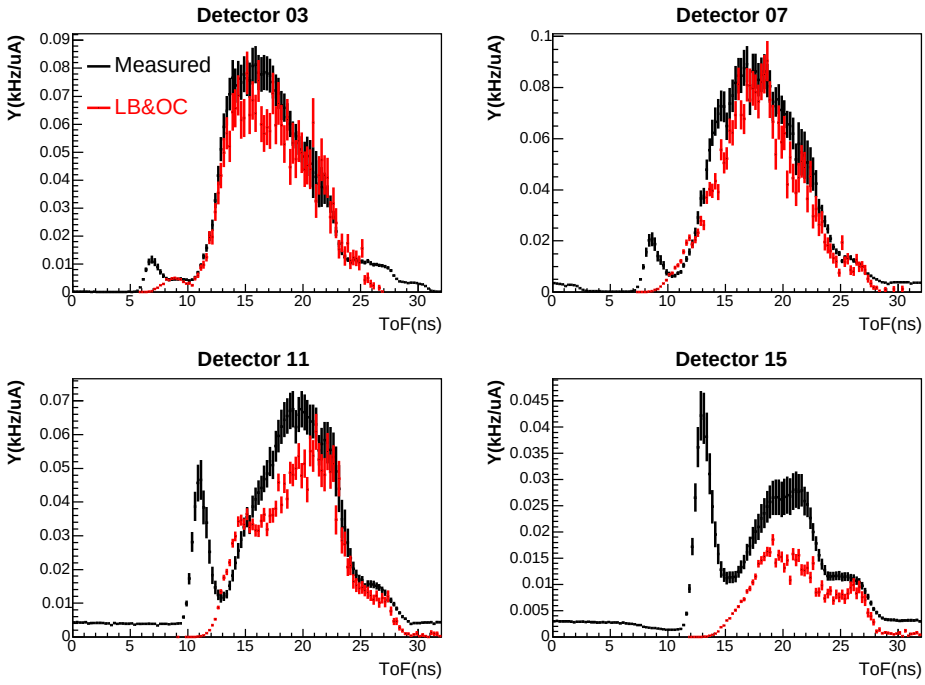

Figure 5.18: *The experimental (black) and simulated (red) yield spectra from the target aluminum windows for detectors 3, 7, 11 and 15.*

W >2 GeV, a region where the prediction of MAID is unreliable.

The LB&OC model of Δ excitation takes a simple form [LOC88]. However, comparing with MAID2003, it was found that the LB&OC underpredicts the total cross section of the Δ resonance by $\sim$ 30%, but over-predicts the non-resonant background and higher resonances by a factor of three or more. Therefore, the original LB&OC model was modified to fit the total cross section given by MAID2003 [Han04b], after which the rates predicted by the two models are in agreement (see Fig. 5.19).

The Orsay generator [Mor01, Arv03] was developed based on a photo-production generator for the Graal experiment, which models the pion photo-production from the threshold up to 4 GeV [Cor94]. So in terms of applicability, the Orsay generator is the most suitable for G^0. However, the Orsay generator was found to significantly underpredict the π^+ rates in G^0 [Han04c]; it was therefore only used for inelastic proton generation.

To compare the three models, in Fig. 5.19, the extracted pure hydrogen spec-

tra, as determined from Eqn. 5.80, are overlaid with the simulated hydrogen inelastic spectra from the three models for four selected detectors. The pions in all three simulated spectra are generated by the same LB&OC generator. For the proton rates in the inelastic region, all three generators give reasonable agreement for lower detectors up to 6. For detectors above 6, both LB&OC and MAID over-predict the yield, whereas the Orsay generator agrees better with the data. We note that all three models predict that the background yield collapses rather rapidly within the elastic peak region. However, looking closely at the cut3 regions (defined in Sec. 5.2), one realizes that all three generators under-predict the yields there [†], as well as the yield in detector 16. Since the simulations fail to reproduce the data in these "superelastic" regions, there is good reason to question the reliability of their predictions underneath the elastic peak.

To summarize, the background yield decomposition has been made using two approaches — the empirical one based on G^0 calibration measurements and the Monte Carlo simulation based on independent cross section parameterization. The background due to the target cells and GHe are well understood. However neither approach sheds light on how to decompose the elastic and inelastic yields from the hydrogen.

5.3.5.2 Behavior of the Background Asymmetry

Besides the inelastic yield contamination underneath the elastic peak, it appears that the background also carries a non-negligible asymmetry. As an overview, in Fig. 5.20 the octant averaged asymmetries vs. time of flight measured by the NA and French octants are overlaid with the measured French yield spectra for all 16 detectors. First of all, the trends of the asymmetries measured from both sets of the electronics are in agreement, which strongly rules out the possibility that the background asymmetries are due to electronic artifacts. Secondly, the asymmetry exhibits an interesting evolution with time of flight. The asymmetries measured

[†]The tails in cut3 are not the electromagnetic radiative tail — the radiative tails of the G^0 proton spectrum are toward the earlier time of flight, or higher Q^2. See discussions in Sec. 5.3.8.

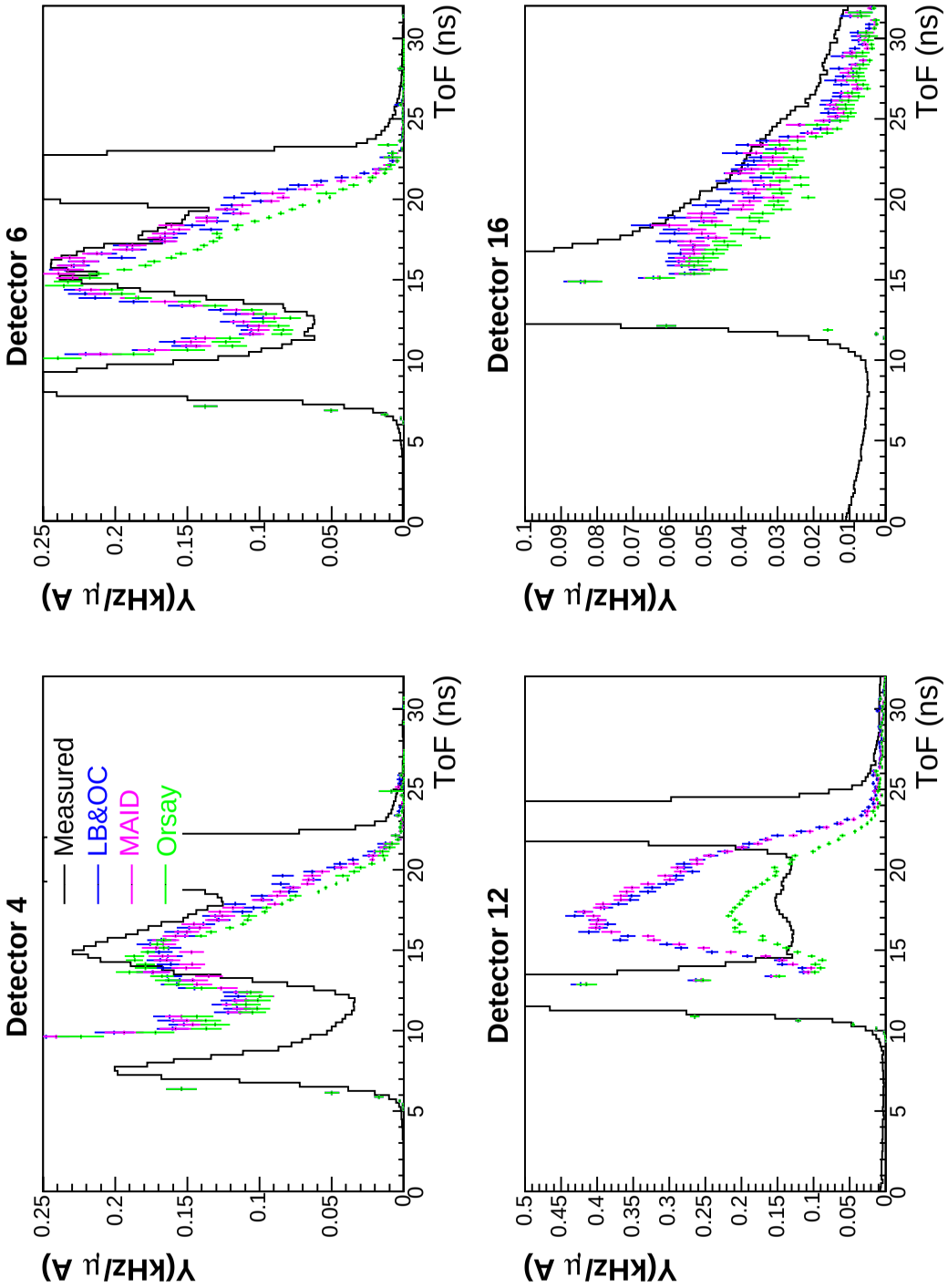

Figure 5.19: *The experimental yield spectra (black) from the pure hydrogen, and those from the simulation with modified LB&OC [LOC88] (blue), MAID [MAID03] (pink) and Orsay [Mor01, Arv03] (green) generators in four selected detectors.*

at the pion peak are large and negative in the lowest detectors, and approach zero for higher numbered detectors. There is a positive asymmetry peak, starting from the "dip" between the pion and inelastic peaks in lower detectors, which "moves" gradually toward the inelastic and elastic peaks in the higher numbered detectors. From the shape of the background asymmetry of detector 16, one can imagine that in detectors 12 to 15, the bump of the inelastic background asymmetry continues into the elastic peak. Third, the evolution of the background asymmetry from cut2 to cut3 regions (defined in Sec. 5.2) of a given detector is smooth. This allows one to make fits in order to evaluate the background asymmetry underneath the elastic peak, which will be elaborated on in Sec. 5.3.6.1. Furthermore, the change of the background asymmetry is progressive across successive detectors, which implies that the underlying physics is smoothly varying in nature. This important feature will be used in the background correction procedure for detector 15 in Sec. 5.3.6.2.

The asymmetry of the pion peak is of less relevance to the elastic proton asymmetry, since it has practically no contamination in the far-away elastic peak except for the small deadtime effect discussed in Sec. 5.3.1.3. Its negative sign is consistent with the parity violating asymmetry of, e.g., the electro-production of the Δ [Muk98]. The large negative pion asymmetry observed in the lower detectors could also be a threshold artifact (the discriminator threshold sits in the middle of the pulse-height distribution of the pions). The positive background asymmetry is again of little relevance for the elastic peak except for detectors 12 and above. Various possibilities were considered to understand the origin of the positive background asymmetry. The first candidate was the aluminum target windows. However, the measured asymmetry in the inelastic cut (defined in Sec. 5.2) for GH2 and the dummy aluminum targets give consistently negative asymmetries, as depicted in the left panel of Fig. 5.21 [†]. To explore the effect of a slight misalignment of the beam spin direction, in the right panel of Fig. 5.21, the asymmetry in the inelastic cut for the full LH2 target with the incident electron beam transversely polarized is plotted

[†]There are some differences in the asymmetry between the empty target and the aluminum frame target, possibly due to the existence of the GH2 in the empty target, as well as the different proportions of the photo- and electro- productions in the empty and frame targets.

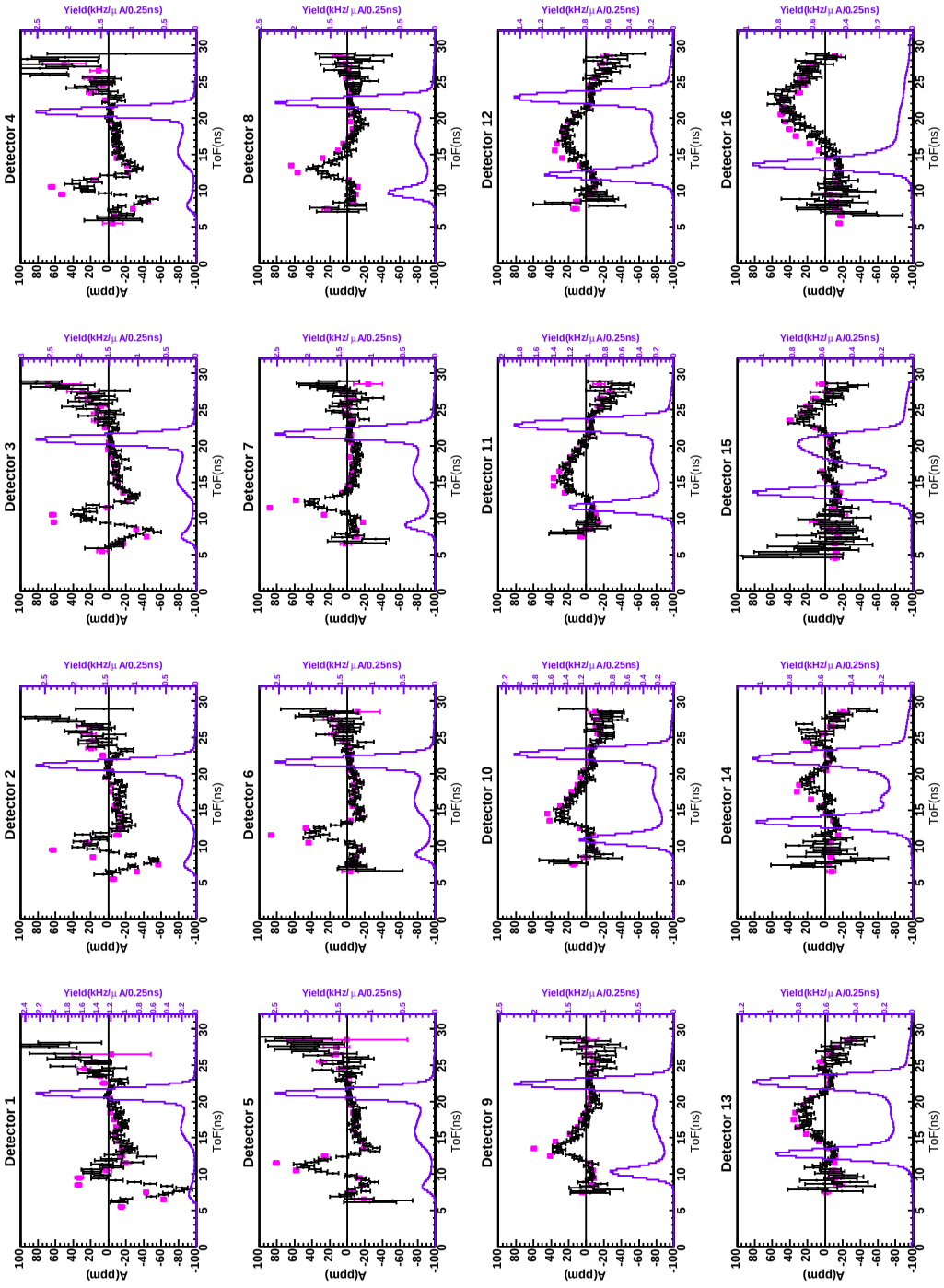

Figure 5.20: *The average asymmetry of the NA (pink) and French (black) octants vs. time of flight for all 16 detectors. The y scale of the asymmetry is from -100 to 100 ppm. Asymmetries are corrected for beam polarization, but blinded by the blinding factor (0.8056). The French yield spectra (violet histograms) are overlaid with scales on the right of the plots.*

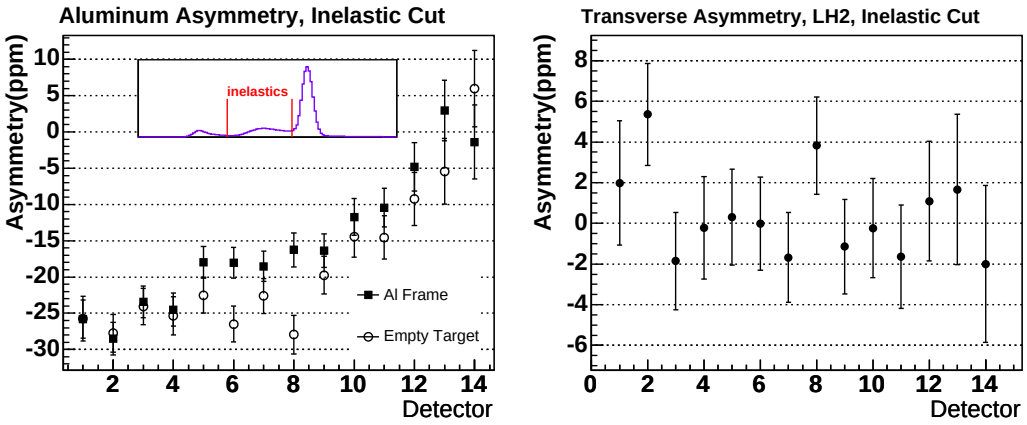

Figure 5.21: *Left figure: the asymmetries of the inelastic cut with the empty target (open circles) and the aluminum frame target (solid squares) for detectors 1 through 14. Right figure: the asymmetries in the same cut for the LH2 target with the beam transversely polarized. All asymmetries are corrected for the beam polarization, but are blinded by the blinding factor (0.8056).*

against the detector number. The positive background asymmetry observed with longitudinally polarized beam is not observed here, from which we conclude that the background asymmetry is really due to some parity violating process, instead of an instrumental artifact.

In Fig. 5.22, the measured asymmetries of cut2 (see definition in Sec. 5.2), averaged over detectors 1 through 14, are plotted against the octant number. The

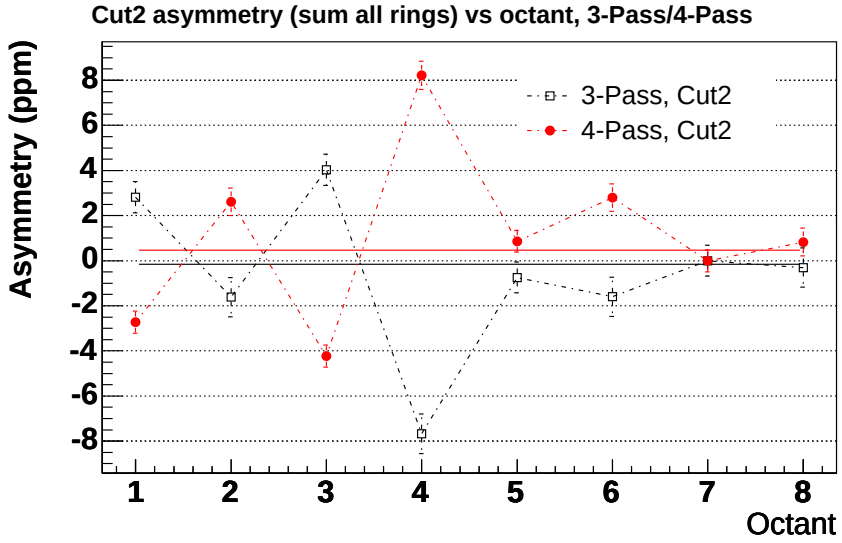

Figure 5.22: *The asymmetries in cut2, averaged over detectors 1 through 14, plotted against the octant number:[black open squares = 3-pass, red solid circles = 4-pass].*

data are split into two sets, with a 3-pass electron beam for one and 4-pass for the other, and their asymmetries are overlaid in the figure. The electron polarizations in Hall C for the 3-pass and 4-pass beam are opposite to each other due to the different spin precessions during the transport (see Sec. 4.2.1.2). On the other hand, the detector asymmetry is calculated based on the helicity bit, which sets the polarity of the Pockels cell in the source with no knowledge of the beam transport (see Sec. 4.2.1.2). Therefore, one expects that the asymmetries for the 3-pass and 4-pass beams exhibit a sign change. This is clearly shown in Fig. 5.22, confirming that the background asymmetries are indeed correlated with the beam spin. One striking feature, as one notes from the figure, is that the background asymmetry exhibits variations from octant to octant. One should not draw conclusions based on the overall difference between the NA (1, 3, 5 and 7) and French (2, 4, 6 and 8) octants, because their definitions of cut2 are different (see Sec. 5.2). Nevertheless, even among the four French octants, octant 4 differs from the other octants far beyond the statistical allowance. The background asymmetries in NA octants 1 and 3 also appear to be different from those in octants 5 and 7 [†].

Both the positive asymmetry of the inelastic region and the octant-by-octant variation can be plausibly explained by hyperon production and decay. The hyperons (the Λ, Σ^+ and Σ^0), can be produced in electron-proton scattering and a large fraction of the polarization of the incident beam is transferred to them [Car03]. The hyperons subsequently decay through a weak interaction process, with the decay particles carrying a large parity violating asymmetry. As substantiated by a detailed Monte Carlo study, a small fraction of these decay particles make it into the detectors through rescattering, generating a large background asymmetry. The details of a Monte Carlo study of the hyperons are presented in Appendix B; one shall see there that the simulation reproduces the measured positive background asymmetry qualitatively. However, the accuracy of the Monte Carlo is limited due to unmeasured parameters in the model, in particular, the transferred polarization

[†]The disagreement within the NA octants can hardly be observed with the statistics of a single FPD, but shows up when one combines all FPDs together.

of the Σ^+ and Σ^0, and the cross sections of these hyperon productions with high enough invariant mass. Therefore, the correction of the background is made by fitting/interpolating the measured data (see Sec. 5.3.6), instead of relying on the simulation. With regard to the octant-by-octant variation of the background asymmetry, it could result from some small azimuthally asymmetric placement of the collimators (since the rescattering is responsible for kicking the hyperon daughter particles into the acceptance), or the octant-by-octant variation of the discriminator thresholds. In any case, it is clear that separate background corrections have to be made for individual octants.

5.3.6 Background Correction to the Elastic Peak

For a given time of flight bin t, the measured yield $Y_m(t)$ consists of the elastic yield $Y_e(t)$ and the background yield $Y_b(t)$. The measured asymmetry, $A_m(t)$, can then be expressed as a weighted average of the elastic asymmetry $A_e(t)$ and the background asymmetry $A_b(t)$ as

$$A_m(t) = (1 - f_b(t))A_e(t) + f_b(t)A_b(t)\,, \tag{5.85}$$

where $f_b(t) = \dfrac{Y_b(t)}{Y_m(t)}$ is the fraction of the background in the measured yield. The general procedure of the background correction is to determine $Y_b(t)$ and $A_b(t)$ through fits or interpolations, then the elastic asymmetry can be extracted from Eqn. 5.85.

5.3.6.1 Two-step Fits: Corrections to Detectors 1 through 14

For detectors 1 through 14, the background correction is made by using a two-step fit procedure. Since the elastic peaks in these detectors are prominent and narrow, the measured yield around the elastic peak can be fitted as a Gaussian peak on top of a polynomial background, from which one determines the background yield fraction $f_b(t)$. To fit the measured asymmetry, we assume that the elastic asymmetry is constant as a function of t, and the background asymmetry is

a polynomial function in t. Based on these, a fit of the measured asymmetry will lead to a simultaneous determination of the elastic and background asymmetries.

The results of the two-step fits to the yield and asymmetry for a typical detector are shown in Fig. 5.23. The yield fit is displayed in the left panel. The

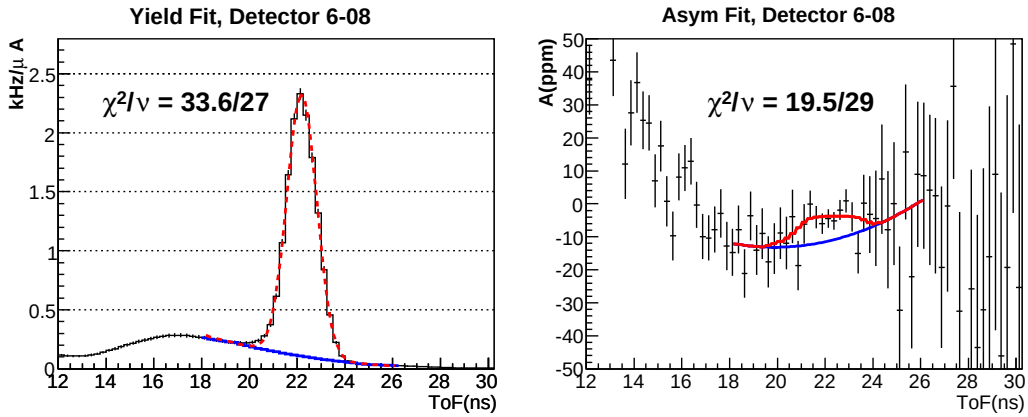

Figure 5.23: *An illustration of the two-step fits for octant 6 detector 8. In the left figure, the measured yield spectrum (black histogram) and the fit (red dashed curve) are shown. Also overlaid is the fitted background yield (binned into the blue histogram). The measured asymmetry spectrum (black data points) and the fit to it (red curve) are shown in the right figure. The blue curve is the fitted background asymmetry.*

uncertainty of the yield in each bin is dominated by systematics such as the change of detector efficiency and the timing variations. The uncertainty for the bins inside the elastic peak is assigned to be 2%, according to the $\sim$2% rate variation of the peaks in different octants. For a given time bin away from the peak, the uncertainty is assigned by scaling this 2% fractional uncertainty as if it were purely *statistical*. For example, if the yield of the elastic peak is 1.6 kHz/μA per bin, and a time bin in the inelastic region is 0.2 kHz/μA, then the fractional uncertainty of this bin is assigned as $2\% \times \frac{\sqrt{1.6}}{\sqrt{0.2}}$. In the example shown in the figure, a quadratic function is chosen for the background yield, and the fit is performed within a range of $\pm$4 ns around the elastic peak, with the resulting fit of the total yield displayed as the red curve. The χ^2 of the yield fit using this procedure is usually quite reasonable. The fraction of the background yield underneath the elastic peak, $f_b(t)$, is computed by first "binning" the fitted background function into time bins, as illustrated by the

blue histogram in the figure, then dividing the latter by the *measured* total yield, instead of the *fitted* total yield. This eliminates some model dependence of the background fraction. The measured asymmetry is then fitted with Eqn. 5.85 by taking $f_b(t)$ obtained in the first step, and the resulting fit is displayed as the red curve in the right panel of Fig. 5.23. Also overlaid is the fitted background asymmetry (blue curve), which has been chosen to be quadratic in t in this example.

In our fitting procedure, the background asymmetries of different octants are assumed to be different, based on the observations from Fig. 5.22. On the other hand, the physics dictates that all eight octants should share the same elastic asymmetry. This constraint is enforced in the asymmetry fits. One can relax this constraint and fit the elastic asymmetry separately for individual octants, and then make an average. The results of the latter method are in excellent agreement with the former.

For the two lowest French detectors (1 and 2), the evolution of the background asymmetry right after the elastic peak is not smooth, which is not observed in the corresponding NA detectors. The situation is illustrated in Fig. 5.24, from which one can see that the polynomial fits are not able to capture the rapid change of the asymmetry on the right side of the peak. The origin of this is unclear, but we shall regard this as an artifact, and simply adopt the fitted background asymmetry in these detectors.

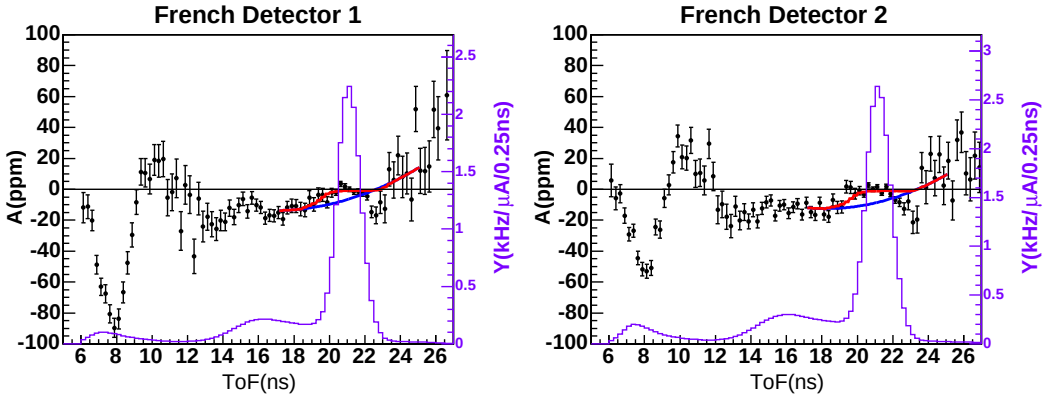

Figure 5.24: *Measured yield and asymmetry spectra in French detectors 1 and 2. The red and blue curves are the fits to the measured and background asymmetries. Notice the dips of the measured asymmetry right after the elastic peaks.*

Various orders of polynomials have been used to parameterize the background yield and asymmetry. The best parameterization for the background yield is chosen as the lowest order polynomial that gives a reasonable χ^2 of the fit. The χ^2 of the asymmetry fit, on the other hand, appears to be insensitive to the choice of the parameterization of the background asymmetry. Therefore, we compare the elastic asymmetries obtained from various polynomial models of the background asymmetry and choose the one that gives the result in the middle of the spread as the best fit. In Table 5.9, the best fit parameterizations of the yield and asymmetry are summarized for individual detectors. The values of the elastic asymmetry obtained from the best

detector	yield fit	asymmetry fit
$1-11$	Gauss + pol2, [−4,4] ns	$A_e(t)$=const, $A_b(t)$=pol2, [−4,4] ns
12	Gauss + pol2, [−4,4] ns	$A_e(t)$=const, $A_b(t)$=pol2, [−7,6] ns
13	Gauss + pol1, [−4,4] ns	$A_e(t)$=const, $A_b(t)$=pol2, [−7,6] ns
14	Gauss + pol5, [14,19] ns	$A_e(t)$=const for each of the two Q^2 bins
	Gauss + pol1, [19,27] ns	$A_b(t)$=pol3, [14,27] ns

Table 5.9: *The best fit parameterizations for the yields and asymmetries for different detectors. "polN" stands for the Nth order polynomial. The notation* $[t_1, t_2]$ *gives the range of the fit relative to the centroid of the elastic peak. For example, if the elastic peak is located at 20.8 ns,* $[-4, 4]$ *ns indicates a fit range from 16.8 to 24.8 ns.*

fits are summarized in Table 5.10. It is comforting to note that the results from an independent analysis [Gui05], by employing a simultaneous fit to both the yield and asymmetry spectra, are in good agreement with the two-step results presented in Table 5.10.

Let us reserve the notation $f_b(t)$, $A_m(t)$ and $A_b(t)$ for the background yield fraction, and the measured and the background asymmetries as a function of t, and reuse f_b, A_m and A_b to denote the *average* of these quantities within the elastic

detector	Q^2	A_m	A_e	A_b	f_b	$\sigma(A_{m,peak})$	$\sigma_{stat}(A_e)$	χ^2/ν
1	0.122	−1.29	−1.14	−2.62	0.089	0.32	0.37	158/136
2	0.128	−0.80	−0.87	−0.03	0.096	0.29	0.34	191/136
3	0.136	−1.31	−1.27	−2.06	0.106	0.30	0.35	120/136
4	0.144	−2.50	−1.99	−5.99	0.111	0.31	0.37	133/136
5	0.153	−2.21	−1.80	−5.13	0.116	0.30	0.36	151/136
6	0.164	−2.99	−2.23	−8.11	0.124	0.30	0.36	140/136
7	0.177	−3.96	−3.25	−7.89	0.124	0.29	0.35	120/136
8	0.192	−4.24	−3.47	−9.43	0.128	0.33	0.40	135/136
9	0.210	−4.72	−3.88	−10.5	0.130	0.32	0.39	142/136
10	0.232	−4.83	−4.66	−6.10	0.138	0.33	0.41	145/136
11	0.262	−4.11	−4.43	−2.61	0.144	0.33	0.41	119/136
12	0.299	−3.97	−6.35	8.18	0.151	0.37	0.47	211/228
13	0.344	−2.54	−7.52	20.02	0.179	0.41	0.54	233/228
14	0.410	−2.15	−8.83	27.61	0.186	0.41	0.55	343/368

Table 5.10: *The measured asymmetry A_m, the elastic asymmetry A_e, the background asymmetry A_b, and the background yield fraction f_b from the best two-step fits for detectors 1 through 14. The parameterizations of the yield and asymmetry fits are summarized in Table 5.9. Q^2 is the four-momentum transfer in units of $(GeV/c)^2$. $\sigma(A_{m,peak})$ is the statistical error of A_m by treating the proton peak as a single bin, and the statistical uncertainty of A_e, $\sigma_{stat}(A_e)$, is computed with Eqn. 5.92. The χ^2 per degree of freedom of the asymmetry fits are listed in the last column. All asymmetries and uncertainties are in units of ppm, and are blinded by the blinding factor ($f_{blind} \equiv 0.8056$). f_b is dimensionless.*

proton cut. The uncertainty in the elastic asymmetry is

$$\sigma^2(A_e) = \sigma^2(A_1) + \sigma^2(A_2) + \sigma^2(A_3) + \Delta\,, \tag{5.86}$$

$$\sigma(A_1) = \frac{\sigma(A_m)}{1 - f_b}\,, \tag{5.87}$$

$$\sigma(A_2) = \frac{|A_m - A_b|}{(1 - f_b)^2}\sigma(f_b)\,, \tag{5.88}$$

$$\sigma(A_3) = \frac{f_b}{1 - f_b}\sigma(A_b)\,, \tag{5.89}$$

in which $\sigma(A_i)(i = 1, 2, 3)$ arise from the uncertainties of the measured asymmetry $\sigma(A_m)$, background yield fraction $\sigma(f_b)$, and background asymmetry $\sigma(A_b)$, respectively. It is important to note that in this two-step procedure, the uncertainties of f_b

and A_b are not independent, and a change in f_b will lead to a correlated change in fitted A_b due to the strong physical constraint that $A_e(t) = \text{constant}$. This correlation is reflected in the term Δ, which can be formally expressed as [Bev92]

$$\Delta = 2\frac{\partial A_e}{\partial f_b}\frac{\partial A_e}{\partial A_b}cov(f_b, A_b) = -2\frac{f_b(A_m - A_b)}{(1-f_b)^3}cov(f_b, A_b)\,, \tag{5.90}$$

in which $cov(f_b, A_b)$ is the covariance between f_b and A_b. We shall later evaluate this term via a Monte Carlo simulation.

Let us first make some remarks about the nature of the four terms. $\sigma(A_1)$ is a purely statistical uncertainty, since it results from the measured uncertainty of A_m. The uncertainty of the background fraction, $\sigma(f_b)$, is dominated by the systematic (model) uncertainty [†] of the background yield, therefore $\sigma(A_2)$ can be regarded as a purely systematic error. For the uncertainty of the background asymmetry $\sigma(A_b)$ in Eqn. 5.89, however, both the statistical and systematic components of $\sigma(A_b)$, $\sigma_{stat}(A_b)$ and $\sigma_{sys}(A_b)$, contribute significantly. So $\sigma(A_3)$ can be decomposed into a statistical and systematic piece, $\sigma_{stat}(A_3)$ and $\sigma_{sys}(A_3)$. $\sigma_{stat}(A_b)$ arises from the counting precision of the background events underneath the elastic peak, which is related to $\sigma(A_m)$ as

$$\sigma_{stat}(A_b) = \frac{1}{\sqrt{f_b}}\sigma(A_m)\,, \tag{5.91}$$

whereas $\sigma_{sys}(A_b)$ is the uncertainty due to a specific choice of the model of the background asymmetry. Δ is an intrinsic feature of the procedure, therefore should be combined into the systematic uncertainty. Taking these all into account, $\sigma(A_e)$ can be separated into statistical and systematic components as

$$\sigma^2(A_e) = \sigma^2_{stat}(A_e) + \sigma^2_{sys}(A_e)\,, \tag{5.92}$$

$$\sigma_{stat}(A_e) = \frac{\sqrt{1+f_b}}{1-f_b}\sigma(A_m)\,, \tag{5.93}$$

$$\sigma_{sys}(A_e) = \sqrt{\sigma^2(A_2) + \sigma^2_{sys}(A_3) + \Delta}\,. \tag{5.94}$$

[†]The "systematic uncertainty" in this context refers to be the model dependent value, which may be different for each spectrum or each data point.

Guided by Eqns. 5.92, 5.93 and 5.94, different components of the uncertainties are evaluated in the following four steps.

First, the statistical uncertainty $\sigma_{stat}(A_e)$ is evaluated. A naive approach would be to take it as the uncertainty of A_e given by the asymmetry fit. However, besides the statistical precision of the measured asymmetry, the fit uncertainty also depends on the precision of the asymmetry measured in the side bands, since a functional form has been assumed for the background asymmetry in the entire fit range. One additional subtlety arises from the bin correlation effect in the French electronics, which implies that the measured uncertainty in each bin can no longer be treated as independent (see discussions at the end of Sec. 5.2.2). Due to these complications, it is difficult to interpret the uncertainty given by the fit. Instead, we start from the "proton peak uncertainty", calculated by treating the proton peak as a single bin (see Sec. 5.2.2), and use Eqn. 5.93 to compute $\sigma_{stat}(A_e)$. The values of the proton peak uncertainty and $\sigma_{stat}(A_e)$ are summarized in two columns in Table 5.10 for individual detectors.

Secondly, $\sigma(A_2)$ (the uncertainty due to the uncertainty of background yield fraction f_b) and Δ (the correlation term) are evaluated using a Monte Carlo simulation. The allowable range of the background yield is conservatively defined as a parallelogram with flat top and bottom, and two slopes starting from the mid-point of the elastic cut, as displayed in Fig. 5.25. The background yield given by various polynomial fits and the G0GEANT simulation are also overlaid in the figure. One sees that this parallelogram encloses the entire range of these models, except for the yield predicted by G0GEANT on the right side of the elastic peak, which is unphysically off. In the Monte Carlo program, large numbers of random points are generated within the parallelogram. Each point is connected to the left and right corners of the parallelogram by two straight lines, beneath which the area is used as a model of the background yield, and applied simultaneously to all eight octants of the same detector. For each copy of this background yield, the measured asymmetry is fitted with Eqn. 5.85 by assuming a quadratic background asymmetry $A_b(t)$. The distribution of f_b, A_b, and the covariance between them can then be determined,

from which one can calculate $\sigma(A_2)$ and Δ. This procedure is performed on all 14 detectors, and a strong correlation between f_b and A_b is observed in all detectors. The values of $\sigma(A_2)$ and Δ are listed in Table 5.11 for each detector. One sees that Δ is negative for all detectors (except detector 10). This observation demonstrates the stability of the two-step fit, i.e., the correlation between f_b and A_b always tries to reduce the variation of the elastic asymmetry, compared to that due to the variation of f_b alone.

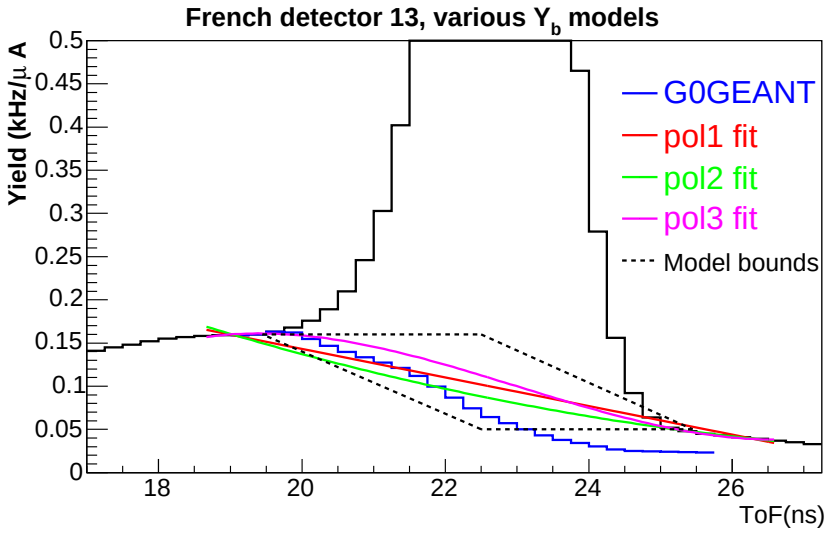

Figure 5.25: *The parallelogram boundary of the allowable background yield $Y_b(t)$ (dashed), and various models of $Y_b(t)$: [blue = G0GEANT, red = 1st order polynomial, light green = 2nd order polynomial, pink = 3rd order polynomial]. The solid black histogram with a peak is the measured yield spectrum. For the background yield, the best G0GEANT model (See Sec. 5.3.5.1) is the LB&OC model [LOC88] for detectors 1 through 6, and the Orsay model [Mor01, Arv03] for detectors above 6.*

Next, we evaluate $\sigma_{sys}(A_3)$ by making variations of the background asymmetry $A_b(t)$. In this step, the background asymmetry is assumed to be different orders of polynomial functions in t, and the ranges of the fits are also varied, while the background yield is fixed at its best fit value (see Table 5.9). The upper and lower bounds of the background asymmetry underneath the elastic peak are constructed as shown in Fig. 5.26. One side is defined as a straight line connecting the values of the background asymmetry ± 3 ns from the elastic peak given by the 2nd order

detector	$\sigma(A_2)$ (ppm)	Δ (ppm^2)
1	0.0414	-0.0011
2	0.0107	-0.0003
3	0.0327	-0.0031
4	0.1027	-0.0125
5	0.0937	-0.0130
6	0.1639	-0.0338
7	0.1524	-0.0158
8	0.1761	-0.0353
9	0.1877	-0.0348
10	0.0613	0.0054
11	0.0387	-0.0065
12	0.6704	-0.2142
13	0.8686	-0.2852
14	0.9822	-0.4792

Table 5.11: *$\sigma(A_2)$ and Δ determined from the simulation using the background yield bounded by the parallelogram in Fig. 5.25. All 8 octants averaged. See text for details.*

polynomial fit (bound 1), and the other side is a kink defined by the two lines tangential to the fit of the background asymmetry in the side bands (bound 2). Unlike the boundary of the background yield, for some detectors the polynomial fits can exceed these bounds, since the behavior of the background asymmetry in the side bands are not as well constrained as that of the yield. Nevertheless, for detectors 12 and above, where the background asymmetry exhibits a clear positive bump, bounds 1 and 2 indeed enclose the range of all polynomial fits.

$\sigma_{sys}(A_3)$ is estimated based on the distribution of the elastic asymmetries obtained via all models of the background asymmetry above (including bounds 1 and 2). For individual detectors, the half spreads of the elastic asymmetries are tabulated in the column "spread/2" in Table 5.12. Since our choices of various models of $A_b(t)$ are somewhat arbitrary, simply using the half spread as $\sigma_{sys}(A_3)$ would be too model-dependent. Therefore the distribution is remade by weighting the values of the elastic asymmetry by the χ^2 probability of the corresponding fit. For most of the detectors, the outliers (e.g., bounds 1 and 2 for higher numbered detectors)

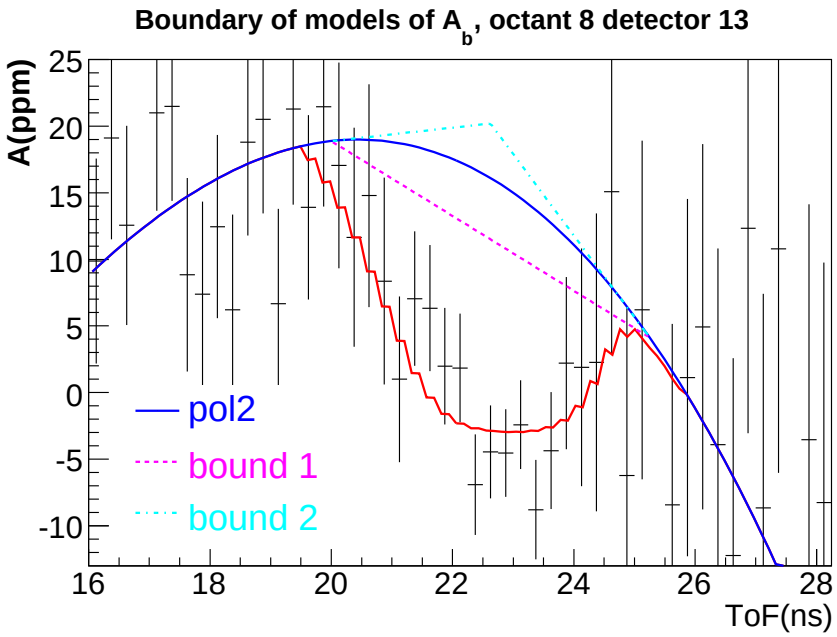

Figure 5.26: *The measured asymmetry spectrum in octant 6 detector 13 (black data points) and the fit to the data (red curve). The fitted quadratic background asymmetry is overlaid (blue curve). The boundary of the background asymmetry is defined by the pink dashed (bound 1) and light blue dot-dashed (bound 2) lines.*

are highly suppressed by their low fit probabilities. The standard deviations of the weighted distribution of the elastic asymmetries are also listed in Table 5.12, and, as expected they are always less than the unweighted half spreads. The average between the two is taken as a conservative estimate of $\sigma_{sys}(A_3)$.

According to Table 5.12, $\sigma_{sys}(A_3)$ does not vary smoothly in detectors 2 and 3, compared with the adjacent detectors 1 and 4. On the other hand, the general trend of the background asymmetry from cut2 to cut3 (see definitions in Sec. 5.2) does not look very different for these 4 detectors, except for the dips in cut3 measured in French detectors 1 and 2 (see Fig. 5.20). To help reduce the fluctuation of $\sigma_{sys}(A_3)$ due to the limited statistical precision of a single detector, the measured asymmetry spectra of these four detectors are combined. The same model variation of the background asymmetry is then made on the combined spectrum, and the resulting half spread of the elastic asymmetries among all models is ~ 0.17 ppm, comparable with the average of $\sigma_{sys}(A_3)$ for these four detectors (first four rows in Table 5.12).

Detector	spread/2 (ppm)	weighted std. dev. (ppm)	$\sigma_{sys}(A_3)$ (ppm)
1	0.23	0.16	0.20
2	0.09	0.05	0.07
3	0.12	0.06	0.09
4	0.37	0.19	0.28
5	0.31	0.22	0.27
6	0.37	0.24	0.31
7	0.25	0.17	0.21
8	0.24	0.15	0.20
9	0.30	0.16	0.24
10	0.34	0.20	0.27
11	0.17	0.09	0.13
12	0.38	0.25	0.32
13	0.77	0.33	0.55
14	0.77	0.29	0.53
$1-4$	0.17		0.17

Table 5.12: *An evaluation of $\sigma_{sys}(A_3)$ based on the distribution of the elastic asymmetries associated with various models of the background asymmetry $A_b(t)$. Column "spread/2" is the half spread between the maximum and minimum values of the elastic asymmetry among all models of the background asymmetry. The weighted standard deviation is obtained by weighting the elastic asymmetries by the χ^2 probabilities of the asymmetry fits. Column $\sigma_{sys}(A_3)$ is taken as the average of the former two. The last row gives the half spread of the elastic asymmetries when the model variation is made on the combined spectrum of detectors 1 through 4.*

This value is tabulated in the last row in Table 5.12 and is assigned as a common $\sigma_{sys}(A_3)$ shared by these four detectors.

Lastly, the systematic uncertainty of A_e, $\sigma_{sys}(A_e)$, is obtained by combining the results in Tables 5.11 and 5.12 using Eqn. 5.94, and their values are summarized later in Table 5.13. In general, the systematic uncertainty increases with detector number. The curious small value of the uncertainty for detector 11 can be understood from the fact that its background asymmetry at both sides of the elastic peak evolves linearly (see Fig. 5.20), and the fitted background asymmetry underneath the elastic peak is quite small.

$\sigma_{sys}(A_e)$ obtained above could be correlated from detector to detector, if there

is a common bias in our assumption of $Y_b(t)$ or $A_b(t)$. It is therefore desirable to evaluate the global component in the total systematic uncertainty. The evaluation is made by looking for global change of the elastic asymmetries in different detectors when the functional form of $Y_b(t)$ or $A_b(t)$ is changed globally. The detailed procedure is as follows.

For $\sigma(A_2)$, the functional form of $Y_b(t)$ is varied globally between the 1st, 2nd and 3rd order polynomials. In general, the 1st and 3rd order polynomials give the least and most negative values of A_e, respectively. The average of A_e given by the three models is used as a reference value. Then for all 14 detectors, the fractional difference between A_e from a given model and the reference value are histogrammed. In Fig. 5.27, the histograms associated with the 1st, 2nd, and 3rd order polynomial fits are displayed in gray, blue and green colors, respectively. The pink histogram

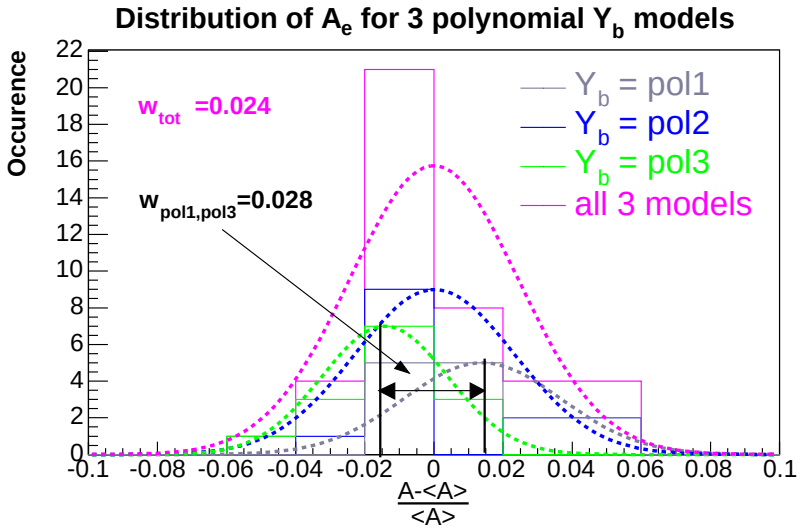

Figure 5.27: *An illustration of the procedure to evaluate the global uncertainty in $\sigma(A_2)$. The 1st, 2nd, and 3rd order polynomial models of the background yield are considered. The pink histogram is the distribution of the fractional differences of the elastic asymmetry given by any one of the three models relative to the average of the three for detectors 1 through 14, with a width w_{tot}. The individual distributions of the fractional differences for the 1st, 2nd, and 3rd order polynomial fits are displayed as the gray, blue and green histograms, respectively. The distributions associated with the 1st and 3rd order polynomial fits are separated by $w_{pol1,pol3}$.*

gives the sum of the former three, hence its width w_{tot} reflects the overall systematic uncertainty. The distributions associated with the 1st and 3rd order polynomial fits

(gray and green histograms), as expected, are separated by a gap $w_{pol1,pol3}$, which represents the global change of the elastic asymmetry if the background yield of all detectors is changed from one end to the other end in the "model space". The ratio of $\frac{1}{2}w_{pol1,pol3}$ to w_{tot} is 0.58, which is used as an estimate of the ratio of the global component of $\sigma(A_2)$ to $\sigma(A_2)$ itself.

We treated $\sigma_{sys}(A_3)$ in a similar fashion. In general, the 1st and 3rd order polynomial fits of $A_b(t)$ lead to the most and least negative values of A_e for detectors below 11, and the other way around for detectors above 11. The change at detector 11 is expected, since the background asymmetry crosses zero at this detector from negative (below detector 11) to positive (above detector 11). Let us denote A_e obtained from the 1st, 2nd, and 3rd order polynomial models of $A_b(t)$ as A_{pol1}, A_{pol2}, and A_{pol3}, respectively. A_{pol2} is chosen as the reference value, and the relative differences $\frac{|A_{pol3}-A_{pol2}|}{|A_{pol2}|}$ and $\frac{|A_{pol1}-A_{pol2}|}{|A_{pol2}|}$ are computed. Note that we have taken the absolute values of these quantities to eliminate the ambiguity of the sign change of the background asymmetry at detector 11. In Fig. 5.28, the values of $\frac{|A_{pol3}-A_{pol2}|}{|A_{pol2}|}$ are plotted against $\frac{|A_{pol1}-A_{pol2}|}{|A_{pol2}|}$ for the 14 detectors [†]. The correlation coefficient between $\frac{|A_{pol3}-A_{pol2}|}{|A_{pol2}|}$ and $\frac{|A_{pol1}-A_{pol2}|}{|A_{pol2}|}$, based on the 14 data points in the figure, is 0.45. Therefore, $0.45 \times \sigma_{sys}(A_3)$ is used as an estimate of the global uncertainty in $\sigma_{sys}(A_3)$ [Bev92].

Since the ratio of the global to overall uncertainty is ~ 0.50 for both $\sigma(A_2)$ and $\sigma_{sys}(A_3)$ [‡], we simply assign $0.5 \times \sigma_{sys}(A_e)$ as the global systematic uncertainty for all detectors, and the remaining portion as the point-point systematic uncertainty, i.e.,

$$\begin{aligned} \sigma_{sys}^{glob}(A_e) &= 0.50 \times \sigma_{sys}(A_e) \\ \sigma_{sys}^{pt-pt}(A_e) &= \sqrt{1-0.50^2}\sigma_{sys}(A_e) = 0.87 \times \sigma_{sys}(A_e) \end{aligned} \tag{5.95}$$

To summarize, the background corrected elastic asymmetry and the uncer-

[†]Detector 14 has no valid pol1 fits, so we used the value associated with bound 1 (see Fig. 5.26) instead.

[‡]The global/point-point separation of Δ has been omitted.

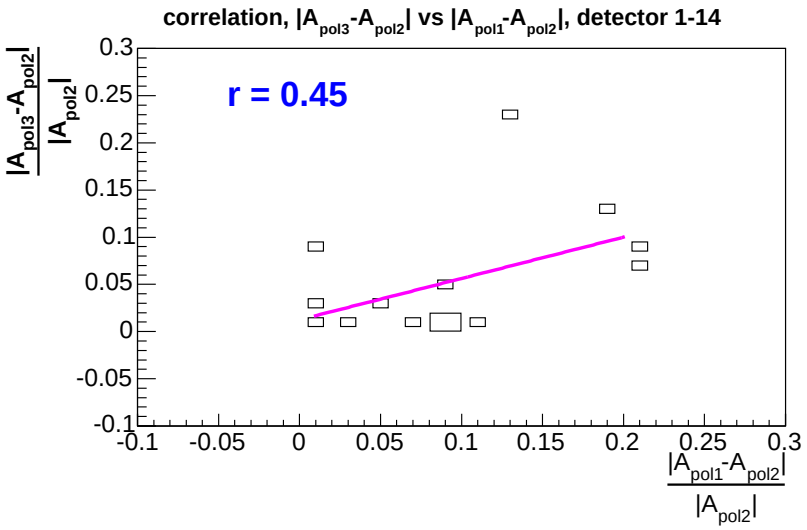

Figure 5.28: *An illustration of the procedure to estimate the global uncertainty in* $\sigma_{sys}(A_3)$. *The y (x) axis is the fractional difference (as absolute value) of the values of the elastic asymmetry between the 3rd (1st) and 2nd order polynimial fits of the background asymmetry. The correlation coefficient, r, between the y and x is taken as an estimate of the fractional global systematic uncertainty in* $\sigma_{sys}(A_3)$.

tainty budget for detectors 1 through 14 are listed in Table 5.13. For reference, the average Q^2, the measured asymmetry A_m, the background yield fraction f_b, and the background asymmetry A_b within the elastic proton cut (defined in Sec. 5.2) are also listed.

5.3.6.2 Interpolation across Detectors: Correction for Detector 15

The focus of the background correction of detector 15 is the same as all other detectors — one needs to know both the background yield and asymmetry. The difficulty arises from the fact that detector 15 has a wide ($\sim$ 6.25 ns) elastic peak due to the optics of the spectrometer discussed in Sec. 4.2.3. Therefore a simple fit to the yield or asymmetry over the time of flight by assuming some functional form of the background is difficult to justify. A well-grounded determination of the background contributions has to resort to the measurements from other detectors. In this section, we shall combine the background yields and asymmetries in detectors 12, 13, 14 and 16 to determine the corresponding values in detector 15, and subsequently to obtain

FPD	$\langle Q^2 \rangle$	A_e	σ_{stat}	σ_{sys}	σ_{sys}^{pt-pt}	σ_{sys}^{glob}	A_m	f_b	A_b
1	0.122	−1.14	0.37	0.17	0.15	0.086	−1.29(0.32)	0.089	−2.62(1.74)
2	0.128	−0.87	0.34	0.17	0.15	0.085	−0.80(0.29)	0.096	−0.03(1.60)
3	0.136	−1.27	0.35	0.16	0.14	0.082	−1.31(0.30)	0.106	−2.06(1.43)
4	0.144	−1.99	0.37	0.16	0.14	0.082	−2.50(0.31)	0.111	−5.99(1.36)
5	0.153	−1.80	0.36	0.26	0.23	0.13	−2.21(0.30)	0.116	−5.13(2.06)
6	0.164	−2.23	0.36	0.30	0.26	0.15	−2.99(0.30)	0.124	−8.11(2.19)
7	0.177	−3.25	0.35	0.23	0.20	0.11	−3.96(0.29)	0.124	−7.89(1.48)
8	0.192	−3.47	0.40	0.19	0.16	0.094	−4.24(0.33)	0.128	−9.43(1.36)
9	0.210	−3.88	0.39	0.24	0.21	0.12	−4.72(0.32)	0.130	−10.50(1.61)
10	0.232	−4.66	0.41	0.36	0.31	0.18	−4.83(0.33)	0.138	−6.10(1.69)
11	0.262	−4.32	0.41	0.11	0.094	0.055	−4.11(0.33)	0.144	−2.61(0.77)
12	0.299	−6.35	0.47	0.58	0.50	0.29	−3.97(0.37)	0.151	8.18(1.80)
13	0.344	−7.52	0.54	0.88	0.76	0.44	−2.54(0.41)	0.179	20.02(2.52)
14	0.410	−8.83	0.55	0.88	0.76	0.44	−2.15(0.41)	0.186	27.61(2.32)

Table 5.13: *A summary table of the background correction for detectors 1 through 14.* $\langle Q^2 \rangle$ *is the average four-momentum transfer in units of* $(GeV/c)^2$. A_e, σ_{stat} *and* σ_{sys} *are the elastic asymmetry and its statistical and systematic uncertainty due to the background correction. Columns* σ_{sys}^{pt-pt} *and* σ_{sys}^{glob} *represent the point-point and global components in the systematic uncertainty.* A_m, f_b, *and* A_b *are the measured asymmetry, the background yield fraction, and the background asymmetry. The values in parentheses in columns* A_m *and* A_b *are the statistical uncertainty of* A_m, *and the model uncertainty of* A_b, *respectively. The asymmetries and their uncertainties are in units of ppm, and are blinded by the blinding factor (*$f_{blind} \equiv 0.8056$*).* f_b *is dimensionless.*

the elastic asymmetry. The systematic uncertainties from this procedure will also be discussed.

Determination of the Background Yield of Detector 15

First, let us take a close look at the behavior of the *fitted* background yield in detectors 12 through 14, which have been determined in Sec. 5.3.6.1, and the pure background yields *measured* in detector 16. For a physical comparison, the time of flight spectra are shifted relative to that of detector 15, such that a constant time

of flight slice on the shifted spectra in these detectors corresponds to a continuous band in proton (p, θ) phase space, as illustrated in Fig. 5.29. The shifts required for

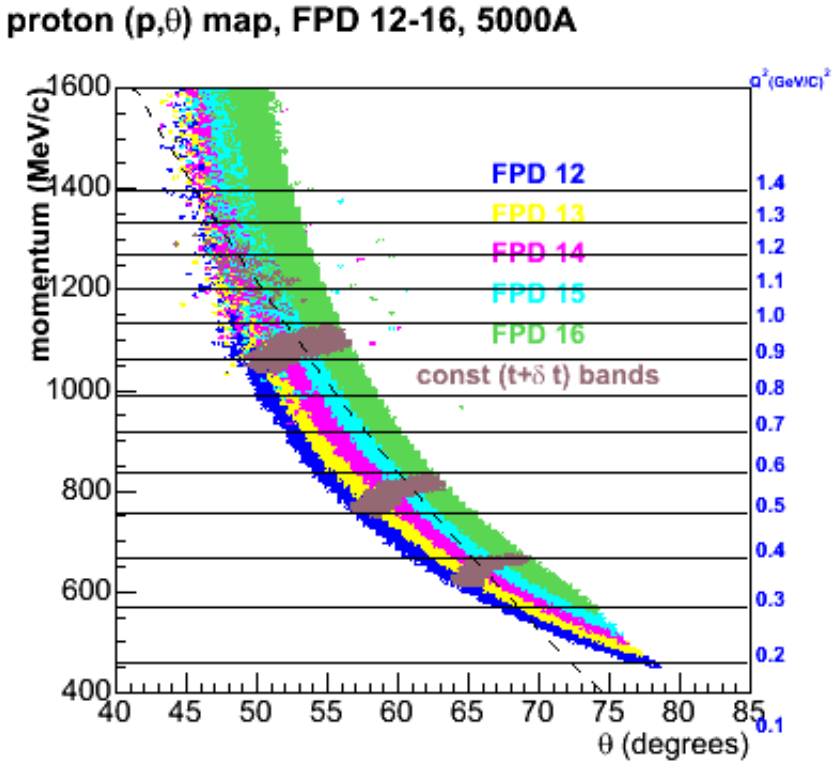

Figure 5.29: *An illustration of the constant time-of-flight bands for detectors 12 through 16 in the proton (p, θ) space, after applying the time shifts in Table 5.14. See detailed explanations of the (p, θ) map in the caption of Fig. 4.13.*

individual detectors are summarized in Table 5.14. The realigned background yield

Detector	12	13	14	15	16
Shift(ns)	1.75	1.0	0.25	0	−0.25

Table 5.14: *Required time shifts for detectors 12 through 16 so that a constant time of flight slice on the shifted spectra lie on a smooth band in (p, θ). A positive shift moves the spectrum to higher time of flight and vice versa, e.g., a +1 ns shift moves a peak previously located at 20 ns to 21 ns.*

spectra are displayed in Fig. 5.30. So far, the proton yields in these detectors do not exhibit a clear trend: the spectra for detectors 12 through 14 contain bumps, which do not exist in detector 16. Furthermore, there is a cross over between the yields in detectors 13 and 14.

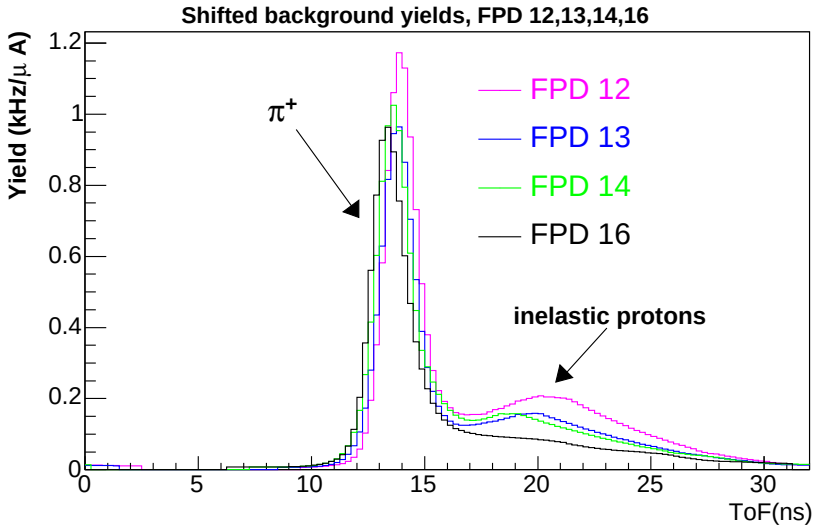

Figure 5.30: *Background yield spectra of detectors 12, 13, 14 and 16, with shifts in Table 5.14 applied. Events between 11 and 16 ns are dominated by pions, and inelastic protons dominate the region at larger ToF.*

The situation is changed drastically after one takes out the varying acceptances of these detectors. The acceptance function, $\mathcal{A}(i,t)$, is defined as the probability of a proton passing through the spectrometer and making a hit in time bin t of detector i. It can be determined via the G0GEANT simulation [G0GEA99] by generating protons isotropically at the target in momentum and solid angle, and it follows that

$$\mathcal{A}(i,t) = \frac{N(i,t)}{N_{thrown}}\,, \tag{5.96}$$

where N_{thrown} is the total number of generated protons and $N(i,t)$ is the number of hits in detector i, time of flight bin t. Then, an acceptance-corrected background yield of detector i can be computed as

$$\tilde{Y}_b(i,t) = \frac{Y_b(i,t)}{\mathcal{A}(i,t)} \times \mathcal{A}(15,t)\,, \tag{5.97}$$

in which both $Y_b(i,t)$ and $\mathcal{A}(i,t)$ have been shifted according to Table 5.14. The resulting spectra of $\tilde{Y}_b(i,t)$ are plotted in Fig. 5.31, and one observes that $\tilde{Y}_b(i,t)$ now exhibits a clear hierarchy with respective to the detector number. Furthermore, as illustrated in Fig. 5.32, $\tilde{Y}_b(i,t)$ of each time of flight bin t can be parameterized as

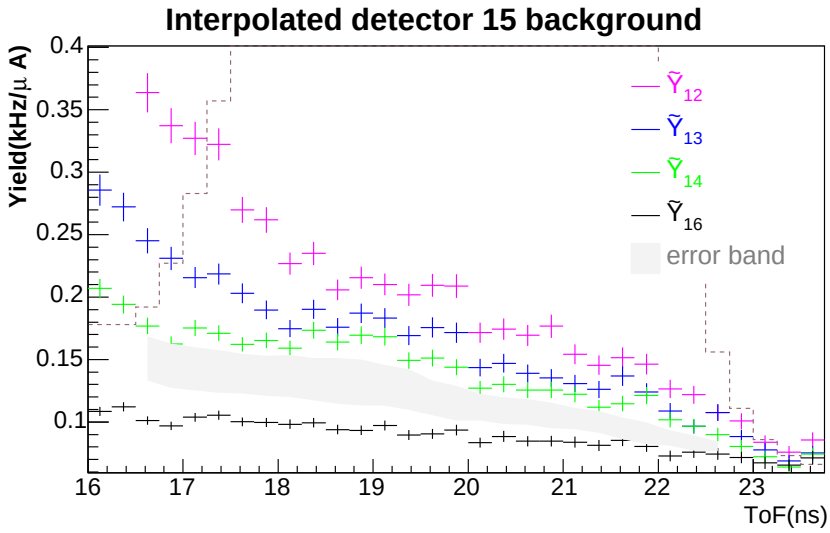

Figure 5.31: *Acceptance-corrected background yield spectra, $\tilde{Y}_b(i,t)$, for detectors 12 (pink), 13 (green), 14 (blue), and 16 (black). See text for explanations. The dashed histogram is the measured yield in detector 15. The gray band represents the systematic uncertainty of the detector 15 background yield, estimated as the half gap between $\tilde{Y}_b(14,t)$ and $\tilde{Y}_b(16,t)$.*

a linear function with respect to detector number i. Since the acceptance function of detector 15 has been multiplied in $\tilde{Y}_b(i,t)$, the linearly interpolated value of $\tilde{Y}_b(i=15,t)$ is readily taken as the background yield for detector 15.

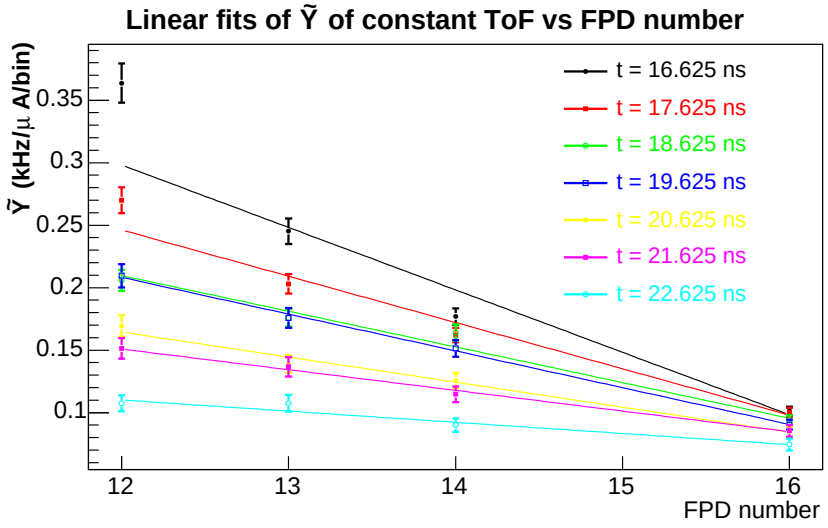

Figure 5.32: *$\tilde{Y}_b(i,t)$ for selected values of t, fitted linearly against the detector number i.*

In Fig. 5.33, the result of the above procedure is displayed in pink data points.

Also overlaid are the background yield determined from a few alternative procedures. The red data points represent a variation of the above approach, in which $Y_b(15,t)$ is determined by simply averaging the neighboring detectors, i.e.,

$$Y_b(15,t) = 0.5 \times \tilde{Y}_b(14,t) + 0.5 \times \tilde{Y}_b(16,t)\,. \tag{5.98}$$

The blue data points represent the results from an interpolation procedure in the (p,θ) space as follows. Based on the background yields in Fig. 5.30 and the detector acceptance, the differential cross section of inelastic protons is formally determined, followed by an interpolation of the resulting cross section in (p,θ) across the acceptance of detector 15. The interpolated cross section is then used as an event generator in G0GEANT to calculate the background yield in detector 15. One sees that the results from the three interpolation methods are in good agreement.

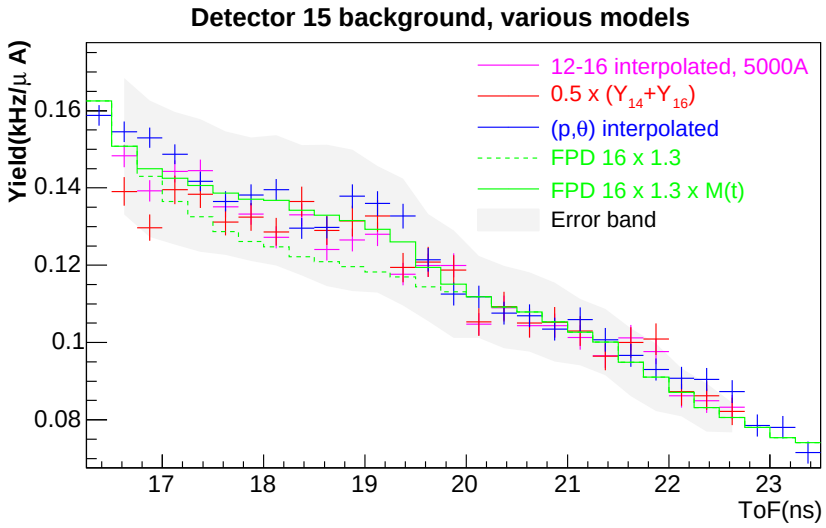

Figure 5.33: *Background yield of detector 15, determined using different approaches, and the $\pm 1\sigma$ error band. The approaches and the error band are explained in the text.*

It is desirable to find a simpler parameterization for the background yield in detector 15. As a first trial, the measured yield of detector 16 [†] is scaled by 1.3. The resulting spectrum is displayed as the green dashed histogram in Fig. 5.33. One sees that this simple parameterization captures the scale and trend of the

[†]Note this is the raw measured yield with no acceptance correction.

interpolated background, although some discrepancies exist in the time of flight range from 17 to 20 ns. The dashed green histogram is therefore corrected by an empirical multiplicative spectrum $\mathcal{M}(t)$, i.e.,

$$Y_b(15,t) = \mathcal{M}(t) \times 1.3 \times Y(16,t)\,. \tag{5.99}$$

The solid green histogram in Fig. 5.33 represents the modified spectrum, which is now in excellent agreement with the interpolated results. Due to its simplicity, Eqn. 5.99 will be used as the best model of the background yield for detector 15.

The systematic uncertainty of the background yield in detector 15 is assigned as one quarter of the difference between $\tilde{Y}_b(14,t)$ and $\tilde{Y}_b(i,t)$. Put differently, in the context of the interpolation procedure, the values of $\tilde{Y}_b(i,t)$ at $i = 14.5$ and $i = 15.5$ are taken as the upper and lower bound of $Y_b(15,t)$. The $\pm 1\sigma$ (or "± 0.5 detector") error band thus determined is displayed in Figs. 5.31 and 5.33. As can be seen in Fig. 5.33, the spread of various models is well covered by the error band. The span between the upper and lower bounds is $\pm 12\%$, $\pm 13\%$ and $\pm 9\%$ (fractional of the background yields themselves) for the three Q^2 bins (see definitions in Table 5.15), respectively.

So far the discussion has been restricted to the French electronics, for which the timing resolution is 0.25 ns per bin. The timing resolution of the NA electronics is 1 ns per bin, which makes the Q^2 separation difficult. On the other hand, the so-called hybrid data (signals from NA detectors 14 and 15 plugging into the French electronics, see Sec. 4.2.4.2) have 0.25 ns timing resolution, so they will be used in the following analysis. As with the French electronics, Eqn. 5.99 is used to determine the background yield in the NA detectors. However, the yield of the NA detector 16 is not measured by the hybrid electronics. The solution for this is to take the raw NA spectrum (1 ns-binned) for detector 16 and split it into 1/4 ns bins, by assuming linearly varying yield within each 1 ns bin. This is a very good approximation for a monotonic spectrum as that of detector 16.

For the following asymmetry analysis, the elastic peak of detector 15 is divided

into three Q^2 bins. The definition of the three Q^2 bins is summarized in Table 5.15.

$\langle Q^2 \rangle (\mathrm{GeV/c})^2$	time of flight cuts (ns)
0.788	[16.5, 18.5]
0.631	[18.5, 20.0]
0.511	[20.0, 22.75]

Table 5.15: *The definitions of the three Q^2 bins of detector 15.*

Determination of the Background and Elastic Asymmetries of Detector 15

Let us now focus on the determination of the background asymmetry. As with the background yield determination, we attempt to look for an evolution of the background asymmetry $A_b(t)$ across different detectors. $A_b(t)$ of detectors 12, 13, and 14 have been obtained through the two-step fitting procedure, with the parameterization of $A_b(t)$ shown in Table 5.9. For detector 16, the measured asymmetry is fitted by a 4th order polynomial within the range from 14 to 29 ns. For the background asymmetry beyond the fit ranges, the measured asymmetries in these detectors are taken. To improve the statistical precision, the measured asymmetries from octants 2, 6, and 8 are first combined, upon which the two-step fit is then made. Octant 4 is fitted separately since its background asymmetry appears to be very different from the rest (see Fig. 5.22). After proper timing shifts (see Table 5.14), the fitted background asymmetries of detectors 12, 13, 14 and 16 are displayed in Fig. 5.34. Once again, a progressive change of the background asymmetries in these detectors is observed.

Therefore, similar to the treatment of the background yield, a linear interpolation is made on the background asymmetries for each time bin vs. the detector number. The interpolated values with the "detector coordinate" at 15 is taken naturally as the background asymmetry. To be precise, let $A_{b,268}(i,t)$ be the interpolated background asymmetry of detector i, obtained based on two-step fits to the combined spectra of octants 2, 6, and 8, and $A_{b,4}(i,t)$ be that based on those of octant

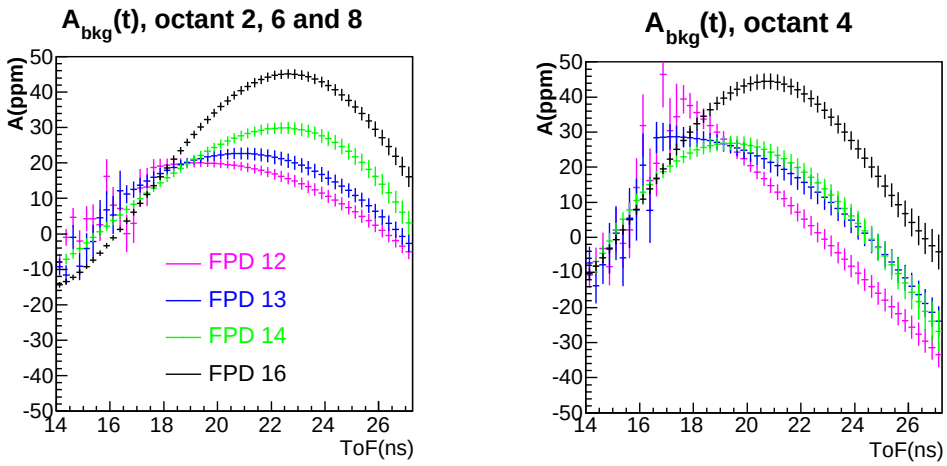

Figure 5.34: *Fitted background asymmetries of detectors 12, 13, 14 and 16. Fits are performed on the combined spectrum of octants 2, 6, and 8, and that of octant 4, separately. The error bars on the curves are the uncertainties propagated from the uncertainties of the fit parameters, so on the same curve they are highly correlated.*

4. $A_{b,268}(i = 15, t)$ is used as the best fit of the background asymmetry of detector 15 for all seven octants except octant 4. For octant 4, $A_{b,4}(i = 13, t)$ is taken as the best fit instead, since $A_{b,4}(i = 15, t)$ fails to reproduce the measured asymmetry in the pure background region above 23 ns (see Fig. 5.35). The measured asymmetries and the best fits of the background asymmetries of individual octants are displayed in Fig. 5.35. Note that for each octant, the interpolated background asymmetry is shifted by a small amount ($\sim$<1 ns) in order to optimize the agreement between the measured and interpolated asymmetries in the side bands.

The background asymmetry can also be fitted using the second step of the two-step fit procedure (Sec. 5.3.6.1), by taking the interpolated background yield determined earlier. Like before, the background asymmetry is once again modeled as a polynomial function in t, and the fit range is chosen to be from 14 to 27 ns. The best parameterization, judging from the values of the χ^2 of the fits, is a 3rd order polynomial. The fits of $A_b(t)$ for individual octants are also overlaid in Fig. 5.35 in dashed curves.

Having determined the background yield and asymmetry, the elastic asymmetry can be readily extracted. The elastic asymmetry in each Q^2 bin is assumed

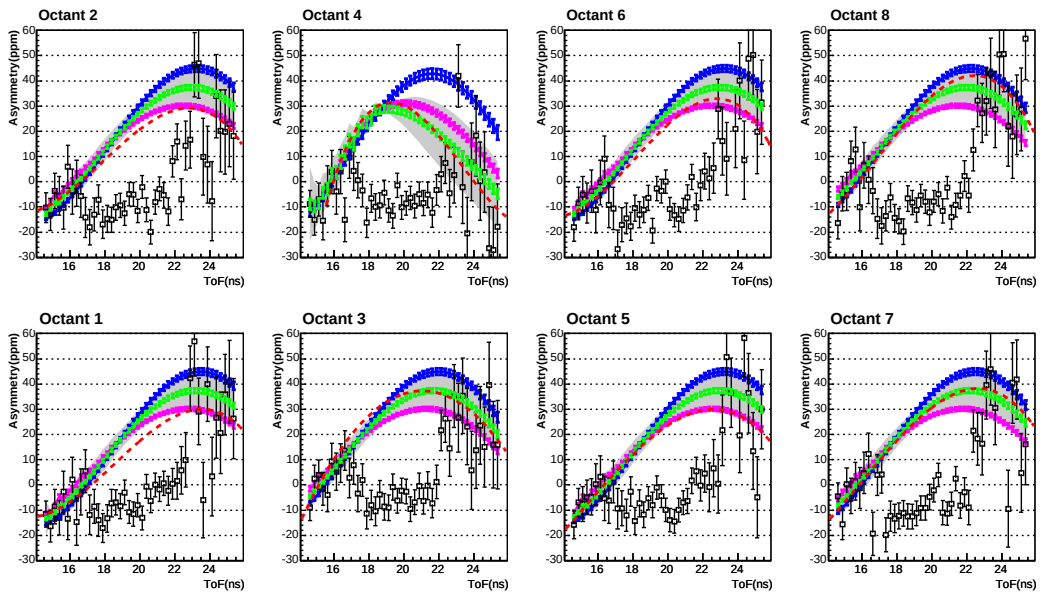

Figure 5.35: *The best fit (green curves) and the $\pm 1\sigma$ error bands (light gray bands) of the background asymmetries from the interpolation procedure for all 8 octants. The best fit of the background asymmetry is determined via the interpolation procedure: $A_{b,4}(i = 13, t)$ for octant 4, and $A_{b,268}(i = 15, t)$ for all other seven octants. See text for explanations. The black data points are the measured asymmetries. Also overlaid are the interpolated background asymmetries for detectors 14 (pink curves) and 16 (blue curves). The red dashed curves are the background asymmetry obtained from the two-step fits (by assuming a 3rd order polynomial functional form).*

to be a constant for all eight octants, and then the measured asymmetry $A_m(t)$ is fitted according to Eqn. 5.85 bin by bin, from which one obtains the three elastic asymmetries. The interpolated background asymmetries, and the fits to the measured data are displayed in Fig. 5.36 for all eight octants, and the values of the elastic asymmetries in the three Q^2 bins are summarized in Table 5.16. As a check, the same analysis is performed but by making the elastic asymmetry float for each individual octant. The averages of the resulting asymmetries over all eight octants are identical to that obtained earlier, and the statistical agreement among different octants is excellent [Liu05]. For comparison, the elastic asymmetries obtained using the two-step fit procedure are also given in Table 5.16.

To quantify the agreement between measured asymmetry data and the fit (pink curves in Fig. 5.36), the values of the reduced χ^2 of the fit were calculated within two

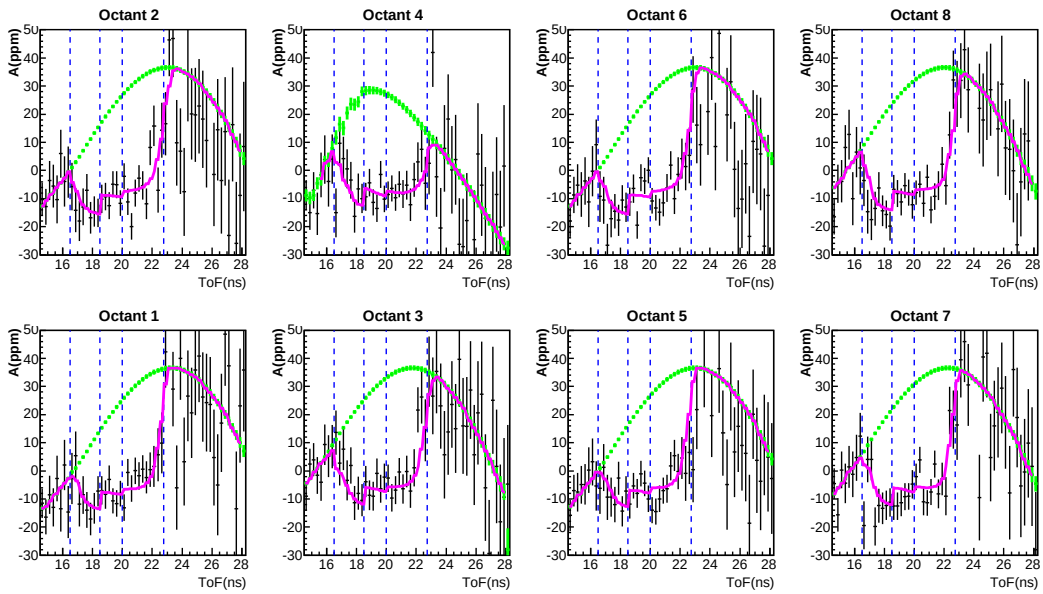

Figure 5.36: *The measured asymmetries (black data points), interpolated background asymmetries (green curves), and the fits to the data (pink curves) for individual octants of detector 15. The three Q^2 bins are separated by vertical blue dashed lines.*

Model	$A_{e,i}$ (ppm)	wide range		narrow range	
		χ^2/ν	Prob	χ^2/ν	Prob
Interpolation	-24.45, -15.87, -13.57	489.2/439	4.9%	192.5/197	57.8%
Two-step fit	-23.81, -15.34, -12.94	423.9/407	27.2%	179.9/197	80.3%

Table 5.16: *A summary of detector 15 elastic asymmetries, and the fit qualities for the interpolation and the two-step approaches. Column $A_{e,i}$ contains the elastic asymmetries of the three Q^2 bins, as defined in Table 5.15, in order of decreasing Q^2. The wide and narrow ranges correspond to [14,27] ns and [16.5,22.75] ns, respectively, and the column "Prob" gives the χ^2 probability of the fits. Asymmetries are blinded by the blinding factor (0.8056).*

ranges: a wide range ([14,27] ns), or a narrow range of the defined elastic Q^2 cuts ([16.5,22.75] ns). Since the interpolated background asymmetry is pre-determined, the only free parameters of the fit are the three elastic asymmetries, so the number of degrees of freedom ν is computed as

$$\nu = \text{number of bins} - 3\,. \tag{5.100}$$

The qualities of the fit within the two ranges are summarized in Table 5.16, and for comparison, those from the two-step procedure with a 3rd order polynomial background asymmetry are also shown in the table. One observes that in general, the quality of the fit using the interpolation method is worse than that using the two-step procedure. This is expected, since the interpolated asymmetry does not have equally sufficient flexibility as a polynomial fit to optimize the agreement between the data and the fit. On the other hand, unlike the two-step fit, the interpolation procedure employs physical constraints from other detectors, therefore the results from it are far better grounded.

The assignment of the systematic uncertainty of the background asymmetry follows a very similar procedure as that of the background yield. To be conservative, we start with a "± 1 detector" uncertainty: the interpolated asymmetries at detectors 14 and 16 are taken as the lower and upper bounds of the background asymmetry for all octants other than 4. Then, for octant 4, since the best fit is chosen as the interpolated values at detector 13, quite different compared to other octants, therefore the full width of the error band are conservatively set as the difference between the interpolated background asymmetries for detectors 12 and 15 instead. Finally, we slightly enlarge the error band such that it also covers the variation when the background asymmetry is shifted by ± 0.5 ns. The resulting $\pm 1\sigma$ error bands are overlaid with the best fit for different octants in Fig. 5.35. On average, the difference between the interpolated and the two-step fitted background asymmetries is well covered by the error band.

Systematics due to the Q^2 separation

The definition of the three Q^2 bins in Table 5.15 are somewhat arbitrary. To investigate whether there is any complication arising from this specific choice of the division of the time of flight spectrum, we systematically divide the whole elastic peak into 1, 2, 3, 4, and 5 bins according to Table 5.17, and repeat the background correction procedure discussed above.

The elastic asymmetries obtained via different sets of Q^2 binnings are shown

Q^2 bin	ToF cuts (ns)	$\langle Q^2 \rangle$
15.0	[16.5, 22.75]	0.60
15.1	[16.5, 19.75]	0.70
15.2	[19.75, 22.75]	0.515
15.1	[16.5,18.5]	0.788
15.2	[18.5,20.0]	0.631
15.3	[20.0,22.75]	0.511
15.1	[16.5,18.0]	0.817
15.2	[18.0,19.5]	0.675
15.3	[19.5,21.0]	0.546
15.4	[21.0,22.75]	0.480
15.1	[16.5,17.75]	0.834
15.2	[17.75,19.0]	0.717
15.3	[19.0,20.25]	0.593
15.4	[20.25,21.5]	0.510
15.5	[21.5,22.75]	0.469

Table 5.17: *Various sets of Q^2 binning for detector 15. $\langle Q^2 \rangle$ is the average four-momentum transfer of the elastic events in a given cut, in units of $(GeV/c)^2$.*

in Fig. 5.37. Linear fits are made to individual sets of elastic asymmetries against the values of Q^2, which are also overlaid in Fig. 5.37. Summarized in Table 5.18 are the qualities of the fits to the measured data associated with different sets of Q^2 binnings, and the corresponding slopes and offsets of the linear fits in Fig. 5.37. Clearly the fits with only one and two Q^2 bins are much less favored; they simply do not have sufficient resolution to reflect the variation of the elastic asymmetry. On the other hand, the fit qualities (to the measured data) are comparable for the three, four and five Q^2 bins, and the behavior of the resulting elastic asymmetries are in excellent agreement. This shows that the elastic asymmetries obtained with our definition of Q^2 bins in Table 5.15 correctly capture the underlying variation of the elastic asymmetry vs. Q^2.

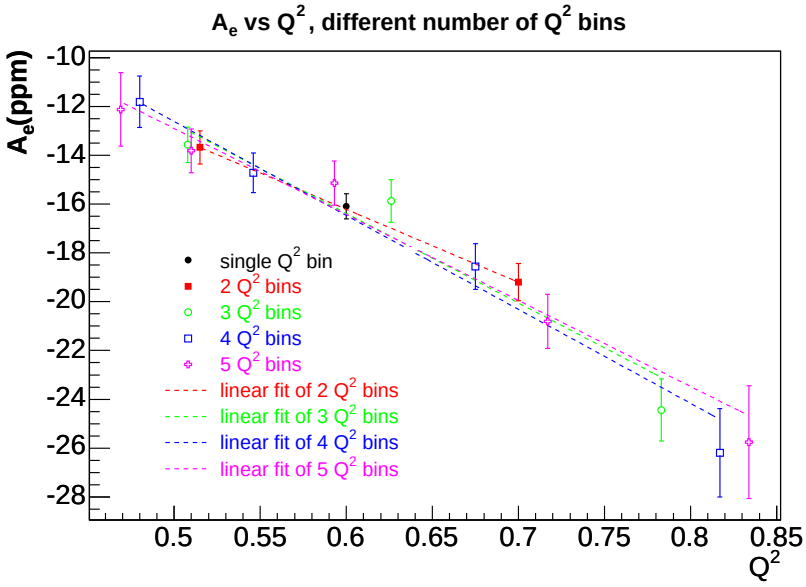

Figure 5.37: *The elastic asymmetries obtained from the interpolation method, with different sets of Q^2 binnings, plotted against the values of Q^2 with linear fits. See Table 5.17 for definitions of the Q^2 bins. Asymmetries are blinded by the blinding factor (0.8056).*

# of Q^2	χ^2/ν	Probability	$A_e(Q^2 = 0.6)$	$\frac{dA}{dQ^2}$
1	248/199	1.0%	−16.09(0.51)	n/a
2	219/198	14.6%	−16.22(0.51)	−29.84(5.55)
3	192/197	58.7%	−16.38(0.51)	−36.74(5.15)
4	191/196	58.7%	−16.47(0.51)	−38.50(5.14)
5	198/195	42.7%	−16.42(0.51)	−35.25(5.09)

Table 5.18: *Results of detector 15 elastic asymmetries associated with various sets of Q^2 binnings. The χ^2/ν represents the χ^2 per degree of freedom of the fit to the measured asymmetry (see the pink curves in Fig. 5.36), computed within the range from 16.5 to 22.75 ns. The corresponding χ^2 probabilities are summarized in the next column. The offsets and the slopes of the linear fits to the elastic asymmetries against Q^2 are listed in the last two columns. Asymmetries are in units of ppm, and are blinded by the blinding factor (0.8056).*

Systematic Uncertainty of the Elastic Asymmetries

As with that of detectors 1 through 14, the systematic uncertainty of the elastic asymmetry of detector 15 has two sources, the systematic uncertainties due to the background yield ($\sigma(A_2)$) and asymmetry ($\sigma_{sys}(A_3)$) (see Eqn. 5.94). But

unlike the two-step fit procedure, here the determination of the background yield and asymmetry are *independent* of each other, therefore f_b and A_b are completely decoupled and the correlation term Δ in Eqn. 5.94 is no longer present.

In principle, the uncertainty of the elastic asymmetry can be determined by employing error propagation as in Eqns. 5.88 and 5.89, or by evaluating the spread of elastic asymmetries when setting background yield and asymmetry at the upper and lower bounds (Figs. 5.33 and 5.36). Here, instead of the above two methods, a simple Monte Carlo simulation is used to allow more sophisticated model variations. In the simulation, the background yield is varied within the upper and lower bounds with a random scaling variable common to all 8 octants. To mimic the possible misalignment of the background yield spectrum relative to the measured spectrum, a random timing jitter is introduced with a variance of 0.5 ns octant by octant. The background asymmetry is also varied with a random scaling variable within the error bands. However, since the background asymmetry of octant 4 is sufficiently different from the others, an independent scaling variable is used for octant 4. The standard deviation of the distributions of the resulting elastic asymmetries give the overall systematic uncertainties, and they are summarized in Table 5.19.

$\langle Q^2 \rangle$ (GeV/c)^2	$\sigma(A_2)$ (ppm)	$\sigma_{sys}(A_3)$ (ppm)
0.788	1.79	2.30
0.631	0.88	1.15
0.511	0.87	1.44

Table 5.19: *The Monte Carlo (see text) results of the overall systematic uncertainties of the elastic asymmetries for the three Q^2 bins in detector 15 due to the uncertainties of the background yield and asymmetry. Uncertainties are blinded by the blinding factor (0.8056).*

The uncertainties of the three Q^2 bins from the above procedure are nearly 100% correlated, since the systematic variation of the background yields and asymmetries in the three bins are almost fully dictated by a single degree of freedom (a scaling variable). It is desirable to introduce more realistic variations beyond scaling and separate the point-point and global uncertainties. Let us consider the

background asymmetry first. A reasonable variation should lie (statistically) within the prescribed error band, be continuous in t, and have a negative curvature (positive bump) within the fit range. Guided by these, a quadratic background asymmetry function with varying curvature and end-points is chosen, which contains three degrees of freedom, apparently more versatile than a scaling variation. The Monte Carlo simulation is thus modified to choose the values of the background asymmetry randomly at the end-points (16.5 and 22.75 ns) according to the width of the error band. The curvature of the quadratic function is chosen randomly within $[-2., -1.5]$ ppm/ns^2 for octant 4, and $[-1, -0.5]$ ppm/ns^2 for the others [†]. For demonstration purposes, 20 copies of background asymmetries with such variation are plotted in Fig. 5.38. The correlation coefficients between the elastic asymmetry in each individual Q^2 bin and the average of the other two are computed. These coefficients are found to be $\sim$0.7, with the value for the middle Q^2 bin higher than that for the two bins on either side [‡] . This suggests an *equal division* of the point-point and the global systematic uncertainties (in quadrature) for $\sigma_{sys}(A_3)$.

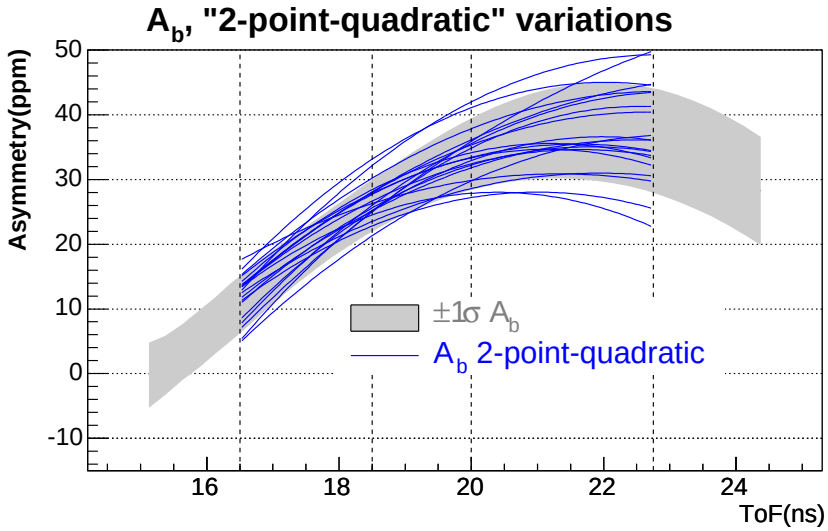

Figure 5.38: *An illustration of 20 copies of $A_b(t)$ generated by a quadratic model with varying end points and curvature for octant 5 of detector 15.*

A similar treatment is applied to the background yield. As a modification to

[†]The range of the curvature is determined empirically by the magnitude of the curvature of the background asymmetry from the two-step fits.

[‡]This is expected since the middle Q^2 bin is in direct contact with the other two.

the global scaling variation, the values of $Y_b(t)$ at the boundaries of each Q^2 bin, i.e. 16.5, 18.5, 20.0, and 22.75 ns, are chosen randomly based on the width of the error band, and then connected with straight lines. The same variation is applied to all 8 octants [§]. The resulting correlation coefficients of the elastic asymmetries among various bins appear to be ~0.5, less than those for the background asymmetry. Nevertheless, to be conservative, an *equal division* of the point-point and global systematic uncertainties of $\sigma(A_2)$ is again adopted.

The separation of the global and point-point uncertainties discussed above is fairly model dependent and the allowable variations for both $A_b(t)$ and $Y_b(t)$ are certainly not unique. However, one expects that the systematic uncertainties of detector 15 are more globally correlated than those of detectors 1 through 14, not only because the three Q^2 bins come from the same time of flight spectrum, but also due to the fact that the interpolation procedure relies on the fits of other detectors. In this regard, the equal division of the global and point-point systematic uncertainty in quadrature for detector 15 is quite reasonable as compared with the 0.50 global fraction being assigned to lower detectors (see Eqn. 5.95).

Results

The elastic asymmetries of the three Q^2 bins of detector 15 and their uncertainty budgets are summarized in Table 5.20. For reference, the average measured asymmetry A_m, the background yield fraction f_b, and the background asymmetry A_b within each Q^2 bin are also tabulated. Similar to the treatment of the statistical uncertainty of detectors 1 through 14 (Eqn. 5.93), to avoid the bin correlation effect (Sec. 5.2), the statistical uncertainty of the elastic asymmetry is determined by treating each Q^2 bin as a single time bin, then correcting for the background dilution, deadtime, and the beam polarization using

$$\sigma_{stat}(A_e) = \frac{f_{blind}}{f_{pol}\sqrt{N_{tot}}} \frac{\sqrt{1+f_b}}{1-f_b} \sqrt{1+f_{dead}}\,. \tag{5.101}$$

[§]Note this is different from the variation of background asymmetry, in which octant 4 is varied separately from the others.

In this expression, $f_{pol} \simeq 0.737$ is the average polarization of the beam, N_{tot} and f_b are the total number of protons and the background yield fraction within each Q^2 bin, and f_{dead} is the deadtime loss factor measured by the asymmetry slope (see Eqn. 5.44 and Table 5.3). The factor $\sqrt{1+f_{dead}}$ arises from the loss of the statistical precision due to the existence of the deadtime (see the discussions which leads to Eqn. 5.10). Note that Eqn. 5.101 is slightly different from the treatment for detectors 1 through 14 in Sec. 5.3.6.1, where the "proton peak uncertainty" was taken in Eqn. 5.93 to calculated $\sigma(A_{stat})$. Here we use the (deadtime modified) counting statistics relation to calculate the expected statistical precision of the measured asymmetry in a given Q^2 bin, since the "Q^2 bin asymmetry" (by grouping all time bins in a given Q^2 cut as a single bin) was not implemented in the replay engine. Nevertheless, as shown in Fig. 5.4, this counting statistics estimate is a good approximation. Note also that we have blinded $\sigma_{stat}(A_e)$ by $f_{blind} \equiv 0.8056$ here, just so that it is consistent with other blinded values in the table. The overall systematic uncertainty $\sigma_{sys}(A_e)$ is obtained by combining the values of $\sigma(A_2)$ and $\sigma_{sys}(A_3)$ in Table 5.19. The point-point and global systematic uncertainties $\sigma_{sys}^{pt-pt}(A_e)$ and $\sigma_{sys}^{glob}(A_e)$ are obtained by equally dividing $\sigma_{sys}(A_e)$ in quadrature. For a quick comparison with the theory, the values of the non-vector-strange asymmetry A_{NVS} (multiplied by the blinding factor 0.8056), are listed in the last column. The detailed calculation of A_{NVS} will be presented in Sec. 6.1.

Discussion

To help digest the results in Table 5.20, we shall seek to address the question: "To what degree do our data differ from the non-vector-strange asymmetries?".

Let us first consider the statistical compatibility. According to Table 5.20, the difference between our best fit values of A_e and the non-vector-strange asymmetries A_{NVS} is statistically significant. Another way of demonstrating this is to compare the qualities of the fits to the measured data, when setting the elastic asymmetries at their best fit values, or fixing them at the non-vector-strange values. In both cases, the interpolated background asymmetries are used. The values of the χ^2

$\langle Q^2 \rangle$	A_e	$\sigma_{stat}(A_e$	$\sigma_{sys}(A_e)$	σ_{sys}^{pt-pt}	σ_{sys}^{glob}	A_m	f_b	A_b	A_{NVS}
0.788	−24.45	1.49	2.91	2.06	2.06	−10.20(0.76)	0.399	12.61(4.70)	−28.01
0.631	−15.87	0.89	1.45	1.02	1.02	−7.85(0.65)	0.197	25.41(4.81)	−19.95
0.511	−13.57	0.72	1.68	1.19	1.19	−4.67(0.53)	0.191	32.92(6.57)	−14.43

Table 5.20: *The elastic asymmetries and their uncertainty budgets for the three Q^2 bins of detector 15. $\langle Q^2 \rangle$ is the average four-momentum transfer in $(GeV/c)^2$. A_e, $\sigma_{stat}(A_e)$ and $\sigma_{sys}(A_e)$ are the elastic asymmetry and its statistical and systematic uncertainties. The columns σ_{sys}^{pt-pt} and σ_{sys}^{glob} represent the point-point and global components in the systematic uncertainty. A_m, f_b, A_b and A_{NVS} are the measured asymmetry, the background yield fraction, the background asymmetry, and the "non-vector-strange" elastic asymmetry. The values in parentheses in columns A_m and A_b are the statistical uncertainty of A_m, and the model uncertainty of A_b, respectively. All asymmetries and their uncertainties are in units of ppm, and are blinded by the blinding factor ($f_{blind} \equiv 0.8056$). f_b is dimensionless.*

between the fits and the data are computed within the range from 16.5 to 22.75 ns. The best fit gives a χ^2 of 192.5 with 197 degrees of freedom, as have already been shown in Table 5.16. The non-vector-strange "fit", on the other hand, increases the χ^2 by 31.3 from the best fit, corresponding to a likelihood (in the space of three elastic asymmetries) of $\sim 10^{-6}$ relative to the best fit. Therefore, in the absence of systematic uncertainties, the non-vector-strange asymmetries would be highly disfavored.

One further notices from Table 5.20 that even with the systematic uncertainties taken into account, the non-vector-strange asymmetries still differ from the elastic asymmetries beyond the 1σ level. One might be concerned about the possibility that our treatment of background asymmetry was biased, and as a result, A_{NVS} could not be corroborated. *This concern can only be addressed in the context of the best knowledge we have on the background asymmetry.* The background asymmetry in detector 15 is not only constrained by what is measured in its side bands, but also more strictly constrained by the progressive (linear) change of the background asymmetries along the "detector coordinate" in detectors 12 up to 16. In this regard, taking the best fit as the values of the interpolation with the "detector coordinate" at 15 is an unbiased choice, and the "± 1 detector" error band (see Fig. 5.35) is a

natural, if conservative, assignment.

For demonstration purposes, the average background asymmetry in each Q^2 bin is recalculated by setting the corresponding elastic asymmetry at A_{NVS}. The results are shown as the pink data points in Fig. 5.39 octant by octant. Also overlaid in the figure are the ± 1 detector error bands of the background asymmetry. As one can see, although there exists fluctuations from octant to octant, in general the recalculated non-vector-strange background asymmetries lie outside the error band, particularly at the middle Q^2 bin. This visually demonstrates that the non-vector-strange asymmetry is much less favored by our data.

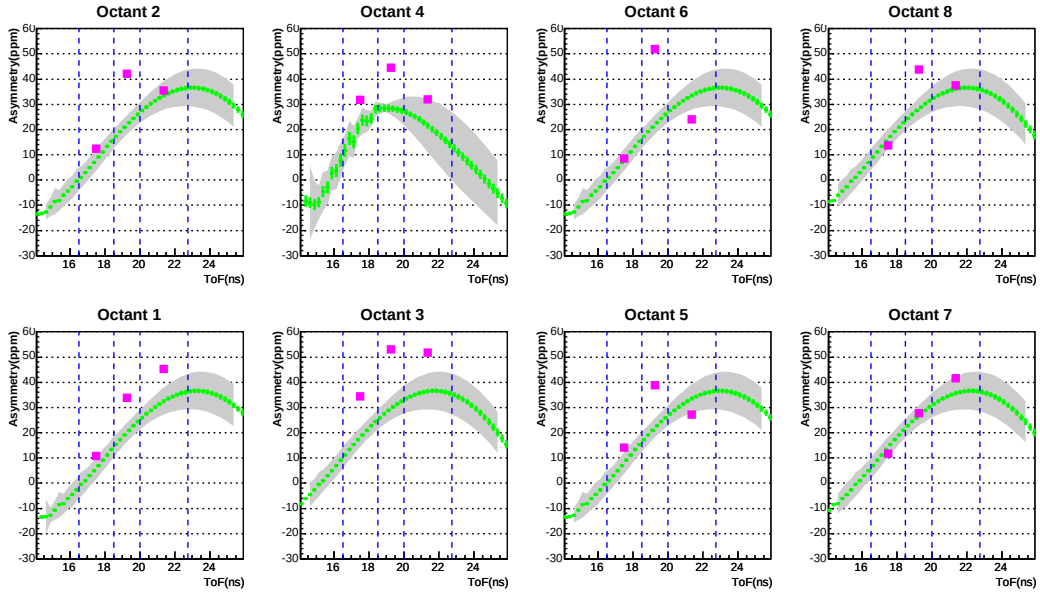

Figure 5.39: *The interpolated background asymmetry (green curve), its* ± 1 *detector error band (light gray band), and the required background asymmetry when demanding* $A_e = A_{NVS}$ *(pink data points). The time of flight ranges of the three* Q^2 *bins are indicated by the blue dashed lines. All asymmetries are blinded by* $f_{blind} \equiv 0.8056$.

To summarize, we have discussed the background correction for detector 15. Both the background yield and asymmetry are evaluated using an interpolation across detectors 12, 13, 14 and 16. The elastic peak is divided into three Q^2 bins, and the elastic asymmetry in each bin is extracted. Based on the interpolation procedure, the systematic uncertainty of the background yield is assigned as "± 0.5 detector", and the that of the background asymmetry is estimated conservatively as

"±1 detector". The elastic asymmetries appear to be different from the non-vector-strange values by more than 1σ.

5.3.6.3 Special Treatment: the High Q^2 Bin of Detector 14

As a consequence of the optics of the spectrometer (see Sec. 4.2.3), detector 14 has two elastic peaks: the main peak with Q^2 =0.41 (GeV/c)^2, and a secondary one located at earlier time of flight with an average four-momentum transfer of 1.0 (GeV/c)^2. The situation for the high Q^2 point is similar to that of detector 15: the NA electronics do not have enough resolution. Therefore the French and hybrid data will be used in the analysis. The result of the main elastic peak has been presented in Sec. 5.3.6.1. Let us now take a closer look at the second elastic peak. The yield spectrum of detector 14 is displayed in Fig. 5.40. The main and the secondary peaks are located at 16.5 and 22 ns, respectively. As summarized in Table 5.9, the fit of the yield is broken down into two ranges — the tail of the pion and the second elastic peak (from 14 to 19 ns) is parameterized with a 5th order polynomial background plus a Gaussian peak, and the main elastic peak (from 19 to 27 ns) is fitted with a Gaussian distribution plus a linear background. The fitted elastic yield in the second peak is only 54% of that predicted from the G0GEANT simulation, or alternatively, (G0GEANT-Fit)/Fit = 84%. Since the elastic events in this peak are at the very edge of the acceptance, the discrepancy could be due to the difference between the geometry in the Monte Carlo and the true physical setup. We shall treat the systematic uncertainty due to this difference later. The fit of the asymmetry is made by assuming that the elastic asymmetry A_e in each Q^2 bin is a constant, and the background asymmetry $A_b(t)$ within the entire range between 14 and 27 ns is a polynomial function. The asymmetry fit of octant 7, with a 3rd order polynomial background asymmetry, is plotted in Fig. 5.41. Table 5.21 summarizes the values of the two elastic asymmetries and the fit qualities when using various orders of polynomials for $A_b(t)$. The fit quality is not very sensitive to the choice of the polynomial model for $A_b(t)$. Therefore for the second elastic peak, instead of choosing a best fit, we take a straight average of the elastic asymmetries obtained

from the fits with $A_b(t)$ being the 2nd, 3rd, 4th and 5th order polynomials. The result is

$$A_e = -30.56 \text{ ppm}\,, \tag{5.102}$$

which is still blinded by $f_{blind} \equiv 0.8056$.

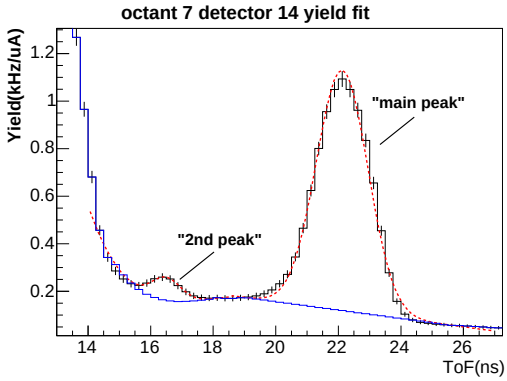

Figure 5.40: *The yield spectrum of octant 7 detector 14. The fit is performed in two ranges: a Gaussian peak with a 5th order polynomial background from 14 to 19 ns, and a Gaussian peak with a linear background from 19 to 27 ns. The red curve is the fit to the total measured yield and the blue histogram is the fitted and then binned background yield distribution.*

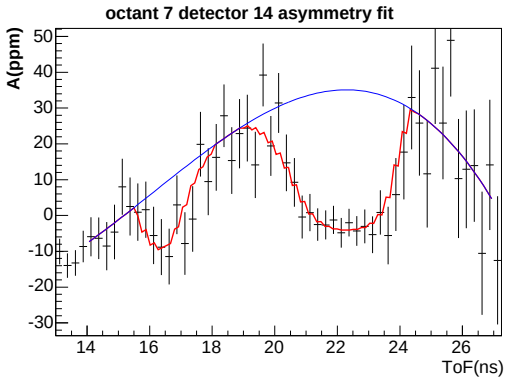

Figure 5.41: *The asymmetry spectrum of octant 7 detector 14. The elastic asymmetry in each Q^2 peak is assumed to be a constant. The background asymmetry is assumed to be a 3rd order polynomial within the entire range from 14 to 27 ns. The red and blue curves are the fits to the measured and background asymmetries, respectively.*

$A_b(t)$ (ppm)	$A_{e,main}$ (ppm)	$A_{e,2nd}$ (ppm)	χ^2/ν	probability
pol2	-8.82	-32.80	352.4/376	81%
pol3	-8.83	-32.36	343.3/368	82%
pol4	-8.86	-29.69	333.8/360	83%
pol5	-9.00	-27.38	331.1/352	78%

Table 5.21: *The corrected asymmetries of the two elastic peaks of detector 14, $A_{e,main}$ and $A_{e,2nd}$, obtained from the two-step fits using various polynomial models of the background asymmetry $A_b(t)$. The values of the χ^2 per degree of freedom of the fits and their probabilities for different models are also tabulated. The asymmetries are blinded by $f_{blind} \equiv 0.8056$.*

As with all other Q^2 bins, the statistical uncertainty of the elastic asymmetry

for the second peak is evaluated based on counting statistics using Eqn. 5.101, with the background dilution, deadtime and the beam polarization taken into account. Within a ± 2 σ window around the elastic peak, the background yield fraction f_b is $\sim 78\%$, and the deadtime fraction f_{dead} is $\sim 20\%$ based on the asymmetry slope (see Sec. 5.3.1.3). These lead to

$$\sigma_{stat}(A_e) = 5.83 \text{ ppm}, \tag{5.103}$$

which is blinded by the blinding factor (0.8056).

The evaluation of the systematic uncertainties of the second elastic peak is a combination of the procedures described in Sections. 5.3.6.1 and 5.3.6.2. The systematic uncertainty due to the uncertainty of f_b, $\sigma(A_2)$, and the correlation term Δ, are evaluated with the Monte Carlo described in Sec. 5.3.6.1. The uncertainty of the background yield fraction is estimated as follows. The octant to octant variation of the fitted elastic yield Y_e is $\sim$12%, which can be used as an estimate of the (fractional) uncertainty of Y_e. On the other hand, as mentioned earlier, Y_e predicted from the G0GEANT simulation is higher than the fitted value by $\sim 84\%$, so $\sim$ 42% is another reasonable estimate of the uncertainty of Y_e. An average of these two estimates, 27%, is therefore taken as the fractional uncertainty of Y_e, which leads to $f_b = 78 \pm 6\%$. Therefore, in the Monte Carlo, f_b is varied from the best fit with a single random scaling variable within $\pm 6\%$ (statistically), from which σA_2 and Δ in Eqns. 5.88 and 5.90 can be evaluated. The result (blinded by the factor of 0.8056) from this procedure is

$$\sqrt{\sigma^2(A_2) + \Delta} = 5.72 \text{ ppm}. \tag{5.104}$$

For the model uncertainty due to the background asymmetry, $\sigma_{stat}(A_3)$, instead of using the spread among various polynomial fits, on a trial basis we conservatively use the "± 1 detector" uncertainty, similar to the procedure for detector 15 in Sec. 5.3.6.2. The "± 1 detector" error band gets further modified by a ± 0.5 ns timing jitter. The background asymmetries and their error bands for the eight oc-

tants are drawn in Fig. 5.42. In this figure, the error bands of octants 1 and 3 are centered at the interpolated asymmetry of detector 16 in order to better reproduce the measured data in the side bands. The uncertainty of the elastic asymmetry is evaluated by setting the background asymmetry at the lower and upper bound (simultaneously for all eight octants). The resulting model uncertainties of the background asymmetry ($\sigma_{sys}(A_b)$), and $\sigma_{sys}(A_3)$ of the two Q^2 peaks are tabulated in Table 5.22.

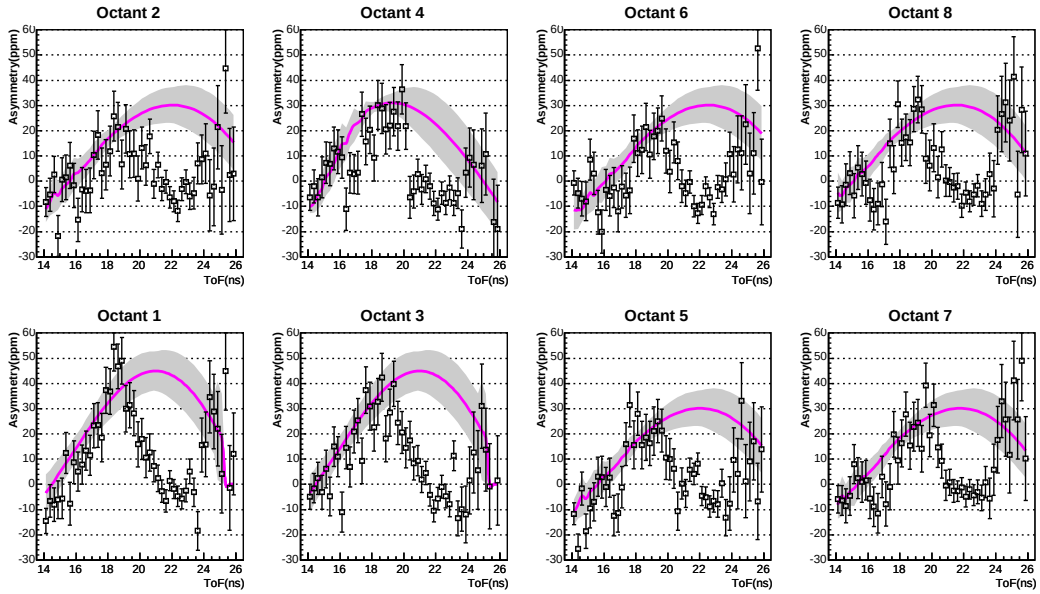

Figure 5.42: *An illustration of a preliminary estimate of the systematic uncertainty of the background asymmetry for detector 14 using the "±1 detector" procedure. The pink curve is the best fit and the gray band is the "±1 detector" error band.*

Q^2 (GeV/c)^2	$\sigma_{sys}(A_b)$ (ppm)	$\sigma_{sys}(A_3)$ (ppm)
0.41	8.21	1.53
1.0	5.21	13.49

Table 5.22: *A preliminary estimate of the systematic uncertainty of the background asymmetry $\sigma_{sys}(A_b)$, and the resulting uncertainty of the elastic asymmetry $\sigma_{sys}(A_3)$ using the "±1 detector" method. The uncertainties are blinded by the blinding factor (0.8056).*

In reality, the background asymmetry in detector 14 is more constrained than that of detector 15, since both elastic peaks are narrow and the background asym-

metries in the side bands of both peaks are directly measured. Compared with $\sigma_{sys}(A_3)$ of the main peak of detector 14 in Table 5.12, it appears that the corresponding value in Table 5.22 over-estimates the uncertainty by roughly a factor of 3, implying that the error band in Fig. 5.42 over-estimate the uncertainty of the background asymmetry by a factor of 3. Therefore, for the the second elastic peak, we scale down the uncertainties in Table 5.22 as

$$\sigma_{sys}(A_b) = \frac{1}{3}5.21 = 1.74 \text{ ppm}\,, \quad \sigma_{\rm sys}({\rm A}_3) = \frac{1}{3}13.49 = 4.50 \text{ ppm}\,. \tag{5.105}$$

So the total systematic uncertainty, combining Eqns. 5.104 and 5.105 is

$$\sigma_{sys}(A_e) = \sqrt{\sigma^2(A_2) + \Delta + \sigma^2_{sys}(A_3)} = 7.28 \text{ ppm}\,. \tag{5.106}$$

One expects that this systematic uncertainty is unlikely to be correlated with those of other Q^2 bins, primarily because this secondary elastic peak is located at the pion tail, which is not within the fit range for any other detector. Moreover, the values in Table 5.21 suggest that the values of the elastic asymmetries of the two peaks of detector 14 are not strongly coupled either, despite the fact that the fit to the background asymmetry is a continuous function across the entire range. Therefore, the systematic uncertainty obtained in Eqn. 5.106 is regarded as a 100% point-point systematic uncertainty.

To summarize this analysis, the results of the second Q^2 peak of detector 14 is listed in Table 5.23. The arrangement of the columns is identical to that in Table 5.13 for detectors 1 through 14. The measured asymmetry A_m, the background yield fraction f_b, and background asymmetry A_b are all computed within a $\pm 2\sigma$ window around the second elastic peak.

5.3.7 Determination of the Four-momentum Transfer

The determination of the mean and the uncertainty of the four-momentum transfer (Q^2) of elastic protons in each Q^2 bin will be presented in this section.

$\langle Q^2 \rangle$	A_e	$\sigma_{stat}(A_e)$	$\sigma_{sys}(A_e)$	σ_{sys}^{pt-pt}	σ_{sys}^{glob}	A_m	f_b	A_b
0.997	-30.56	5.83	7.28	7.28	0	3.39(0.96)	0.780	13.59(1.74)

Table 5.23: *The elastic asymmetry and its uncertainty budget of the 2nd Q^2 bin of detector 14. $\langle Q^2 \rangle$ is the average four-momentum transfer of the peak in $(GeV/c)^2$. A_e, $\sigma_{stat}(A_e)$ and $\sigma_{sys}(A_e)$ are background corrected elastic asymmetry and its statistical and systematic uncertainties. The columns σ_{sys}^{pt-pt} and σ_{sys}^{glob} represent the point-point and global components in the systematic uncertainty. A_m, f_b, and A_b are the measured asymmetry, the background yield fraction, and the background asymmetry. The values in parentheses in columns A_m and A_b are the statistical uncertainty of A_m, and the model uncertainty of A_b, respectively. The asymmetries and their uncertainties are in units of ppm, and are still blinded by $f_{blind} \equiv 0.8056$. f_b is dimensionless.*

Two methods have been explored, both require a comparison of the experimental data against a simulation of the spectrometer. The details of the analysis have been summarized previously in a few documents [Bat03, Bat04, Que05, Kox05]. Only a general description of the methodology will be given here.

The first method used the time of flight difference between elastic proton and pion peaks ($\Delta t_{\pi p}$) as a gauge of the magnetic field. The usage of $\Delta t_{\pi p}$ eliminated the need of absolute calibration of timing offsets in the electronics. In principle, by comparing the measured $\Delta t_{\pi p}$ with what is obtained from the simulation ($\Delta t_{\pi p}^{sim}$) at the nominal field, one can extract the offset of the actual B field from the nominal (nominal magnet current was 5000 A). Using this actual field as the input to the simulation allows one to determine $\langle Q^2 \rangle$. A $\sim$50 ps precision of $\Delta t_{\pi p}$ will lead to a $< 0.2\%$ and $< 1\%$ determinations of the magnetic field and four-momentum transfer for each Q^2 bin, respectively. However, it turns out that $\Delta t_{\pi p}$ is also quite sensitive to the potential longitudinal and the radial offsets of the detectors. A global fit was therefore made with the measured $\Delta t_{\pi p}$ of all detectors based on their sensitivities to the magnetic field and the FPD positions given by the simulation. This allows for a simultaneous determination of the field strength and the detector positioning offset. The current of the magnet was determined in this method to be 5015 ± 1 A, and the position offsets of the FPDs were determined to range from a few mm to 1.5 cm (detector by detector) with a precision of $\sim$3 mm [Bat03]. The $\langle Q^2 \rangle$ of individual

Q^2 bins were then determined by applying 5015 A to the simulation. The impact of the fitted position offsets to the average Q^2 was $\sim< 1\%$, which was used as a conservative estimate of uncertainty of the Q^2 [Kox05].

The second method employed the fact that elastic rates in detector 15 and 16 are very sensitive to the actual magnet field. As a function of the magnetic current, elastic rates (based on the simulation) in these two detectors are depicted in Fig. 5.43. The increase of the magnetic field leads to an increase of the elastic Q^2 in detector 15, which corresponds to a decrease in the cross section. On the other hand, the elastic acceptance increases with the magnetic field [†]. The competing trends of the cross section and the acceptance give rise to a bump of the detector 15 elastic rate around 4880 A (the red curve in Fig. 5.43). For detector 16, elastic protons can be detected at a field lower than the nominal. However, when the magnet current increases up to ~4900 A and above, elastic protons are bent outside of its acceptance, which gives rise to the distinct plateau (with very low rates) in the black curve in Fig. 5.43. The "theoretical" curves in Fig. 5.43 were compared with the direct measurements (the backgrounds needed to be subtracted from the measured rates), in which the magnet current was scanned from 4700 to 5000 A. Based on the offsets between them, the actual magnet current was here determined to be 5003.5 ± 5 A [Kox05].

The fields extracted from the two methods were not in perfect agreement, however within a 2 σ tolerance. One should note, that the second method does not provide enough constraints to take into account the detector position offsets. Therefore, $\langle Q^2 \rangle$ and its uncertainty (1%) determined by the first method were adopted. This 1% uncertainty is uncorrelated with the uncertainty of the measured asymmetry, but it can be translated into an effective uncertainty of the asymmetry as

$$\sigma_{eff}(A_{Q^2}) = \frac{\partial A}{\partial Q^2}\sigma(Q^2)\,. \tag{5.107}$$

Since in leading order, the asymmetry is $\propto Q^2$, the 1% uncertainty of Q^2 translates

[†]This can be understood from the fact that at the nominal field, the (p, θ_p) acceptance of detector 15 is parallel to the elastic line, which maximizes the acceptance.

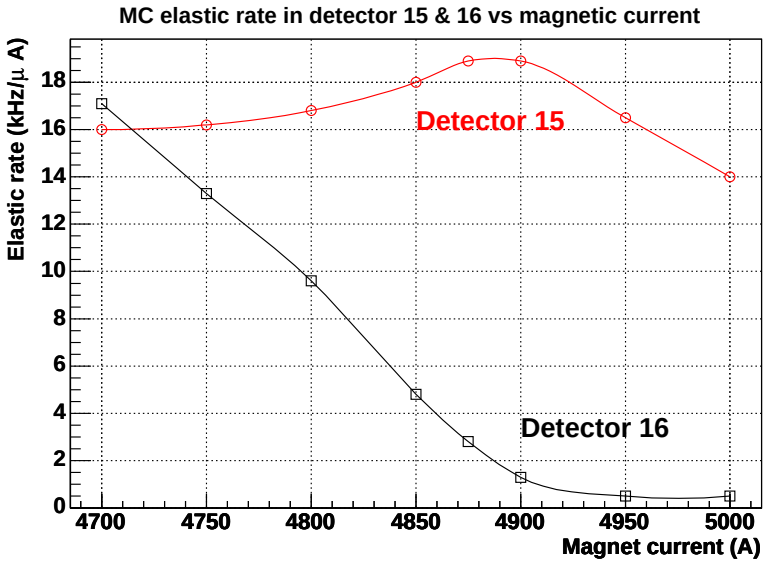

Figure 5.43: *Elastic rates in detectors 15 (red open circles) and 16 (black open squares) vs. the magnet current from the simulation. The data points in the figures were read off from the same figure in [Que05].*

into an 1% uncertainy in the measured asymmetry. The average four-momentum transfers of individual Q^2 bins (as defined below in Eqn. 5.109) have been listed in Tables 5.13, 5.20 and 5.23.

As a final caution, let us note that the elastic asymmetry measured in each Q^2 bin is an average asymmetry weighting by the yield,

$$\langle A(Q^2)\rangle = \frac{\int A(Q^2)Y(Q^2)dQ^2}{\int Y(Q^2)dQ^2}\,. \tag{5.108}$$

Similarly, the average Q^2 in a given Q^2 bin is

$$\langle Q^2\rangle = \frac{\int Q^2Y(Q^2)dQ^2}{\int Q^2dQ^2}\,. \tag{5.109}$$

One can make a Taylor expansion of $A(Q^2)$ around $\langle Q^2\rangle$ as

$$A(Q^2) = A(\langle Q^2\rangle) + \frac{\partial A}{\partial Q^2}(Q^2 - \langle Q^2\rangle) + \cdots \tag{5.110}$$

If higher order terms in Eqn. 5.110 are ignored ("$\cdots$" on the right-hand side),

Eqn. 5.108 becomes

$$\langle A(Q^2)\rangle = A(\langle Q^2\rangle)\,. \tag{5.111}$$

We note that for G^0 this is a legitimate approximation due to the fact that $A(Q^2)$ is linear with Q^2 in leading order (see Eqn. 2.80), and that the width of the Q^2 distribution within each Q^2 bin is small, ranging from 5% (detector 1) to 10% (the three Q^2 bins of detector 15) of $\langle Q^2\rangle$. Therefore, one can safely interpret the measured elastic asymmetry of each bin as the elastic asymmetry at the average four-momentum transfer.

5.3.8 Electromagnetic Radiative Correction

Due to the non-relativistic nature of the recoiling protons, the electro-magnetic (EM) radiative emission from them is small. However, the radiative emission from the incident electron changes the kinematics of the elastic reaction and therefore makes the measured elastic asymmetry different from the tree-level Born asymmetry without photon radiation.

The details of the EM radiative correction for G^0 are documented in [AN05]. For completeness, we will briefly outline the treatment here. A dedicated GEANT simulation was developed for this purpose. The energy loss of electrons in the target through ionization and the external Bremsstrahlung radiation is treated in GEANT. The computation of the internal radiative correction follows the framework of [MT69, Tsa74]. The parity violating asymmetry of the elastic events are computed, based on the kinematics at the reaction vertex after the radiative emission. This asymmetry is used for comparison with the asymmetry without the radiative correction (or the Born asymmetry), by assuming $G_E^s = G_M^s = 0$.

As a consequence of the radiative emission, a tail shows up in the yield spectrum towards the earlier time of flight of the elastic peak — this increases the average Q^2 in each bin, effectively increasing the magnitude of the measured elastic asymmetry from the Born asymmetry. To avoid confusion, let us label the radiated asymmetry as A_e, corresponding to the elastic asymmetry from the measurement,

and the Born asymmetry as A_{phys}. The radiated and Born asymmetries are averaged within the elastic cut, $\sim$4 ns and $\sim$5 ns for the French and NA electronics respectively. A ratio between the Born and the radiated asymmetries is calculated as

$$R = \frac{A_{phys}}{A_e}\,, \tag{5.112}$$

and in general R is slightly less than 1. R vs. Q^2 [†] of the first 17 Q^2 bins is plotted in Fig. 5.44. The radiative effect of the second Q^2 bin of detector 14 is negligible compared with its statistical precision, and is therefore ignored. The fractional

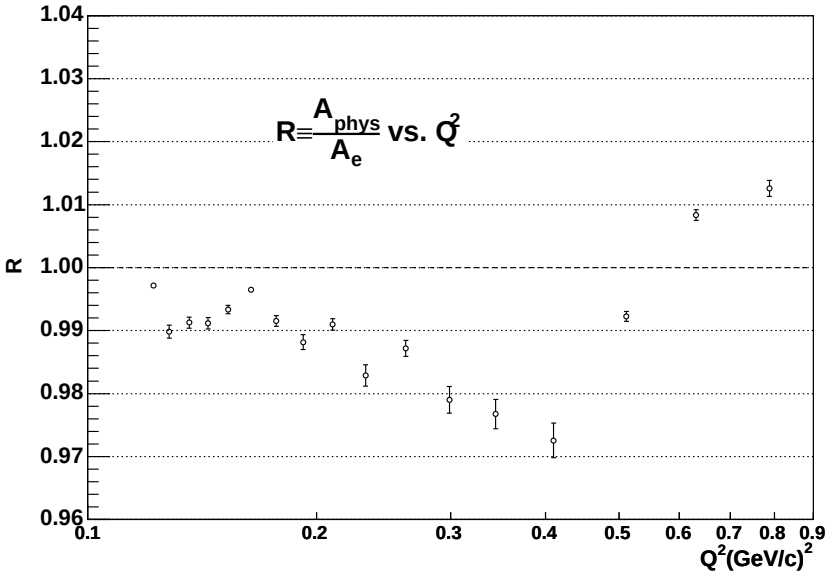

Figure 5.44: *Calculated R factor defined in Eqn. 5.112 vs. Q^2 for the first 17 Q^2 bins of G^0.*

correction, $1 - R$, is typically $\sim$1% and the its uncertainty of is estimated to be 10% (of $1 - R$) based on the difference of the correction factors computed in the NA and French elastic proton cuts. Due to the smallness of the correction, the 10% uncertainty of the correction is negligible in the final uncertainty budget.

The Born asymmetry, which is to be compared with the theory, is then

$$A_{phys}(Q^2) = R \times A_e\,. \tag{5.113}$$

[†]The average Q^2 is computed based on the Born scattering cross section.

5.4 Unblinded Physics Asymmetries

After all corrections described above are performed, the blinding factor (0.8056) is divided out, and in Table 5.24, an overview of the systematic corrections which lead to A_{phys} is presented. For the deadtime, helicity correlated beam properties and the radiative corrections, although the actual corrections are made detector by detector, only a representative value for each is listed in the table. For the background correction, the range of the corrections and the uncertainties are given, according to detailed values in Tables 5.13, 5.20 and 5.23. The systematic uncertainty due to the bin correlation effect (Eqn. 5.12), leakage (Eqn. 5.53), the beam polarization (Sec. 5.3.4), the global component of the background correction (Tables 5.13, 5.20 and 5.23), the four-momentum transfer (Sec. 5.3.7), and a 0.01 ppm uncertainty due to the potential transverse polarization effects are combined as the global systematic uncertainty. All others are combined into the point-point systematic uncertainties. Generally, the background correction uncertainty dominates both the point-point and global systematic uncertainties, with the exception at detectors 1 through 4 and detector 11, for which the leakage correction dominates the global systematics.

Source	Correction (ppm)	Uncertainty (ppm)
Bin correlation	0	0.043
Electronics deadtime	0.2	0.05
Helicity-correlated beam properties	0.01	0.01
Leakage	0.71	0.14
Beam polarization	$\frac{1}{73.7\%}$ (factor)	1.3% (fractional)
Background subtraction	0.1−40	0.2−9
four-momentum transfer	0	1%
Radiative corrections	1% (fractional)	0.1% (fractional)
Transverse beam polarization	0	0.01

Table 5.24: *An overview of the sizes of the systematic corrections and their uncertainties.*

As a summary, in Table 5.25, the final asymmetries of all 18 Q^2 bins from this

analysis are shown. The officially published data table will be presented in Table 6.2 later in Sec. 6.1.

Q^2	A_{phys}	σ_{stat}	σ_{sys}^{pt-pt}	σ_{sys}^{glob}	A_m	A_b	f_b
$(\mathrm{GeV/c})^2$	ppm	ppm	ppm	ppm	ppm	ppm	1
0.122	−1.54	0.46	0.24	0.18	−1.60(0.40)	−3.25(2.16)	0.089
0.128	−1.12	0.42	0.20	0.18	−0.99(0.36)	−0.04(1.99)	0.096
0.136	−1.57	0.44	0.18	0.18	−1.63(0.37)	−2.56(1.78)	0.106
0.144	−2.45	0.46	0.18	0.18	−3.10(0.38)	−7.44(1.69)	0.111
0.153	−2.14	0.45	0.29	0.22	−2.74(0.37)	−6.37(2.55)	0.116
0.164	−2.69	0.45	0.32	0.24	−3.71(0.37)	−10.07(2.72)	0.124
0.177	−3.92	0.44	0.25	0.21	−4.92(0.36)	−9.79(1.84)	0.124
0.192	−4.19	0.50	0.21	0.20	−5.26(0.41)	−11.71(1.69)	0.128
0.210	−4.72	0.49	0.26	0.22	−5.86(0.40)	−13.03(1.99)	0.130
0.232	−5.64	0.51	0.39	0.28	−6.00(0.41)	−7.57(2.09)	0.138
0.262	−5.27	0.51	0.12	0.18	−5.10(0.41)	−3.24(0.96)	0.144
0.299	−7.76	0.58	0.63	0.41	−4.93(0.46)	10.15(2.23)	0.151
0.344	−9.13	0.67	0.95	0.58	−3.15(0.51)	24.85(3.13)	0.179
0.410	−10.71	0.68	0.94	0.59	−2.67(0.51)	34.27(2.88)	0.186
0.511	−16.69	0.89	1.48	1.51	−5.80(0.66)	40.86(8.16)	0.191
0.631	−19.84	1.11	1.27	1.32	−9.74(0.81)	31.54(5.97)	0.197
0.788	−30.71	1.85	2.56	2.61	−12.66(0.94)	15.65(5.83)	0.399
0.997	−38.01	7.24	9.03	0.64	4.21(1.19)	16.87(2.16)	0.780

Table 5.25: *G^0 asymmetry data for individual Q^2 bins from this analysis. The columns in the table are: the average four-momentum transfer Q^2, the physics asymmetry A_{phys} and its statistical, point-point, and global systematic uncertainties σ_{stat}, σ_{sys}^{pt-pt}, and σ_{sys}^{glob}. To indicate the size of the background correction, the average raw asymmetry A_m, the background asymmetry A_b, and the background yield fraction f_b for each Q^2 bin are also listed. The statistical uncertainty of A_m and the model uncertainty of A_b are included in parentheses in the corresponding columns. All asymmetries are unblinded.*

Chapter 6

From Physics Asymmetries to Strange Form Factors

6.1 Non-Vector-Strange Asymmetries

As presented in Sec. 2.5, the full form of the physics asymmetry that leads to the strange form factors is

$$\begin{aligned} A_{phys} = & -\frac{G_F Q^2}{4\sqrt{2}\pi\alpha}\frac{1}{[\epsilon(G_E^p)^2+\tau(G_M^p)^2]} \\ & \times \{(\epsilon(G_E^p)^2+\tau(G_M^p)^2)(1-4\sin^2\theta_W)(1+R_V^p) \\ & -(\epsilon G_E^p G_E^n+\tau G_M^p G_M^n)(1+R_V^n) \\ & -\epsilon G_E^p(G_E^s+\eta G_M^s)(1+R_V^{(0)}) \\ & -\epsilon'(1-4\sin^2\theta_W)G_M^p G_A^e\}\,, \end{aligned} \tag{6.1}$$

with

$$G_A^e = -(1+R_A^{T=1})G_A^{T=1}+\sqrt{3}R_A^{T=0}G_A^{(8)}+(1+R_A^{(0)})G_A^s\,. \tag{6.2}$$

and

$$\tau=\frac{Q^2}{4M_p^2}\,,\quad \epsilon=\left(1+2(1+\tau)\tan^2\frac{\theta}{2}\right)^{-1}\,,\quad \epsilon'=\sqrt{\tau(1+\tau)(1-\epsilon^2)}\,,\quad \eta=\frac{\tau G_M^p}{\epsilon G_E^p}\,.$$

We have also stated in Sec. 2.5 that all electroweak parameters in Eqn. 6.1 will be evaluated under the $\overline{\text{MS}}$ renormalization scheme, with the renormalization scale set at the mass of Z^0.

Before extracting the value of $G_E^s+\eta G_M^s$, it is helpful to insert an intermediate step to compute a non-vector-strange asymmetry, A_{NVS}, with $G_E^s=G_M^s=0$ enforced. Some observations can then be made directly based on the difference between the measured asymmetry and A_{NVS}, as presented at the end of Sec. 5.3.6.2.

With $G_E^s = G_M^s = 0$ applied to Eqn. 6.2, A_{NVS} is

$$\begin{aligned} A_{NVS} = & -\frac{G_F Q^2}{4\sqrt{2}\pi\alpha} \frac{1}{\epsilon (G_E^p)^2 + \tau (G_M^p)^2} \\ & \times \{\epsilon (G_E^p)^2 + \tau (G_M^p)^2 (1 - 4\sin^2\theta_W)(1 + R_V^P) \\ & - (\epsilon G_E^p G_E^n + \tau G_M^p G_M^n)(1 + R_V^n) \\ & - \epsilon' (1 - 4\sin^2\theta_W) G_M^p G_A^e \} \,. \end{aligned} \tag{6.3}$$

Then the strange form factors, $G_E^s + \eta G_M^s$, which are the goal of this experiment, take a simple form:

$$G_E^s + \eta G_M^s = \frac{4\pi\sqrt{2}\alpha}{G_F Q^2} \frac{\epsilon (G_E^p)^2 + \tau (G_M^p)^2}{\epsilon G_E^p (1 + R_V^{(0)})} (A_{phys} - A_{NVS}) \,. \tag{6.4}$$

6.1.1 Parameterizations of the Electromagnetic Form Factors of the Nucleons

Let us first introduce a "classical" parameterization of the nucleon electromagnetic (EM) form factors. The prescription is to use the same dipole form to fit G_E^p, G_M^p and G_M^n, and use the so-called Galster parameterization for G_E^n. The dipole fit takes the form of

$$G(Q^2) = G(Q^2 = 0) \frac{1}{(1 + Q^2/\Lambda^2)^2} \,, \tag{6.5}$$

in which G can be either G_E^p, G_M^p or G_M^n, Q^2 is the four-momentum transfer, and Λ is the dipole mass with $\Lambda^2 = 0.710$ GeV^2 [Kel04]. The Galster parameterization of the neutron electric form factor, first proposed in [Gal71], is a modified dipole fit,

$$G_E^n(Q^2) = \frac{A\tau}{1 + B\tau} \frac{1}{(1 + Q^2/\Lambda^2)^2} \,, \tag{6.6}$$

in which $\tau = \dfrac{Q^2}{4M_p^2}$ with M_p being the mass of the proton. However, with the wealth of data now available on the form factors, the dipole form no longer provides satisfactory fits. For example, the dipole fit of G_M^n disagrees with the data by $\sim 6\%$ at $Q^2 = 1$ (GeV/c)^2 (see Fig. 6.1(a) where the ratios of the data to the dipole fit are

shown). Therefore, we shall focus on a few more recent parameterizations in this analysis.

The experimental determination of the nucleon EM form factors can be made via either an unpolarized cross section measurement [Ros50], or by accessing the polarization degrees of freedom in elastic scattering [ACG81]. Generally, the results from the polarization measurements are more precise, especially in the region with four-momentum transfer higher than 1 $(\mathrm{GeV/c})^2$. In [Kel04], Kelly provided a simple parameterization for all four nucleon form factors. The selected world data set for his fits had an emphasis on the recoil or target polarization measurements. The functional forms of G_E^p, G_M^p and G_M^n were taken to be the same, consistent with $1/Q^4$ scaling behavior in the perturbative regime, and a Galster fit was made for G_E^n. Friedrich and Walcher also published a coherent phenomenological treatment for all four form factors [FW03]. The selection of their data set was similar to that of Kelly, favoring the polarization measurements. Motivated by the pion cloud model, these authors allowed some structure in their fits around $Q^2 = 0.2 - 0.3$ $(\mathrm{GeV/c})^2$. A parameterization of G_E^p and G_M^p, based on a global fit to the world cross section data alone, was made by Arrington in [Arr04]. The goal of Arrington's analysis was to shed light on the recently discovered discrepancy of proton form factors resulting from the cross section and polarization measurements [HWDJ04]. This topic is still under intensive investigation, but the impact of it on the parity violating asymmetry at G^0 kinematics is negligible.

Comparisons of the above three parameterizations for all four form factors are displayed in Fig. 6.1(a) over the four-momentum transfer range of G^0. G_E^p, G_M^p and G_M^n are put on the same scale by normalizing by their corresponding dipole fits. The data points in the plots represent Kelly's data set [Kel04]. For $Q^2 > 0.6$ $(\mathrm{GeV/c})^2$, Arrington's fit of G_E^p deviates from the other two, as a result of the disagreement between the polarization and cross section measurements mentioned above. In Arrington's fits, the normalization factor of each experiment was also allowed to vary, which makes his values for G_M^p systematically lower than the other two fits. The fits of Friedrich-Walcher exhibit bumps in all four form factors around

$Q^2 = 0.2-0.3$ (GeV/c)^2, as a direct consequence of their pion cloud ansatz. However, despite the differences, the qualities of all three fits are good, and it is difficult to make a choice from a physics point of view. Kelly's parameterization is the simplest and it lacks the potential bias due to the underlying physics assumption; it is therefore adopted in our analysis.

The uncertainty of the form factor parameterization, in principle, contains two pieces. One is statistical, calculable from the error matrix of the fit, and the other is the systematic (or model) uncertainty associated with a specific choice of the fit function and data set, which can be estimated from the spread among different models. In Fig. 6.1(b), the statistical error bands calculated from the Kelly fits are displayed, together with the fits from the other two models. One sees that for all four form factors, the difference among models is much larger than the statistical error band. Henceforth, we shall neglect the statistical uncertainties. From Fig. 6.1(b), the fractional spread among the three models is estimated to be $\sim 1.5\% Q^2$ (G_E^p) with Q^2 in units of (GeV/c)^2, $\sim 1\%$ (G_M^p), $\sim 15\%$ (G_E^n) and $\sim 1\%$ (G_M^n). However, naively propagating these uncertainties into $G_E^s + \eta G_M^s$ is problematic, since the (model) uncertainties of these form factors are correlated, e.g., going from the Kelly to the Arrington fit would on average move G_E^p and G_M^p simultaneously in opposite directions. Therefore, in Sec. 6.2 we shall adopt the strategy of showing explicitly the values of $G_E^s + \eta G_M^s$ corresponding to different sets of form factor parameterizations to reflect this aspect of the model uncertainty.

6.1.2 Parameterization of the Axial Form Factor

As one can observe from Eqn. 6.1, the contribution of the G_A^e term to the parity violating asymmetry is suppressed by a factor of $-1 + 4\sin^2\theta_W \sim -0.07$, the weak charge of the electron. Therefore, as mentioned at the end of Sec. 2.4, the uncertainty of the axial form factor does not contribute much to the forward G^0 measurement.

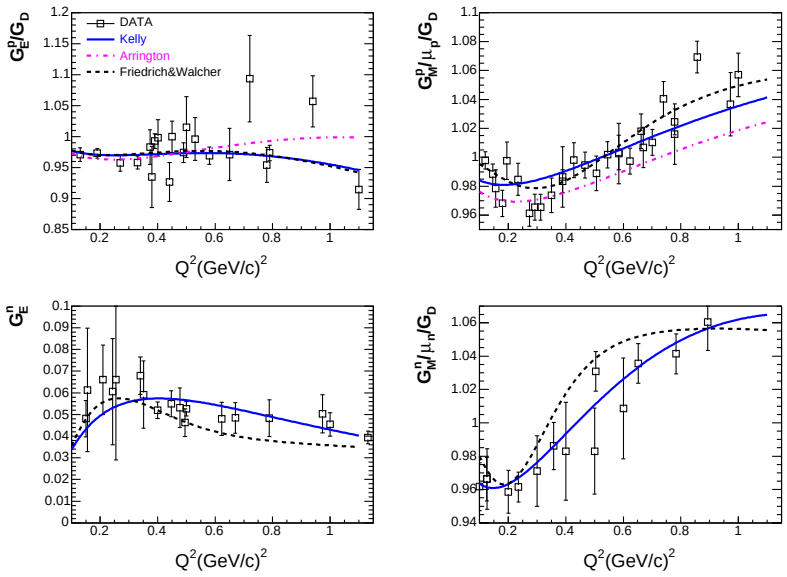

(a) Fits of EM Form Factors with Data

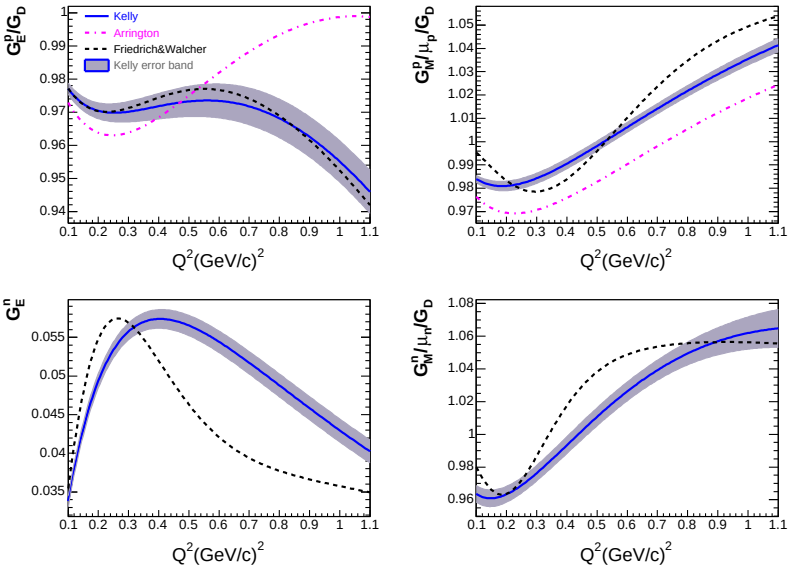

(b) Fits of Form Factors with Error Bands, No Data

Figure 6.1: *The form factor fits for G_E^p, G_M^p, G_E^n and G_M^n with a range of Q^2 from 0.1 to 1.1 $(GeV/c)^2$. G_E^p, G_M^p and G_M^n are put on the same scale by normalizing by their corresponding dipole fits. The experimental data in [Kel04] are displayed in (a). Different curves in the figures represent different form factor parameterizations: [blue solid = Kelly [Kel04], pink dot-dashed = Arrington [Arr04], and black dashed = Friedrich-Walcher [FW03]]. The Arrington parameterization is for G_E^p and G_M^p only. The lower figure (b) contains the same fits (but no data) with the $\pm 1\sigma$ error bands computed from the Kelly fits.*

The tree level expression of the proton axial form factor given in Sec. 2.3.2 is

$$G_A^{Z,tree}(Q^2) = -G_A^{T=1}(Q^2) + G_A^s(Q^2)\,, \tag{6.7}$$

and as mentioned there, $G_A^{Z,tree}(Q^2)$ is a good approximation of the axial form factor as seen by a neutrino probe. The isovector $G_A^{T=1}(Q^2)$ can be measured via charged current quasi-elastic scattering of $\nu(\bar{\nu}) + n \to e + p$, and the Q^2 dependence of $G_A^{T=1}$ is commonly parameterized in a dipole form as

$$G_A^{T=1}(Q^2) = \frac{G_A^{T=1}(0)}{\left(1 + Q^2/\Lambda_A^2\right)^2}\,, \tag{6.8}$$

where $G_A^{T=1}(0) = -g_A/g_V = 1.2695 \pm 0.0029$ is well-measured in neutron β decay [PDG04], and $\Lambda_A \sim 1$ GeV is the so-called axial mass of the nucleon. With updated EM form factors of the nucleon, a recent global fit of neutrino charged current cross section data was presented in [BBA03], resulting in a $\Lambda_A = 1.001 \pm 0.02$ GeV[†]. This value is adopted into our analysis.

The strange axial form factor, $G_A^s(Q^2)$, is conventionally assumed to have the same Q^2 dependence as $G_A^{T=1}(Q^2)$. As shown in Eqn. 2.57, at zero momentum transfer, $G_A^s(0) = \Delta s$, which is the strange quark contribution to the nucleon spin. The determination of Δs from polarized deep inelastic scattering data has been discussed in Sec. 1.2.3, where we have emphasized the large model dependent uncertainty. In this analysis, Δs (in the $\overline{\rm MS}$ renormalization scheme) is taken to be [Arv05]

$$\Delta s = -0.084 \pm 0.040\,, \tag{6.9}$$

based on two recent next-to-leading-order QCD analyses by Leader, Sidorov and Stamenov [LLS02, LLS03].

As discussed in Sec. 2.5, electroweak radiative corrections modify G_A^e of the

[†]This is in good agreement with $\Lambda_A = 1.014 \pm 0.016$ obtained from near threshold charged pion electro-production data, after chiral correction of finite pion mass [BEM02].

proton to

$$G_A^e = Q_A^{T=1} G_A^{T=1} + Q_A^{T=0} G_A^{(8)} + Q_A^{(0)} G_A^s$$
$$= -(1 + R_A^{T=1}) G_A^{T=1} + \sqrt{3} R_A^{T=0} G_A^{(8)} + (1 + R_A^{(0)}) G_A^s \,, \tag{6.10}$$

with the values of $R_A^{T=1}$, $R_A^{T=0}$ and $R_A^{(0)}$ given in Table 2.5. The SU(3) octet (isoscalar) term $G_A^{(8)}(Q^2)$, which does not contribute to the tree level expression, now appears. At zero momentum transfer, $G_A^{(8)}$ is

$$2\sqrt{3} G_A^{(8)}(0) = 3F - D \,, \tag{6.11}$$

in which F and D are the baryon beta decay parameters introduced in Sec. 1.2.3, and they can be determined by combining data from neutron and hyperon beta decays under the assumption of SU(3) flavor symmetry. One might be concerned about the uncertainty due to the non-exact SU(3) symmetry. However, global fits to beta decays of all baryon octet channels show little symmetry breaking effects on the values of F and D (see, e.g., [Son96]). In this analysis, the value $3F - D = 0.585 \pm 0.025$ from a recent global fit [Got00] is adopted. The Q^2 dependence of $G_A^{(8)}$ has not been measured and here it is simply assumed to have a dipole form with the same axial mass Λ_A.

To summarize, the expression for $G_A^e(Q^2)$ that enters into our calculation is

$$G_A^e(Q^2) = \left[\frac{g_A}{g_V} (1 + R_A^{T=1}) + \frac{3F - D}{2} R_A^{T=0} + \Delta s (1 + R_A^{(0)}) \right] G_D(Q^2) \,, \tag{6.12}$$

with

$$G_D(Q^2) = \frac{1}{(1 + Q^2/\Lambda_A^2)^2} \,. \tag{6.13}$$

6.1.3 Summary of Parameters

For reference, in Table 6.1 we summarize the values (and in some cases also the uncertainties) of the standard model coupling constants, electroweak radiative

correction factors, and the parameters used in the form factor and kinematics calculations. The values of α, $\hat{s}_Z^2$, G_F, M_p, μ_p, μ_n and g_A/g_V are taken from [PDG04]. The value of the dipole mass Λ^2 is taken from [Kel04]. Our choices for Λ_A^2, Δs and $3F - D$ are discussed in Sec. 6.1.2, and the values of electroweak radiative correction factors to the weak charges (R_V^p, R_V^n, $R_V^{(0)}$, $R_A^{T=1}$, $R_A^{T=0}$ and $R_A^{(0)}$) have been discussed in Sec. 2.5.

Parameter	Value	Parameter	Value
α	1./137.03599976	g_A/g_V	-1.2695
$\hat{s}_Z^2$	0.23120	$3F - D$	0.585(0.025)
G_F	$1.16639 \times 10^{-5}/\text{GeV}^2$	Δs	$-0.084(0.040)$
M_p	0.98272 GeV	R_V^p	$-0.045(3)$
μ_p	2.79285	R_V^n	$-0.0118(2)$
μ_n	-1.91304	$R_V^{(0)}$	$-0.0118(2)$
Λ^2	0.710 GeV^2	$R_A^{T=1}$	$-0.26(0.35)$
Λ_A^2	1.002(0.04) GeV	$R_A^{T=0}$	$-0.24(0.20)$
E_b	3.030(0.001) GeV	$R_A^{(0)}$	$-0.55(0.55)$

Table 6.1: *Parameters (with some uncertainties in parentheses) used to calculate $G_E^s + \eta G_M^s$. For references see text.*

6.2 $G_E^s + \eta G_M^s$

The published physics asymmetries for the 18 Q^2 bins in this experiment [Arm05] are recapped in Table 6.2. Listed in the last column are the non-vector-strange asymmetries A_{NVS} calculated from Eqn. 6.3 with Kelly form factors [Kel04] and the parameters in Table 6.1. The values of the published asymmetries are slightly different from those presented here (Table 5.25) due to three reasons. First, the asymmetries of the first fourteen Q^2 bins in [Arm05] were taken from the analysis in [Nak06], where the background correction fits were slightly different from the best fits in this work (Table 5.10). Nevertheless, as one can see, the agreement between

Q^2	A_{phys}	σ_{stat}	σ_{sys}^{pt-pt}	σ_{sys}^{glob}	A_m	A_b	f_b	A_{NVS}
$(\mathrm{GeV/c})^2$	ppm	ppm	ppm	ppm	ppm	ppm	1	ppm
0.122	−1.51	0.44	0.22	0.18	−1.38 (0.40)	−3.69 (2.51)	0.061	−1.96
0.128	−0.97	0.41	0.20	0.17	−1.07 (0.36)	−4.36 (0.78)	0.084	−2.11
0.136	−1.30	0.42	0.17	0.17	−1.34 (0.37)	−5.49 (0.90)	0.085	−2.29
0.144	−2.71	0.43	0.18	0.18	−2.67 (0.38)	−4.05 (2.81)	0.077	−2.50
0.153	−2.22	0.43	0.28	0.21	−2.46 (0.37)	−6.13 (2.46)	0.096	−2.75
0.164	−2.88	0.43	0.32	0.23	−3.13 (0.37)	−7.94 (2.82)	0.100	−3.05
0.177	−3.95	0.43	0.25	0.20	−4.47 (0.36)	−9.76 (1.91)	0.110	−3.44
0.192	−3.85	0.48	0.22	0.19	−5.01 (0.41)	−15.39 (1.66)	0.110	−3.91
0.210	−4.68	0.47	0.26	0.21	−5.73 (0.40)	−13.53 (1.99)	0.116	−4.47
0.232	−5.27	0.51	0.30	0.23	−6.08 (0.41)	−9.73 (2.06)	0.136	−5.23
0.262	−5.26	0.52	0.11	0.17	−5.55 (0.41)	−5.35 (0.99)	0.154	−6.31
0.299	−7.72	0.60	0.53	0.35	−5.40 (0.46)	8.33 (2.25)	0.174	−7.78
0.344	−8.40	0.68	0.85	0.52	−3.65 (0.51)	18.37 (3.11)	0.182	−9.66
0.410	−10.25	0.67	0.89	0.55	−1.70 (0.51)	36.49 (2.80)	0.180	−12.74
0.511	−16.81	0.89	1.48	1.50	−5.80 (0.79)	40.86 (8.16)	0.190	−17.96
0.631	−19.96	1.11	1.28	1.31	−9.74 (0.94)	31.54 (5.97)	0.200	−24.77
0.788	−30.83	1.86	2.56	2.59	−12.66 (1.01)	15.65 (5.83)	0.400	−34.57
0.997	−37.93	7.24	9.00	0.52	4.21 (1.19)	16.08 (2.22)	0.780	−48.61

Table 6.2: *G^0 asymmetry data for individual Q^2 bins as in [Arm05]. The columns in the table are: the average four-momentum transfer Q^2, the physics asymmetry A_{phys} and its statistical, point-point, and global systematic uncertainties σ_{stat}, σ_{sys}^{pt-pt}, and σ_{sys}^{glob}, the raw measured asymmetry A_m, the background asymmetry A_b, the background yield fraction f_b, and the non-vector-strange asymmetry A_{NVS}. The statistical uncertainty of A_m and the model uncertainty of A_b are included in parentheses in the corresponding columns. The small differences between this table and Table 5.25 are explained in the text.*

two different analyses is excellent. Second, the residual deadtime corrections to the NA data for the last four Q^2 bins in this analysis were based on the residual asymmetry slopes measured in the hybrid electronics (last two rows in Table 5.4), whereas in [Arm05] the asymmetry slopes of the NA detectors 14 and 15 in the last

two rows in Table 5.5 were applied. Finally, the systematic uncertainty due to the bin correlation effects was neglected in [Arm05], whereas it has been conservatively included in this analysis (see Eqn. 5.12).

In Fig. 6.2, the physics asymmetries in Table 6.2 are plotted vs. the four-momentum transfer. The inner error bar on each data point is the statistical uncer-

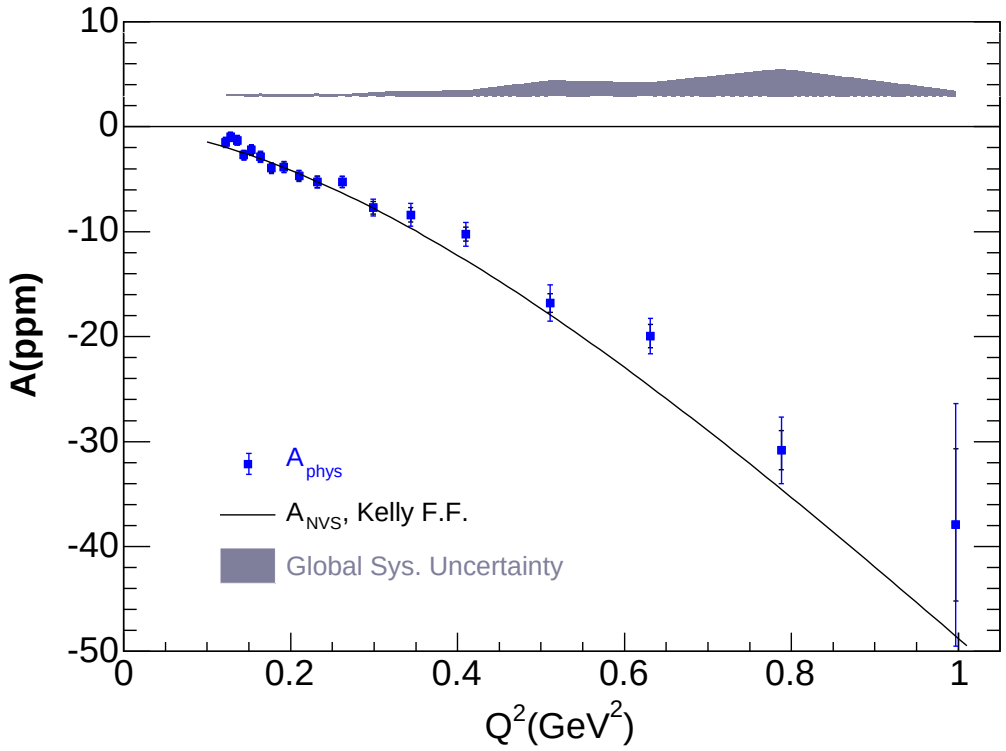

Figure 6.2: *A_{phys} and A_{NVS} vs. Q^2. The inner and outer error bars are the statistical uncertainties, and statistical and point-point systematic uncertainties combined in quadrature. The gray band represents the global systematic uncertainty of A_{phys}. The solid curve is A_{NVS} computed based on the Kelly form factors.*

tainty, and the outer one is the statistical and point-point systematic uncertainties combined in quadrature. The global systematic experimental uncertainty is plotted as the gray band on the top of the figure. The solid black curve represents the non-vector-strange asymmetry calculated using Eqn. 6.3 with Kelly form factors. As mentioned in Sec. 5.4, the systematic uncertainties (both point-point and global) of the data primarily arise from the uncertainty of the background correction, except for the lowest four Q^2 bins and the one at $Q^2 = 0.262$ (GeV/c)^2, where the leakage beam correction dominates the *global* systematic uncertainty. The highest Q^2 bin

at $\sim$1 (GeV/c)^2 corresponds to the second elastic peak in detector 14. Because in the space of (FPD, ToF), it is far away from other elastic peaks, its background correction uncertainty is much less correlated with that of other Q^2 bins, resulting in a significantly smaller global systematic uncertainty.

Using Eqn. 6.4, the difference between A_{phys} and A_{NVS} in Table 6.2 leads to $G_E^s + \eta G_M^s$. In Table 6.3, the values of $G_E^s + \eta G_M^s$ with different form factor parameterizations (Kelly [Kel04], Arrington [Arr04], and Friedrich-Walcher [FW03]) are listed. In the literature, sometimes the form factor uncertainty is combined into the systematic uncertainty. Here we choose to show the results with different form factor parameterizations separately, and use the difference among them to indicate the model uncertainty. The values of $\eta = \frac{\tau G_M^p}{\epsilon G_E^p}$ in the table are computed using the form factors of Kelly [Kel04]. Different components of the uncertainty of $G_E^s + \eta G_M^s$ are also given in Table 6.3. It contains the statistical, point-point systematic, and global systematic uncertainties from the experimental physics asymmetry. In addition, it also contains the model uncertainty of the non-vector-strange asymmetry, which includes the uncertainties associated with the axial form factors and the electroweak radiative corrections, as well as the beam energy and four-momentum transfer. Note that due to the Q^2 in the denominator of Eqn. 6.4, some double-counting of uncertainty contributions would arise if one computes the uncertainty of A_{NVS} due to the uncertainty of Q^2 (1%) first, then propagates it into $G_E^s + \eta G_M^s$. Instead, one must take the full expression of $G_E^s + \eta G_M^s$ and evaluate its derivative with respect to Q^2. The model uncertainty of $G_E^s + \eta G_M^s$ in [Arm05] and what is shown in Table 6.3 differ slightly in this regard. In Table 6.4, different ingredients of the model uncertainty are listed for a few representative Q^2 bins. As one can see, the uncertainties due to Q^2 and $R_A^{T=1}$ (the "many quark" correction to the isovector axial charge in Table 2.5) are the dominating pieces.

The results in Table 6.3 are also plotted in Fig. 6.3. The data points are taken from the "Kelly" column, and the inner (outer) error bars are the statistical (statistical and point-point systematic combined) uncertainties. The model uncertainty is plotted as the light green band at the bottom, and the gray band on the top

Q^2 (GeV/c)^2	η	$G_E^s + \eta G_M^s$ Kelly	Arrington	F&W	σ_{stat}	σ_{sys}^{pt-pt}	σ_{sys}^{glob}	σ_{model}
0.122	0.098	0.037	0.037	0.036	0.036	0.019	0.015	0.003
0.128	0.103	0.090	0.089	0.089	0.032	0.016	0.014	0.002
0.136	0.110	0.074	0.074	0.073	0.032	0.013	0.013	0.003
0.144	0.116	−0.014	−0.014	−0.017	0.030	0.013	0.012	0.003
0.153	0.124	0.034	0.035	0.032	0.028	0.019	0.014	0.003
0.164	0.133	0.010	0.011	0.007	0.026	0.020	0.014	0.003
0.177	0.143	−0.028	−0.028	−0.033	0.024	0.014	0.011	0.004
0.192	0.156	0.003	0.003	−0.003	0.025	0.011	0.010	0.004
0.210	0.171	−0.010	−0.009	−0.014	0.022	0.012	0.010	0.004
0.232	0.189	−0.002	−0.001	−0.006	0.021	0.012	0.010	0.004
0.262	0.214	0.038	0.038	0.035	0.019	0.004	0.006	0.004
0.299	0.245	0.002	0.002	0.002	0.018	0.016	0.011	0.005
0.344	0.283	0.033	0.033	0.038	0.018	0.022	0.014	0.005
0.410	0.341	0.053	0.052	0.064	0.014	0.019	0.012	0.005
0.511	0.431	0.019	0.017	0.035	0.014	0.024	0.024	0.006
0.631	0.543	0.060	0.056	0.078	0.014	0.016	0.016	0.007
0.788	0.700	0.036	0.029	0.049	0.018	0.024	0.025	0.007
0.997	0.932	0.076	0.065	0.082	0.052	0.064	0.004	0.008

Table 6.3: *$G_E^s + \eta G_M^s$ measured in the G^0 forward experiment. Columns "Kelly", "Arrington" and "F&W" correspond to the values of $G_E^s + \eta G_M^s$ using the form factors of Kelly [Kel04], Arrington [Arr04] and Friedrich-Walcher [FW03]. The uncertainties on $G_E^s + \eta G_M^s$ are identical for all three models above, and are separated into statistical (σ_{stat}), point-point and global systematic (σ_{sys}^{pt-pt} and σ_{sys}^{glob}), and model (σ_{model}) uncertainties. The model uncertainties given in [Arm05] are slightly larger than those in the last column here, due to the double-counting of Q^2 uncertainty in [Arm05]. See text for details.*

represents (experimental) global systematic uncertainty. One should note that both of these uncertainties are global to all data points, and they should be combined in quadrature. The unsmooth behavior of the experimental global band is primarily due to the variation of the uncertainty for the background correction from detector

Q^2 bin (GeV/c)^2	0.144	0.192	0.299	0.631
E_b	2.2×10^{-6}	3.0×10^{-6}	4.7×10^{-6}	1.0×10^{-5}
Q^2	0.0028	0.0030	0.0036	0.0038
Λ_A	4.6×10^{-5}	7.4×10^{-5}	0.00015	0.00038
$R_A^{T=1}$	0.0020	0.0024	0.0034	0.0052
$R_A^{T=0}$	0.00026	0.00032	0.00044	0.00069
$R_A^{(0)}$	0.00020	0.00025	0.00035	0.00054
$3F - D$	1.3×10^{-5}	1.6×10^{-5}	2.3×10^{-5}	3.5×10^{-5}
Δs	7.9×10^{-5}	9.9×10^{-5}	0.00014	0.00021
total	0.0034	0.0039	0.0050	0.0065

Table 6.4: *The model uncertainty budget for $G_E^s + \eta G_M^s$ for four representative Q^2 bins. Individual rows in the table are the model uncertainties due to the uncertainties of E_b, Q^2, Λ_A^2, $R_A^{T=1}$, $R_A^{T=0}$, $R_A^{(0)}$, $3F - D$ and Δs.*

to detector (see Table 5.13). The two curves in the figures are the non-vector-strange "zero-lines", defined as the difference with respect to the Kelly values, corresponding to the Arrington (pink dot-dashed) and Friedrich-Walcher (black dashed) fits. So the effect of using different nucleon form factor fits can be visualized from the figure: the differences between the data and the dashed "zero-lines" are the corresponding "signals" $(G_E^s + \eta G_M^s)$ for the non-Kelly models. For example, if the Friedrich-Walcher parameterization is used instead, it will bring the data points further in positive direction for $Q^2 > 0.3$ (GeV/c)^2.

6.3 Interpretation

6.3.1 "Zero-line" Hypothesis

Looking at Fig. 6.3, the first question one might ask is, what is the probability that the measured data *rejects* the zero-line hypothesis, i.e., $G_E^s + \eta G_M^s = 0$? A somewhat related discussion for the three data points of detector 15 has been presented at the end of Sec. 5.3.6.2, and here we will put the discussion into a broader scope. This question can be addressed by a classical χ^2 test, i.e., if the underlying

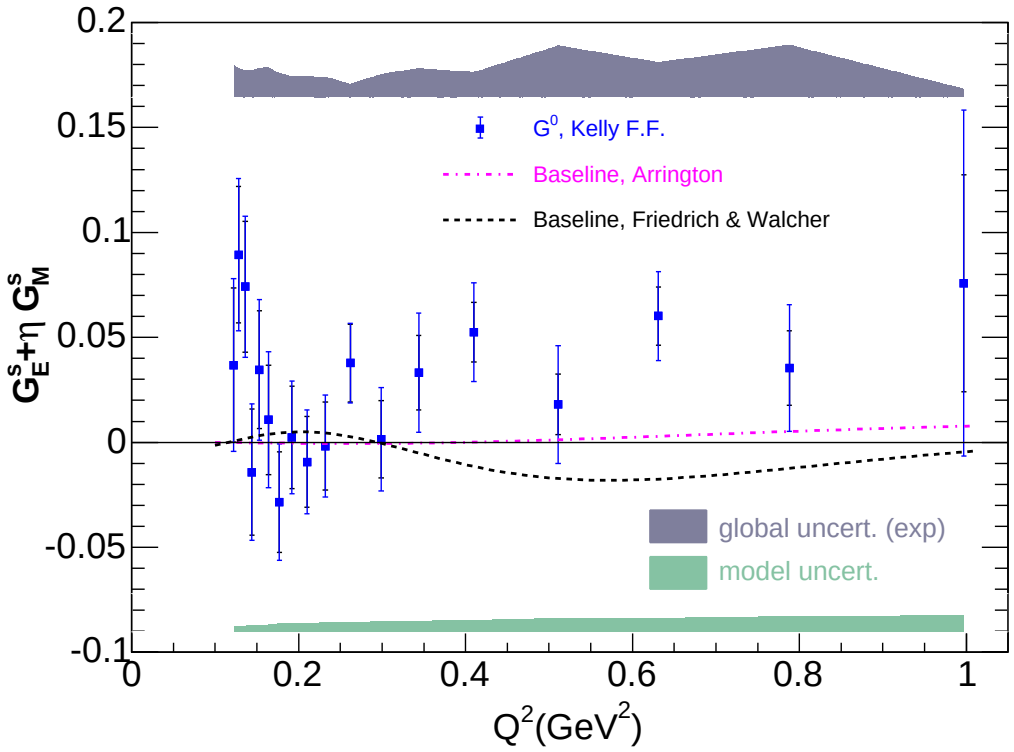

Figure 6.3: $G_E^s + \eta G_M^s$ *vs.* Q^2 *measured in the* G^0 *forward experiment. The central values of the data points are calculated using the Kelly form factors. The inner and outer error bars are the statistical uncertainties, and statistical and point-point systematic uncertainties combined in quadrature. The lower green and upper gray bands represent the model and experimental global systematic uncertainties, respectively. The two curves in the figure represent the differences between the Kelly and Arrington (pink dot-dashed), and the Kelly and Friedrich-Walcher (black dashed) form factor parameterizations. The figure here is slightly different from the one in [Arm05] in two aspects. First, the model uncertainty band in [Arm05] is slightly wider than shown here due to the double-counting of* Q^2 *uncertainty of* A_{NVS}*. Second, there was a numerical error in the Friedrich-Walcher zero-line in [Arm05]. See text for more explanation.*

physics is the zero-line in that figure, what is the probability of having a random data set drawn from it that would yield *equal or smaller* values of χ^2 (with respect to the zero-line) compared to the same χ^2 computed from the measured data?

For a large ensemble of N data points with *purely random* uncertainties, drawn from a common underlying physics curve with m degrees of freedom, the distribution of the χ^2 (with respect to the physics curve) follows the standard χ^2 distribution with a probability density $\mathcal{P}(\chi^2, N-m)$ [Bev92]. The integrated probability of having

a value of χ^2 less than a given χ^2_0, $\int_0^{\chi^2_0} \mathcal{P}(\chi^2, N-m)d\chi^2$, can be simply looked up or calculated. As a familiar example, for a single data point, the integrated probability of having a χ^2 less than 1 relative to a given theoretical value is 68.3%. However, this simple recipe is not valid for our data due to the existence of global uncertainties. Therefore we determine the probability with a Monte Carlo (MC) approach, by generating data samples dispersed around the zero-line according to our random and global uncertainties. Specifically, for each data point, different pieces of uncertainty are first grouped into a random and a correlated uncertainty as

$$\sigma^2_{ran} = (\sigma_{stat})^2 + (\sigma^{pt-pt}_{sys})^2\,, \quad \sigma^2_{corre} = (\sigma^{glob}_{sys})^2 + (\sigma_{model})^2\,, \tag{6.14}$$

where σ_{stat}, σ^{pt-pt}_{sys}, σ^{glob}_{sys}, and σ_{model} are statistical, point-point systematic, global systematic, and model uncertainties of $G^s_E + \eta G^s_M$, respectively. Then a copy of $G^s_E + \eta G^s_M$ is generated, for data point j, such as

$$G^j = 0 + r^j \sigma^j_{ran} + r^0 \sigma^j_{corre}\,, \tag{6.15}$$

where G^j is a compact symbol for $G^s_E + \eta G^s_M$ of the jth data point, and r^j and r^0 are both Gaussian-distributed (centered at 0, with 1 as the standard deviation) random numbers. The nature of the random and correlated uncertainties is reflected in that for each set of the MC data, r^j is different for each data point, whereas r^0 is common for all of them. The χ^2 relative to the zero-line is calculated for each copy of the MC data, and compared with the same χ^2 of the measured data using the form factors of Kelly (35.2 for 17 degrees of freedom). Note that the uncertainty of each data point in calculating χ^2 is taken as the random uncertainty in Eqn. 6.14. The result of this analysis is plotted in Fig. 6.4. The black histogram is the χ^2 probability distribution of the MC data relative to the zero-line, and the vertical red line is that of the measured data. The area of the black histogram below the red line is the probability that the zero-line hypothesis is *rejected*; it is 89.6%. The χ^2 distribution for a pure random data sample with 17 degrees of freedom is also

overlaid in the figure as the blue histogram to demonstrate the "distortion" of the MC distribution from the random expectation, due to the correlated uncertainties among the data. Lastly, for completeness, the same analysis is repeated by using the overall uncertainty (statistical and systematic combined) for each data point in calculating χ^2, resulting into an almost identical χ^2 distribution and a rejection probability of 89.3%.

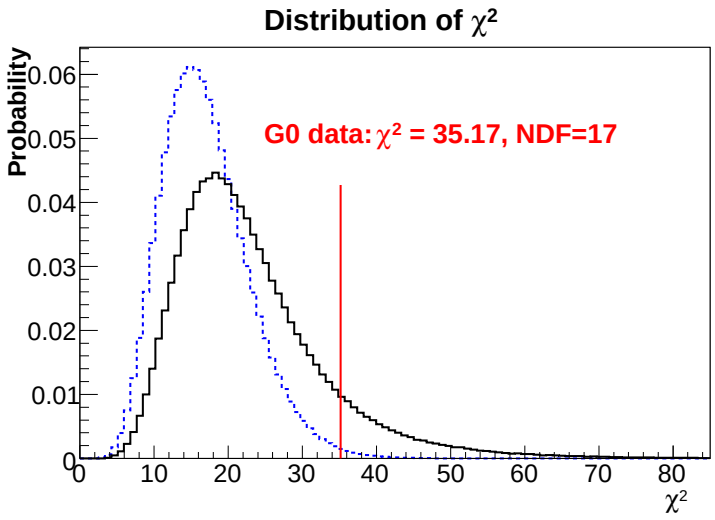

Figure 6.4: *The χ^2 distribution (solid black histogram) for the Monte Carlo data generated according to the random and correlated uncertainties of the G^0 data (Eqn. 6.15), with the hypothesis of $G_E^s + \eta G_M^s = 0$. The red line is the χ^2 of G^0 data relative to the zero-line, and the blue dashed histogram is the distribution of the χ^2 if the correlated uncertainties of all 18 data points of G^0 are assumed also to be uncorrelated.*

6.3.2 Combined Analysis to the World Data

To make statements about G_E^s and G_M^s independently, one needs to combine the G^0 forward data with results from other experiments. However, since the nucleon form factors and electroweak radiative corrections were handled differently in different measurements, one can not directly combine the published values of $G_E^s + \eta G_M^s$. The approach we take here is to start from the measured physics asymmetry in each experiment, use the same nucleon electromagnetic and axial form factors, as well as the electroweak parameters to calculate $G_E^s + \eta G_M^s$, and then combine the results.

In total, the existing world data overlap with the coverage of G^0 at three different values of four-momentum transfer: 0.1 (GeV/c)^2 (SAMPLE-I [Spa04], HAPPEx-H-II [Ani05], HAPPEx-He [Ani05b] and PVA4-II [Maa05]), 0.23 (GeV/c)^2 (PVA4-I [Maa04]) and 0.477 (GeV/c)^2 (HAPPEx-H-I [Ani04]). The SAMPLE deuterium data [Has00, Ito04] are primarily sensitive to G_A^e, and are therefore omitted in this analysis. The kinematics and the measured asymmetries from these experiments have already been summarized earlier in Table 3.1. For convenience, the same values are listed here in Table 6.5.

Experiment	Q^2 (GeV/c)^2	θ_{lab} (deg)	A_{phys} (ppm)	Reference
SAMPLE-I	0.098	144.8	$-5.61 \pm 0.67 \pm 0.88$	[Bei05]
HAPPEx-H-II	0.099	6.0	$-1.14 \pm 0.24 \pm 0.06$	[Ani05]
HAPPEx-He	0.091	5.7	$6.72 \pm 0.84 \pm 0.21$	[Ani05b]
PVA4-II	0.108	35.52	$-1.36 \pm 0.29 \pm 0.13$	[Maa05]
PVA4-I	0.23	35.45	$-5.44 \pm 0.54 \pm 0.26$	[Maa04]
HAPPEx-H-I	0.477	12.3	$-15.05 \pm 0.98 \pm 0.56$	[Ani04]

Table 6.5: *A summary of the world data prior to G^0: the average kinematics and the measured asymmetries from the publications. The first and the second uncertainties of the measured asymmetries are statistical and systematic, respectively. The central kinematics of the two PVA4 measurements and the SAMPLE measurement are obtained from [AM05p] and [Bei05p], respectively.*

The average values of four-momentum transfer of the G^0 Q^2 bins do not coincide exactly with those from other measurements, therefore for a global analysis some interpolation is necessary. For $Q^2 = 0.1$ (GeV/c)^2, we chose to use the lowest three Q^2 bins of G^0, (0.122, 0.128, 0.136) (GeV/c)^2. For the other two momentum transfers, $Q^2 = 0.23$ and 0.477 (GeV/c)^2, three adjacent G^0 points in Table 6.2 are used for interpolation: Q^2 =(0.210, 0.232, 0.262) (GeV/c)^2 and Q^2 =(0.410, 0.511, 0.631) (GeV/c)^2.

For $Q^2 = 0.1$ (GeV/c)^2, to apply the physical constraint that $(G_E^s + \eta G_M^s)(Q^2 =$

0) = 0 [†], a linear interpolation is made directly for $G_E^s + \eta G_M^s$ using the "Kelly" values in Table 6.3. The procedure is illustrated in Fig. 6.5(a). The uncertainty of the interpolated value of $G_E^s + \eta G_M^s$ is separated into four components: the statistical and point-point systematic uncertainties are given simply by the fit based on the corresponding uncertainties of those of the three Q^2 bins involved; the global uncertainty is taken as a straight average of those of the three data points (0.014, see Table 6.3). The model uncertainty of the interpolation is assigned to be the half difference between the constant (ignoring (0,0)) and linear fits at the desired Q^2, as illustrated in the figure. The red solid data point in the figure is the interpolated $G_E^s + \eta G_M^s$, with all components of uncertainty combined. For the other two Q^2 points, the physics asymmetries are first normalized by their corresponding Q^2 value to take out the leading Q^2 dependence, for which a linear and constant fit is made, as illustrated in Figs. 6.5(b) and 6.5(c). The central value of $A_{phys}(Q^2)$ (pink solid data point in the figure) is taken as the average between the two fits. The uncertainty of the interpolated asymmetry is assigned in the same way as the uncertainty at $Q^2 = 0.1$ (GeV/c)^2. One should note, however, that the G^0 electron angles are different for the three Q^2 bins involved, which leads to some ambiguity in the value of η associated with the interpolated result. In this analysis, we simply calculate the electron angle and η using the G^0 beam energy (3.03 GeV) and the value of the desired four-momentum transfer, and associate them with the interpolated results. The interpolated asymmetries at Q^2 =0.23 and 0.477 (GeV/c)^2 are summarized in Table 6.6, and the result of $G_E^s + \eta G_M^s$ at $Q^2 = 0.1$ (GeV/c)^2 can be found in Table 6.7.

Before we proceed with a global analysis at Q^2=0.1 (GeV/c)^2, since a measurement on a ^{4}He target [Ani05b] will be involved, let us review the formalism here. The ^{4}He nucleus is spin zero, parity even and isoscalar. In the standard $J^\pi T$ notation it is labeled as 0^+0. A nice feature of this type of target is that with isospin symmetry, the parity violating asymmetry for elastic electron scattering is

[†]This is due to the fact that $G_E^s(0) = 0$ and $\eta(0) = \frac{\tau G_M^p}{\epsilon G_E^p} = 0$. Therefore this procedure is an interpolation, not an extrapolation.

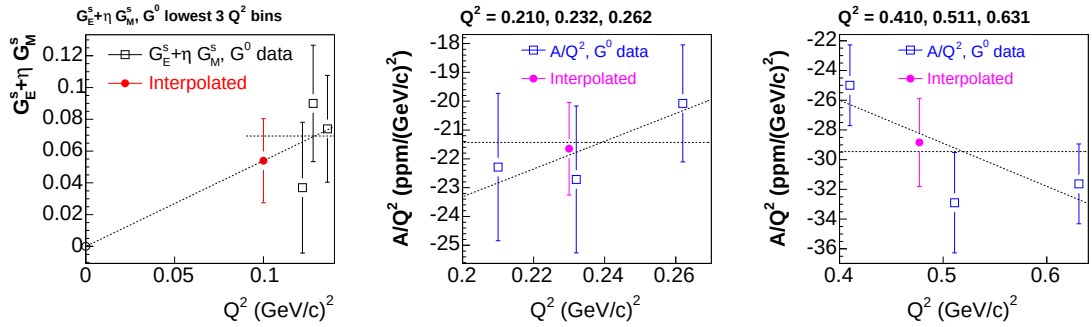

(a) $Q^2 = 0.1$ *(GeV/c)*^{2} (b) $Q^2 = 0.23$ *(GeV/c)*^{2} (c) $Q^2 = 0.477$ *(GeV/c)*^{2}

Figure 6.5: *The interpolation of the G^0 data around Q^2 =0.1, 0.23 and 0.477 (GeV/c)^2. The G^0 data are shown as the blue data points, with the error bars being statistical and point-point systematic combined. Interpolations are made on $G_E^s + \eta G_M^s$ (Q^2=0.1 (GeV/c)^2) and $\frac{A_{phys}}{Q^2}$ (Q^2=0.23 and 0.477(GeV/c)^2), with linear and constant fits (dashed lines). The adopted centroids and overall uncertainties of the interpolated values are shown as the red solid (a) and pink solid (b and c) data points. The model uncertainty of this interpolation is estimated to be half of the difference between the linear and constant fits. See text for details.*

Q^2	θ_{lab}	A_{phys}	σ_{stat}	σ_{sys}^{pt-pt}	σ_{sys}^{glob}	σ_{intp}	σ_{sys}
(GeV/c)^2	deg	ppm	ppm	ppm	ppm	ppm	ppm
0.23	9.27	−4.98	0.29	0.10	0.20	0.05	0.23
0.477	13.68	−13.76	0.48	0.66	1.12	0.29	1.33

Table 6.6: *The interpolated physics asymmetries of G^0 at Q^2 =0.23 and 0.477 (GeV/c)^2, based on the G^0 data in Table 6.2 (using the Kelly form factors). σ_{stat} is the pure statistical uncertainty. σ_{sys}^{pt-pt}, σ_{sys}^{glob} and σ_{inpt} are the point-point and global systematic uncertainties, and the uncertainty assigned to the interpolation procedure, respectively. σ_{sys} is the combination of the latter three.*

only sensitive to G_E^s (with no dependence on G_M^s and G_A^e) [Mus94]. At tree level, the parity violating asymmetry can be expressed as

$$A_{PV}^{0^+0,tree} = \frac{G_F Q^2}{4\pi\sqrt{2}\alpha}\left(4\sin^2\theta_W + \frac{2G_E^s}{G_E^p + G_E^n}\right).$$

When the electroweak radiative corrections are included, it is modified to become [Mus94]

$$A_{PV}^{0^+0} = \frac{G_F Q^2}{4\pi\sqrt{2}\alpha}\left(4\sin^2\theta_W(1+R_V^{T=0}) + \frac{2(1+R_V^{(0)})G_E^s}{G_E^p+G_E^n}\right), \tag{6.16}$$

where the isoscalar and isosinglet R factors are related to R_V^p and R_V^n in Table 6.1 as [Mus94]

$$\begin{aligned} R_V^{T=1} &= \frac{R_V^n + (1-4\sin^2\theta_W)R_V^p}{2(1-2\sin^2\theta_W)} = -0.0141(3)\,, \\ R_V^{T=0} &= \frac{R_V^n - (1-4\sin^2\theta_W)R_V^p}{4\sin^2\theta_W} = -0.0091(3)\,. \end{aligned} \tag{6.17}$$

The uncertainties of these two factors are propagated from the uncertainties in R in Table 2.3.

Based on the results in Tables 6.5 and 6.6, one can compute $G_E^s+\eta G_M^s$ using a common set of parameters (nucleon form factors, electroweak radiative corrections, etc.). For the hydrogen data, the values of A_{phys} are translated into $G_E^s + \eta G_M^s$ using Eqn 6.1, and for the ^{4}He point, Eqn. 6.16 is used to calculate G_E^s. The form factors of Kelly [Kel04] have been used in this global analysis, and the electroweak parameters are taken from Table 6.1. The resulting world data of $G_E^s + \eta G_M^s$ at Q^2 =0.1, 0.23, and 0.477 (GeV/c)^2 are summarized in Table 6.7.

Using the data from Table 6.7, we can make a combined analysis at three different four-momentum transfers. In the (G_E^s, G_M^s) space, each measurement constrains a linear band of

$$G_E^s + \eta_i G_M^s = g_i \pm \sigma(g_i)\,, \tag{6.18}$$

in which η_i, g_i and $\sigma(g_i)$ represent the values of η, $G_E^s + \eta G_M^s$ and its uncertainty for a given measurement i. Intuitively, with more than one of such bands, the best values of (G_E^s, G_M^s) lie within the overlapping area. In Fig. 6.6, the five bands at $Q^2 = 0.1$ (GeV/c)^2 are overlaid. For each band, the inner dashed lines and the outer solid lines represent statistical, and the statistical and (experimental) systematic combined uncertainties, respectively. Visually the five bands have a common area

Experiment	Q^2 (GeV/c)^2	η	$G_E^s + \eta G_M^s$	σ_{stat}	σ_{sys}
SAMPLE-H	0.0980	1.6771	0.5632	0.3319	0.4360
HAPPEx-H-II	0.0990	0.0795	0.0303	0.0251	0.0063
HAPPEx-He	0.0910	0.0000	-0.0386	0.0416	0.0104
PVA4-II	0.108	0.1045	0.0661	0.0288	0.0129
G0	0.1000	0.0803	0.0539	0.0193	0.0181
PVA4-I	0.23	0.2248	0.0374	0.0239	0.0115
G0	0.23	0.1872	0.0074	0.0120	0.0095
HAPPEx-H-I	0.4770	0.3976	0.0167	0.0172	0.0098
G0	0.4770	0.4000	0.0415	0.0085	0.0234

Table 6.7: *The world data of $G_E^s+\eta G_M^s$ recalculated using the standard G^0 parameter inputs at Q^2 =0.1, 0.23, and 0.477 (GeV/c)^2. The Kelly form factors are used. σ_{stat} and σ_{sys} are the statistical and (experimental) systematic uncertainties of $G_E^s+\eta G_M^s$.*

of interception, showing that they are in good agreement.

Technically, the evaluation of the best (G_E^s, G_M^s) follows the method of least squares, i.e., we define the χ^2 function as

$$\chi^2(G_E^s, G_M^s) = \sum_i \left[\frac{g_i - (G_E^s + \eta_i G_M^s)}{\sigma(g_i)} \right]^2 , \tag{6.19}$$

and the solution of (G_E^s, G_M^s) is the pair that gives the minimum $\chi^2 = \chi^2_{min}$. The value of χ^2_{min}, when having redundant constraints, gives a measure of the consistency among measurements. The contour of (G_E^s, G_M^s) with a fixed $\chi^2 = \chi^2_{min} + \Delta\chi^2$, takes an elliptical shape [PDG04]. The ellipse with $\chi^2 = \chi^2_{min} + 1$ is conventionally called the error ellipse, since the projection of the ellipse onto a given axis gives ± 1 unit of the estimated uncertainty of the corresponding variable. Similarly the contour of $\chi^2 = \chi^2_{min} + 4$ is the so-called 2σ ellipse. One should note, that this simple prescription requires an independent uncertainty $\sigma(g_i)$ for each measurement. Therefore only the total experimental uncertainties (the combination of σ_{stat} and σ_{sys} in Table 6.7) are taken to compute χ^2. The model uncertainties, such as the electroweak radiative corrections, and the variation due to the form factor parameterizations,

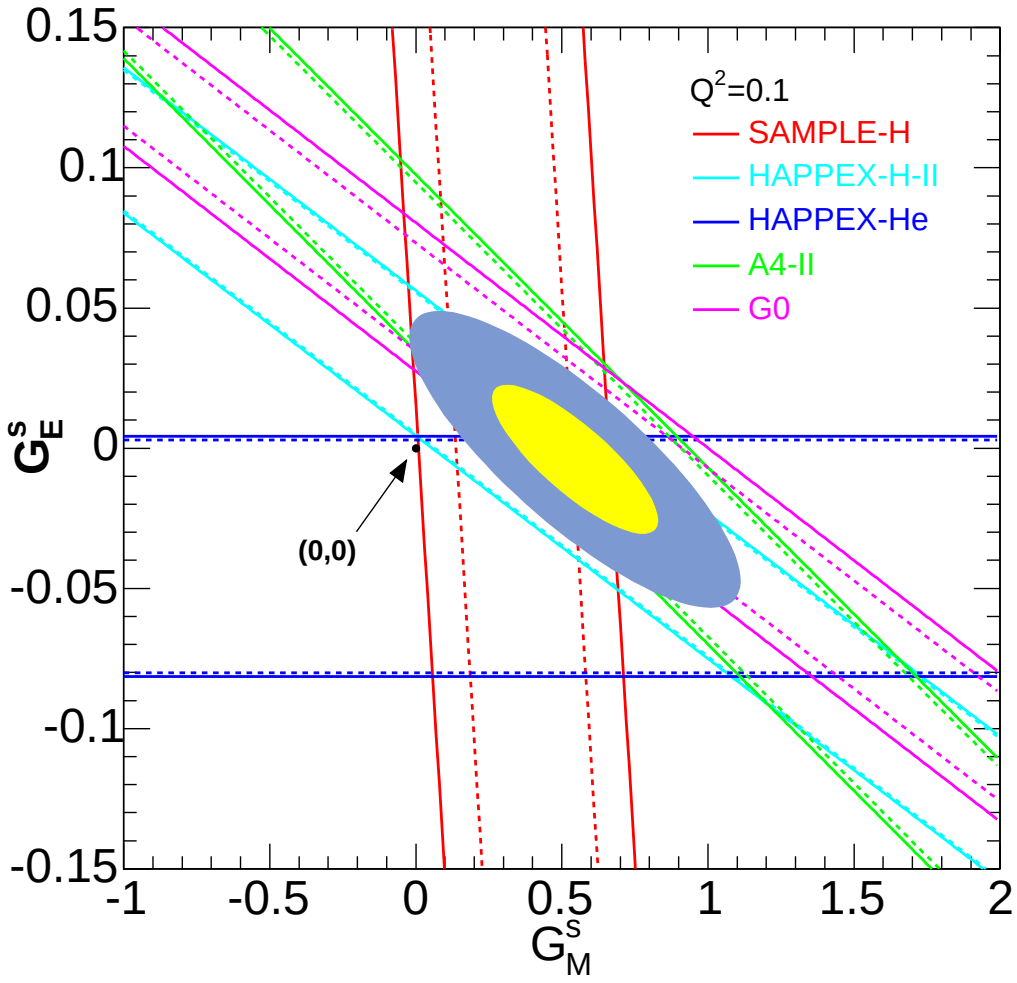

Figure 6.6: *The world data of $G_E^s + \eta G_M^s$ at $Q^2 = 0.1$ $(GeV/c)^2$. The form factors of Kelly are used. Different bands in the plot represent: HAPPEx-H-II [Ani05] (light blue), HAPPEx-He [Ani05b] (blue), PVA4-II [Maa05] (light green), SAMPLE [Spa04] (red) and G^0 [Arm05] (pink). The inner dashed lines and the outer solid lines represent the statistical and total experimental uncertainties for each measurement, respectively. The yellow and gray blue (dark) ellipses are the 1σ and 2σ error ellipses for the point of maximum likelihood of all experiments at $(G_E^s = -0.004, G_M^s = 0.55)$. The black point represents $G_E^s = G_M^s = 0$.*

will be treated separately.

Applying the above technique to the five measurements in Fig. 6.6, the best fit of $(G_E^s,\, G_M^s)$ is

$$G_E^s = -0.004 \pm 0.026\,, \quad G_M^s = 0.55 \pm 0.28$$

with a correlation of -0.82 between the two, and a minimum $\chi^2_{min} = 1.63$ with 3 degrees of freedom. Let us make some remarks at this point. First, the value of χ^2 quantitatively shows that the agreement among the five independent measurements is excellent, and the resulting G_M^s is large and positive at the $\sim 2\sigma$ level, Second, the five measurements used in this analysis have some slight differences ($<\sim 10\%$) in Q^2. One could try to shift the values of $G_E^s + \eta G_M^s$ to a common Q^2, by, e.g., assuming that the data scale with Q^2. This correction leaves the values of the separated G_E^s and G_M^s virtually unchanged. Third, in terms of probability, $\Delta\chi^2 = \chi^2 - \chi^2_{min}$ obeys the χ^2 distribution with 2 degrees of freedom [Bev92]. The 1σ error ellipse is shown as the yellow area in the figure; for a joint estimate of two parameters, the area enclosed by it corresponds to the 39.3% confidence interval. The gray blue (dark) ellipse is the 2σ ellipse, corresponding to a confidence interval of 86.5%. Fourth, $G_E^s = G_M^s = 0$ (shown as the black point in the figure) yields a $\Delta\chi^2 = \chi^2 - \chi^2_{min} = 10.1$, corresponding to a confidence level of only 0.6%. Although the model uncertainties have not yet been taken into account, this at least indicates the unlikeliness of the non-vector-strange hypothesis at this momentum transfer. Lastly, since the (electroweak) model uncertainty of $G_E^s + \eta G_M^s$ is dominated by the contribution of $R_A^{T=1}$ (Table 6.4), we perturb $R_A^{T=1}$ according to its uncertainty in Table 6.1 and re-evaluate $G_E^s + \eta G_M^s$ for each measurement, then repeat the least squares procedure described above. The resulting variation of G_E^s and G_M^s are ± 0.008 and ± 0.14 respectively. The non-negligible variation of G_M^s is primarily driven by the variation of the SAMPLE result, since as a backward measurement it is more sensitive to the axial form factor. The uncertainty due to the nucleon EM form factors was evaluated similarly by applying Arrington or Friedrich-Walcher parameterization globally to all the measurements. The effect of this turns out to be negligible compared with the electroweak model uncertainty. Therefore, we arrive at the final extracted G_E^s and G_M^s at $Q^2 = 0.1$ (GeV/c)^2:

$$G_E^s(Q^2 = 0.1) = -0.004 \pm 0.026 \pm 0.008\,, \tag{6.20}$$

$$G_M^s(Q^2 = 0.1) = 0.55 \pm 0.28 \pm 0.14\,. \tag{6.21}$$

In each expression, the first uncertainty is experimental, and the second is the model variation. Let us recall Eqns. 2.27 and 2.28, that G_E^s and G_M^s need to be both multiplied by $-\frac{1}{3}$, the electric charge of the strange quark, to give the strangeness contribution to the nucleon form factors. Taking this into account, the measured value of G_M^s implies that the contribution of strange quarks to the proton's magnetic form factor is $\sim -10\%$.

The world data at $Q^2 = 0.23$ and 0.477 $(\mathrm{GeV/c})^2$ are plotted in Figs. 6.7(a) and 6.7(b), respectively. At $Q^2 = 0.23$ $(\mathrm{GeV/c})^2$, following the same procedure as

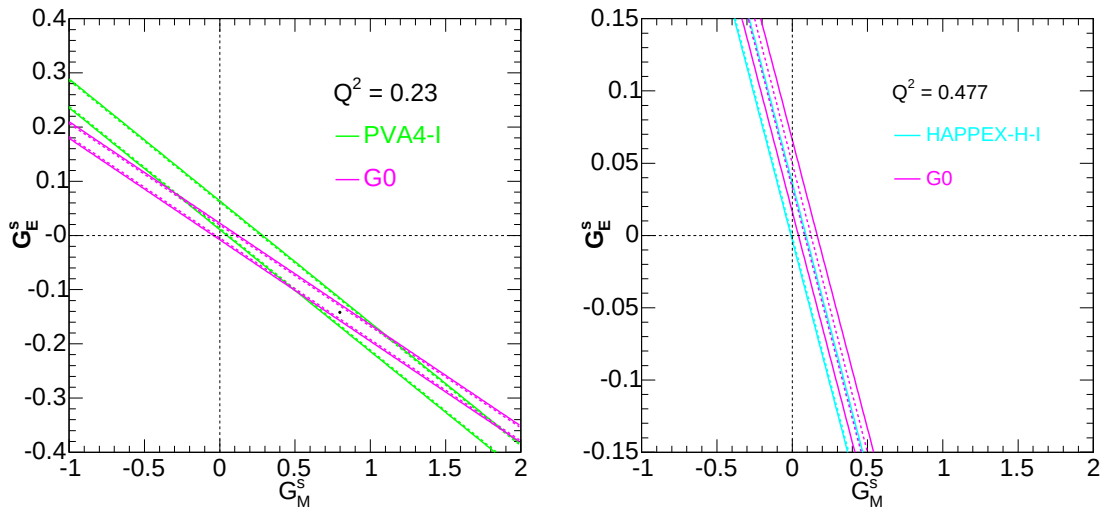

(a) $Q^2 = 0.23$ $(\mathrm{GeV/c})^2$ (b) $Q^2 = 0.48$ $(\mathrm{GeV/c})^2$

Figure 6.7: *The world data of $G_E^s + \eta G_M^s$ at $Q^2 = 0.23$ and 0.477 $(GeV/c)^2$. The Kelly form factors are used in both plots. The dashed and solid lines represent the statistical and total experimental errors for individual measurements. The pink, light green and light blue bands are the results from G^0 [Arm05], PVA4-I [Maa04] and HAPPEx-I [Ani04], respectively. The black point in (a) is the best fit of (G_E^s, G_M^s) at $Q^2 = 0.23$ $(GeV/c)^2$. (0,0) are indicated in both figures.*

above, we get

$$G_E^s(Q^2 = 0.23) = -0.14 \pm 0.16\,, \quad G_M^s(Q^2 = 0.23) = 0.80 \pm 0.81\,, \tag{6.22}$$

with the small model uncertainties neglected. Although with large uncertainties, these results tend to favor a negative G_E^s and a positive G_M^s. For the measurements at $Q^2 = 0.477$ (GeV/c)^2, the G^0 forward and HAPPEx-I had very similar kinematics, therefore the two bands in Fig 6.7(b) are almost parallel. As one can see, the agreement between the two measurements is excellent, but no separation of G_E^s and G_M^s can be made.

To summarize, the G^0 forward angle results have been compared with previous measurements and yield excellent agreement. A global analysis of the world data has been made, which yields a positive G_M^s at the 2σ level at $Q^2 = 0.1$ (GeV/c)^2, implying that the strange quark contributes to the proton magnetic form factor to $\sim -10\%$, and favors a positive G_M^s and negative G_E^s at $Q^2 = 0.23$ (GeV/c)^2.

6.3.3 Speculations Regarding the Q^2 Behavior of G_E^s and G_M^s, and Comments on Theoretical Predictions

Now let us take the full data set of G^0 (Fig. 6.3) into account and speculate about the Q^2 behavior of G_E^s and G_M^s in a wider scope. One should first note that the linear combination coefficient η is a function of the four-momentum transfer, and for the G^0 kinematics $\eta \sim 0.94Q^2$. In other words, in the G^0 forward angle data, the weight of G_M^s increases monotonically with Q^2. Let us first focus on the low Q^2 regions in Fig. 6.3. The positive data in this region can be understood from the results in Fig. 6.6, that a *positive and large* G_M^s drives the data in the positive direction, despite the smallness of η. As Q^2 increases to 0.2 (GeV/c)^2, despite the increase of η, the combined $G_E^s + \eta G_M^s$ decreases, which suggests that either G_E^s or G_M^s rapidly becomes negative. The results from Fig. 6.7(a) imply that it is G_E^s that becomes negative, while G_M^s stays positive. As Q^2 increases beyond 0.3 (GeV/c)^2, the data exhibit a significant positive trend, and they are consistent with HAPPEx-H-I measurement(Fig. 6.7(b)). Since η has been fairly large there, it is possible that G_M^s is *positive* in this region.

Lest one becomes too aggressive about the above picture, one should be aware

of the sparsity and level of precision of the existing world data. Therefore the arguments above can at best be speculations, except for the statement at $Q^2 = 0.1$ (GeV/c)^2, which is reasonably well-grounded. The separation of G_E^s and G_M^s at other four-momentum transfers awaits the results from future experiments, which will be briefly introduced in Sec. 6.3.4.

Let us reiterate the physical interpretation of the signs of G_E^s and G_M^s, as discussed in Sec. 2.6. A *negative* G_E^s, which is favored by the G^0 and PVA4 data at $Q^2 = 0.23$ (GeV/c)^2, leads to a *positive* Sachs strangeness radius $\langle r_s^2 \rangle_E$, which implies that on average the s quark is spatially outside the $\bar{s}$ quark in the nucleon. Note that this is consistent with the well-known picture of the neutron charge distribution that it has a positively charged "core" and a negatively charged "skin". One should also note that this is contradictory to the naive kaon ($u\bar{s}$) cloud picture, which would infer an $\bar{s}$ outer layer. For G_M^s, a naive non-relativistic argument is given in [HRG00], implying that a kaon cloud picture would naturally lead a *negative* μ_s, which too is contradictory with the *positive* μ_s that the world data indicate. In this regard, the signs of G_M^s and G_E^s that are favored by the data are physically consistent.

It is precocious, however interesting, to compare the positive signs of μ_s and $\langle r_s^2 \rangle_E$ with the theoretical predictions summarized in Sec. 2.6. Among all the predictions that have been discussed, only the HBχPT calculation in [HKM99] (Sec. 2.6.1), the resonance saturation model in [RMI97] (Sec. 2.6.2), and a hybrid of VMD and kaon loop calculation in [Mei97] (Sec. 2.6.3) predicted positive signs for both quantities. The first one was a lowest order HBχPT calculation, which was later shown to become uncertain when the calculation was extended to higher order [Ham03]. The second calculation, as noted by the authors in [RMI97], was a conceptually inconsistent treatment. The last one was a calculation only looking at the OZI allowed ϕ meson coupling to the kaon loop, without the consideration of the ω–ϕ mixing, and the predicted values of μ_s and $\langle r_s^2 \rangle_E$ are very small. Even if one takes these predictions seriously, it is difficult to translate them into an intuitive and coherent physics picture.

Quite recently, an interesting idea has been proposed by Riska et al., who have considered the consequence of a five-quark $uuds\bar{s}$ wave function mixture in the proton under the assumption of spin dependent hyperfine interaction between quarks [ZR05, ARZ05, RZ05]. These authors show that in all possible five-quark configurations (with at most one quark orbitally excited), the lowest energy state is with $\bar{s}$ in the ground state and the $uuds$ subsystem in the P-state. This configuration leads to a positive G_M^s, and a negative G_E^s and Δs. This theoretical approach is still under active investigation, and it is certainly too early from the experimental perspective to draw conclusions. Nevertheless, this five quark picture is possibly one of the most intuitive theoretical treatments to date, and so far is experimentally favored.

6.3.4 Future Outlook

After the completion of the G^0 forward angle experiment in spring 2004, the worldwide program of parity violating electron scattering has been continuing, with the primary goal to further elucidate the physics situation of the nucleon vector strangeness.

The backward G^0 experiment [G0Bkw1, G0Bkw2] will soon be launched in Hall C at the Jefferson Lab. A schematic drawing of the G^0 backward setup is displayed in Fig. 6.8. The spectrometer is turned around with the polarity of the magnet reversed, selecting only backward-scattered negatively charged particles. Additional cryostat exit scintillation detectors (CED) and aerogel Čerenkov counters are installed to separate elastic and inelastic electrons, and negative pions. The G^0 backward running is currently planned at two values of four-momentum transfer: 0.63 (GeV/c)^2 and 0.23 (GeV/c)^2, with beam energies of 687 and 360 MeV respectively. Both measurements will be performed on hydrogen and deuterium targets, and in combination with the results obtained from the forward angle, a model independent separation of G_E^s, G_M^s and $G_A^{e(T=1)}$ can be made at these two kinematics. In Figs. 6.9 and 6.10, the expected uncertainties of G_E^s, G_M^s and $G_A^{e(T=1)}$ are shown. With projected accuracies, the measurement at Q^2 =0.63 (GeV/c)^2 will

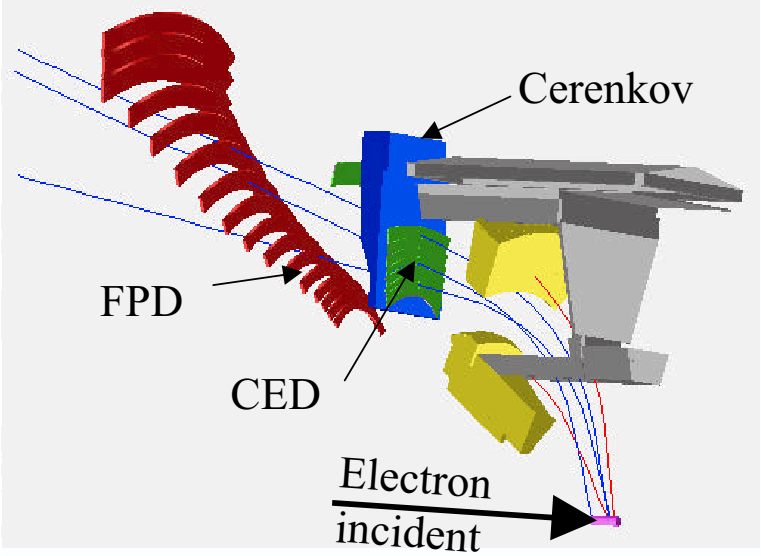

Figure 6.8: *G^0 backward angle setup. Electrons and negative pions are selected by the magnetic field. One segment of the spectrometer is shown. Additional cryostat exit scintillation detectors (green), in combination with the focal plane detectors (brown) allow the separation of elastic and inelastic electrons. The π^- background is vetoed by aerogel Čerenkov counters (blue).*

provide insight into the origin of the significant positive trend measured in high Q^2 region in the G^0 forward data (Fig. 6.3), and the lower Q^2 measurement will further constrain the intriguing possibility of a negative G_E^s and a positive G_M^s implied by the PVA4 and G^0 forward angle measurements (Fig. 6.7(a)). Additional important physics outcomes from the G^0 backward experiment include measurements of parity violating asymmetries in the $N \rightarrow \Delta$ transition [Wel04], and in π^- photoproduction from deuterium [Mar04], as well as a measurement of the vector analyzing power in elastic electron-proton scattering [Wel04b].

The PVA4 backward experiment began data collection in Jan. 2006 at the Mainz Microtron in Germany. Similar to the G^0 backward running, PVA4 uses the same detector package as described in Sec. 3.3 at backward angle. The collaboration plans to measure backward asymmetries on both hydrogen and deuterium at $Q^2 = 0.23$ (GeV/c)^2 [Maa06p]. The expected precision of the PVA4 backward measurement is comparable to that of the G^0 backward experiment at the same Q^2. With two measurements employing distinctly different techniques made at the same

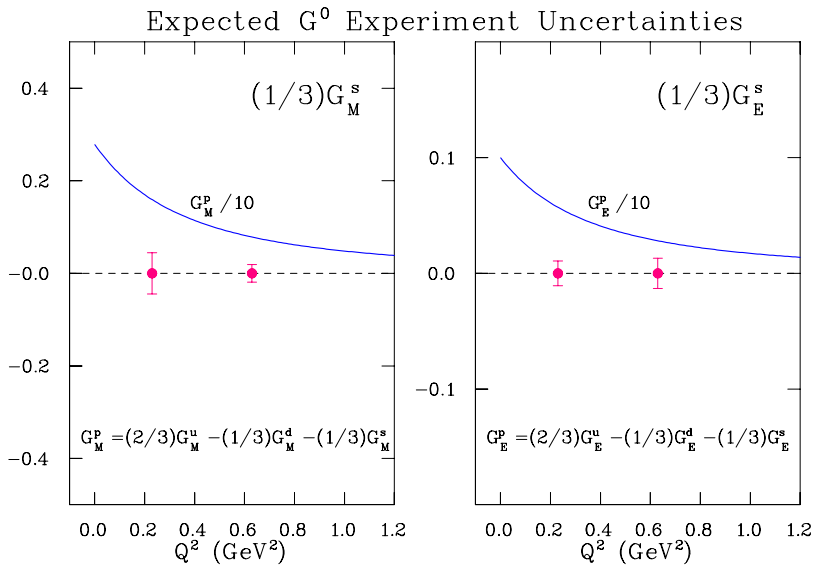

Figure 6.9: *Expected uncertainties of G_M^s (left) and G_E^s (right) at Q^2 =0.63 and 0.23 (GeV/c)^2 by combining the forward and backward G^0 measurements. Both form factors have been multiplied by a factor of 1/3 to reflect their contribution to the nucleon electromagnetic form factors. To indicate the scale, the corresponding proton form factors are divided by 10 and overlaid in the plots (blue curves). Figure taken from [G0Bkw2].*

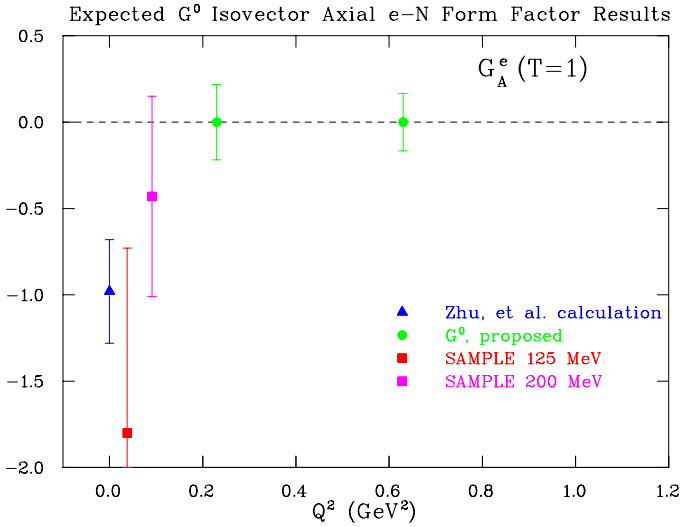

Figure 6.10: *Same as Fig. 6.9 but for $G_A^{e(T=1)}$. The two existing SAMPLE measurements [Bei05] (square), and a theoretical calculation at zero momentum transfer [Zhu00] (triangle) are also shown. Figure taken from [G0Bkw2].*

Q^2, crucial crosschecks on the results can be made, and if in agreement, the physics at this Q^2 point will be answered with a much improved accuracy.

The HAPPEx collaboration has recently completed a low Q^2 ($\sim$0.1 (GeV/c)^2) measurement on hydrogen and ^{4}He, with results expected soon. With a much improved statistical precision at $Q^2 = 0.1$ (GeV/c)^2, their measurements will yield a very precise determination of the sign and size of G_M^s, and a better constrained G_E^s at this Q^2 point. Currently another HAPPEx forward angle measurement at $Q^2 = 0.63$ (GeV/c)^2 is planned in Hall A of the Jefferson Lab [Pas05]. Such a high precision forward angle measurement, together with the G^0 forward and backward measurements, will provide a more accurate separation of G_E^s, G_M^s and $G_A^{e(T=1)}$ at this value of Q^2.

6.3.5 Conclusions

The strangeness content of the nucleon's electromagnetic form factors, G_E^s and G_M^s, describes the contribution of the strange sea to the charge and magnetization distributions of the nucleon. They open a unique window to study the role of the non-perturbative QCD sea in low energy nucleon properties. Parity violating electron scattering provides a powerful neutral weak probe, which interacts with quarks inside the nucleon differently, as compared to the widely used electromagnetic probe. By combining measurements from these two probes, the contribution from strange quarks can be separated.

In this work, we have reported one of such parity violating electron scattering measurement, the G^0 forward angle experiment. The parity violating asymmetry of elastic electron-proton scattering has been measured over a wide range of four-momentum transfer from 0.12 to 1.0 (GeV/c)^2, from which linear combinations of G_E^s and G_M^s have been determined in 18 Q^2 bins. The G^0 forward angle data, combined with previous world data, indicate that both G_E^s and G_M^s are non-zero and Q^2-dependent. In particular, the world data have led to a positive G_M^s at the 2σ level at $Q^2 = 0.1$ (GeV/c)^2, implying a $\sim -10\%$ contribution of strange quarks to the proton's magnetic form factor. The data also suggest that G_E^s might be negative around $Q^2 = 0.2$ (GeV/c)^2. These results are contradictory with most of the theoretical predictions presently available. Several similar types of experiments

are in preparation or ongoing. These measurements together will lead to a clean separation of G_E^s and G_M^s at different momentum transfers in the near future, and deepen our understanding of this intriguing problem in strong interactions.

Appendix A

Leakage Correction

A.1 Introduction

At the CEBAF electron source, three separate laser systems illuminate a common photo-cathode to produce electrons for the three experimental halls. Under normal running conditions, all 3 lasers are pulsed at the same repetition rate of 499 MHz, with their phases separated by $\pi/3$. During the G^0 running period, the Hall C Ti:Sapphire laser was pulsed at a repetition rate of 31.1875 MHz instead.

Although the driving pulse lengths of the seed lasers are generally short ($\sim<$ 100 ps), the outputs of the lasers require finite time to be turned off. Therefore, there is a small component of the beam in one hall due to the tails of all three lasers. In addition, each laser has a DC component due to the amplified spontaneous emission (ASE), which creates a DC electron beam for all halls. These are the two sources of the so-called leakage beam, and their difference will become apparent in our discussion of the G^0 laser leakage in Sec. A.3.2. Just to set the scale, the nominal G^0 beam current is $\sim$40 μA, and a typical leakage current is $\sim$50 nA.

Because of the different time structure, the detected rates due to the G^0 and leakage beams have different time of flight (ToF) distributions. In Figure A.1(a), a typical measured ToF spectrum is overlaid with the spectrum due to the leakage beam. As one can see, the leakage spectrum is nearly DC with only $\sim$0.1% of the total rate. However if the leakage beam has a large charge asymmetry, it will introduce a time-of-flight dependent false asymmetry contamination to the measured asymmetry. Qualitatively, this can be understood from an exaggerated cartoon shown in Fig. A.1(b). Suppose that the average rates due to the G^0 and leakage beams are the same, but with different shapes as illustrated, and the two beams have non-zero but exact opposite charge asymmetries. Then there will be a false asymmetry in the measured spectrum, which is different in sign for the "leakage"

and "proton" regions in Fig. A.1(b), despite the fact that the integrated charge asymmetry of the combined beam is zero.

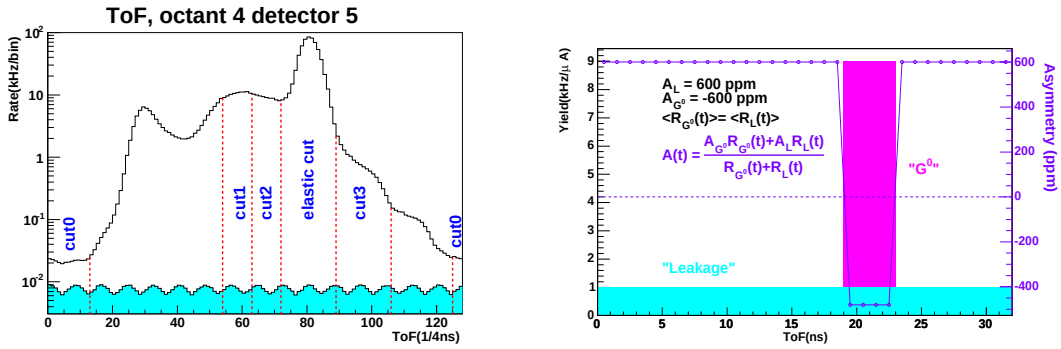

(a) *Measured ToF spectrum.* (b) *A exaggerated "cartoon" of (a).*

Figure A.1: *(a): an example of the measured (black) and leakage (light blue) ToF spectra. The y axis is in log scale. (b): a cartoon to illustrate the origin of the false asymmetry arising from the leakage (see text).*

A.2 The False Asymmetry Due to the Leakage

A.2.1 Formulation

The beam charge monitors (BCMs) in the hall measure the integrated beam charge every 1/30 s, so they are only sensitive to the combined average current of the G^0 and leakage beams. Therefore we have

$$I_m = I_{G^0} + I_L \,, \tag{A.1}$$

where I_{G^0}, I_L, and I_m are the average current of the G^0, leakage, and combined beams, respectively. The time-encoding electronics also measure a combined rate $R_m(t)$ as

$$R_m(t) = R_{G^0}(t) + R_L(t) = Y_{G^0}(t) I_{G^0} + Y_L(t) I_L \,, \tag{A.2}$$

where $R_{G^0}(t)(Y_{G^0}(t))$ and $R_L(t)(Y_L(t))$ are the rates (yields) due to the G^0 and leakage beams, respectively. Note we have treated the beam currents as DC and

absorbed the time-structure into the rates and yields ($R(t)$ and $Y(t)$). Since the leakage rate is approximately flat, the leakage yield $Y_L(t)$ is simply the time average of the G^0 yield $Y_{G^0}(t)$.

Normalizing the total rate by the beam current, we have

$$Y_m(t) = \frac{R_m(t)}{I_m} = \frac{Y_{G^0}(t) I_{G^0} + Y_L(t) I_L}{I_{G^0} + I_L}\,, \tag{A.3}$$

in which $Y_m(t)$ is raw experimental yield. This equation can be cast in terms of asymmetries as

$$\begin{aligned} A_m(t) = & \frac{R_{G^0}(t)}{R_m(t)} A_{Y_{G^0}}(t) + \frac{R_L(t)}{R_m(t)} A_{Y_L}(t) \\ & + \left(\frac{R_{G^0}(t)}{R_m(t)} - \frac{I_{G^0}}{I_m} \right) A_{I_{G^0}} + \left(\frac{R_L(t)}{R_m(t)} - \frac{I_L}{I_m} \right) A_{I_L}\,, \end{aligned} \tag{A.4}$$

where $A_{Y_{G^0}}(t)$ and $A_{Y_L}(t)$ are the physics asymmetries of the G^0 and leakage yields, and $A_{I_{G^0}}$ and A_{I_L} are the charge asymmetries of the G^0 and leakage beams, respectively. Again, due to the flatness of the leakage rate, its physics asymmetry $A_{Y_L}(t)$ is the time average of the G^0 asymmetry $A_{Y_{G^0}}(t)$. The origin of the leakage problem becomes apparent from Eqn. A.4. The different time structures of the G^0 and leakage beams lead to the following inequalities:

$$\frac{R_{G^0}(t)}{R_m(t)} \neq \frac{I_{G^0}}{I_m}\,, \quad \frac{R_L(t)}{R_m(t)} \neq \frac{I_L}{I_m}\,, \text{and } A_{Y_{G^0}}(t) \neq A_{Y_L}(t)\,, \tag{A.5}$$

so the measured asymmetry is no longer the physics asymmetry of G^0. Conversely if the G^0 and leakage beams were to have the same time structure, there would be no false asymmetry, however large the leakage current and asymmetry were. Furthermore, it can be observed from Eqn. A.4 that if the charge asymmetries of the G^0 and leakage beam are the same, the leakage contamination also approximately vanishes. Therefore, any *component* of the leakage beam can be omitted if it shares the same charge asymmetry as the main beam, regardless of its detailed time structure. This fact will later be used in Sec. A.3.2.

The total charge asymmetry measured by the beam charge monitors is an average of the charge asymmetries of the G^0 and leakage beams, weighted by the corresponding currents:

$$A_{I_m} = \frac{I_{G^0}}{I_m} A_{I_{G^0}} + \frac{I_L}{I_m} A_{I_L} \,. \tag{A.6}$$

So Eqn. A.4 can be rewritten as

$$A_m(t) = \frac{R_{G^0}(t)}{R_m(t)} A_{Y_{G^0}}(t) + \frac{R_L(t)}{R_m(t)} A_{Y_L}(t) + \left(\frac{R_{G^0}(t)}{R_m(t)} \frac{I_m}{I_{G^0}} - 1 \right) A_{I_m} - \frac{I_L}{I_{G^0}} \frac{1 - \frac{Y_L(t)}{Y_{G^0}(t)}}{1 + \frac{R_L(t)}{R_{G^0}(t)}} A_{I_L} \tag{A.7}$$

For the four terms on the right hand side of this equation, each is an asymmetry quantity with a coupling coefficient. Let us first make some order of magnitude estimate for these asymmetries. $A_{Y_{G^0}}(t)$, the physics asymmetry of G^0, has a typical size of -5 ppm, and varies with t. The physics asymmetry of the leakage yield, $A_{Y_L}(t)$, is the time average of $A_{Y_{G^0}}(t)$, therefore has a similar size. The measured charge asymmetry A_{I_m} is very small (~ 0 ppm) due to the charge asymmetry feedback system, and the charge asymmetry of the leakage beam A_{I_L} has a typical size of $\sim$600 ppm. The coupling coefficients $\frac{R_{G^0}(t)}{R_m(t)}$ and $\frac{R_L(t)}{R_m(t)}$ are the ratio of the G^0 and leakage rates to the total measured rate. For most regions on the ToF spectrum, $\frac{R_L}{R_m} \simeq \frac{R_L}{R_{G^0}} \ll 1$ and $\frac{R_{G^0}}{R_m} \simeq 1$. With the above preparation, Eqn. A.7 can be simplified to become

$$A_m(t) \simeq A_{Y_{G^0}}(t) - \frac{I_L}{I_{G^0}} \left(1 - \frac{Y_L(t)}{Y_{G^0}(t)} \right) A_{I_L} = A_{Y_{G^0}}(t) - \left(\frac{I_L}{I_{G^0}} - \frac{R_L}{R_{G^0}} \right) A_{I_L} \,, \tag{A.8}$$

or

$$A_{false}(t) = A_m(t) - A_{Y_{G^0}}(t) \simeq -\frac{I_L}{I_{G^0}} \left(1 - \frac{Y_L(t)}{Y_{G^0}(t)} \right) A_{I_L} \,, \tag{A.9}$$

in which $A_{false}(t)$ is the false asymmetry due to the leakage. One observes that $A_{false}(t)$ is inversely proportional to the G^0 beam current I_{G^0}; this fits into the intuitive picture that the more the G^0 current, the less contribution the leakage contamination. Furthermore, $A_{false}(t)$ is proportional to the leakage current I_L and its asymmetry A_{I_L}. Therefore the key of the leakage correction is to properly

determine these two quantities.

A.2.2 Examples

We shall consider the leakage contamination for a few representative regions of the ToF spectrum. The standard PID cuts have been defined in Sec. 5.2.1 and some of them are indicated in Fig. A.1(a). For the leakage discussion, we introduce one more cut, "cut0", defined as the "forbidden" low rate regions of the ToF (very early and very late regions in the spectrum). This cut is also indicated in Fig. A.1(a), and it is only defined for the French detectors 1 through 7 (see details in Sec. A.4.1).

For the nominal beam current (40 μA) with a typical leakage current (50 nA), the average measured, leakage, and G^0 rates per detector[†], R_m, R_L and R_{G^0}, and $\frac{R_L}{R_m}$ of these cuts are shown in Table A.1. The measurement of leakage rate R_L will be discussed in Sec. A.3. Also tabulated are the current-normalized yields Y_{G^0} and Y_L, and their ratio $\frac{Y_L}{Y_{G^0}}$. From the table, one can see that for all the cuts except cut0,

PID cuts	R_m	R_L	R_{G^0}	$\frac{R_L}{R_m}$	Y_{G^0}	Y_L	$\frac{Y_L}{Y_{G^0}}$
total	1137.4	1.422	1136.0	1.25×10^{-3}	28.43	28.43	1
proton	647.1	0.2054	646.9	3.17×10^{-4}	16.19	4.11	0.25
cut1	102.3	0.1164	102.2	1.14×10^{-3}	2.56	2.33	0.91
cut2	106.2	0.1165	106.1	1.10×10^{-3}	2.66	2.33	0.88
cut3	20.15	0.1920	20.0	9.53×10^{-3}	0.5	3.84	7.69
cut0	5.97	2.47	3.5	0.41	0.09	49.4	563.87

Table A.1: *The average measured, leakage, and G^0 rates per detector, R_m, R_L, and R_{G^0}, in various PID cuts, and the ratio $\frac{R_L}{R_m}$, with a beam current of 40 μA and a leakage current of 50 nA. The (beam current) normalized G^0 and leakage yields, Y_{G^0} and Y_L, and their ratio $\frac{Y_L}{Y_{G^0}}$ are also tabulated. The rates and yields are in units of kHz and kHz/μA, respectively.*

$\frac{R_L}{R_m} \simeq \frac{R_L}{R_{G^0}} \ll 1$, and $\frac{R_{G^0}}{R_m} \simeq 1$, which justify the assumptions that lead to Eqns. A.8 and A.9.

[†]For cut0, the rates are integrated over all four French octants of detectors 1 through 7.

The factor $\left(1 - \frac{Y_L(t)}{Y_{G^0}(t)}\right)$ in Eqn. A.9 is of particular interest. It shows that the sign of A_{false} in a given time bin t depends on the relative sizes of Y_L (the time averaged yield), and the G^0 yield in this bin. For example, in the proton cut where $Y_{G^0} \gg Y_L$, A_{false} and the leakage charge asymmetry A_{I_L} are opposite in sign. This can be qualitatively understood from the fact that the charge asymmetry of G^0, $A_{I_{G^0}}$, which is opposite in sign to A_{I_L} (as a consequence of the zero overall charge asymmetry), has a dominating contribution in this region. For cut3, on the other hand, since $Y_{G^0} \ll Y_L$, therefore A_{I_L} dominates and A_{false} shares the same sign as A_{I_L}.

In the extreme situation that the whole G^0 spectrum is just a δ function proton peak and the leakage beam is continuous, Eqn. A.9 becomes $A_{false} \simeq -\frac{I_L}{I_{G^0}} A_{I_L} \sim -1.25 \times 10^{-3} A_{I_L}$. In reality, the proton peak is not infinitely narrow, and using the values in Table A.1, we have

$$A_{false} \simeq -0.75 \frac{I_L}{I_{G^0}} A_{I_L} \sim -9.4 \times 10^{-4} A_{I_L} .$$

Cut3 sits on the other side of the hierarchy; according to Table A.1, $\frac{Y_L}{Y_{G^0}} = 7.69$. Therefore Eqn. A.9 can be written as

$$A_{false} \simeq -(1 - 7.69) \frac{I_L}{I_{G^0}} A_{I_L} \sim +8.4 \times 10^{-3} A_{I_L} .$$

Note again that the false asymmetry changes sign from the proton cut to cut3.

Cut0 can be regarded as the extreme of cut3, where $\frac{Y_L}{Y_{G^0}} \sim 600 \gg 1$, or $\frac{R_L}{R_{G^0}} \gg \frac{I_L}{I_{G^0}}$ (see Table A.1). However the approximations leading to Eqn. A.8 no longer hold. So we start from Eqn. A.7 instead and simplify it as

$$A_{cut0} \simeq \frac{R_{L,cut0}}{R_{m,cut0}} A_{I_L} , \tag{A.10}$$

where $R_{m,cut0}$ and $R_{L,cut0}$ are the measured and leakage rates in cut0, respectively.

A.3 Direct Measurements of the Leakage Current and Asymmetry

A.3.1 Leakage Due to the A and B Lasers

The leakage currents and asymmetries due to individual lasers can be directly measured. For the A and B lasers, this was accomplished by turning off the G^0 laser; then the leakage beam is completely responsible for the rates in Hall C. The leakage current was computed by scaling the leakage rate measured by the FPDs by that measured at the nominal G^0 beam current (40 μA). The luminosity detectors (see Appendix C), operating at a high gain mode, were used to measure the leakage charge asymmetry [†]. The leakage spectra due to the A and B lasers are shown in Fig. A.2(a). Although both exhibit 2 ns beam structure, the width of the structure is small compared to the width of typical PID cuts (4 – 5 ns). Therefore, in the following discussion, the A and B leakages will be treated as flat.

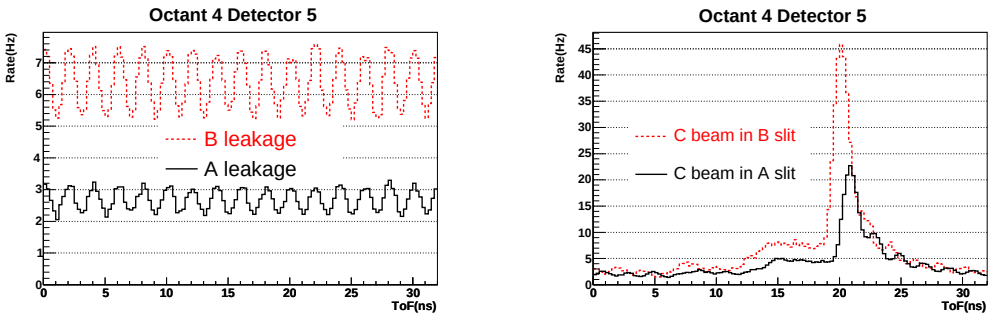

(a) *A and B leakage.* (b) *C Leakage.*

Figure A.2: *Measured leakage ToF spectra with the G^0 spectrometer. (a): leakage ToF spectra due to the A (black solid) and B (red dash) lasers; (b): leakage ToF spectra due to the G^0 laser itself when putting the main pulse onto the A (black solid) and B (red dash) slits. See text for details.*

[†]Due to the much higher particle rate, LUMIs measure A_{I_L} with better statistical precision compared with the FPDs.

A.3.2 Leakage Due to the G^0 Laser

To access the leakage component of the G^0 beam, we "rotated" its main pulses onto either the A or B slit (see a discussion of the CEBAF injector operation in Sec. 4.2.1.1), which allows a measurement of the leakage in Hall C.

Figure A.2(b) shows the spectra of FPD 5 when the main G^0 pulse was put onto either the A or B slit. In either case, one observes a G^0-like spectrum superimposed on a flat background. Apparently they correspond to the two sources of the leakage introduced in Sec. A.1: the G^0 structure is due to the tail of the G^0 main pulse and the flat background is due to the ASE. We speculate that after the G^0 laser delivers its main pulse (∼50 ps FWHM), there exists a long tail, the electrons from which are bunched as well and leak through when the C slit rotates around, which makes an obvious G^0 structure in the leakage spectrum. From Fig. A.2(b), one observes that when the G^0 main pulse was put onto the B slit, the height of the proton peak measured in Hall C is roughly a factor of two compared with that of the A slit, which indicates that the chopper rotation sequence is A-B-C and the decay time constant of the G^0 beam tail is $\sim$ 1 ns [†]. Therefore under the normal situation when the G^0 main pulse is put onto the C slit, one can project from Fig. A.2(b) that each time the chopper rotates around to the C slit, the tail of the G^0 laser would make secondary peaks of 11.2, 1.4, 0.17, $\cdots$ Hz subsequently. The first one would be $\frac{11.2 \text{ Hz}}{100 \text{ kHz}} \sim 1 \times 10^{-4}$ of the main peak in strength, and offset by 2 ns, and so on. The multiple decaying peaks right after the elastic peaks in Fig. A.2(b) indeed support this picture.

The G^0 main laser pulse and its tail arise from the same driving pulse, so they share the same initial properties upon arriving onto the helicity pockels cell and the photocathode. Hence they should interact with the control devices in the same way at the source, and it is very likely that the tail of the G^0 beam has the same charge

[†] One should treat the interpretation of this $\sim$ 1 ns time constant with some care; it is not the time scale to turn off the laser. When the G^0 main pulse is put onto the B slit, it would have made an elastic proton peak with a height of ∼100 kHz per bin, were there a G^0 detector in Hall B. $\frac{2}{3}$ ns later when the chopper rotates to the C slit, the residual G^0 structure only contains a peak of 45 Hz (see Fig. A.2(b)). So the initial "turning-off" of the G^0 main pulse is very sharp. Only the residual tail of the main pulse is decaying slowly.

asymmetry as the main pulse. Then as discussed in Sec. A.2.1, the G^0 tail can be simply omitted. Therefore only the ASE (DC) component of the G^0 leakage will be considered in the following analysis [†].

One subtlety persists however. Due to the existence of the G^0 tail, the measured leakage rates and asymmetries are not the same rates and asymmetries of the ASE component. From Fig. A.2(b), we estimate that the average contribution of the ASE component is 50% of the total G^0 leakage. Therefore we use 50% of the measured FPD rate to calculate the current of the ASE leakage, and the ASE asymmetry is evaluated as twice the asymmetry measured by the LUMIs.

A.3.3 Summary

Based on the discussion above, we will treat the leakage ToFs from all three lasers as flat. This important fact later enables us to apply the measurement in cut0 to correct for the leakage throughout the ToF spectra.

In Table A.2 the results (I_L and A_{I_L}) of the direct leakage measurements of individual lasers are summarized. For the G^0 laser, the extracted values for the ASE components are shown. The last column, R_{cut0}, is the total measured rate in cut0, which will be discussed in Sec. A.4. During all of these measurements, we had kept the G^0 parity feedback devices at their normal settings to mimic the normal running conditions. As one can see, the leakage beam properties are not stable over time.

A.4 Cut0 Technique

A.4.1 Definition

Due to the unstable properties of the leakage beam, using the direct measurements in Table A.2 to correct for the full data set is not an acceptable option.

[†] An unlikely scenario would be that the G^0 tails has a large charge asymmetry — let us assume that $A_q \sim 300$ ppm (see Table A.2). The fraction of the first child peak underneath the main peak is $\sim 0.5 \times 10^{-4}$ (a factor 0.5 is to take into account the 2 ns offset). Then A_{false} due to the tail is only $0.5 \times 10^{-4} \times 300$ ppm ~ 0.015ppm, much less than the systematic uncertainty we assign later in Sec. A.5.

Run	A/B/C	IHWP	I_L(nA)	A_{I_L}(ppm)	R_{cut0}(kHz)
22071	A	IN	13	−1879(20)	0.63
22120	A	IN	12	−1121(20)	0.56
21865	B	IN	38	−690(20)	1.85
21866	B	OUT	39	435(20)	1.90
22030	B	OUT	31	−511(10)	1.51
22062	B	IN	16	−162(20)	0.76
22067	B	IN	15	−101(22)	0.70
22102	B	IN	21	40(10)	1.03
22104	B	IN	14	559(17)	0.69
22152	B	OUT	26	−565(10)	1.26
22162	B	OUT	29	−974(11)	1.46
22028	C	OUT	11	−446(52)	0.54
22029	C	OUT	11	−204(54)	0.54
22060	C	IN	11	−614(58)	0.55
22069	C	IN	12	−370(70)	0.57
22096	C	IN	11	−200(14)	0.55
22106	C	IN	12	686(32)	0.60

Table A.2: *Direct measurements of the leakage currents and asymmetries for individual lasers. Column "IHWP" gives the state of the insertable halfwave plate during the measurements. For the C leakage, the extracted values for the ASE components of the G^0 laser are shown (see text).*

Instead we needed to find a "leakage monitor" in the data that allows us to determine the leakage current I_L and its asymmetry A_{I_L} at the time the data were taken.

Let us consider a given region of the measured spectrum, "cutX", with a total rate $R_{m,cutX}$ and a leakage rate $R_{L,cutX}$. For simplicity, let us further assume that the charge asymmetry of the G^0 beam and the physics asymmetry in "cutX" is negligible. Then as in Eqn. A.10, the measured asymmetry in cutX is simply a

diluted leakage asymmetry, so that the leakage asymmetry can be expressed as

$$A_{I_L} \simeq \frac{R_{m,cutX}}{R_{L,cutX}} A_{cutX} \,,$$

which has a statistical uncertainty of

$$\sigma(A_{I_L}) \propto \frac{R_{m,cutX}}{R_{L,cutX}} \frac{1}{\sqrt{R_{m,cutX}}} \propto \frac{\sqrt{R_{m,cutX}}}{R_{L,cutX}} \,. \tag{A.11}$$

Therefore, for a given $R_{L,cutX}$, the less the rate in cutX, the more sensitive it is to the leakage asymmetry. As indicated in Fig. A.1(a), since the prompt charged particles from the main beam pulses hardly reach the "forbidden" regions before the pion peak or after the "shoulder" of the slowest deuterons knocked out from the aluminum target cells (the regions after the "deuteron" band in Fig. 5.16(b)), these regions ("cut0") are selected as the leakage monitor. The cuts were made on the first 7 French detectors (0.25 ns timing resolution). For higher numbered detectors, the slowest deuterons wrap around the spectrum and overlap with the rising edge of the pion peak, so those detectors were omitted.

A.4.2 Cut0 Rate Decomposition

Although the prompt charged particles cannot reach cut0, the main G^0 pulses can produce a photon/neutron background, which creates extra events in cut0 unrelated to the leakage beam. Let us denote the leakage rates in cut0 due to the A, B lasers as R_{A_L}, R_{B_L}, respectively, and that due to the G^0 laser as $R_{C_{std}}$, which contains a a leakage component R_{C_L} and a background component $R_{C_{bkg}}$. To quantify the sensitivity of cut0 to the leakage beam, one needs to know the fraction of this extra background rate $R_{C_{bkg}}$ in cut0.

The rate decomposition in cut0 was studied with a series of leakage and standard measurements. We made direct leakage measurements with the A and B lasers, or the B laser alone, interleaved with standard measurements with both the G^0 and the leakage beams present. The difference of rates in cut0 between the above two

measurements gives the total C component $R_{C_{std}}$. As mentioned in Sec. A.3.2, the measurement of the G^0 leakage is made by putting the G^0 main pulses onto the A or B slit, which was destructive to other halls. From the few measurements we made (Table A.2), R_{C_L} seems quite stable over time. Therefore we simply took the average value of R_{C_L}, 0.56 kHz, and subtracted this from $R_{C_{std}}$ to get $R_{C_{bkg}}$.

In Table A.3 the decomposed rates in cut0 are listed. R_{B_L} appears to change with time, so in Table A.3 only a typical value is given, whereas R_{A_L} and R_{C_L} seem to be stable[†]. The extracted background component $R_{C_{bkg}}$ in cut0 is ~3.5 kHz for 40 μA G^0 beam, therefore contributing to ~60% of the rate in cut0, and is stable at the level of $\pm$ 5%.

Component	Rate in cut0 (kHz)	$I_{L,direct}$ (nA)
R_{A_L}	0.60	12.2
R_{B_L}	1.4	28.4
R_{C_L}	0.56	11.3
$R_{C_{bkg}}$	3.5(0.17)	n/a

Table A.3: *Rate decomposition in cut0 with 40 μA G^0 beam and a typical leakage beam. The leakage current I_L from each laser is also shown in the table. The uncertainty of the non-leakage C rate $R_{C_{bkg}}$ (in the parenthesis) is taken as the standard deviation of $R_{C_{bkg}}$ from all measurements.*

A.4.3 From Cut0 to the Leakage Current and Asymmetry

Once $R_{C_{bkg}} = 3.5$ kHz is established, the total leakage rate in cut0, $R_{L,cut0}$, can be extracted as

$$R_{L,cut0} = R_{m,cut0} - R_{C_{bkg}} = R_{m,cut0} - 3.5 \text{ kHz}\,, \tag{A.12}$$

[†]It appears that the leakage current I_L is related to the beam current that goes into each hall. Throughout these measurements we kept the main G^0 beam at 40 μA and Hall A was running stably with ~90 μA. But Hall B ran with various different beam currents.

for any standard G^0 run. Since the leakage spectrum is flat, the leakage current I_L can then be deduced by dividing the leakage rate in cut0 by the average G^0 yield as

$$I_{L,deduced} = \frac{R_{L,cut0}/w_{cut0}}{\langle Y_{G^0}^{1-7} \rangle} = \frac{(R_{m,cut0} - 3.5 \text{ kHz})/w_{cut0}}{\langle Y_{G^0}^{1-7} \rangle}, \tag{A.13}$$

where w_{cut0} is the total width ($\sim$58 ns) of cut0 (French FPDs 1 through 7), and $\langle Y_{G^0}^{1-7} \rangle$ is the time averaged yield of the G^0 rates per ns in the same detectors.

In parallel, applying Eqn. A.10, A_{I_L} can be deduced from $A_{m,cut0}$ as

$$A_{I_L} = \frac{R_{m,cut0}}{R_{L,cut0}} A_{cut0} = \frac{R_{m,cut0}}{R_{m,cut0} - 3.5 \text{ kHz}} A_{cut0}\,. \tag{A.14}$$

A.4.4 Certification of the Cut0 Technique

In the previous section, a procedure to determine I_L and A_{I_L} from cut0 was presented. The goal of this section is to certify this technique.

As discussed in Sec. A.4.2, we have made interleaved direct leakage measurements and the standard measurements to study the rate composition in cut0. Here we will use the same measurements to compare the *deduced* leakage current I_L and its asymmetry A_{I_L} from cut0 with those *directly measured* in the adjacent leakage runs.

For each standard run, the leakage current ($I_{L,deduced}$) is deduced with Eqn. A.13. For the interleaved (non-destructive) leakage runs, the leakage current due to Halls A and B, I_{AB_L}, is directly measured. The total leakage current due to all 3 lasers, $I_{L,direct}$, is then obtained by combining I_{AB_L} with a constant $I_{C_L} = 11.3$ nA (see Table A.3).

In Fig. A.3, $I_{L,deduced}$ is plotted against $I_{L,direct}$. A 3 nA uncertainty is assigned on each data point of $I_{L,deduced}$ based on the uncertainty of $R_{C_{bkg}}$ (Table A.3). A fit of $I_{L,deduced} = \alpha I_{L,direct}$ is also made, from which one can see that $I_{L,deduced}$ and $I_{L,direct}$ agree within a few percent.

A similar analysis can be performed for the *deduced* and *direct* leakage asymmetries, $A_{I_{L,deduced}}$ and $A_{I_{L,direct}}$. For the standard runs, $A_{I_{L,deduced}}$ is calculated using

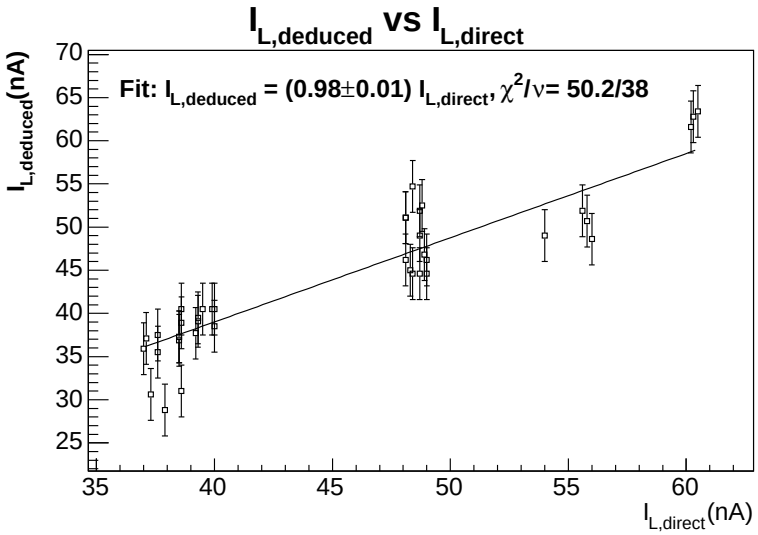

Figure A.3: *The deduced leakage current $I_{L,deduced}$ vs. the directly measured leakage current $I_{L,direct}$. See text for details.*

Eqn. A.10. For the direct measurements, once again the (non-destructive) leakage runs only allow us to measure the leakage asymmetry from Halls A and B, $A_{I_{AB_L}}$. For the leakage asymmetry due to the G^0 laser, $A_{I_{C_L}}$, there are only six (destructive) measurements available (Table A.2) — we apply them to six consecutive sets of runs correspondingly. Then the overall direct leakage asymmetry is obtained by averaging $A_{I_{AB_L}}$ and $A_{I_{C_L}}$, weighted by the corresponding current components.

In Fig. A.4, $A_{I_{L,deduced}}$ versus $A_{I_{L,direct}}$ is shown, with the fit of $A_{I_{L,deduced}} = \alpha A_{I_{L,direct}}$ overlaid. The statistical uncertainty of the slope is inflated by the value of the square root of the reduced χ^2, to effectively take into account the systematic effects. From the slope and the (inflated) uncertainty of the fit, 1.12 ± 0.22, one concludes that $A_{I_{L,deduced}}$ is verified to agree with $A_{I_{L,direct}}$ at the level of 22%.

A.4.5 Leakage Situation During the Entire G^0 Production Period

The leakage current and asymmetry deduced from cut0 during the entire G^0 data taking period are shown in Figure A.5. The average I_L and A_{I_L} for each insertable halfwave plate state are plotted against the run number. On average I_L ~50 nA and $A_{I_L} \sim +570$ ppm, after correcting for the beam polarization (0.737)

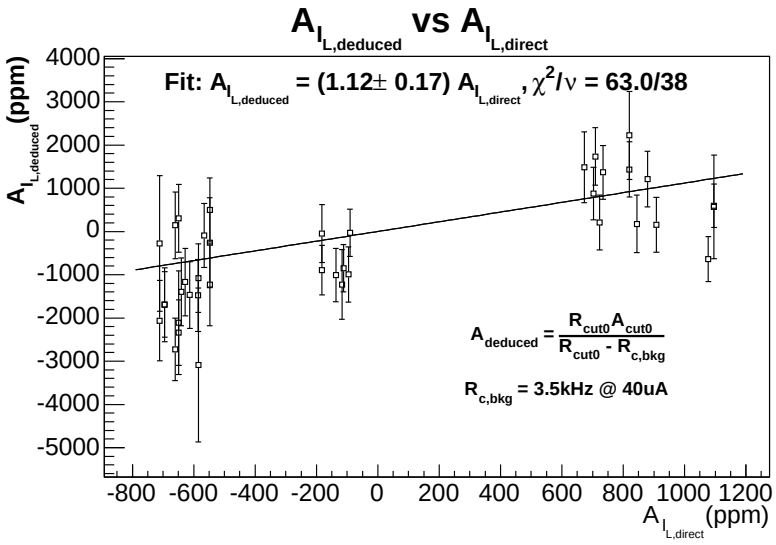

Figure A.4: *The deduced leakage charge asymmetry $A_{I_{L,deduced}}$ vs. that from the direct measurement, $A_{I_{L,direct}}$. The uncertainty of the slope (0.17) is purely statistical. See text for details.*

and the blinding factor (0.8056). The statistical uncertainty of A_{I_L} (combining both IHWP states) is $\sim$5% of A_{I_L}. Furthermore, one observes that both I_L and A_{I_L} were changing throughout the period. Interestingly, A_{I_L} has a sign flip around run 21400, corresponding to when Hall A resumed running; and it was this large false asymmetry that led us to realize the leakage problem.

A.5 Correction to the Leakage Effects and Its Systematic Uncertainty

A.5.1 Effectiveness of the Correction

Eqn. A.9 can be rewritten as

$$A_{Y_{G^0}}(t) = A_m(t) + \Delta\,, \quad \Delta \equiv -A_{false} \simeq \frac{I_L}{I_{G^0}}\left(1 - \frac{Y_L(t)}{Y_{G^0}(t)}\right) A_{I_L}\,, \tag{A.15}$$

in which Δ is the correction for the leakage. The correction was made to the production data on a run-by-run basis. The average asymmetry of each ToF bin or PID cut was corrected according to Eqn. A.15, with the leakage current I_L and

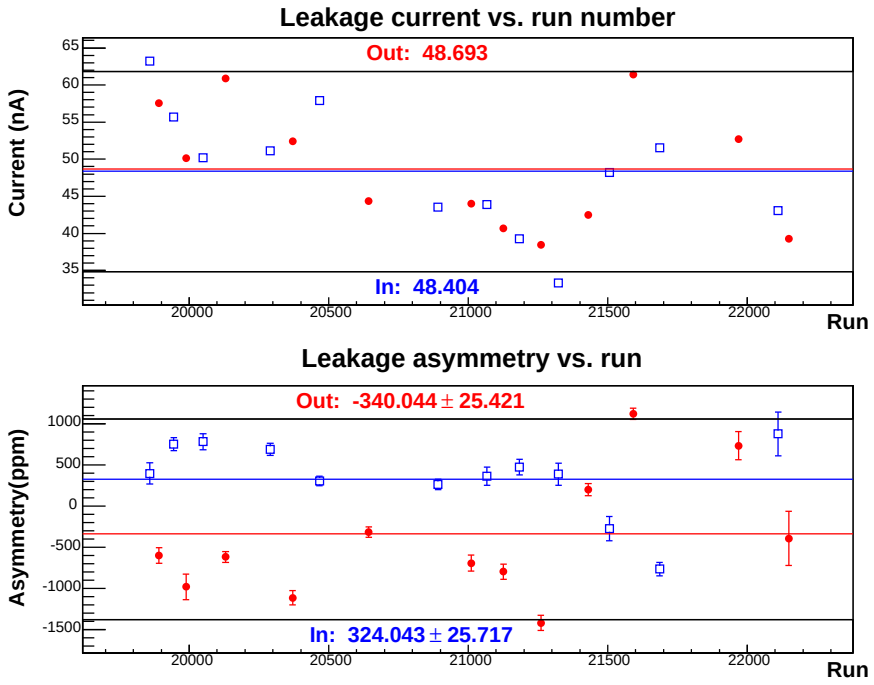

Figure A.5: *The leakage current and asymmetry vs. the run number during the entire experiment. Data are grouped according to the state of the insertable halfwave plate: [blue open squares = "IN", red solid circles = "OUT"]. The leakage asymmetries shown on the plot are not corrected for the beam polarization (0.737) nor the blinding factor (0.8056).*

its asymmetry A_{I_L} computed from the measurements of cut0 during the same run using Eqns. A.13 and A.14.

In Figs. A.6(a) and A.6(b) the average asymmetries of the proton (integrated over all FPDs), before and after the leakage correction, are plotted vs. the run number. Figs. A.7(a) and A.7(b) are the same plots for cut3. One can see the raw data clearly drift after run 21400, corresponding to the sign flip of the leakage asymmetry A_{I_L} due to Hall A. Furthermore, the leakage asymmetry drives the measured proton and cut3 asymmetries in opposite directions, as expected from the discussion in Sec. A.2.2. After the correction, the statistical agreement among the results for different periods is much improved, as indicated by the reduced χ^2 in Figs. A.6(b) and A.7(b).

Another way of justifying the correction is to cross-compare the corrections made at various values of beam current, which, according to Eqn. A.15, would lead

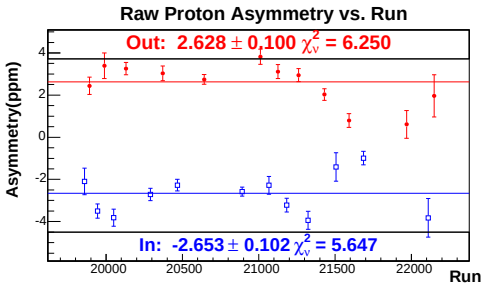

(a) *Raw asymmetry.*

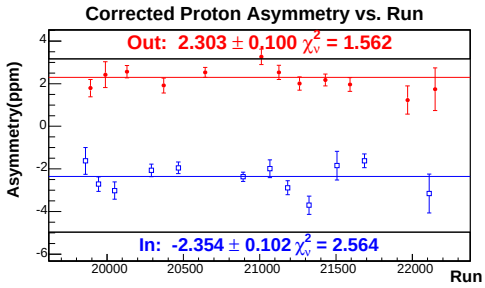

(b) *Leakage corrected asymmetry.*

Figure A.6: *The raw (a) and leakage corrected (b) asymmetries of the proton cut (averaged over all FPDs) vs. the run number. Each data point is an average value over a consecutive set of runs with a given state of the insertable halfwave plate: [blue open squares = "IN", red solid circles = "OUT"]. Asymmetries are not corrected for the beam polarization (0.737), nor the blinding factor (0.8056).*

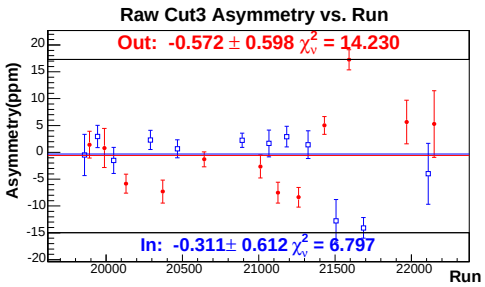

(a) *Raw asymmetry.*

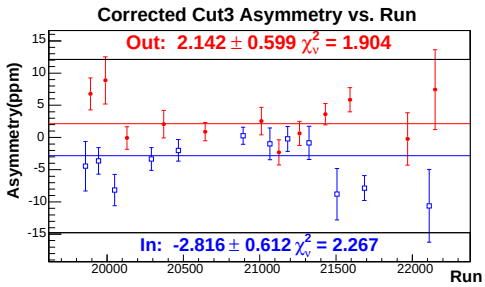

(b) *Leakage corrected asymmetry.*

Figure A.7: *Same as Fig. A.6 but for cut3. Asymmetries are not corrected for the beam polarization (0.737), nor the blinding factor (0.8056).*

to different sizes of the correction. On the other hand, if the corrections are ideal, the corrected asymmetries at all beam currents should converge to a constant physics asymmetry. Therefore, if one plots the raw asymmetry vs. the correction for various beam currents, ideally the data should lie on a straight line with a slope -1. Having a slope more negative than -1 indicates that the data have been under-corrected. This type of plot is shown in Figs. A.8(a) and A.8(b) for the proton cut and cut3, respectively. The slope of the linear fit of the proton cut agrees well with -1. The slope of cut3 suggests some under-correcting, but agrees with -1 to within 20%.

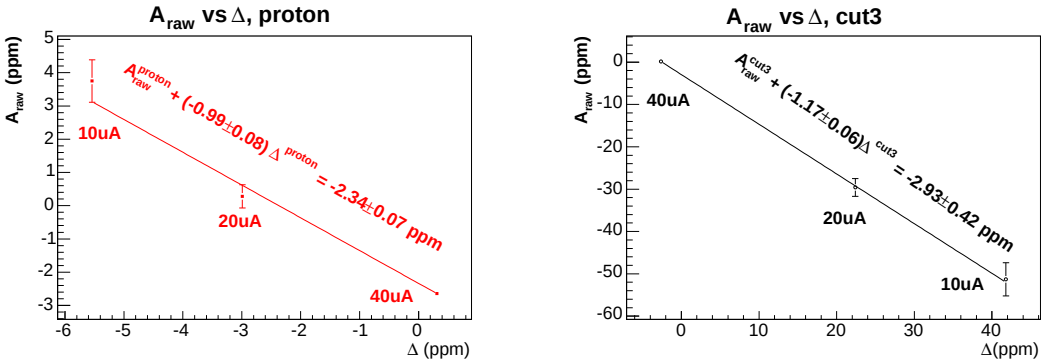

(a) *Proton cut.* (b) *Cut3.*

Figure A.8: *The raw asymmetry A_{raw} vs. the correction Δ for the proton cut (a) and cut3 (b).*

A.5.2 Systematic Uncertainty of the Correction

From Fig. A.3 one sees that the cut0 technique determines the leakage current very well, therefore the uncertainty of the correction is driven by how well the leakage asymmetry A_{I_L} is determined. In Sec. A.4.4 we discussed that during the "cut0 certification", A_{I_L} is determined at the level of 22%; this value is a natural assignment of the fractional uncertainty of the correction. Two more independent evaluations will be presented below.

Among all ToF regions other than cut0, cut3 is the most sensitive to the leakage. As already shown in Fig. A.7(b), the statistical property of A_{cut3} is significantly improved after the leakage correction. Nevertheless, the reduced χ^2 after the correction is $\sim$2, indicating that there is a residual systematic fluctuation in the data samples with roughly the same size as the statistical uncertainty, $\sim$0.6 ppm [†]. Therefore a systematic uncertainty of the correction of 0.6 ppm was assumed, which corresponds to a fractional uncertainty of 23% relative to the size of the correction (-2.61 ppm).

One can also use a different perspective of Figs A.8(a) and A.8(b) to evaluate the systematic uncertainty of the correction. For the three different beam cur-

[†] Conservatively we only take the statistical uncertainty of one IHWP (in/out) state.

rents in Figs A.8(a) and A.8(b), the averaged raw and corrected asymmetries (A_{raw} and A_{corr}) of the proton cut and cut3 are summarized in Table A.4. To increase the sensitivity, cut3 was also broken into two parts, labeled "cut3.1" (earlier) and "cut3.2" (later), and their asymmetries are tabulated as well. For each given beam current, the correction Δ is computed according to Eqn. A.15. In Table A.4 they do not simply scale with the inverse of the G^0 beam current, since the leakage asymmetries during the three measurement periods were different, nevertheless it is apparent that the correction is the smallest when $I_{G^0} = 40$ μA. If one further assumes that at $I_{G^0} = 40$ μA, the corrected asymmetry approaches the physics asymmetry, then for any other lower beam current, one can calculate the correction needed to bring the measured asymmetry to the physics asymmetry, Δ_{ideal}. The difference between Δ_{ideal} and Δ then gives an evaluation of the systematic uncertainty of the correction, $\sigma_{sys}(\Delta)$. The values of Δ, Δ_{ideal} and $\sigma_{sys}(\Delta)$ for various cuts are also summarized in Table A.4. The column $\frac{\sigma_{sys}(\Delta)}{\Delta}(\%)$ in the table gives the fractional uncertainty of the correction, and on average it is $\sim$17%. For reference, the statistical uncertainty of the raw asymmetry, $\sigma_{stat}(A_{raw})$, is listed in the last column.

All of the discussion above suggests that the systematic uncertainty of the leakage correction is $\sim$20% of the correction itself. In principle, the statistical uncertainty of A_{I_L} also contributes to the uncertainty of the correction. However, as shown in Fig. A.5, the statistical uncertainty of A_{I_L} throughout the entire experiment is $\sim$5% of A_{I_L}; this contribution is therefore omitted.

A.5.3 Uncertainty in the Elastic Asymmetry Due to the Leakage Correction

So far, we have discussed the leakage correction to the measured asymmetry. Based on the leakage corrected data, the background correction discussed in Sec. 5.3.6 is made, from which one obtains the elastic asymmetry A_e. The question now is, how does one translate the (20%) uncertainty of the leakage correction to the measured asymmetry into an uncertainty of the elastic asymmetry?

PID	I_b	A_{raw}	A_{corr}	Δ	Δ_{ideal}	$\sigma_{sys}(\Delta)$	$\frac{\sigma_{sys}(\Delta)}{\Delta}$ (%)	$\sigma_{stat}(A_m)$
proton	40	−2.64	−2.33	0.31	n/a	n/a	n/a	0.07
	20	0.28	−2.71	−2.99	−2.61	0.38	−12.7	0.35
	10	3.75	−1.79	−5.54	−6.08	−0.54	9.7	0.64
cut3	40	0.14	−2.47	−2.61	n/a	n/a	n/a	0.43
	20	−29.60	−7.20	22.40	27.13	4.73	21.1	2.10
	10	−51.30	−9.50	41.80	48.83	7.03	16.8	3.90
cut3.1	40	−0.86	−2.65	−1.79	n/a	n/a	n/a	0.53
	20	−22.30	−6.30	16.00	19.65	3.65	22.8	2.70
	10	−35.10	−4.70	30.40	32.45	2.05	6.7	4.90
cut3.2	40	2.07	−2.12	−4.19	n/a	n/a	n/a	0.74
	20	−40.78	−8.58	32.20	38.65	6.45	20.0	3.34
	10	−79.30	−17.80	61.50	77.18	15.67	25.5	6.44

Table A.4: *A summary of the leakage correction at different beam currents for various PID cuts. The proton cut and cut3 are defined in Sec. 5.2.1. Cut3.1 and cut3.2 are the earlier and later parts of cut3.* I_b *is the beam current in* μA. A_{raw} *and* A_{corr} *are the raw and leakage corrected asymmetries, respectively, with the correction* $\Delta \equiv A_{corr} - A_{raw}$. Δ_{ideal} *is an estimated "ideal" correction, and the systematic uncertainty of the correction,* $\sigma_{sys}(\Delta)$*, is estimated as the difference between* Δ *and* Δ_{ideal}. *For reference,* $\sigma_{stat}(A_{raw})$*, the statistical uncertainty of the measured asymmetry, is listed in the last column. All asymmetries, corrections, and uncertainties are in units of ppm, and are NOT corrected for the beam polarization and the blinding factor. See text for more details.*

In Sec. 5.3.6, the elastic asymmetry A_e is obtained as

$$A_e = \frac{A_m - f_b A_b}{1 - f_b}\,, \tag{A.16}$$

where A_m and A_b are the measured and background asymmetries in the elastic peak, and f_b is the fraction of the background yield in the total yield. The background asymmetry is evaluated in Sec. 5.3.6 by fitting or interpolating the measured background asymmetry away from the elastic peak. Here, without loss of generality, let us consider a simple model that $A_b = 0.5(A_{cut2} + A_{cut3})$. As shown in Eqn. A.15,

the leakage correction in any time bin or cut is proportional to $I_L A_{I_L}$. Since A_e is linear in A_m, A_{cut2} and A_{cut3}, the correction of A_e due to the leakage correction, Δ_e, is also proportional to $I_L A_{I_L}$. Therefore based on the discussion in Sec. A.5.2, the fractional uncertainty of Δ_e is also 20%. Δ_e can be determined "experimentally" by taking the difference between the elastic asymmetries $A_{e,corr}$ and $A_{e,raw}$, obtained by applying the same background correction procedure on the corrected and the raw data, and we get $\Delta_e = A_{e,corr} - A_{e,raw} = 0.71$ ppm [†], with the beam polarization corrected and the blinding factor removed. Therefore, the final systematic uncertainty of A_e due to the leakage correction, $\sigma(\Delta_e)$, is

$$\sigma(\Delta_e) = 20\%\Delta_e = 0.14 \text{ ppm}\,, \tag{A.17}$$

which is a global systematic uncertainty to all detectors (Q^2 bins).

[†]This quantity has some small difference ($\sim$5%) from detector to detector, which can be safely omitted.

Appendix B

Hyperon Simulation

B.1 Physics

The hyperons are baryons containing one or more strange quarks. They can be produced in electron-proton scattering via photo- or electro-production. For the G^0 forward angle kinematics, the dominant hyperon production channels are

$$\gamma^* + p \longrightarrow \Lambda + K^+ ,$$
$$\gamma^* + p \longrightarrow \Sigma^+ + K^0 ,$$
$$\gamma^* + p \longrightarrow \Sigma^0 + K^+ ,$$

where γ^* can be either a real or virtual photon. The relative photo-production rates for Λ, Σ^0 and Σ^+, measured by SAPHIR [Tra98, Law05], are approximately $\sim$3:2:1.

The hyperons (Y) undergo subsequent decays. The main decay modes of Λ and Σ^+ are non-leptonic weak decays, in which a hyperon turns into a nucleon (N) and a pion (π). For example, Λ has the following two non-leptonic decay channels:

$$\Lambda \longrightarrow p + \pi^- ,$$
$$\Lambda \longrightarrow n + \pi^0 .$$

Due to the parity violating nature of the weak interaction, the decays of Λ and Σ^+ are self-analyzing: if the hyperon Y is initially polarized with a polarization $\vec{P}$, the angular distribution of the outgoing nucleon with a momentum $\vec{k}_N$ in the rest frame of the hyperon can be expressed as

$$\frac{dN}{d\Omega} = \frac{N}{4\pi}(1 + \alpha P_Y \cos(\theta^{RF}_{\vec{P},\vec{k}_N})) , \tag{B.1}$$

in which $\theta^{RF}_{\vec{P},\vec{k}_N}$ is the angle between $\vec{P}$ and $\vec{k}_N$, and α is a parameter characterizing the parity violation of the decay, first introduced in [LY57].

The Σ^0 hyperon, on the other hand, is very short-lived ($\tau \sim 10^{-20}$ s), and it decays radiatively (M1) into a Λ:

$$\Sigma^0 \longrightarrow \Lambda + \gamma\,. \tag{B.2}$$

If Σ^0 is initially polarized, the daughter Λ retains $-\frac{1}{3}$ of the initial polarization [DP62], and the latter then decays weakly. Therefore, a Σ^0 with polarization P_{Σ^0} can be effectively viewed the same as a Λ with polarization $-\frac{1}{3}P_{\Sigma^0}$. In the remainder of this appendix, the polarization and the decay of Σ^0 will always refer to those of the daughter Λ. The lifetimes, decay channels, branching ratios, and the values of the weak decay parameter α for the three hyperons are summarized in Table B.1.

Hyperon	Lifetime (s)	Reaction	Branching Ratio (%)	α
Λ	2.632×10^{-10}	$\Lambda \to p + \pi^-$	63.9	0.642
		$\Lambda \to n + \pi^0$	35.8	0.65
Σ^+	0.8018×10^{-10}	$\Sigma^+ \to p + \pi^0$	51.57	-0.980
		$\Sigma^+ \to n + \pi^+$	48.31	0.068
Σ^0	7.4×10^{-20}	$\Sigma^0 \to \Lambda + \gamma$	100%	n/a

Table B.1: *The lifetimes of the Λ, Σ^+, and Σ^0 hyperons, their major decay channels, branching ratios, and the values of the α parameters for non-leptonic decays (for the Λ and Σ^+ only) [PDG04].*

The coordinate systems describing an electro-production of a hyperon and its subsequent weak decay are depicted in Fig. B.1. Three scattering planes are involved. The electron plane contains the incident and scattered momenta of the electron, with $\hat{z}$ being the unit vector along the virtual photon momentum, and $\hat{x}$ being the in-plane transverse direction. The hyperon production plane is defined by the virtual photon and the hyperon momenta. The azimuthal angle between the electron and hyperon production planes is Φ. The last plane, the hyperon decay plane, is made by the momenta of the nucleon and pion. The photo-production can

be depicted in the same way, except that both the electron and the photon are along $\hat{z}$, therefore the orientation of the electron plane is arbitrary.

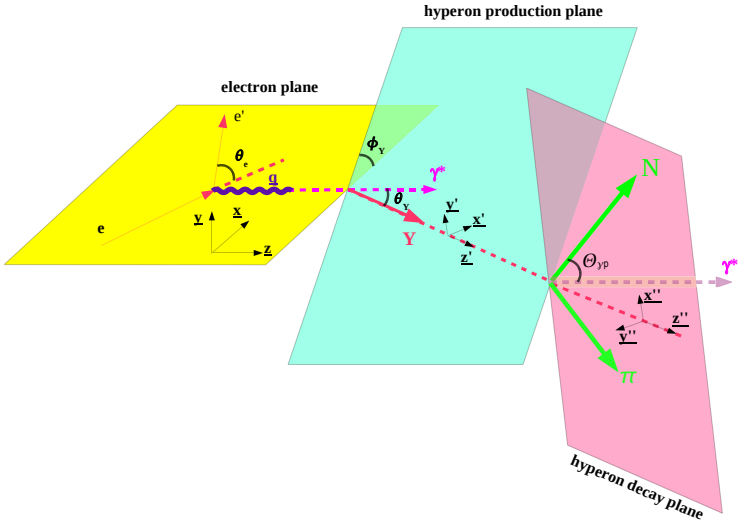

Figure B.1: *Coordinate systems describing an electro-production of a hyperon and its subsequent weak decay.*

Let us consider a longitudinally polarized electron beam with polarization P_b. The polarization of the produced hyperon ($\vec{P}$) is the sum of a (helicity-independent) induced polarization ($\vec{P}^0$), and a (helicity-dependent) transferred polarization ($\vec{P}'$):

$$\vec{P} = \vec{P}^0 \pm P_b \vec{P}' \,. \tag{B.3}$$

Both $\vec{P}^0$ and $\vec{P}'$ are defined with respect to a particular set of spin-quantization axes, of which one standard choice is ξ=$\hat{x}$,$\hat{y}$,$\hat{z}$ (see Figure B.1). Then with respect to ξ, Eqn. B.1 for each beam helicity state (+ or −) can be expressed as

$$\frac{dN^{\pm}_{\xi}}{d\Omega} = \frac{N}{4\pi}(1 + \alpha(P^0_{\xi} \pm P_b P'_{\xi}) \cos(\theta^{RF}_{\xi,\vec{k}_N}))\,, \tag{B.4}$$

in which P^0_{ξ} and P'_{ξ} are the components of $\vec{P}^0$ and $\vec{P}'$ along ξ, and $\theta^{RF}_{\xi,\vec{k}_N}$ is the angle between ξ and $\vec{k}_N$ in the rest frame of the hyperon. Therefore, the parity violating (PV) asymmetry of the decay nucleon cross section between two beam helicity states

is

$$A_\xi(\cos\theta^{RF}_{\xi,\vec{k}_N}) = \frac{\frac{dN^+_\xi}{d\Omega} - \frac{dN^-_\xi}{d\Omega}}{\frac{dN^+_\xi}{d\Omega} + \frac{dN^-_\xi}{d\Omega}} = \frac{\alpha P_b P'_\xi \cos(\theta^{RF}_{\xi,\vec{k}_N})}{1 + \alpha P^0_\xi \cos(\theta^{RF}_{\xi,\vec{k}_N})}\,. \tag{B.5}$$

In the case of G^0, since the scattered electron is not detected, only the Φ-averaged polarizations are relevant. As shown in [Sch98, Car03], after averaging over Φ , P^0_x, P^0_z and P'_y vanish identically. Therefore only $A_{\xi=\hat{x},\hat{z}}$ survive [†] and they take the simple form of

$$A_\xi = \alpha P_b P'_\xi \cos(\theta^{RF}_{\xi,\vec{k}_N})\,, \quad \xi = \hat{x}, \hat{z}\,. \tag{B.6}$$

Clearly, a measurement of A_ξ as a function of $\theta^{RF}_{\xi,\vec{k}_N}$ allows the extraction of P'_ξ.

The first measurement of P'_x and P'_z of Λ in the exclusive reaction $\vec{e}p \to e'K^+\vec{\Lambda}$ was given in [Car03], where it was reported that $P'_z \sim 0.75$ and $P'_x \sim 0$ over a wide range of invariant mass ($1.6 - 2.2$ GeV) and kaon angle. Taking into account the circular polarization of the virtual photon in their experiment (~ 0.8), one concludes that $\sim 100\%$ of the polarization of the photon gets transferred to the Λ. In this work, the same P'_z in [Car03] is assumed for the electro-production of the Λ . For photo-production, the average circular polarization of the Bremsstrahlung photons is calculated using the formulation in [OM59] to be ~ 0.85 for the G^0 kinematics, which yields a very similar value of P'_z. Therefore in both cases, we simply adopt $\vec{P}' \parallel \hat{z}$ and

$$P'_{z,\Lambda} = 0.75\,. \tag{B.7}$$

The transferred polarizations of Σ^0 and Σ^+ have not yet been directly measured, therefore some ad hoc assumptions have to be made. The interpretation of the observed polarization of Λ presented in [Car03], implies that Σ^0 is polarized along $-\hat{z}$, opposite to that of Λ [Car03, Mes05p]. Thus the polarization of the daughter Λ is also along $\hat{z}$ (but reduced by 1/3), and

$$P'_{z,\Sigma^0} = (-0.75)(-\frac{1}{3})\,, \tag{B.8}$$

[†] The Φ-averaging is implicit in the rest of this appendix.

is adopted in this work. As stated earlier, although we have used "Σ^0" in the subscript, P'_{z,Σ^0} refers to the polarization of the daughter Λ. For the Σ^+, we simply assume that Σ^+ shares the same polarization as Λ, so that

$$P'_{z,\Sigma^+} = 0.75\,. \tag{B.9}$$

To summarize, $\vec{P}'$ of all three hyperon channels have been taken to be along $\hat{z}$, and the asymmetry of the decay (Eqn. B.6) can be written explicitly as

$$A = \alpha P_b P'_z \cos(\theta^{RF}_{\hat{z},\vec{k}_N})\,, \tag{B.10}$$

in which $\theta^{RF}_{\hat{z},\vec{k}_N}$ is the angle between the decay nucleon momentum and $\hat{z}$ (the direction of the photon) in the rest frame of Λ or Σ^+. Note that the size of this asymmetry is of the order 1 ($\mathcal{O}(1)$), much larger compared to a typical asymmetry being measured by G^0 ($\mathcal{O}(10$ ppm)).

B.2 Monte Carlo Details

The contribution of hyperons to the G^0 experiment is studied with a detailed Monte Carlo (MC) simulation [Bei04, Liu06]. The simulation code was written based on a customized GEANT code developed for the G^0 experiment (G0GEANT, version May 2004) [GEA94, G0GEA99] [†]. In this section, a detailed discussion of the simulation will be given.

B.2.1 Cross Section Tuning

The source code of KAON-MAID (version 2002), which is an isobar model for kaon photo- and electro-production on the nucleon [KMAID], is implemented into our simulation to calculate the differential cross section of the photo-production of the hyperons, $\frac{d\sigma_\gamma}{d\Omega^K_{cm}}$. This cross section is a function of the photon energy E_γ, and

[†] A copy of the MC code can be downloaded from
`http://www.jlab.org/~jianglai/geant/g0geant_hyp_jianglai.tar.gz`.

θ^K_{cm} and ϕ^K_{cm}, the polar angles of the kaon in the center-of-momentum (CM) frame of the $\gamma - p$ system.

The KAON-MAID calculation is compared with the data from SAPHIR [Tra98, Law05] in Fig. B.2. One sees that it works well for Λ and Σ^0, but fails on Σ^+. However, as shown by the blue curve in the figure, if the KAON-MAID calculation of Σ^0 is scaled down by 0.3, it reproduces the Σ^+ data reasonably well. This recipe is therefore adopted for Σ^+. It should be noted that the KAON-MAID contains some empirical parameters that need to be tuned against the data. The SAPHIR's Σ^+ data are newer than the KAON-MAID 2002 release, which is the reason of the discrepancy in Fig. B.2, and should be fixable in the newer release of the code.

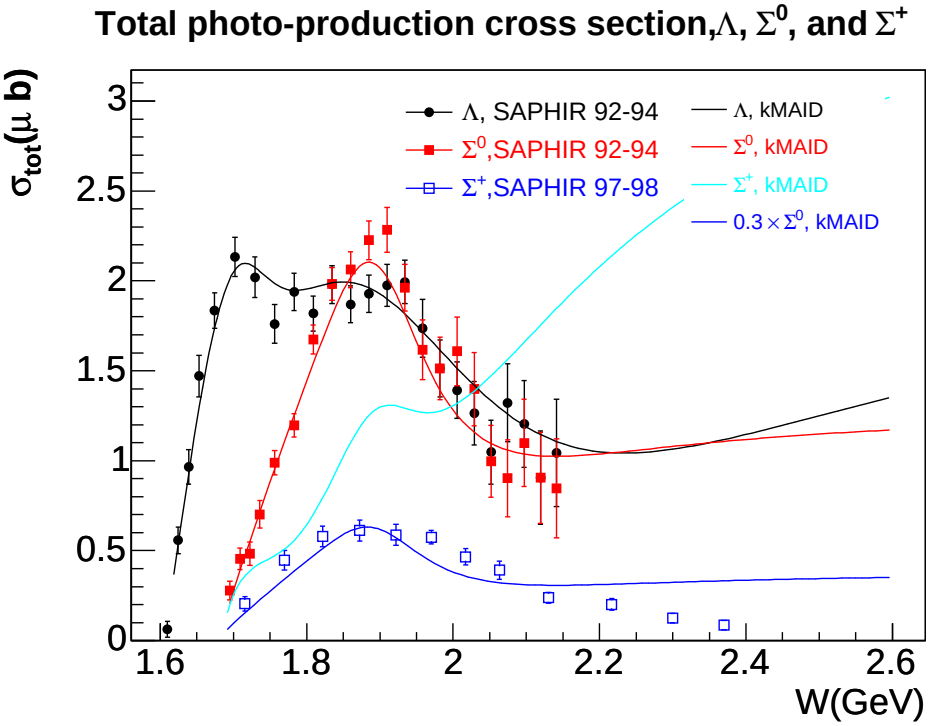

Figure B.2: *A comparison of the measured total cross section of the Λ (black solid circle) [Tra98], Σ^0 (red solid square) [Tra98], and Σ^+ (blue open square) [Law05], with the KAON-MAID calculations (curves) [KMAID], as functions of the invariant mass W. Various curves represent the KAON-MAID calculations of the Λ (black), Σ^0 (red), Σ^+ (light blue), and $0.3 \times \Sigma^0$ (blue).*

The invariant mass of the $\gamma - p$ system, W, is related to E_γ as

$$W = \sqrt{2E_\gamma M_p + M_p^2}\,, \tag{B.11}$$

in which M_p is the mass of the proton. For all three hyperon channels, the KAON-MAID predicts an increasing cross section for $W > 2.2$ GeV, which is not supported by the data. Therefore in our simulation, we take the value at $W = 2.2$ GeV and make a flat extrapolation to the region beyond it, i.e.,

$$\frac{d\sigma_\gamma}{d\Omega^K_{cm}}(W > 2.2 \text{ GeV}) = \frac{d\sigma_\gamma}{d\Omega^K_{cm}}(W = 2.2 \text{ GeV})\,. \tag{B.12}$$

B.2.2 Event Generator

Photo-production

In the case of photo-production, the minimum photon energy to create a KY final state is

$$E_{thres,r} = \frac{(M_K + M_Y)^2 - M_p^2}{2M_p}\,, \tag{B.13}$$

in which M_K and M_Y are the masses of the kaon and hyperon, respectively. E_γ of the Bremsstrahlung photon is randomly selected between $E_{thres,r}$ and the incident beam energy E_b (3.03 GeV). The standard formula to compute the Bremsstrahlung spectrum is given in [Mat73]. For a given radiator material, the number of photons per incident electron per unit photon energy and radiator thickness, $\frac{dN_\gamma}{dE_\gamma dt}$, is given as a function of E_b and E_γ. For each event, the reaction vertex is randomly chosen along the LH2 target, with a distance t_H relative to the upstream end of the hydrogen cell. The total photon flux, Γ_{real}, can be written as the sum of the flux from liquid hydrogen, and all the target components upstream of it:

$$\Gamma_{real} = \frac{dN_\gamma^H}{dE_\gamma dt} t_H + \frac{dN_\gamma^{Al}}{dE_\gamma dt} t_{Al} + \frac{dN_\gamma^{gHe}}{dE_\gamma dt} t_{gHe}\,, \tag{B.14}$$

in which $\frac{dN_\gamma^H}{dE_\gamma dt}$, $\frac{dN_\gamma^{Al}}{dE_\gamma dt}$ and $\frac{dN_\gamma^{gHe}}{dE_\gamma dt}$ are the Bremsstrahlung spectra of the liquid hydrogen, aluminum windows and gaseous helium, and t_{Al} and t_{gHe} are the total thickness of the upstream windows and the helium cell, respectively.

The polar angles of the hyperon in the $\gamma-p$ CM frame, θ_{cm} and ϕ_{cm}, are also randomly generated within the ranges from 0 to π and 0 to 2π, respectively. The three-fold differential cross section for photo-production can then be calculated as

$$\frac{d\sigma_\gamma}{dE_\gamma d\Omega_{cm}^K} = \Gamma_{real} \frac{d\sigma_\gamma}{d\Omega_{cm}^K}\,, \tag{B.15}$$

in which $\frac{d\sigma_\gamma}{d\Omega_{cm}^K}$ denotes the modified KAON-MAID cross section discussed in Sec. B.2.1. A weight is assigned to each event to reflect its reaction probability:

$$\text{weight} = \frac{d\sigma_\gamma}{dE_\gamma d\Omega_{cm}^K} \sin(\theta_{cm}) \Delta_{phase}\,, \tag{B.16}$$

in which the factor $\sin(\theta_{cm})$ is the Jacobian between $d\Omega_{cm}^K$ and $d\theta_{cm} d\phi_{cm}$. Δ_{phase} is the constant phase space volume into which the events were generated; in this case it is

$$\Delta_{phase} = (E_b - E_{thres,r}) 2\pi^2\,. \tag{B.17}$$

For a given set of $(E_\gamma, \theta_{cm}, \phi_{cm})$, the kinematics of the outgoing hyperon is determined. The lab momentum vector of the hyperon is fed to GEANT, after which the tracking starts.

Electro-production

The electro-production is treated in a very similar way. A virtual photon with energy E_{γ^*} is now in the place of a real photon. In addition to $(E_{\gamma^*}, \theta_{cm}, \phi_{cm})$, the lab polar angles of the scattered electron (relative to the natural coordinate of the experiment with beam along $\hat{z}$), θ_e and ϕ_e, are also randomly chosen within the ranges from 0 to $\pi/8$ [†] and 0 to 2π respectively.

[†]In principle, θ_e can go as high as $\pi/2$. We set the cutoff at $\pi/8$, beyond which the events hardly contribute to the rate.

To first order, the four-momentum transfer Q^2 is

$$Q^2 \simeq 4E_b E' \sin^2(\frac{\theta_e}{2}), \tag{B.18}$$

in which $E' = E_b - E_{\gamma^*}$ is the energy of the scattered electron. For a finite Q^2, the minimum energy of the photon to produce a KY state is now

$$E_{thres,v} = \frac{(M_K + M_Y)^2 + Q^2 - M_p^2}{2M_p},$$

which is larger than $E_{thres,r}$ in Eqn. B.13. To avoid having a different generator limit for each event, we choose E_{γ^*} randomly within $(E_{thres,r}, E_b)$, but set the event weight to zero if $E_{\gamma^*} < E_{thres,v}$.

The virtual photon flux $\Gamma_{virtual}$ is given by [Dre92]

$$\Gamma_{virtual}(E_b, E', Q^2) = \frac{\alpha}{2\pi^2}\frac{E'}{E_b}\frac{k_\gamma}{Q^2}\frac{1}{1-\epsilon}, \tag{B.19}$$

where α is the fine structure constant, $k_\gamma = (W^2 - M_p^2)/2M_p$, and

$$\epsilon = (1 + 2\frac{|\vec{q}|^2}{Q^2}\tan^2(\frac{\theta_e}{2}))^{-1},$$

in which $\vec{q}$ is the three-momentum vector of the virtual photon.

According to Eqn. B.18, $Q^2 \to 0$ when $\theta_e \to 0$, at which point Eqn. B.19 diverges. However, Eqn. B.18 is only an approximation when ignoring the mass of the electron. When keeping the lowest order of the electron mass in the expression [Mar04p], Q^2 becomes

$$Q^2 \simeq 4E_b E' \sin^2(\frac{\theta_e}{2}) + \frac{m_e^2(E_b - E')^2}{E_b E'}. \tag{B.20}$$

This expression is taken instead of Eqn. B.18 to remove the singularity at $\theta_e = 0$.

The five-fold differential electro-production cross section [Dre92] is then

$$\frac{d\sigma}{dE_{\gamma^*}d\Omega_e d\Omega^K_{cm}} = \Gamma_{virtual}(E_b, E', Q^2)\frac{d\sigma_\gamma}{d\Omega^K_{cm}}\,, \tag{B.21}$$

and the event weight is

$$\text{weight} = \frac{d\sigma}{dE_{\gamma^*}d\Omega_e d\Omega^K_{cm}}\sin(\theta^K_{cm})\sin(\theta_e)\Delta_{phase}\,, \tag{B.22}$$

$$\Delta_{phase} = (E_b - E_{thres,r})\frac{\pi^4}{2}\,. \tag{B.23}$$

It is noteworthy that in the case of electro-production, the hyperon CM angles (θ_{cm}, ϕ_{cm}) are defined in the "photon coordinate", i.e. they are relative to the photon momentum $\vec{q}$ and the electron plane. Therefore, after obtaining the hyperon momentum in the lab frame with respect to the photon coordinate, one has to make vector rotations to obtain the momentum vector in the natural lab coordinate (with beam along $\hat{z}$).

B.2.3 Weak Decay Vertex and the Asymmetry Calculation

A flow diagram of the event processing in the simulation is displayed in Fig. B.3. After the event generation, the hyperon is tracked by GEANT through the media. All secondary trackings are activated in this simulation. Some of the hyperons interact with the target materials hadronically and disappear into pions and nucleons. If these particles or their secondaries make it into the detectors, they are assumed to not carry a PV asymmetry. Occasionally, hyperons will scatter elastically and remain in the final state; we shall also ignore the PV asymmetry of its subsequent weak decay, since the polarization of the hyperon after the scattering becomes uncertain. Therefore, the only events of interest are those in which the hyperons decay directly, then the daughter nucleons or pions make direct or secondary hits into the detectors.

The hyperon decay is handled internally by GEANT. However, GEANT only treats the hyperon as unpolarized and the decay is carried out isotropically (no parity

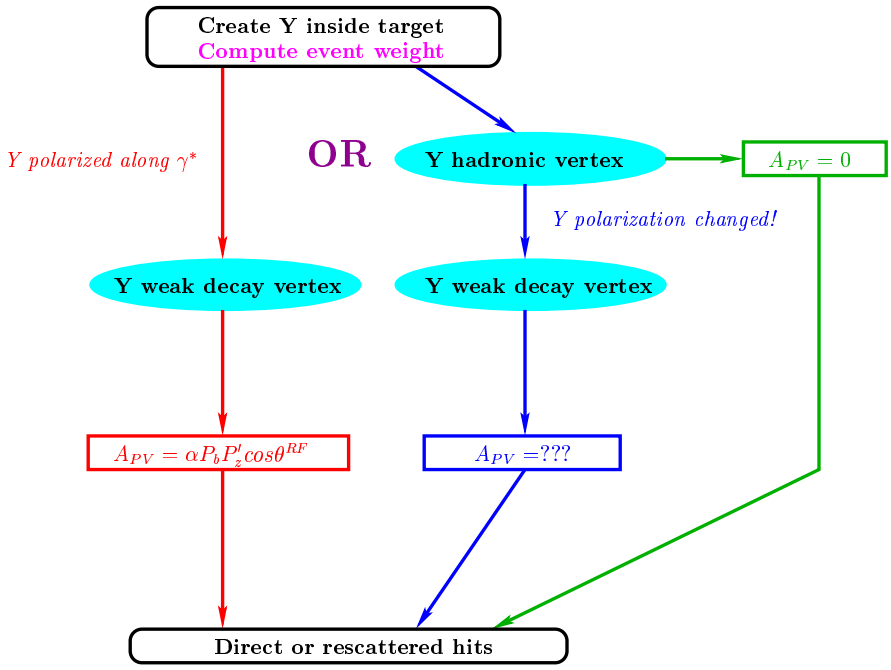

Figure B.3: *A flow diagram of the treatment of various types of hyperon events at the tracking time, and the calculation of the parity violating asymmetry.*

violation). Therefore at the weak decay vertex, we calculated a PV asymmetry manually according to Eqn. B.10, with the values of P'_z of each hyperon channel taken from Eqn. B.7, B.8 or B.9. Note that $\theta^{RF}_{\hat{z},\vec{k}_N}$ in Eqn. B.10 is the rest frame angle of the momentum of the nucleon relative to the photon direction, even if a decay pion is tracked. Since after the weak decay, all secondary processes do not yield additional asymmetries (nucleons will rescatter hadronically, and pions do not carry net spin), the asymmetry at the weak decay vertex is shared by all subsequent tracks in this event.

B.2.4 Coincidence Hit Selection

A particle making it into an active volume in GEANT is called a "hit" and the information of the hit, such as the flight time and particle id, are usually stored in a list of variables. In G0GEANT, each scintillator is an active detector volume, therefore it is very common to have events with multiple hits (for example when a front-back coincidence occurs). The handling of the multi-hits in G0GEANT is

illustrated in Fig. B.4. In this case, each hit variable gets expanded into an array, with each "column" in the array attaching to a certain hit.

In the real experiment, a good hit requires a coincidence of the front and back scintillators. This requirement is implemented in the MC software. Specifically, the hit arrays of a given event are looped over and comparisons are made between the hits. If a pair of hits has

- the same octant and detector numbers;
- the same particle id;
- one "front", the other "back";
- less than 1 ns difference in ToF;
- high enough deposited energy (will be elaborated in Sec. B.2.5);

then this pair is identified as a good detector hit. In the example in Fig. B.4, hits $n1$ and $n3$ make a good coincidence pair. It is also possible that for a given event, more than one good hit is identified.

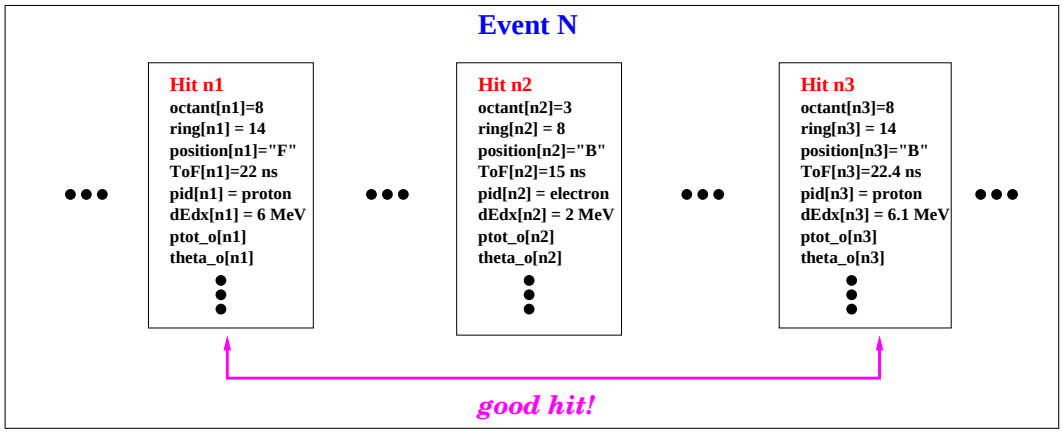

Figure B.4: *A schematic diagram to illustrate the storage of hits, and the selection of good hits in the simulation. In this example, hits "n1" and "n3" satisfy the coincidence requirement, and is therefore identified as a good hit.*

B.2.5 Threshold Setting

If a particle hits the scintillator, the deposited energy ΔE is computed by GEANT and stored into the hit array. This energy, in the form of scintillation light, propagates towards the photomultiplier tubes (PMTs) located at both ends of the scintillator. The PMT signals are discriminated, which effectively sets a cut on ΔE.

The light propagation along the scintillator is modeled by a linear attenuation relation. The attenuation factor, α, is defined as the fractional loss of the light when it travels the full length (L) of a scintillator. This factor has been measured for each scintillator. Empirically it can be approximated as a function of the detector number i [Roc04p]:

$$\alpha = 0.1 + 0.025 \times \mathrm{i}\,. \tag{B.24}$$

Now consider an impact point with a distance xL to the far end of the scintillator ($\frac{1}{2} \leq x \leq 1$). Initially the light carrying $\frac{1}{2}\Delta E$ propagates to either end. Due to the attenuation, the energy reaching the PMT at the far end is $\frac{1}{2}\Delta E(1-\alpha x)$.

For a given detector, the elastic proton has a well-defined momentum, therefore deposits a constant energy ΔE_0 into the scintillator. In the experiment, these elastic protons are used to calibrate the threshold set on each PMT. One selects the most-attenuated elastic proton signals, with the impact points at the very far end of the scintillator ($x = 1$), and sets the threshold at $\sim \frac{1}{4}$ of that signal amplitude. In other words, the energy threshold (T) at the PMT can be expressed as

$$T = \frac{1}{4} \times \frac{1}{2}\Delta E_0(1-\alpha)\,. \tag{B.25}$$

T can be translated into an energy threshold at the impact point. For any hit, to ensure a coincidence between the left and right PMTs, the energy reaching the PMT at the far end has to be greater than T, i.e.,

$$\frac{1}{2}\Delta E(1-\alpha x) > T = \frac{1}{4} \times \frac{1}{2}\Delta E_0(1-\alpha)\,, \tag{B.26}$$

which turns into an effective energy threshold $\Delta E_{th}(x)$ of

$$\Delta E_{th}(x) \equiv \frac{1}{4}\frac{(1-\alpha)}{1-\alpha x}\Delta E_0\,. \tag{B.27}$$

Eqn. B.27 is used as a cut on ΔE for each hit in the simulation. For reference, ΔE_0 and the average ΔE_{th} for each detector are summarized in Table B.2. For detectors 13 to 16, it turns out that the threshold needs further tuning. Setting them to 2.1 MeV seems to reproduce the side-band asymmetry better; it is therefore adopted as the default thresholds for detectors 13 to 16 [Liu06].

ring	ΔE_0 (MeV)	ΔE_{th} (MeV)
1	6.0	1.45
2	5.7	1.36
3	5.4	1.28
4	10.4	2.41
5	9.8	2.27
6	9.3	2.13
7	8.7	1.97
8	8.0	1.80
9	7.5	1.67
10	6.8	1.50
11	6.2	1.35
12	5.6	1.20
13	5.1	1.09
14	4.5	0.96
15	3.7	0.76
16	3.8	0.76

Table B.2: *The energy deposited into the scintillator by elastic protons (ΔE_0), and the average threshold (ΔE_{th}) calculated from Eqn. B.27 for each detector.*

B.2.6 Rates and Asymmetries

The detector rate can be computed by combining the differential cross section defined in Eqn. B.15 or B.21 with the detector acceptance. Taking photo-production

as an example, the detector rates can be formally expressed as

$$R = \mathcal{L} \times \langle \frac{d\sigma_\gamma}{dE_\gamma d\Omega^K_{cm}} \sin(\theta_{cm}) \rangle \Delta_{phase,acc} \,, \tag{B.28}$$

in which $\frac{d\sigma_\gamma}{dE_\gamma d\Omega^K_{cm}}$ is the three-fold differential cross section given by Eqn. B.15, $\Delta_{phase,acc}$ is the actual volume within the generator phase space (Eqn. B.17) that is covered by the detector acceptance, and the luminosity factor $\mathcal{L}$ is defined as

$$\mathcal{L} \equiv \#\text{ of incident electrons per second} \times \#\text{ of protons in the target per cm}^2 \,. \tag{B.29}$$

Since the events are uniformly thrown into the phase space, the ratio between $\Delta_{phase,acc}$ and Δ_{phase} would be the same as the fraction of the number of good hits (N_{hits}) in the total number of generated events (N_{thrown}). Therefore we have

$$\Delta_{phase,acc} = \Delta_{phase} \frac{N_{hits}}{N_{thrown}} \,, \tag{B.30}$$

and Eqn. B.28 becomes

$$R = \mathcal{L} \times \langle \frac{d\sigma_\gamma}{dE_\gamma d\Omega^K_{cm}} \sin(\theta_{cm}) \rangle \Delta_{phase} \frac{N_{hits}}{N_{thrown}} = \mathcal{L} \frac{\sum^i \text{weight}^i}{N_{thrown}} \,, \tag{B.31}$$

where weight^i is the event weight associated with a good hit, and $\sum^i$ is over all good hits.

In parallel, the mean asymmetry can be obtained by making weighted averaging for the asymmetry as

$$\langle A \rangle = \frac{\sum^i \text{weight}^i A^i}{\sum^i \text{weight}^i} \,, \tag{B.32}$$

in which A^i is the asymmetry of a good hit calculated with Eqn. B.10 at the weak decay vertex.

B.3 Results

B.3.1 G^0 Acceptance and the Direct and Rescattered Protons

As discussed in Sec. 4.2.3 (Fig. 4.13), the acceptance of the G^0 spectrometer for the protons originating from the the target is usually plotted as a 2D map of the proton's initial momentum and angle, (p, θ). The left edge of the acceptance map is defined by the lower primary collimator (LPC); protons with angles less than $\sim< 48°$ are blocked by it. However, with high enough momentum ($>\sim$ 1 GeV/c), the protons can penetrate the LPC and make it into the detectors. This "leak-through" is also apparent in the (p, θ) map.

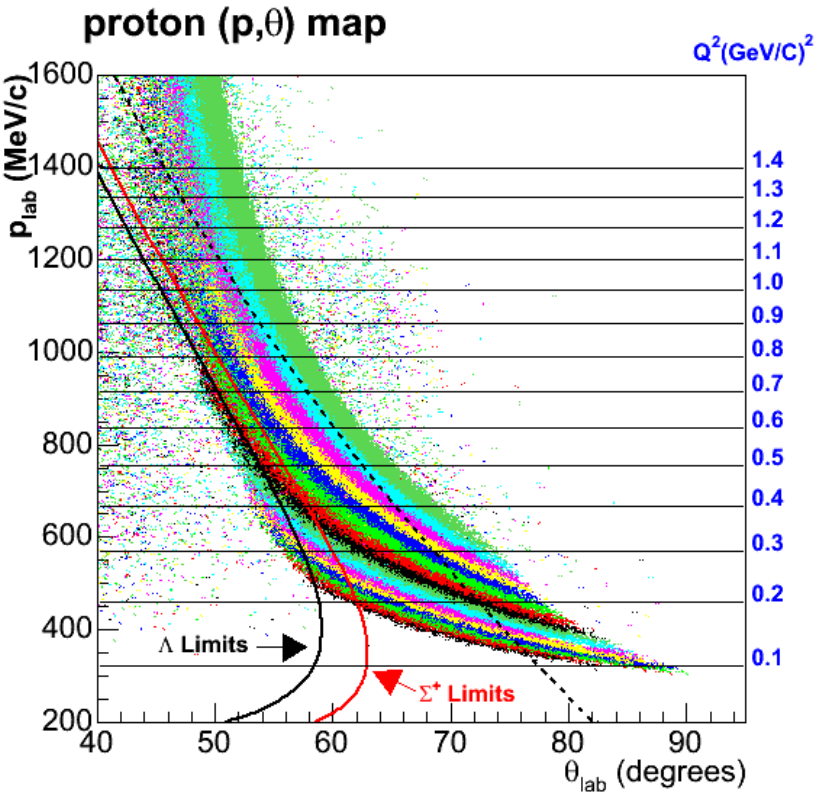

Figure B.5: *The kinematic limits of the protons from the hyperon decays, shown as the two solid curves in the proton (p, θ) space: [black = Λ, red = Σ^+]. The colored bands correspond to the acceptance of individual FPD detectors. See more explanation of the (p, θ) map in the caption of Fig. 4.13.*

Let us consider the protons produced at the weak decay vertices. Due to the

short lifetime of the hyperons (Table B.1), most of the protons can be regarded as originating from the target. The outgoing proton's momentum and angle a kinematic limit. The two solid curves in Fig. B.5 correspond to the limits of decay protons from the Λ (black) and Σ^+ (red), produced by 3.03 GeV electron beam; the allowable (p, θ) is the area to the left of the curves. One can see that in general, the G^0 acceptance only overlaps with the very edge of the phase space of "direct" protons from the hyperon decays; the direct protons from the Λ only go up to detector 9 and those from the Σ^+ go up to detector 11. The kinematically allowed region for $\Sigma^0 \to \Lambda \to p$ overlaps even less with the G^0 acceptance. Compared with the elastic protons in the same detector, these protons are with higher momentum and smaller angle, therefore have shorter flight times.

The suppression of the direct events gives a significant boost to the relative importance of the rescattering. Particles can rescattered inside the spectrometers and strike the detectors without being constrained by the kinematic limits in Fig. B.5. From the simulation, the total detected proton rates due to rescattering is a factor of 4−6 to those of the direct hits for the three hyperon channels.

B.3.2 ToF Spectra

The hyperon rates along the ToF bins can be computed with Eqn. B.31. In Fig. B.6 are shown the ToF spectra arising from the Λ photo-production for nine selected detectors. The spectra from other hyperon channels have very similar shapes. For comparison, the measured G^0 spectra (with an arbitrary scale) are also overlaid. Due to rescattering, the Λ rate goes all the way up to detector 16, instead of being cut off beyond detector 9. In general, the hyperons make a continuous bump in the ToF, which overlaps more and more with the elastic peak as the detector number increases. For reference, the average rates per detector of the three channels are listed in Table B.3 for individual FPDs. The contributions from the photo- and electro-production have been combined; approximately the relative contributions scale as $\frac{\text{photo}}{\text{electro}} \sim 1 : 2(\Lambda, \Sigma^+); 1 : 1.5(\Sigma^0)$. Although these rates are very low compared to the measured rates, they carry very large asymmetries, therefore can potentially make

a significant contribution.

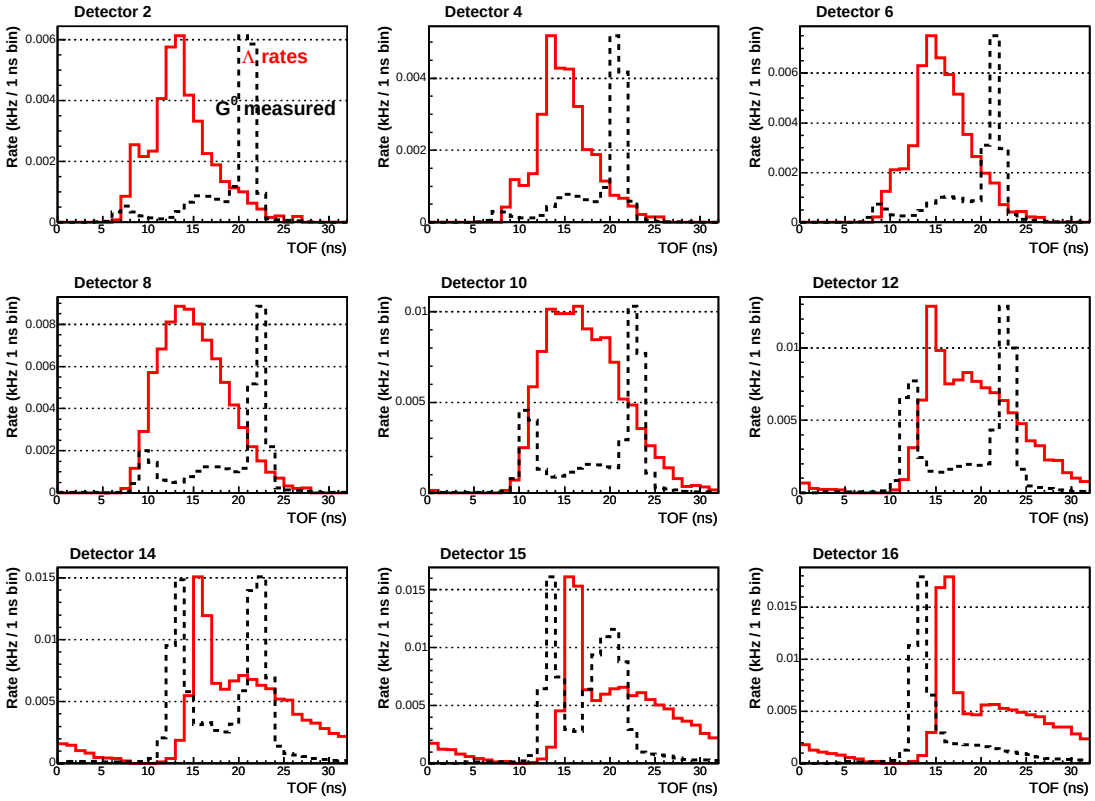

Figure B.6: *The ToF spectra due to* Λ *photo-production (red solid), overlaid with the measured* G^0 *spectra with an arbitrary scale (black dashed) for nine selected detectors.*

B.3.3 Various Types of Hits and Their θ^{RF} Distributions

Decay protons are not the only source that contribute to the detector rates; some pions generated by the weak decay and their secondaries also make it into the detectors. Generally, the hits can be sorted into the following categories, based on the particle type and their origins:

- direct protons ($> 48°$) — primary protons that go through the opening defined by the higher and lower collimators;
- direct protons ($< 48°$) — primary protons that penetrate the LPC;

FPD	Measured (MHz)	Λ (Hz)	Σ^+ (Hz)	Σ^0 (Hz)
1	0.82	81.8	37.3	54.9
2	1.09	126.2	57.3	87.1
3	1.16	149.8	65.9	102.4
4	0.96	38.2	41.8	65.8
5	1.03	145.9	63.4	98.9
6	1.12	166.8	80.0	117.6
7	1.20	255.5	126.1	192.2
8	1.07	262.4	121.7	184.8
9	1.20	317.7	138.8	242.8
10	1.24	352.7	143.7	278.2
11	1.27	395.6	164.7	305.7
12	1.02	340.1	141.4	257.7
13	0.88	239.4	96.4	182.9
14	0.92	268.9	108.3	209.5
15	1.00	270.5	114.5	207.5
16	0.47	246.2	100.5	184.3

Table B.3: *Total measured rates and the simulated rates from the Λ, Σ^+ and Σ^0 (per detector) for individual FPDs.*

- fast charged particles: $\pi^{\pm}$, $\mu^{\pm}$ and $e^{\pm}$ — directly or indirectly originating from the weak decay;
- indirect protons — the rescattered/secondary protons indirectly originating from the weak decay.

In Fig. B.7, the ToF distributions of these four types of hits for rings 4, 8, 12 and 16 from Λ photo-production are displayed. One can see that in general the indirect protons dominate the total rates. The direct protons ($< 48°$) and the fast charged particles usually have shorter flight time, located at the "dip" in between the pions and inelastics. The direct protons ($> 48°$) overlap with the earlier half of the inelastic bump (cut1), but get cut off for higher numbered detectors. On the other hand, the indirect protons make a continuous bump across the inelastic and elastic regions. For reference, the average rates for these four types of hits are

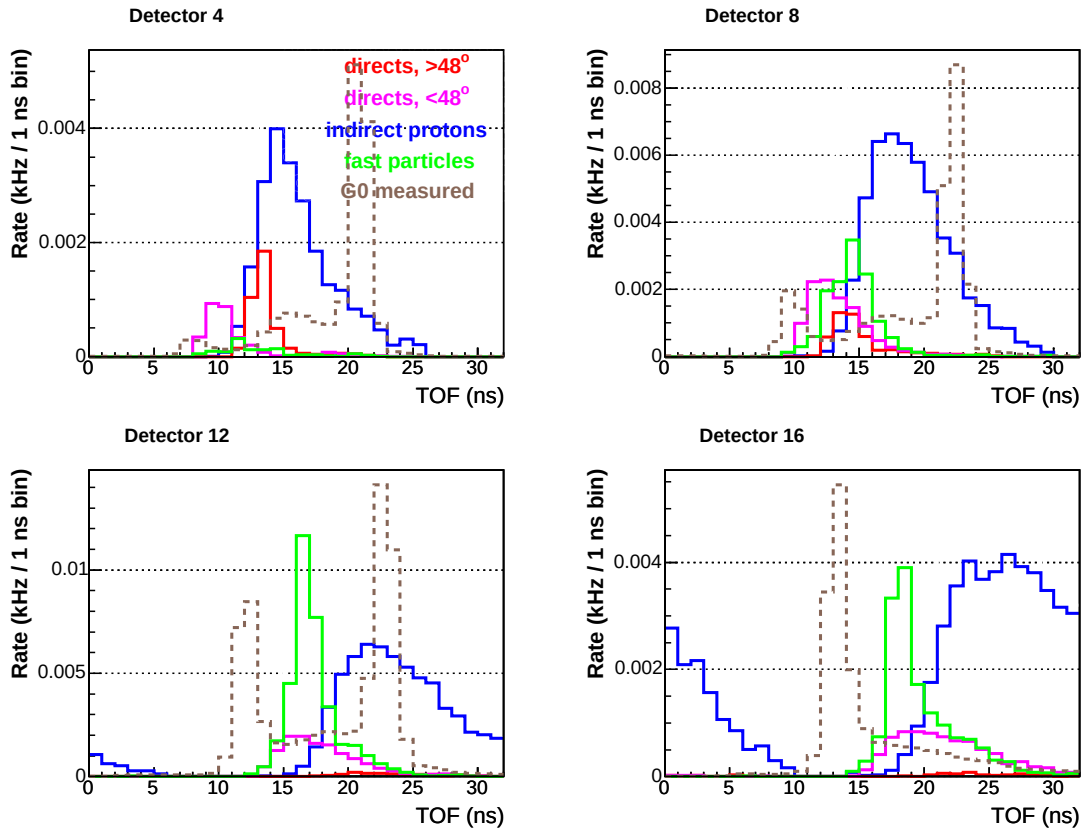

Figure B.7: *The ToF spectra for various types of hits in detectors 4, 8, 12 and 16 from Λ photo-production: [red = direct protons (> 48°), pink = direct protons (< 48°), green = fast charged particles, blue = indirect protons, brown dashed = measured yield with an arbitrary scale].*

displayed on the left panel in Fig. B.8 for individual detectors.

One key parameter in evaluating the PV asymmetry is $\theta^{RF}_{\hat{z},\vec{k}_N}$, the angle of the momentum of the decay nucleon relative to the photon momentum in the rest frame of hyperon. For simplicity we will use the symbol θ^{RF} from now on. To make a general impression, the distributions of θ^{RF} for various types of hits from Λ photo-production are displayed on the right panel in Fig B.8. One can see that the direct ($< 48°$) and indirect protons have slightly forward-distributed θ^{RF}, on the contrary those of the direct ($> 48°$) protons and fast charged particles are backward-distributed. The distribution of θ^{RF} in the electro-production is very similar.

The rates and θ^{RF} for the three hyperon channels (averaged over all 16 rings) are listed in Table B.4. The proton and neutron branches of the weak decay are

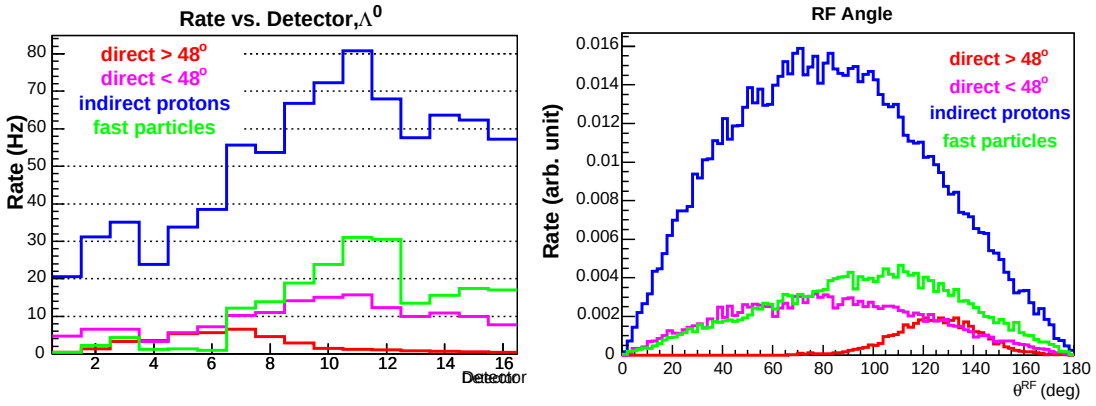

Figure B.8: *The average rates vs. the detector number (left plot), and the distribution of θ^{RF} (right plot) for various types of hits in Λ photo-production. Color code for different histograms is indicated in the legends.*

Y	P'_z	decay	α	direct($>48°$)		direct($<48°$)		indirect p		fast part.	
				R	$\langle c\rangle$	R	$\langle c\rangle$	R	$\langle c\rangle$	R	$\langle c\rangle$
Λ	0.75	$p\pi^-$	0.64	8.1	-0.55	31.4	0.12	66.8	0.12	7.8	-0.1
		$n\pi^0$	0.65	0	n/a	0	n/a	89.5	0.09	29.2	-0.05
Σ^+	0.75	$p\pi^0$	-0.98	6.4	-0.6	9.4	0.17	20.3	0.2	11.7	-0.07
		$n\pi^+$	0.07	0	n/a	0	n/a	42.3	0.14	10.0	-0.28
Σ^0	0.25	$p\pi^-$	0.64	0.40	-0.57	24.0	0.14	50.9	0.15	5.8	-0.13
		$n\pi^0$	0.65	0	n/a	0	n/a	72.2	0.09	20.0	-0.03

Table B.4: *A summary table of the average rates and $\cos(\theta^{RF})$ for different types of hits. The rates are in units of Hz per detector. Columns $\langle c\rangle$ represent $\langle\cos(\theta^{RF})\rangle$. The hits are also separated into the "proton" and "neutron" channels at the hyperon weak decay vertex.*

separated, since they have different values of α (see Table B.1). Let us first consider the contribution of the indirect protons. For Λ and Σ^0, since P'_z, α and $\langle\cos(\theta^{RF})\rangle$ are all positive, on average they lead to a positive asymmetry. Σ^+ on the other hand, has positive P'_z and $\langle\cos(\theta^{RF})\rangle$, but negative α (the contribution of the neutron branch is negligible), therefore on average gives a negative asymmetry. Based on the values in this table, we could repeat this calculation more quantitatively for all types of hits and combine them; the resulting relative contributions (taking into account the

differing rates of the three hyperon channels) are roughly $\Lambda : \Sigma^+ : \Sigma^0 \sim 3 : -1 : 1$. Since the Λ gives rise to a positive asymmetry, the combined contribution from all three hyperon channels is also positive.

It is useful to estimate the scale of the hyperon contamination in the measured asymmetry. The total rate due to hyperons is ~500 Hz per detector, and the total measured rate is $\sim$ 1 MHz. The raw asymmetry of the weak decay is $\alpha P_b P'_z \cos(\theta^{RF}) \sim 0.05$. Therefore the asymmetry in the measured spectrum due to hyperons can be estimated as $0.05 \times \frac{500\text{Hz}}{1\text{MHz}} \sim 25$ ppm, which is the scale of the observed background asymmetry.

B.3.4 Comparison with the G^0 Data

For each ToF bin, the hyperon asymmetry can be computed using Eqn. B.32. The raw asymmetries of the three hyperon channels vs. ToF are plotted in Figure B.9 for nine representative detectors. One observes a non-monotonic behavior of these asymmetries at the low ToF region; they are the consequence of the different θ^{RF} distributions of different types of hits in Table B.4. However, across the elastic peak, where the indirect proton events dominate, the raw asymmetries are smoothly varying.

Before comparing the simulation with the measured data, let us reiterate the procedure of the background correction discussed in Sec. 5.3.6. The measured yield spectrum $Y_m(t)$ is decomposed into an elastic peak $Y_e(t)$ and a background $Y_b(t)$, and then the measured asymmetry $A_m(t)$ can be written as

$$A_m(t) = \frac{Y_e(t)}{Y_m(t)} A_e(t) + \frac{Y_b(t)}{Y_m(t)} A_b(t)\,, \tag{B.33}$$

where $A_e(t)$ is the elastic asymmetry, and $A_b(t)$ should be interpreted as the effective asymmetry carried by the background yield $Y_b(t)$. Under the assumption that the underlying physics is smoothly varying, in Sec. 5.3.6 both $Y_b(t)$ and $A_b(t)$ are determined via fits or interpolations, e.g., by parameterizing them as a second order polynomial in t.

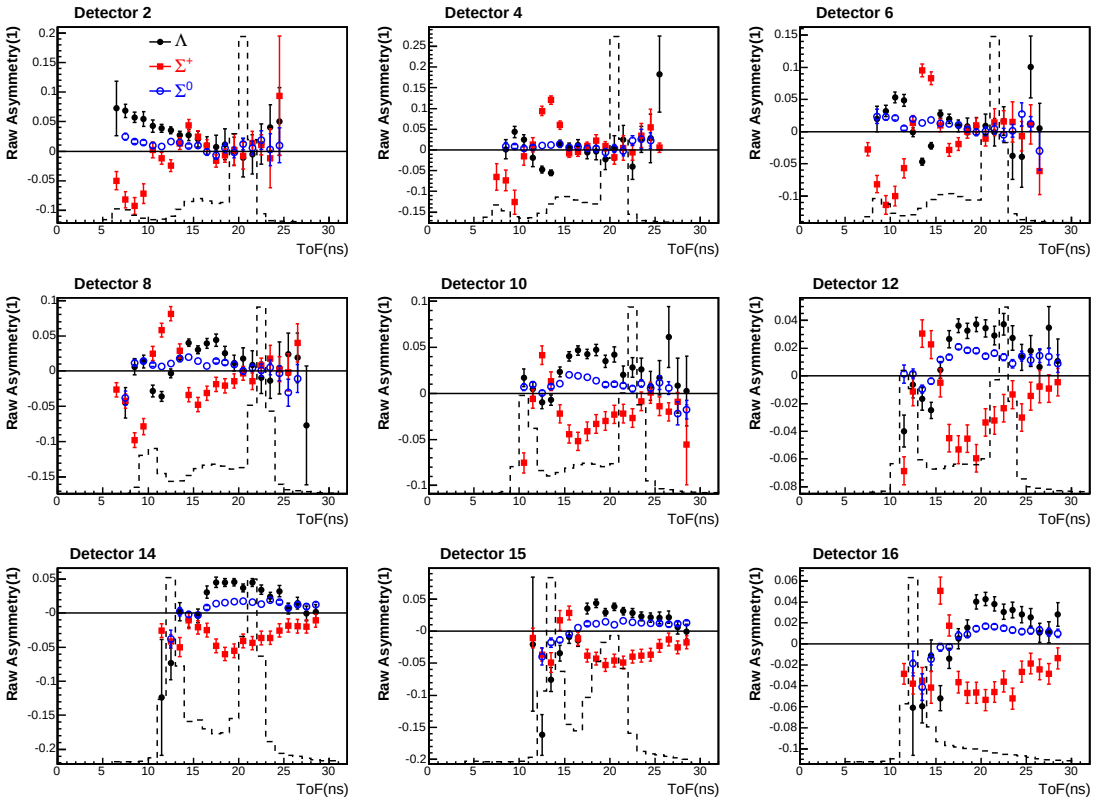

Figure B.9: *The raw asymmetry carried by the* Λ *(solid black circles),* Σ^+ *(solid red squares), and* Σ^0 *(open blue circles) vs. ToF for nine representative detectors. The measured* G^0 *yield spectra with an arbitrary scale are overlaid as the dashed histograms.*

To justify our assumption of $A_b(t)$ in the fit, the raw asymmetries $A_{hyp}(t)$ in Fig. B.9 are cast into an effective background asymmetry as

$$A_{hyp,b}(t) = \frac{Y_{hyp}(t)}{Y_b(t)} A_{hyp}(t)\,, \tag{B.34}$$

in which $Y_{hyp}(t)$ is the simulated hyperon yield, and $Y_b(t)$ is the fitted/interpolated background yield determined in Sec. 5.3.6. $A_{hyp,b}(t)$ of the three hyperon channels (for the nine detectors in Fig. B.9) are plotted in Figure B.10. One can see that the strengths of the three channels agree with our earlier estimate ($\Lambda : \Sigma^+ : \Sigma^0 \sim 3 : -1 : 1$). So approximately the contributions from Σ^+ and Σ^0 cancel, and that from Λ remains. The sum of $A_{hyp,b}(t)$ of the three hyperon channels is shown separately in Fig. B.11 for all 16 detectors. Also overlaid in the figure are the measured yields and

asymmetries. In both Figs. B.10 and B.11 we have made small (<2 ns) timing shifts to $A_{hyp,b}$ in some detectors to better match the measured asymmetry in the sidebands. As mentioned earlier, for detector 13 and beyond, the energy loss thresholds were raised to 2.1 MeV "empirically".

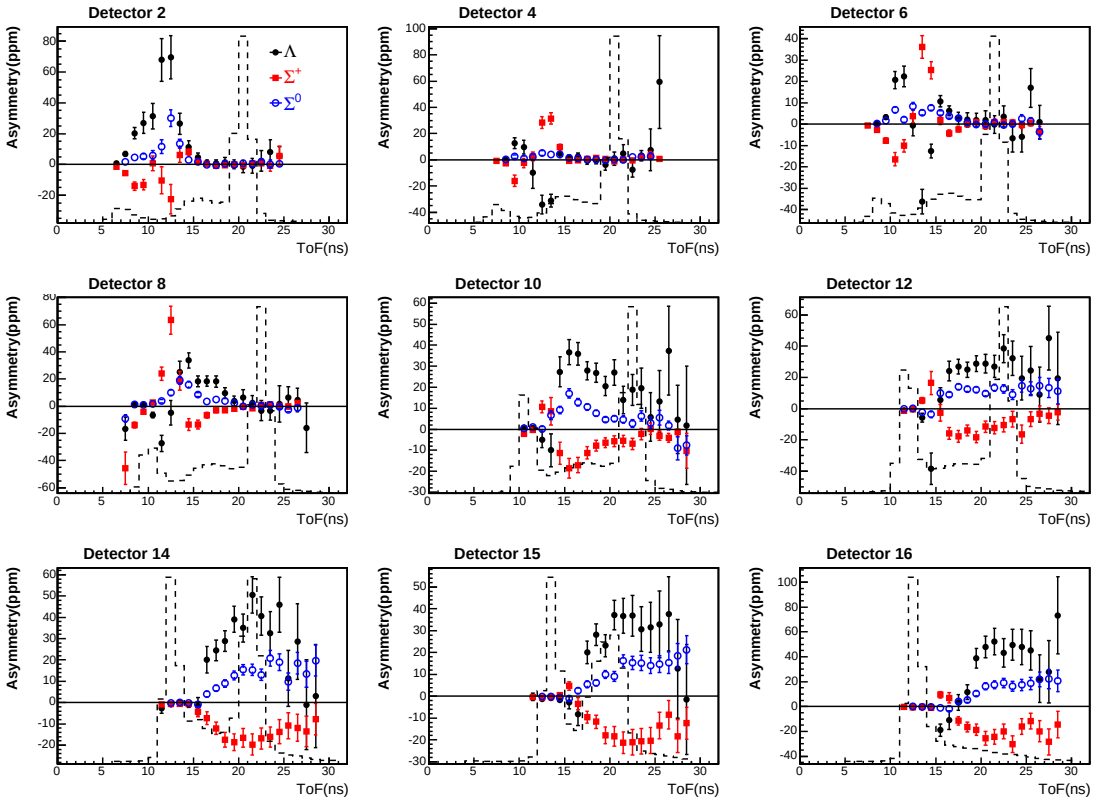

Figure B.10: *Contributions of the three hyperon channels to the background asymmetries $A_b(t)$ for nine representative detectors, calculated using Eqn. B.34 from the raw asymmetries in Fig. B.9: [solid black circles=Λ, solid red squares=Σ^+, open blue circles=Σ^0]. The dashed histograms are the measured yield spectra with an arbitrary scale.*

From Fig. B.11, one observes that for detectors above 8, the simulation reproduces the trend of the data, i.e. there is a smooth and positive bump of the background asymmetry moving towards the elastic peak as the detector number goes higher. The agreement of lower detectors is less satisfactory. Nonetheless, the simulation does predict a positive asymmetry in the low ToF region, with a fading strength toward the elastic peak. The complicated structure of the observed asymmetry at the low ToF regions in detector 4, 5 and 6 is also reproduced by the MC,

although the scales of the two disagree.

As a conclusion, all the above results have suggested that hyperon decay plays a significant role in the G^0 background asymmetry. However, we have emphasized that the simulation contains unmeasured parameters, in particular the transfered polarization of Σ^0 and Σ^+, as well as the cross section of hyperon productions at a invariant mass higher than 2.2 GeV. In addition, since the rescattering plays an important role, one should also be concerned about the accuracy of the handling of rescattering processes in GEANT. Therefore, the results of this Monte Carlo simulation were not directly applied in the background correction discussed in Sec. 5.3.6. Nevertheless, according to the MC, both the hyperon rate and asymmetry vary smoothly across the elastic peak, effectively leading to a smooth varying background asymmetry, which renders an important justification for the assumptions we made in the background correction.

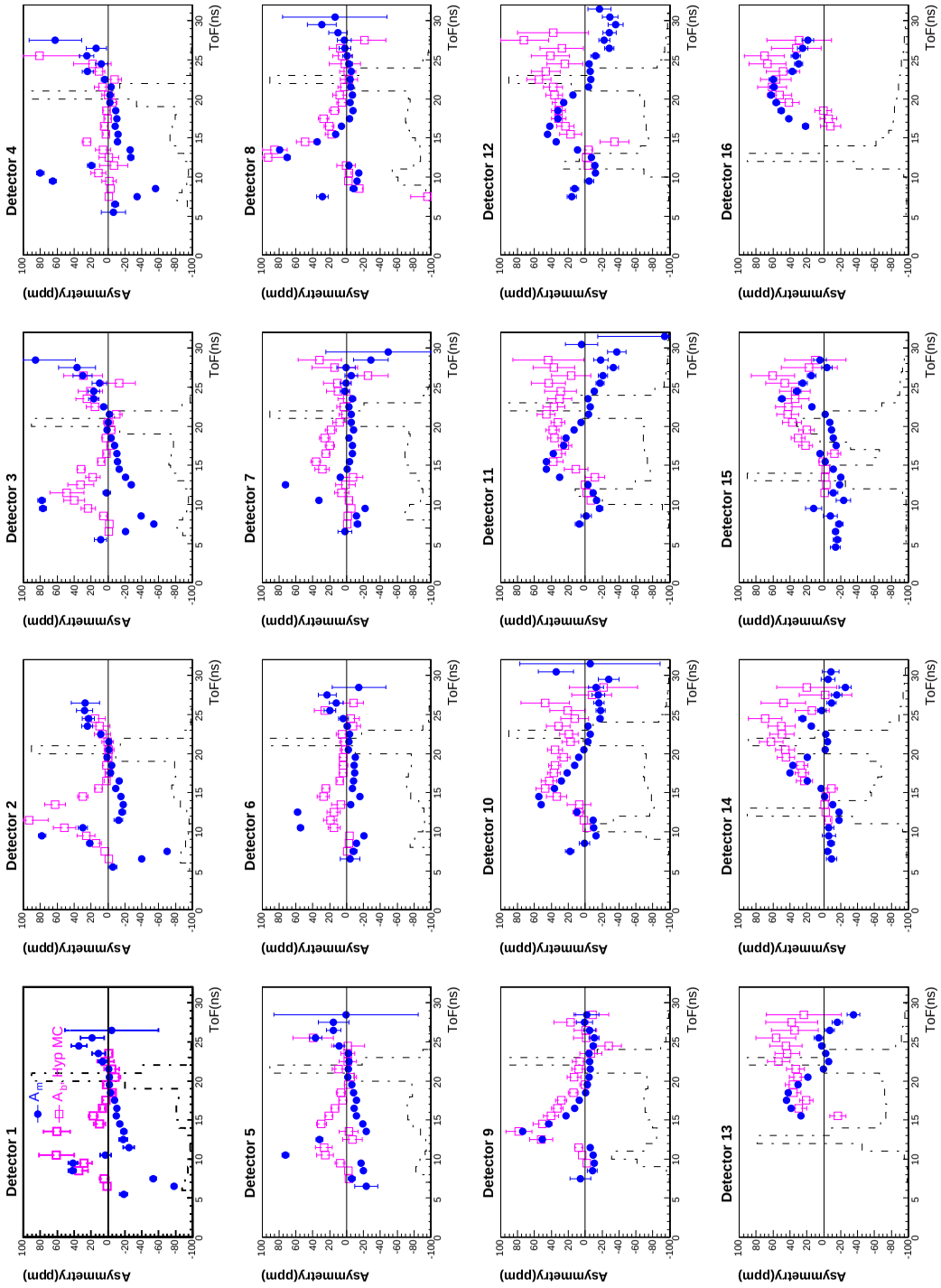

Figure B.11: *The total background asymmetries from the hyperon MC by combining all three channels in Fig. B.10 (open pink squares), overlaid with the G^0 asymmetries measured by the NA detectors (solid blue circles) for all 16 FPDs. Both measured and simulated asymmetries are corrected for the beam polarization, and the blinding factor is removed from the measured asymmetries. The dashed histograms are the measured yield spectra with an arbitrary scale.*

Appendix C

Luminosity Monitors

As introduced in Sec. 4.2.2, eight luminosity detectors (LUMIs) were instrumented in the G^0 forward angle experiment. Placed at very forward angles, these detectors were sensitive devices to check beam induced false asymmetries in the system, as well as to monitor the density reduction and fluctuations of the liquid hydrogen target. In what follows, the physical design of the detectors will be presented in Sec. C.1, followed by a detailed discussion in Sec. C.2 of the detector performance in terms of the linearity (Sec. C.2.1), sensitivities to the beam properties (Sec. C.2.2), and measurements of the target density related effects (Sec. C.2.3).

C.1 Physical Design

C.1.1 Geometry and Kinematics

The G^0 target is a 20 cm liquid hydrogen, with aluminum windows with a total thickness of $\sim$0.0483 cm. At small angles, the dominating scattering processes are elastic scattering between electrons (Møller), electron and proton (e$-$p), and electron and aluminum nuclei (e$-$Al). The luminosity, $\mathcal{L}$, is defined as the number of incident electrons per second, multiplied by the number of scattering centers in the target per unit area. With 40 μA of incident electron beam, $\mathcal{L} = 2.131 \times 10^{38}$ cm^{-2} for the Møller and e$-$p, and 7.27×10^{35} cm^{-2} for e$-$Al, and the differential cross sections of these three processes can be calculated with standard formulas in [Ban97] (Møller), [TW00] (e$-$p) and [Won98] (e$-$Al). Folding differential cross sections with luminosities, the electron rates per unit solid angle can be calculated, and they are displayed against the electron lab angle for these three reactions in Fig. C.1. One sees that at small scattering angles between 1° to 5°, the Møller rate dominates.

The actual layout of the LUMI detectors is illustrated in Fig. C.2. There were

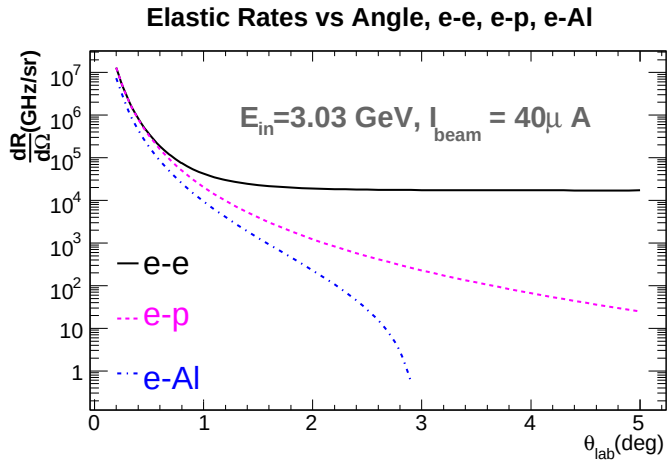

Figure C.1: *The electron rates per unit solid angle vs. electron lab angle for the Møller (black solid), e−p (pink dashed) and e−Al (blue dot-dashed).*

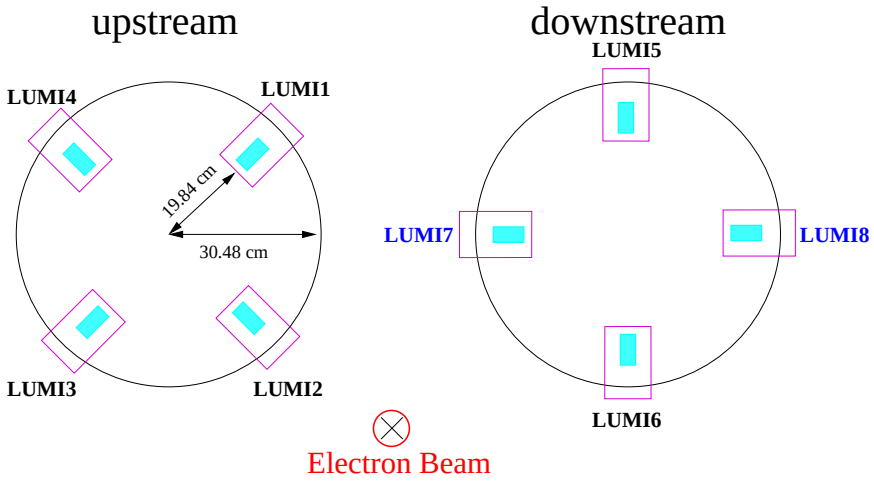

Figure C.2: *An illustration of the layout of the eight LUMI detectors viewed from the target. The cross section of the downstream beam pipe, the quartz crystals, and the aluminum cups that hold the detectors are drawn. The quartz crystals (light blue blocks, not drawn in proportion to the beam pipe) are approximately 0.5 cm from the bottoms of the cups.*

in total eight quartz Čerenkov detectors grouped into two sets. One set of four detectors was placed symmetrically about the beam line and 699.7 cm downstream of the target center, labeled as LUMIs 1 through 4 (see Fig. C.2), and will be referred to as the upstream LUMIs collectively. The four upstream LUMIs were enclosed inside a lead shielding box (to eliminate the low energy background for the main focal plane detectors), and for reasons of space they were put at 45° with respect to vertical

and horizontal axes. The other four "downstream" LUMIs were located at the very end of the beam pipe with a distance of 1073.5 cm from the target center, vertically or horizontally placed, and labeled as LUMIs 5 through 8 (see Fig. C.2). The detectors were placed in 0.159 cm thick aluminum cups, which intruded radially into the (30.48 cm radius) downstream beam pipe. All quartz crystals were cubic with dimensions of 3.56 cm $\times$ 3.56 cm $\times$ 7.62 cm. The long axis of the quartz crystal was parallel to the radial direction, as shown in Fig. C.2, and the front face of the crystal exposed to the target was 7.62 cm $\times$ 3.56 cm = 27.13 cm^2. The average scattering angle was 1.98° and 1.29° for the upstream and downstream LUMIs, respectively. The scattered electron energies for e$-$p or e$-$Al at such a forward angle are very close to the incident beam energy (3.03 GeV), and the Møller electron energies at these two angles are 667 and 1211 MeV, respectively. Ignoring any small magnetic field, the solid angle acceptance $\Delta\Omega$ for each upstream and downstream detector is 0.0554 mrad and 0.0235 mrad, respectively. With such geometrical acceptance, the electron rates for the three scattering processes in each upstream and downstream LUMI are summarized in Table C.1. Also tabulated are the parity violating asymmetries of the individual processes. The asymmetry of Møller scattering is calculated with the formula in [E158P], and the elastic e$-$p asymmetry has been given in Eqn. 6.1. They are both very small for the LUMI acceptance. The asymmetry for elastic e$-$Al scattering is estimated using the formulation in [Fei75, DDS89], in which the isospin and spin of the aluminum nucleus is ignored. Although the magnitude of the aluminum asymmetry is much larger than the other two, it does not contribute significantly to the overall asymmetry due to its low scattering rate. The overall rates for both sets of LUMIs are $\sim$1 GHz per detector, with a physical asymmetry of the order of 0.05 ppm.

The applications of the LUMIs are driven by the physics at small scattering angles discussed above. The smallness of the expected physical asymmetry in these detectors opens the possibility of using these detectors to check for false asymmetries. The high scattering rate leads to much improved statistical precision in these detectors ($\sim<$ 100 ppm per quartet per detector), as compared to the main focal

channel	$\theta_{lab} = 1.98°$, $\Delta\Omega = 0.0554$ mrad		$\theta_{lab} = 1.29°$, $\Delta\Omega = 0.0235$ mrad	
	Rate (GHz)	Asymmetry (ppm)	Rate (GHz)	Asymmetry (ppm)
Møller	1.06	0.033	0.64	0.055
e−p	0.071	−0.082	0.17	−0.032
e−Al	0.014	0.91	0.067	0.39
Total	1.145	0.037	0.877	0.064

Table C.1: *The expected electron rates (per detector) and asymmetries from various reactions, and their overall contributions to the upstream and downstream LUMIs. See text for details of the calculations.*

plane detectors ($\sim$ 1200 ppm per quartet per Q^2 bin). Other noise, such as potential target density fluctuations, will manifest itself as a widening of the measured asymmetry width, which can be studied systematically.

C.1.2 Secondaries and Counting Statistics

For reference, we shall present here a somewhat pedantic discussion of the impact of the secondary particles to the statistics of the measured asymmetry.

If secondary scattering processes are negligible, the statistical width of the quartet asymmetry can be calculated as $\mathcal{W}_{stat} = \frac{1}{\sqrt{4N_p}}$, with N_p being the number of primary particles per MPS (see discussions leading to Eqn. 5.6). When the secondary particles generated by the primaries also make it into the detector, the quartet asymmetry width is modified to become

$$\mathcal{W}_{stat} = \frac{1}{\sqrt{4N_p}}\sqrt{1+b}\,, \tag{C.1}$$

where b is a positive excessive noise factor depending on the details of the secondary process. In the special case that each primary particle on average produces m secondary particles in an MPS, and *only* the secondary particles are detected (such as photons in a calorimeter or a photomultiplier tube), then $b = \frac{var(m)}{m^2}$, where $var(m)$ is the variance of m, and is equal to m if the secondaries are also Poisson distributed [Tei86].

However, the b given above is not applicable in our situation. A customized GEANT simulation [GEA94], with a simplified G^0 geometry including the target windows, the downstream beam pipe, the aluminum cups, and the LUMI detectors [†], shows that *both* the primaries and secondaries contribute significantly to the detected rates, with the secondary rates about a factor of 3 of that of the primaries in both sets of LUMIs. To study the width of the asymmetry with *both* primaries and secondaries detected, a Monte Carlo (MC) simulation was carried out. In the MC, Poisson-distributed random numbers with a mean of 1 are generated one by one to mimic the primary particles, and for each primary particle, a Poisson-distributed number with a mean of m is generated as the number of the secondary particles. This is repeated N_p times (N_p is the average number of primary hits per MPS), and the sum of the total primary and secondary particles is used as the total number of hits within a given MPS. This procedure is repeated large number of times, and for each four consecutive MPS's, a quartet asymmetry is computed and histogrammed. In the end, the width of the asymmetry is obtained for each given value of m; the former is then compared to $\frac{1}{\sqrt{4N_p}}$. In Fig. C.3, the ratio of the two are displayed for various values of m. As one can see, the largest widening of the MC width away from $\frac{1}{\sqrt{4N_p}}$ occurs at $m \sim 1$ by about 12%, and for $m \sim 3$ indicated by the GEANT simulation, the asymmetry width is about $\frac{1.09}{\sqrt{4N_p}}$.

Although containing some realistic features, the above estimate of the excessive noise is still too simplistic. We shall show in Table C.2 that the secondary particle rates in the real experiment are far more significant than that was indicated from the simple GEANT simulation. These extra secondary rates could originate from complicated rescattering or cascading processes, which makes it almost impossible to estimate the excessive noise in the asymmetry. Nevertheless, it is important to note that the "multiplication" of secondary particles remains the same for a given electron beam energy and the geometry of the experiment. Since the rate of the primary particles scales with the beam current I_b, $\mathcal{W}_{stat}$ should scale $\frac{1}{\sqrt{I_b}}$, *regardless*

[†]A copy of the GEANT simulation code can be downloaded from
`http://www.jlab.org/~jianglai/geant/g0lumi_geant_v2.tar.gz`.

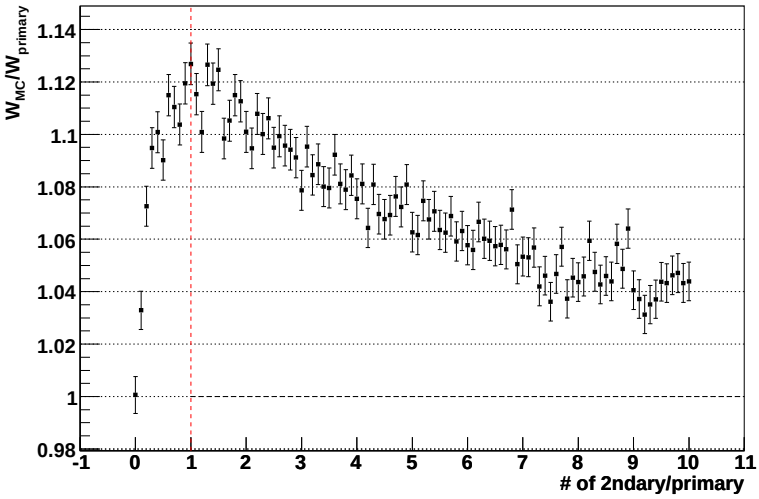

Figure C.3: *The ratio of the quartet asymmetry width obtained from the Monte Carlo to that estimated from the primary statistics* ($\frac{1}{\sqrt{4N_p}}$)*, against the average number of secondary particles per primary particle. See text for details of the Monte Carlo.*

of the details of the secondaries. This important principle shall be referred to as the "counting statistics" in the remainder of this appendix.

C.1.3 Detectors

The quartz crystal detects electrons via Čerenkov photon radiation. When propagating through a medium with an index of refraction n, a charged particle with β greater than a threshold value $\beta_{thres} = \frac{1}{n}$ will radiate Čerenkov photons. These photons are emitted in a sharp cone around the trajectory of the charged particle, with a half-angle $\theta_c = \cos^{-1}(1/n\beta)$ [PDG04]. The quartz crystals used in the LUMI detectors are Spectrosil 2000 (synthetic fused silica) from Saint Gobain Quartz with $n = 1.47$. Since the scattered electrons are relativistic ($\beta \simeq 1$), the Čerenkov cones have a half angle of $\theta_c = 47.1°$, which will be totally reflected on the surface until reaching the end of the quartz. Each quartz crystal was wrapped in aluminum foil and the only open end was attached to the window of a phototube. For the four upstream detectors, Hamamatsu R375 photomultiplier tubes (10-stage) were used. For the downstream set, LUMIs 5 and 6 used Phillips XP2262 photomultiplier tubes (12-stage), and LUMIs 7 and 8 were instrumented with Hamamatsu R4026PT

vacuum photodiodes.

For incident particles with charge Ze, the number of Čerenkov photon per unit path per energy of photon energy is [PDG04]

$$\frac{d^2N}{dxd\lambda} \sim Z^2 370 \sin^2\theta_c \text{ eV}^{-1} \text{ cm}^{-1} . \tag{C.2}$$

However, to estimate the number of photoelectrons generated from the photocathode of the phototube, one will need to take into account the photon collection efficiency and the quantum efficiency (QE) of the cathode material. Due to the internal reflection and the aluminum wrapping, we estimate that 70% of Čerenkov photons reach the photocathode. For the Hamamatsu R375 tubes and photons with a wavelength between 175 nm (1.13 eV) and 550 nm (0.36 eV), the average QE is ∼15%, which collapses rapidly outside this wavelength range [HamCa]. Therefore the average number of photoelectrons generated from the photocathode per incident electron on the quartz is estimated to be

$$\begin{aligned} N_{PE} &= 370 \text{ eV}^{-1} \text{ cm}^{-1} \times \sin^2 47.1^\circ \times 3.5 \text{ cm} \times 70\% \times 15\% \times (1.13 - 0.36) \text{ eV} \\ &= 56 . \end{aligned} \tag{C.3}$$

With an incident rate of 1 GHz, and a typical gain of a photomultiplier tube ($\sim 10^5$), this leads to an anode current of $\sim$ 1 mA, too high for routine operation of the tube. Therefore, a special design was needed to reduce the gain of the tube.

The gain of a photomultiplier tube is directly related to the voltage applied in between its dynodes. Lowering the high voltage is the simplest way of reducing the gain. However, if the voltage between dynodes is too low, non-linearity will arise due to space charge effects. Furthermore, the electric field in between dynodes needs to be kept above certain level in order to maintain proper focusing of the cascading electrons. Therefore we took an alternative approach to use only the first few dynode stages, so that the gain can be reduced without compromising the voltage across active dynodes.

A diagram of the custom-built base for the Hamamatsu R375 tube is shown in Fig. C.4. With this design, only the first 5 dynodes (D_1 through D_5) of the tube were

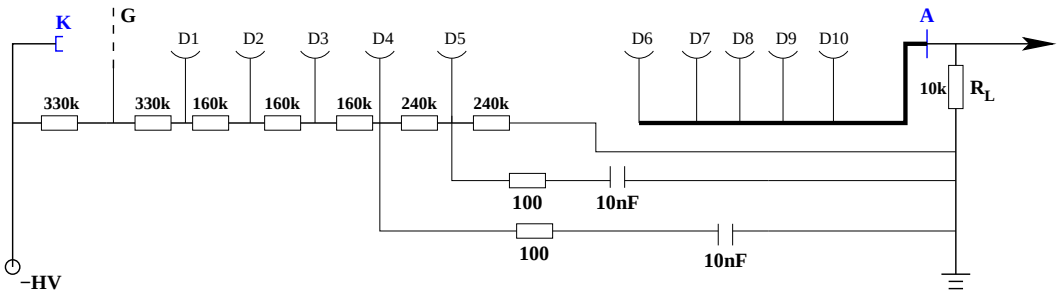

Figure C.4: *The diagram of customized base for the R375 photomultiplier tube. Only the first five stages are active. The signal is extracted at the 6th dynode stage.*

used for multiplication, and D_6 through D_{10} and the anode were shorted together to serve as a "new" anode. The resistor between the cathode and D_1 was significantly larger than the others to help collect cathode electrons and to ensure a high gain of the first dynode. The resistors between D_4 and the anode were also made larger to eliminate space charge accumulation and help the collection of cascading electrons at the anode. The base design for the XP2262 tubes was very similar, except that the signals were extracted at the 7th dynode stage.

For a given photomultiplier tube, the gain of each stage can be parameterized as $G = \beta V^{\alpha}$, in which V is the applied voltage across the stage, and β and α are parameters related to the dynode materials and geometrical structure of the tube [HamCa]. The β and α can be estimated from the gain calibration curve from the manufacturer, and the resulting values are $\alpha \sim 0.59$ and $\beta \sim 0.26$ for the R375, and $\alpha \sim 0.76$ and $\beta \sim 0.11$ for the XP2262. Based on these parameters, the expected gains vs. high voltage for the two types of tubes with our customized low gain bases are displayed in Fig. C.4 [†].

[†]The absolute gain calibration for these LUMI gain bases is difficult, since the amplitude of the single photoelectron is too low to be observed.

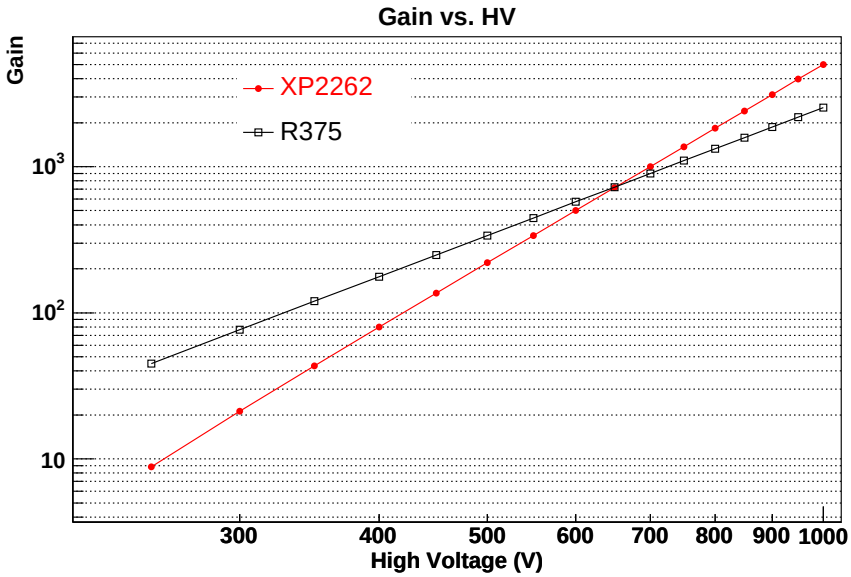

Figure C.5: *The estimated gain vs. high voltage curves for the XP2262 (red) and R375 (black) photomultiplier tubes with customized low gain bases. Both x and y axes are in log scale.*

C.1.4 Electronics

Due to the high particle rate, the pulse counting is no longer practical, therefore only the integrated signals were extracted from the tubes. The anode currents of the photomultiplier tubes were fed into commercial low-noise current to voltage (I–V) pre-amplifiers (Hamamatsu C7319 for LUMIs 1 through 4, and PMT4 and PMT5 from Advanced Research Instruments for LUMIs 5 and 6, respectively) and converted into voltage signals. During normal running, the gain of the tubes were set such that the anode currents of the tubes were kept at $\sim$40 μA, and all the preamplifiers were set at 0.1 V/μA, resulting in an output signal of $\sim$4 V. The voltage signal was then digitized by TRIUMF voltage-to-frequency converters, whose outputs go into scalers being read out for each helicity state (1/30 s). Effectively this electronics worked like an ADC with an 1/30 s integration time. The output of the two vacuum photodiodes (LUMIs 7 and 8) were sent to custom-built preamplifiers located very close to the detectors, and the outputs followed the same path as those for the photomultiplier tubes.

The 30 Hz electronic noise was measured in two ways. One was to use a

battery and resistor to mimic a noiseless anode current signal, and the other was simply by measuring the electronic pedestal. Both measurements looked for the 30 Hz fluctuations at the output of the preamplifier, and showed consistently that the noise was ∼0.09 mV, as compared to a typical signal size of ∼4 V.

C.2 Detector Performance

In this section, the performance of the luminosity detectors during the G^0 forward angle experiment will be summarized. LUMI7 was not operational during a significant period of the experiment, and LUMI8 appeared to be more noisy and non-linear than other detectors, therefore most of the following analysis will be focused on LUMIs 1 through 6.

C.2.1 Detector Linearity

As mentioned, the high voltages on the photomultiplier tubes were set to maintain about ∼40 μA of anode current when 40 μA of beam was on the LH2 target. For reference, the high voltages on the individual detectors during nominal running are summarized in Table C.2. The estimated gains under these high voltages (see Fig. C.5), and the anode currents (based on the rates in Table C.1, the number of photo-electrons in Eqn. C.3, and the tube gains) are also tabulated. The estimated anode currents for the upstream LUMIs are much lower than the measured values, which indicates very significant secondary rates inside the lead shielding box. Nevertheless, as explained in Sec. C.1.2, although the statistical width of the asymmetry is difficult to estimate under such circumstances, it should still follow counting statistics with a characteristic dependence of $\frac{1}{\sqrt{I_b}}$.

Unlike the main FPDs, since the electronics for the LUMIs were integrating, the non-linearity due to electronic deadtime was not present. However, with such a high rate, space charge effects inside the phototube could potentially spoil the linear response of the output with respect to the incident rates. To study the detector linearity without the complication of the hydrogen target density variation,

LUMI	1	2	3	4	5	6
HV(V)	380	280	280	390	730	740
Gain	152	63	63	164	1211	1288
I_{ano}^{esti} (μA)	1.6	0.65	0.65	1.7	9.5	10.1

Table C.2: *The high voltages set on the photomultiplier tubes of individual LUMI detectors during the experiment (40 μA of beam on LH2 target) to get a measured anode current of ~40 μA. The calculated gains (based on Fig. C.5), and the estimated anode currents I_{ano}^{esti} are also tabulated.*

data collected from the aluminum dummy target (flyswatter) were used instead. In Fig. C.6, the (beam current) normalized LUMI yields with the flyswatter target are plotted against the beam current from 10 μA up to 40 μA. As one can see, all six photomultiplier tubes behave linearly over the entire range, and the fractional changes of the normalized detector yields from 0 to 40 μA for all of them are less than 0.4%.

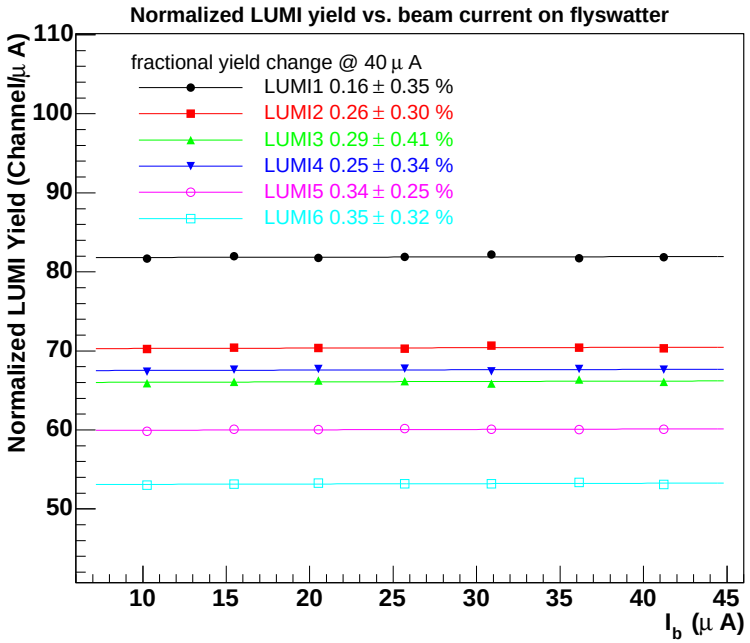

Figure C.6: *The (beam current) normalized LUMI yields vs. the beam current and the corresponding linear fits with the aluminum dummy target (flyswatter). The color code for different LUMIs, and the fractional changes of the fitted yields from 0 to 40 μA are indicated in the legend.*

C.2.2 Sensitivities to Beam Properties

The sensitivity of the LUMI yield with respect to the beam parameters was analyzed the same way as the main FPDs. A linear regression method was employed to compute the yield slope with respect to the beam positions, angles, energy and charge, $(x, y, \theta_x, \theta_y, E_b, Q)$. Similar to those of the main detectors, the slopes of the LUMIs were fluctuating from run to run, but if they are averaged over the entire experiment, the expected sensitivities emerge. In Fig. C.7, the fractional LUMI yield slopes with respect to x and y (average over the entire run) are plotted against the azimuthal angle (Φ) for each detector. A $\cos(\Phi)$ and $\sin(\Phi)$ fit is made on the x and y slopes, respectively. In principle, the upstream and downstream detectors should have different position sensitivities due to their different scattering angles, but due to limited precision of the slopes, we simply fit them with a single sinusoidal function as if they were located on the same "ring". Similar to the FPDs (see Fig. 5.14), for

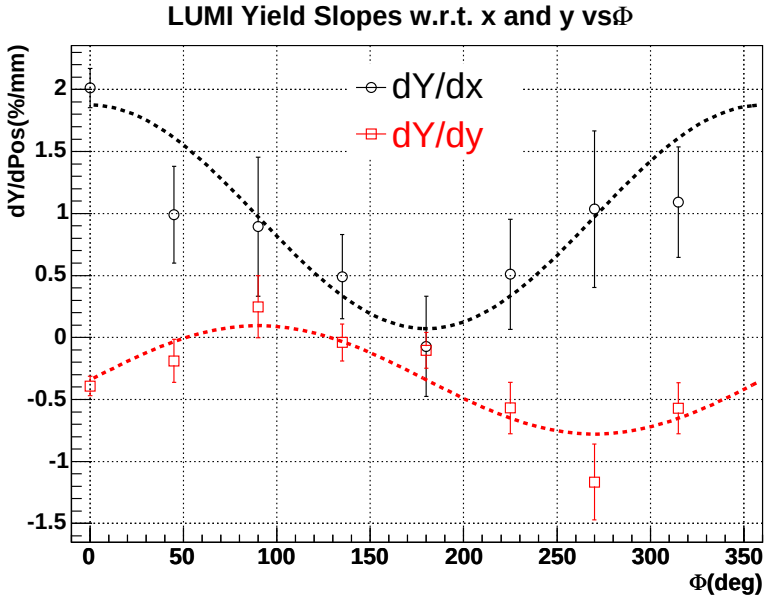

Figure C.7: *The slopes (averaged over the entire experiment) of the LUMI detectors to the beam x and y positions vs. the azimuthal angle. The slopes are in units of %/mm. The uncertainty on each data point is calculated by scaling down the standard deviation of the run-by-run slopes (by a factor of ∼5) in order to get a good χ^2 for the fit.*

both x and y positions, the variation of the LUMI slopes from detector to detector

is consistent with the geometrical expectation. However, both sets of slopes exhibit some offsets from zero, possibly due to a misalignment.

Combining the LUMI slopes with the measured helicity correlated differences or asymmetries of the beam parameters (Table 4.1) using Eqn. 5.56, the false asymmetry due to these parameters is calculated to be of the order $\sim$<0.1 ppm with an uncertainty larger than 100%. In Fig. C.8, the asymmetry computed by treating the sum of yields for LUMIs 1 through 4 as a single detector are plotted against the run number, where the small and uncertain correction has been omitted. Each data point in the figure is an averaged result over a group of consecutive runs associated with a given "IN" or "OUT" state of the insertable halfwave plate. Although

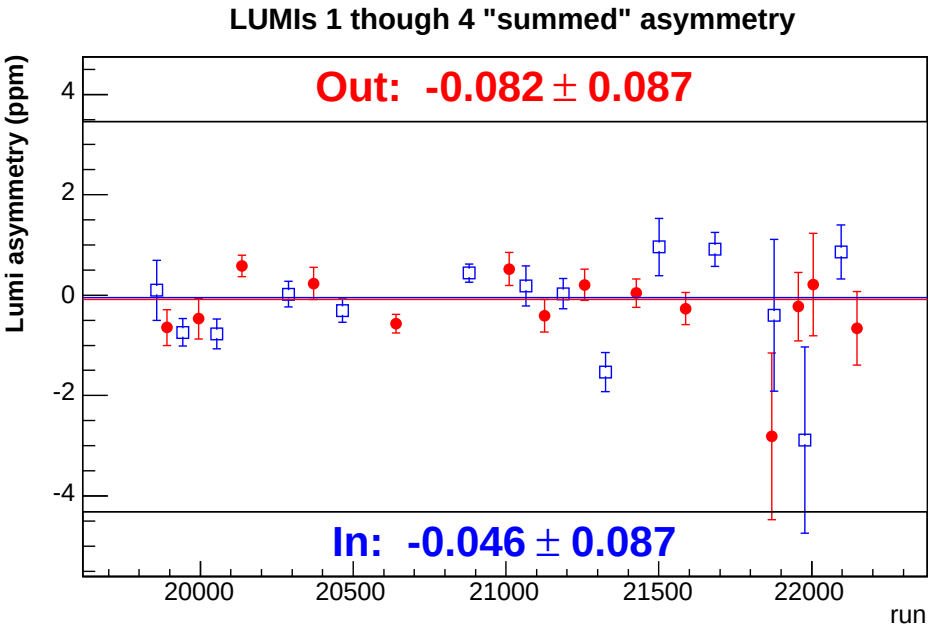

Figure C.8: *The asymmetry computed from the summed yield of LUMIs 1 through 4 vs. the run number. Each data point is an average over a given state of the insertable halfwave plate: [red solid circles = "OUT", blue open squares = "IN"].*

there exist non-statistical fluctuations in the data, the overall averaged asymmetry is 0.02 ± 0.06 ppm, consistent with zero. It is also interesting to note that the uncertainty of the measured asymmetry of each LUMI detector is $\sim$0.07 ppm, and if one treats the total yield in the four LUMIs as a single measurement, the uncertainty of the asymmetry does not go down like $\frac{0.07}{\sqrt{4}}$ due to a significant common uncertainty

arising from the target density fluctuations in these detectors. This effect will be quantified in Sec. C.2.3.

The null LUMI asymmetry in Fig. C.8 has important implications. The asymmetry of the main FPD could be potentially biased by an unmeasured and helicity correlated beam parameter. On the other hand, since LUMIs are expected to be more sensitive to the beam properties, if such a beam parameter did exist, it would manifest itself as a nonzero asymmetry in the LUMIs [†]. Therefore the zero LUMI asymmetry sets a stringent limit on such potential systematics in the FPDs.

C.2.3 Target Boiling Studies

As mentioned in Sec. 4.2.2, with local heating of the electron beam, the liquid hydrogen could boil. The boiling might change the global density of liquid hydrogen, which would lead to a change of the (current normalized) detector yield. On the other hand the density of the boiling hydrogen could fluctuate, increasing the width of the asymmetry distribution. One of the important purposes of the LUMI detectors is to study these two effects and we shall discuss them in turn.

C.2.3.1 Target Density Reduction

The density *reduction* of the liquid hydrogen can not be directly measured by the main FPDs. If the (beam current) normalized FPD yield is decreasing with increasing beam current, it is difficult to tell whether it is due to electronic deadtime in the counting electronics or a target density reduction. On the other hand, as mentioned earlier, the electronics of the LUMIs were integrating, therefore did not have this complication. The linearity of the LUMIs has been studied in Sec. C.2.1 with a control measurement on the dummy aluminum target, where it was demonstrated that the change of the normalized LUMI yield from 0 to 40 μA is less than 0.4%. Therefore the global density change of the liquid hydrogen target can be determined with LUMIs reliably.

[†]This statement does not apply to the leakage beam effect, since the LUMIs use integrating electronics and is insensitive to time structure of the beam. See details in Appendix A.

Similar to Fig. C.6, the normalized LUMI yields measured at different beam currents with the LH2 target (under nominal beam size and pump speed) is displayed in Fig. C.9. As one can see, none of the detectors experiences a significant yield

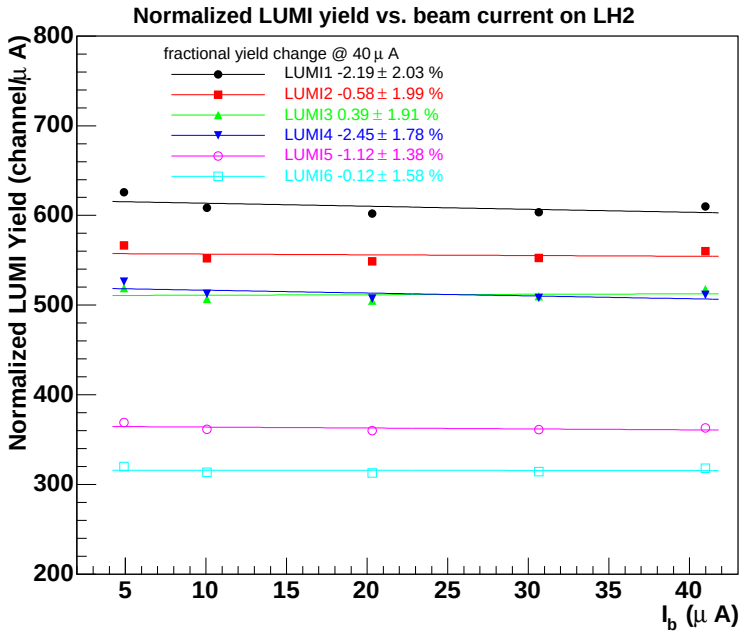

Figure C.9: *Same as Fig. C.6 but with liquid hydrogen target with nominal beam size and pump speed.*

decrease from 5 to 40 μA. The data points at 5 μA appear to be different from the trend of the others, which might be due to the non-linearity of the beam charge monitor at low current. One should also be aware that different LUMIs should in principle see the *same* target density reduction, so the different slopes measured by the six detectors in the figure is an indication of other systematic effects, such as the calibration of the pedestals of these detectors. The average slopes of the six detectors in the figure is $\sim -1.0 \pm 0.7\%$ and we take this as an estimate of the global target density reduction of hydrogen target under nominal running conditions. This is very small compared to the yield slope measured in the focal plane detectors (see Fig. 5.9(a)), which proves in turn that the yield reduction observed in the main FPDs is primarily due to electronic deadtime.

C.2.3.2 Target Density Fluctuations

As briefly discussed in Sec. 4.2.2, target density fluctuations can be controlled by varying the beam current, the rastered beam size on target, and the pump speed. The first two variables affect the boiling directly by changing the power density of the incident beam, and the last one controls the thermal mixing in the liquid, which indirectly affects the boiling.

At nominal running conditions (40 μA beam current, 2×2 mm^2 beam size, and 31 Hz pump speed), the width of the measured quartet asymmetry of each LUMI is $\sim$300 ppm. In Fig. C.10, the asymmetry histograms of LUMI1 with various beam sizes at a fixed 40 μA current and 31 Hz pump speed are overlaid. One clearly

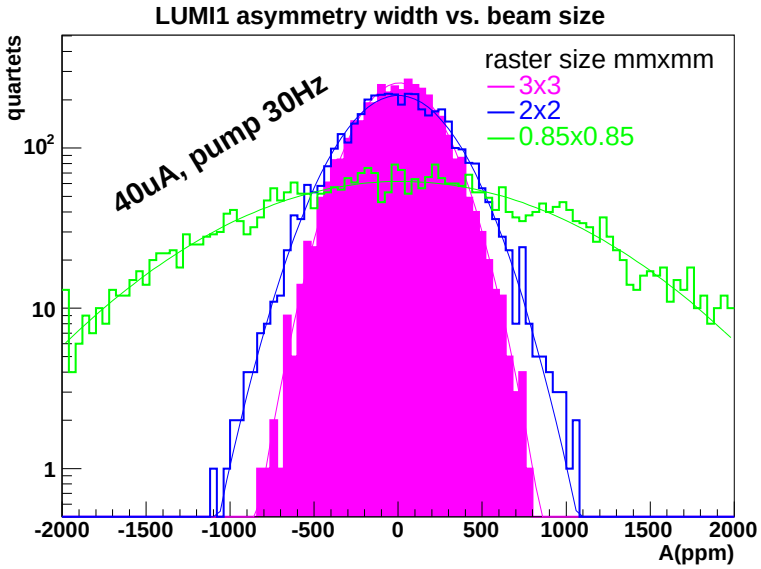

Figure C.10: *The asymmetry distributions of LUMI1 with various beam sizes on target under a fixed 40 μA of beam current and 30 Hz target pump speed. The widest green histogram is with a rastered beam size of* 0.85×0.85 *mm*^{2}*, whereas the blue (pink filled) histogram is that with the* 2×2 *mm*^{2} *(*3×3 *mm*^{2}*) beam size.*

sees that the asymmetry width with a 3×3 mm^2 beam size is the smallest, and it grows wider when the beam size decreases. Therefore the existence of some density fluctuations at the nominal running point (the blue "2×2" histogram in the figure) is without doubt.

The width of the measured asymmetry can be decomposed as

$$\mathcal{W}^2(A_m) = \mathcal{W}^2_{stat} + \mathcal{W}^2_{boil} + \mathcal{W}^2_{noise}\,. \tag{C.4}$$

In this equation, $\mathcal{W}_{stat}$ is the statistical width discussed in Sec. C.1.2, which has a characteristic $\frac{1}{\sqrt{I_b}}$ dependence. $\mathcal{W}_{boil}$ and $\mathcal{W}_{noise}$ are the contributions due to the target density fluctuation and other noise in the system, respectively.

Let us make some remarks about $\mathcal{W}_{noise}$. The 30 Hz electronic noise has been measured to be $\sim$0.09 mV, as compared to the typical signal size of $\sim$4.0 V. This noise contributes $\frac{\sqrt{4 \times (0.09\text{ mV})^2}}{4 \times 4\text{ V}} \sim 11$ ppm to the quartet asymmetry width. The noise due to fluctuations of the beam parameters can be estimated as follows. Let us define $\Delta p = p_1^+ + p_2^+ - p_1^- - p_2^-$ as the helicity correlated difference of a beam parameter p measured in a quartet, and the width of Δp is $\mathcal{W}(\Delta p)$. Then the contribution of $\mathcal{W}(\Delta p)$ to the quartet asymmetry width is $\frac{1}{4Y}\frac{\partial Y}{\partial p}\mathcal{W}(\Delta p)$. For the six beam parameters considered in Sec. C.2.2, the position differences contribute most significantly to the LUMI asymmetry width. Taking a typical value of $\Delta x =$ 15 μm and $\Delta y = 20$ μm, and assuming that $\frac{1}{Y}\frac{\partial Y}{\partial x}$ $\sim$1%/mm and $\frac{1}{Y}\frac{\partial Y}{\partial y}$ $\sim$0.5%/mm (see Fig. C.7), these two parameters alone lead to a 50 ppm contribution to the LUMI asymmetry width, which is small compared to a typical total LUMI width (300 ppm). We further note that the noise induced by these beam parameters can be in principle eliminated by linearly regressing the LUMI yield with respect to these six parameters. The noise due to other sources such as beam scraping or halos remains in the corrected width, and will have an unknown dependence on the beam current.

The key to extracting $\mathcal{W}_{boil}$ from Eqn. C.4 is to determine $\mathcal{W}_{stat}$ and $\mathcal{W}_{noise}$. We shall first demonstrate that $\mathcal{W}_{noise}$ is negligible after the linear regression, using a control measurement on a solid target. In Fig. C.11, the asymmetry widths measured with the aluminum frame target for LUMIs 1 and 4 are plotted against the beam current [†]. Since $\mathcal{W}_{boil} = 0$ for a solid target, the measured asymmetry width only

[†]The asymmetry measurements performed on the flyswatter target with 5 up to 40 μA of beam (see Fig. C.6) were with very low signal sizes ($\sim$ 10% of the typical signal size on hydrogen

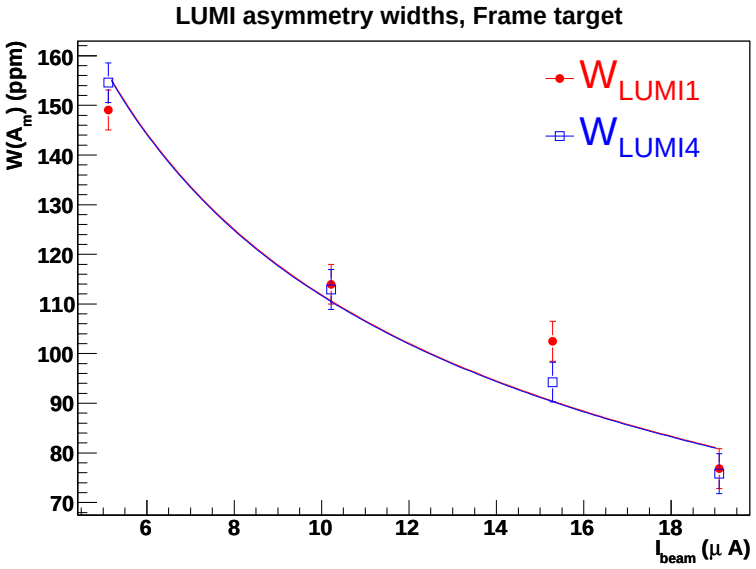

Figure C.11: *The measured asymmetry widths with the aluminum frame target for LUMIs 1 (red solid circles) and 4 (blue open squares) vs. the beam current. The beam current was limited to below 20 μA for this configuration. The counting statistics fits for both LUMIs are also overlaid.*

contains $\mathcal{W}_{stat}$ and $\mathcal{W}_{noise}$. The LUMI asymmetry was corrected using the standard linear regression correction (see Eqn. 5.70) with respect to the six beam parameters $(x, y, \theta_x, \theta_y, E_b, I)$. As an example, the widths of LUMI1 at 19 μA before and after this correction is 95 and 79 ppm, respectively. The corrected LUMI widths in Fig. C.11 are fitted with a counting statistics function $\frac{C}{\sqrt{I_b}}$, with C being a scaling variable, and one can see that the data do not exhibit significant deviation from the counting statistics curve down to a width of less than 80 ppm. Therefore, we conclude that the remaining $\mathcal{W}_{noise}$ in the corrected width is small and can be neglected in the following analysis.

To quantify the contribution of the hydrogen density fluctuation to the asymmetry width, we varied the beam current from 10 to 40 μA, the beam size from 0.85×0.85 mm^2 to 3×3 mm^2, and the pump speed from 31 to 42 Hz. As expected, the larger the beam size and the pump speed, the smaller the width of the asymmetry. Linear regression corrections were applied to the LUMI yields, and in some

target), therefore the contribution due to the electronic noise to the measured asymmetry width was significant. Those results are more difficult to interpret.

cases the corrected width is wider than the raw width; the lesser of the two was adopted. In Fig. C.12, the asymmetry width of LUMI5 under the nominal pump speed (31 Hz) and beam size (2×2 mm^2) is plotted against the beam current. The width of the asymmetry actually increases when the beam current grows above

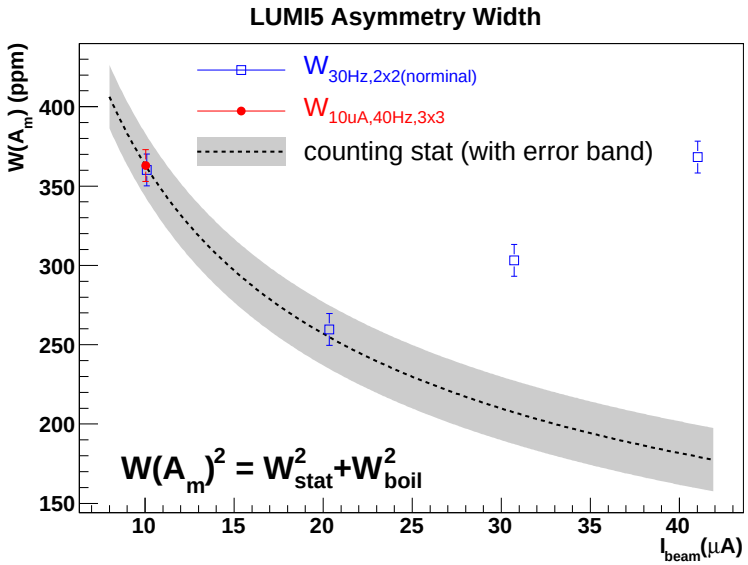

Figure C.12: *The measured asymmetry widths (blue open squares) of LUMI5 vs. the beam current, with rastered beam size of 2×2 mm^2 and 30 Hz pump speed. The red data point is that measured at 10 μA, 3×3 mm^2 beam size, and 42 Hz pump speed. The dashed curve is counting statistics curve extrapolated from the red data point with an estimated error band. See text for more explanation.*

20 μA, which is another demonstration of the effect of the boiling.

In [Cov04, Cov05], the determination $\mathcal{W}_{boil}$ was made by parameterizing $\mathcal{W}_{boil}$ as a function of the beam size, so that

$$\mathcal{W}^2(A_m) = \mathcal{W}^2_{stat} + \mathcal{W}^2_{boil}\,, \quad \mathcal{W}^2_{boil} \propto \frac{1}{s^x} \tag{C.5}$$

where s is the area of the rastered beam size, and x is a fitted parameter. In this work, we adopt an alternative approach by employing the counting statistics constraint on $\mathcal{W}_{stat}$. The starting point is the data at 10 μA, 3×3 mm^2 beam size, and 42 Hz pump speed, and we assume that $\mathcal{W}_{boil} = 0$ under these favorable conditions. The corresponding width of LUMI5 is shown as the solid data point in

Fig. C.12. Next, we assume that $\mathcal{W}_{noise}$ is also negligible at this point, so $\mathcal{W}(A_m) = \mathcal{W}_{stat}$, and the statistical width at any other beam current can be *extrapolated* based on the $\frac{1}{\sqrt{I_b}}$ relation. The extrapolated $\mathcal{W}_{stat}$ as a function of the beam current is overlaid in Fig. C.12 as the dashed curve. Under the further assumption that $\mathcal{W}_{noise}$ is negligible over the entire range, the boiling contribution can be calculated from the difference between the data and the curve as

$$\mathcal{W}_{boil} = \sqrt{\mathcal{W}^2(A_m) - \mathcal{W}^2_{stat}}\,. \tag{C.6}$$

Before presenting the results of $\mathcal{W}_{boil}$, let us first estimate the uncertainty of this extraction. The statistical precision of the measured asymmetry width is very small ($\sim<$ 5 ppm), therefore the uncertainty is dominated by the two "model" uncertainties: that associated with our assumption that the target does *not* boil at the "no boiling" conditions described above, and that due to the omission of $\mathcal{W}_{noise}$. The former uncertainty is estimated by using Eqn. C.5 to fit the asymmetry widths at 10 μA with different beam sizes when the pump speed was fixed at 31 or 42 Hz, similarly to the treatments in [Cov04, Cov05]. The value of x is assumed to be the same for the data with 31 and 42 Hz pump speeds, and we further demand that the extracted statistical $\mathcal{W}_{stat}$ for the two pump speeds is the same. The resulting values of x from the fits are 0.3$-$0.55, and the corresponding $\mathcal{W}_{stat}$ are 3 to 13 ppm lower than the measured width at the "no boiling" conditions for all LUMIs. Therefore 13 ppm is conservatively taken as an estimate of the systematic uncertainty for the "no boiling" assumption. The uncertainty due to the omission of $\mathcal{W}_{noise}$ is estimated to be $\sim$15 ppm, according to the largest deviation of the measured data from the counting statistics fit in the aluminum control measurement (see Fig. C.11). These two uncertainties are combined into an effective uncertainty to the counting statistics curve, displayed as the gray error band in Fig. C.12.

The resulting contributions of the target boiling to the LUMI asymmetry widths at 40 μA, with different raster sizes and pump speeds, are summarized in Table C.3. The last row in the table is obtained by treating the sum of the yields of

LUMI	31 Hz, 2×2	31 Hz, 3×3	42 Hz, 2×2	42 Hz, 3×3
1	260(13)	172(19)	207(16)	158(21)
2	267(12)	154(21)	209(16)	163(20)
3	269(12)	158(21)	199(16)	146(22)
4	260(12)	150(22)	183(18)	94(34)
5	322(11)	172(21)	230(16)	275(13)
6	290(12)	192(18)	249(14)	281(12)
Sum 1-4	265(12)	152(21)	195(17)	159(20)

Table C.3: *The extracted boiling contribution $\mathcal{W}_{boil}$ to the LUMI asymmetry width at 40 μA, with a beam spot size of 2×2 or 3×3 mm^2, and a pump speed of 31 or 42 Hz. All values are in units of ppm. The values in the parentheses are the uncertainties of $\mathcal{W}_{boil}$ under corresponding conditions. The last row represents the results by treating LUMIs 1 through 4 as a single detector. See text for more details.*

LUMIs 1 through 4 as a single detector. The uncertainty of $\mathcal{W}_{boil}$ due to the error band in Fig. C.12, is listed in the parentheses in the table. The agreement among LUMIs 1 through 4 is excellent, but some discrepancy exists between the upstream (1 through 4) and downstream (5 and 6) LUMIs, indicating the systematic uncertainty of this evaluation. The boiling contribution at the nominal running point (40 μA beam current, 2×2 mm^2 beam size, and 31 Hz pump speed), is estimated to be 264 ± 31 ppm, by averaging the values between LUMIs 1 and 4, with the half spread among all LUMIs as the uncertainty. This result is in agreement with that in [Cov04, Cov05] ($\mathcal{W}_{boil} = 238 \pm 65$ ppm).

Lastly, let us remark that target density fluctuations contribute to a common amount to the width of the asymmetries of all FPDs and LUMIs. The contribution of these fluctuations obtained here (264 ± 31 ppm) is negligible compared to a typical FPD asymmetry width in a given Q^2 bin ($\sim$1200 ppm).

BIBLIOGRAPHY

[AB40] L. W. Alvarez and F. Bloch, Phys. Rev. **57**, 111 (1940).

[Abe98] K. Abe et al. [E143 Collaboration], Phys. Rev. D **58**, 112003 (1998).

[ACG81] R. G. Arnold, C. E. Carlson and F. Gross, Phys. Rev. C **23** (1981).

[Ada97] D. Adams et al. [Spin Muon Collaboration], Phys. Rev. D **56**, 5330 (1997).

[Ada99] T. Adams et al. [NuTeV Collaboration], hep-ex/9906038. V. Barone, C. Pascaud, F. Zomer,hep-ph/0004268.

[Ahr87] L. A. Ahrens et al., Phys. Rev. D **35**, 785 (1987)

[Air98] A. Airapetian et al. [HERMES Collaboration], Phys. Lett. B **442** 484 (1998).

[Air05] A. Airapetian et al. [HERMES Collaboration], Phys. Rev. D. **71**, 012003 (2003).

[AM05p] J. Arvieux, F. E. Maas, private communications.

[AN05] J. Arvieux and S. Niccolai, *Electromagnetic radiative corrections*, G^0 Internal Document, G0-doc-608-v1 (2005); J. Arvieux, et al., Eur. Phys. J. A **26**, 429 (2005).

[Ani04] K. A. Aniol *et al.* (HAPPEX), Phys. Rev. C **69**, 065501 (2004).

[Ani05b] K. A. Aniol *et al.* (HAPPEX), nucl-ex/0506010.

[Ani05] K. A. Aniol *et al.* (HAPPEX), nucl-ex/0506011.

[Ant00] P. L. Anthony et al. [E155 Collaboration], Phys.Lett.B **493**, 19 (2000).

[ANW83] G. S. Adkins, C. R. Nappi and E. Witten, Nucl. Phys. B **228**, 552 (1983).

[Arm05] D. S. Armstrong *et al.* (G^0), Phys. Rev. Lett. **95**, 092001 (2005).

[Arr04] J. Arrington, Phys. Rev. C **69**, 022201(R) (2004).

[Arv01] J. Arvieux et al., *Deadtime Corrections for French Electronics*, G^0 Internal Document, G0-doc-199-v1 (2001).

[Arv03] J. Arvieux et al., *Simulations of the SOS data from December 1999*, G^0 Internal Document, G0-doc-374-v1 (2003).

[Arv05] J. Arvieux et al., *Towards a Common PVA4-SAMPLE Analysis: a First Step*, G^0 Internal Document, G0-doc-609-v1 (2005).

[Arv05b] J. Arvieux, private communications.

[ARZ05] C. S. An, D. O. Riska, and B. S. Zou, hep-ph/0511223 (2005).

[Ash89] J. Ashman et al. [European Muon Collaboration], Nucl. Phys. B **328**, 1 (1989).

[Ban97] H. R. Band, G. Mitchell, R. Prepost, T. Wright, Nucl. Instrum. Meth. A **400**, 24 (1997).

[Bar98] L. L. Barz, et al., Nucl. Phys. A **640**, 259 (1998).

[Bat03] G. Batigne et al., Q^2 *Determination in the First Phase of the G0 Experiment*, G^0 Internal Document, G0-doc-330-v1 (2003).

[Bat04] G. Batigne, *Mesure du contenu trange du nuclon : exprience* G^0, Ph.D. thesis, Universit Joseph Fourier, 2004. G^0 Internal Document, G0-doc-478-v1 (2004).

[Bay02] M. Baylac et al., *Jefferson Lab Polarized Source*, Proceeding of the International Workshop on Parity Violation, June 2002.

[BB03] J. Blumlein and H. Bottcher, Nucl. Phys. B **636**, 225 (2002).

[BBA03] H. Budd, A. Bodek and J. Arrington, arXiv:hep-ex/0308005.

[Bec89] D. H. Beck, Phys. Rev. D **39**, 3248 (1989).

[Bei04] E. J. Beise, *Interim report on hyperons*, G^0 Internal Document, G0-doc-610-v1 (2004).

[Bei05] E. J. Beise, M. L. Pitt and D. T. Spayde, Prog. Part. Nucl. Phys. **54**, 289 (2005).

[Bei05p] E. J. Beise, private communications.

[BEM02] V. Bernard, L. Elouadrhiri and U. Meissner, J. Phys. G **28** R1 (2002).

[Bev92] P. R. Bevington and D. K. Robinson, *Data Reduction and Error Analysis for the Physical Sciences*, second ed., McGraw-Hill, Boston, 1992.

[BH01] D. H. Beck, B. R. Holstein, Int. J. Mod. Phys. E **10**, 1 (2001)

[Bij95] J Bijnens, J. Prades and E. de Rafael, Phys. Lett. B **348**, 226 (1995).

[Bim02] L. Bimbot, Proceedings of the XVI International Baldin Seminar On High Energy Physics Problems, G^0 Internal Document, G0-doc-301-v1 (2002).

[Bis04] A. Biselli, *NA Deadtime Simulation*, G^0 Internal Document, G0-doc-502-v1 (2004).

[Bis05] A. Biselli, *Y0 Analysis*, G^0 Internal Document, G0-doc-611-v1 (2005).

[BJ89] See, e.g., R. Machleidt, in *Advances in Nuclear Physics*, Vol. 19, ed. J. W. Negele and E. Vogt, Plenum, New York (1989).

[BJM88] V. Bernard, R. L. Jaffe and Ulf-G. Meissner, Nucl. Phys. B **308**, 753 (1988).

[Bjo66] J. D. Bjorken, Phys. Rev. **148**, 1476 (1966)

[Bjo69] J. D. Bjorken and E. A. Paschos, Phys. Rev. **185**, 1975 (1969).

[Bre04] H. Breuer, G^0 Log Entry #74350 (2004).

[Bru97] R. Brun and F. Rademakers, NIM A **389** 81 (1997). More detailed information can be found at `http://root.cern.ch/`.

[Cab63] N. Cabibbo, Phys. Rev. Lett. **10**, 531 (1963).

[Car03] D. Carman et al., Phys. Rev. Letter. **90**, 131804 (2003).

[Cat05] G. D. Cates, Eur. Phys. J. A **24S2**, 109 (2005).

[CD71] T. P. Cheng and R. F. Dashen, Phys. Rev. Lett. **26**, 594 (1971).

[CFN93] T. D. Cohen, H. Forkel and M. Nielsen, Phys. Lett. B **316** 1 (1993).

[Che88] T. P. Cheng, Phys. Rev. D **38**, 2869 (1988).

[Cho74] A. Chodos, et al., A. Chodos, Phys. Rev. D **9**, 3471 (1974).

[Cla02p] R. Clark, private communications.

[Cla03] R. Clark and B. Quinn, *G0 Forward Angle NA electronics*, G^0 Internal Document, G0-doc-577-v1 (2003).

[Coa92] P. B. Coates, Rev. Sci. Instrum. **63** (3), 2084 (1992); D. A. Gedcke, *Dealing with Dead Time Distortion in a Time Digitizer*, ORTEC AN57 Application Note.

[Cor94] P. Corvisiero et al., Nucl. Instrum. Meth. A **346**, 433 (1994).

[Cov04] S. D. Covrig, *A Measurement of Parity-violating Asymmetries in the G^0 Experiment in Forward Mode*, Ph.D. thesis, California Institute of Technology, 2004. G^0 Internal Document, G0-doc-483-v1 (2004).

[Cov05] S. D. Covrig et al., Nucl. Instrum. Meth. A **551**, 218 (2005).

[DDS89] T. W. Donnelly, J. Dubach, and I. Sick, Nucl. Phys. A **503**, 589 (1989).

[DH98] J. F. Donoghue and B. R. Holstein, Phys. Lett. B **436**, 331 (1998); J. F. Donoghue, B. R. Holstein and B. Borasoy, Phys. Rev. D **59**, 036002 (1999).

[DLW98] S. J. Dong, K. F. Liu and A. G. Williams, Phys. Rev. D **58**, 074504 (1998).

[Don96] S. J. Dong, J. F. Lagae and K. F. Liu, Phys. Rev. D **54**, 5496 (1996).

[DP62] J. Dreitlein and H. Primakoff, Phys. Rev. **125**, 1671 (1962).

[Dre92] Drechsel and Tiator, J. Phys. G: Part. Phys. **18** (1992) 449-497.

[E158P] SLAC proposal E158, *A Precision Measurement of the Weak Mixing Angle in Møller Scattering*, (E. W. Hughes, K. S. Kumar and P. A. Sauder, cospokesperons), 1997.

[Ell95] J. R. Ellis, M. Karliner, D. E. Kharzeev and M. G. Sapozhnikov, Phys. Lett. B **353**, 319 (1995)

[ESW60] F. J. Ernst, R. G. Sachs, and K. C. Wali, Phys. Rev. **119**, 1105 (1960).

[Fei75] G. Feinberg, Phys. Rev. D **12**, 3575 (1975), Erratum-ibid.D **13**, 2164 (1976).

[Fey69] R. P. Feynman, Phys. Rev. Lett. **23**, 1415 (1969)

[Fey72] R. P. Feynman, *Photon-Hadron Interactions*, Benjamin Advanced Book Program, Readings, Masschusetts, 1972.

[For94] H. Forkel, M. Nielsen, X. Jin and T. D. Cohen, Phys. Rev. C **50**, 3108 (1994).

[For97] H. Forkel, Phys. Rev. C **56**, 510 (1997).

[FS33] R. Frisch and O. Stern, Zeit. Physik **85**, 4 (1933).

[Fur03] C. Furget, private communications (2003).

[FW03] J. Friedrich and T. Walcher, Eur. Phys. J. A **17**, 607 (2003).

[G0Bkw1] TJNAF proposal PR05-108, G^0 *Backward Angle Experiment*, (D. H. Beck, spokesperon), presented to JLab PAC 28 (2005).

[G0Bkw2] Update for TJNAF proposal PR05-108 to JLab PAC 29 (2006).

[G0Cer04] G^0 Collaboration, *Results from the G^0 engineering runs (answers to the certification questions)*, G^0 Internal Document, G0-doc-439-v1 (2004).

[G0GEA99] E. Rollinde, *G0-Geant Manual*, G^0 Internal Document, G0-doc-101-v1 (1999).

[G0NIM] R. Carr et al. (G^0 collaboration), in preparation for Nucl. Instrum. Meth..

[Gal71] S. Galster et al, Nucl. Phys. B **32**, 221 (1971).

[Gas84] J. Gasser and H. Leutwyler, Ann. Phys. (N.Y.) **158** 142 (1984).

[Gas85] J. Gasser and H. Leutwyler, Nucl. Phys. B **250** 465 (1985).

[Gas91] J. Gasser, H. Leutwyler and M. E. Sainio, Phys. Lett. B **253**, 252 (1991).

[Gas91b] J. Gasser, H. Leutwyler and M. E. Sainio, Phys. Lett. B **253**, 260 (1991).

[GEA94] CERN Program Library Long Writeup W5013, *GEANT, Detector Description and Simulation Tool Version 3.2.1* (1994).

[Gel55] M. Gell-Mann, Proc. 1955 Pisa Conf. on Elmentary Particles, Suppl. Nuovo Cimento **4**, 848 (1955).

[Gel64] M. Gell-Mann, Phys. Lett. **8** 214 (1964).

[GI97] P. Geiger and N. Isgur, Phys. Rev. D **55** 299 (1997).

[GLW93] G. T. Garvey, W. C. Louis, D. H. White, Phys. Rev. C **48**,761 (1993).

[Got00] Y. Goto et al, Phys. Rev. D. **62**, 034017 (2000).

[Gra00] J. M. Grames, *Measurement of a Weak Polarization Sensitivity to the Beam Obit of the CEBAF Accelerator*, Ph.D. thesis, University of Illinois at Urbana-Champaign, 2000.

[Gui04] B. Guillon et al., *Determination of the Yield Coming From the Target Walls Through an Experimental Approach*, G^0 Internal Document, G0-doc-444-v1 (2004).

[Gui05] B. Guillon, Ph.D. Thesis, LPSC-Grenoble, October 2005.

[Ham03] H.-W. Hammer, S. J. Puglia, M. J. Ramsey-Musolf and Shi-Lin Zhu, Phys. Lett. B **562**, 208 (2003).

[HamCa] Hamamatsu Catalogue, *Photomultiplier Tubes and Assemblies For Scintillation Counting & High Energy Physics.*

[Han04] L. Hannelius, *Beam position sensitivities from MC*, G^0 Internal Document, G0-doc-612-v1 (2004).

[Han04b] L. Hannelius, G^0 *GEANT Simulation Update*, G^0 Internal Document, G0-doc-458-v1 (2004).

[Han04c] L. Hannelius, private conversations.

[Han05] L. Hannelius, *Asymmetry Bin Correlations*, G^0 Internal Document, G0-doc-613-v1 (2005).

[Has00] R. Hasty et al. (SAMPLE), Science **290**, 2117 (2000).

[Hau01] M. Hauger et al, NIM A **462** 382 (2001).

[Haw98] E. A. Hawker et al., Phys. Rev. Lett. **80**, 3715 (1998).

[Het97] E. Hecht and A. Zajac, *Optics, 3rd Edition*, Addison-Wesley Publishing Company (1997).

[Hey94] G. Heyes et al., *The CEBAF On-line Data Acquisition System*, Proceedings of the CHEP conference (Apr. 1994), pp. 122-126. More detailed information at `http://coda.jlab.org/`.

[HF04] L. Hannilieus and C. Furget, G^0 Log Entry #74527 (2004).

[HKM99] T. R. Hemmert, B. Kubis and U. -G. Meissner, Phys. Rev. C **60**, 045501 (1999).

[HKS04] M. Hirai, S. Kumano and N. Saito [Asymmetry Analysis Collaboration], Phys. Rev. D **69**, 054021 (2004).

[HM84] F. Halzen and A. D. Martin, *Quarks and Leptons: An Introductory Course in Modern Particle Physics*, John Wiley & Sons, New York, 1984

[HMD96] H. W. Hammer, Ulf-G. Meissner and D. Drechsel, Phys. Lett. B **367**, 323 (1996).

[HMS98] T. R. Hemmert, Ulf-G. Meissner and S. Steininger, Phys. Lett. B **437**, 184 (1998).

[Hof55] R. Hofstadter and R. W. McAllister, Phys. Rev. **98**, 217 (1955).

[Hoh76] G. Hohler et al., Nucl. Phys. B **114**, 505 (1976).

[Hov96] C. Hovater et al., *The CEBAF RF Separator System*, Proceeding of the 16th International Linac Conference, Geneva, Switzerland, Aug., 1996.

[HR00] L. Hannelius and D. O. Riska, Phys. Rev. C **62**, 045204 (2000).

[HRG00] L. Hannelius, D. O. Riska and L. Ya. Glozman, Nucl. Phys. A **665**, 353 (2000).

[HRM98] H.-W. Hammer and M. J. Ramsey-Musolf, Phys. Lett. B **416**, 5 (1998).

[HRM99a] H.-W. Hammer and M. J. Ramsey-Musolf, Phys. Rev. C **60**, 045204 (1999).

[HRM99b] H.-W. Hammer and M. J. Ramsey-Musolf, Phys. Rev. C **60**, 045205 (1999).

[HS86] G. Holzwarth and B. Schwesinger, Rept. Prog. Phys. **49**, 825 (1986).

[HWDJ04] C. E. Hyde-Wright, K. de Jager, Ann. Rev. Nucl. Part. Sci. **54**, 217 (2004).

[Ito04] T. M. Ito et al., Phys. Rev. Lett. **92**, 102003 (2004).

[Jam94] F. James, CERN Program Library Long Writeup D506, *MINUIT, Function Minimization and Error Analysis Reference Manual, Version 94.1*, 1994.

[JM91] E. Jenkins and A. V. Manohar, Phys. Lett. **255** 558 (1991).

[Kaz04] Reza Kazimi et al., EPAC-2004-TUPLT164, Proceeding of the 9th European Particle Accelerator Conference (EPAC 2004), Lucerne, Switzerland, July 2004.

[Kee01] M. Keesee, R. Dickson and R. Flood, Proceedings of the 8th International Conference of the Accelerator and Large Experimental Physics Control Systems (ICALEPCS 2001), San Jose, California, Nov. 2001.

[Kel04] J. J. Kelly, Phys. Rev. C **70**, 068202 (2004).

[KHP92] W. Koepf, E. M. Henley and S. J. Pollock, Phys. Lett. B **288**, 11 (1992).

[Kit95] C. Kittel, Introduction to Solid State Physics, 7th edition, John Wiley & Sons (1995).

[KLZ67] N. M. Kroll, T. D. Lee and B. Zumino, Phys. Rev. **157**, 1376 (1967).

[KM88] D. B. Kaplan and A. Manohar, Nucl. Phys. B **310** (1988).

[KMAID] The theoretical references of the code, and a web-based calculator can be found at `http://www.kph.uni-mainz.de/MAID/kaon/kaonmaid.html`. The source code can be obtained from the author, Terry Mart.

[Kos02] M. V. Kossov, Eur. Phys. J. A **14**, 377 (2002).

[Kox05] S. Kox et al., Q^2 *Determination: Status Report*, G^0 Internal Document, G0-doc-543-v1 (2005).

[Jaf89] R. L. Jaffe, Phys. Lett. B **229**, 275 (1989).

[Law05] R. Lawall et al., Eur. Phys. J. A **24** (2) (2005).

[Lei05] D. B. Leinweber et al., Phys. Rev. Lett. **94**, 212001 (2005).

[Lei96] D. B. Leinweber, Phys. Rev. D **53**, 5115 (1996).

[Liu01] J. Liu and E. J. Beise, *Helicity Correlated Time Shift and the Asymmetry in G0*, G^0 Internal Document, G0-doc-221-v1 (2001).

[Liu02] J. Liu and E. J. Beise, *Studies of False Asymmetry and Deadtime Using G0 Mock Data*, G^0 Internal Document, G0-doc-221-v1 (2002).

[Liu05] J. Liu, *Detector 15 Background Asymmetry Correction and An Evaluation of the Systematic Uncertainties*, G^0 Internal Document, G0-doc-550-v1 (2005).

[Liu06] J. Liu, *G0 Hyperon background simulation*, G^0 Internal Document, G0-doc-552-v2 (2006).

[LLS02] E. Leader, A. V.Sidorov, D. B. Stamenov, Eur. Phys. J. C **23**, 479 (2002)

[LLS03] E. Leader, A. V.Sidorov, D. B. Stamenov, Phys. Rev. D **67**, 074017 (2003).

[LOC88] J. W. Lightbody and J. S. O'Connell, Computers in Physics, vol **2**, issue 3, 57 (1988).

[LS96] J. N. Labrenz and S. R. Sharpe, Phys. Rev. D **54**, 4595 (1996).

[LT00] D. B. Leinweber and A. W. Thomas, Phys. Rev. D **62**, 074505 (2000).

[LTW00] D. B. Leinweber, A. W. Thomas and S. V. Wright, Phys. Lett. B **482**, 109 (2000).

[LWW03] R. Lewis, W. Wilcox and R. M. Woloshyn, Phys. Rev. D **67**, 013003 (2003).

[LY57] T. D. Lee, J. Steinberger, G. Feinberg, P. K. Kabir and Chen-Ning Yang, Phys. Rev. **106**, 1367 (1957).

[Lyu02] V. E. Lyubovitskij et al., Phys. Rev. C **66**, 055204 (2002).

[Maa04] F. E. Maas *et al.* (PVA4), Phys. Rev. Letter. 93, 022002 (2004).

[Maa05] F. E. Maas *et al.* (PVA4), Phys. Rev. Letter. 94, 152001 (2005).

[Maa06p] F. E. Maas, private communications (2006).

[MAID03] D. Drechsel, S. S. Kamalov, L. Tiator, Nucl. Phys. A **645** 145 (1999). A web-based calculator can be found at `http://www.kph.uni-mainz.de/MAID/maid2003/maid2003.html`.

[Mar04] *Parity Violating Photoproduction of Negative Pions from Deuterium on the* Δ *Resonance*, (J. W. Martin, contact person), JLab PAC proposal (2004).

[Mar04p] J. W. Martin, private communications.

[Mar05p] D. Marchand, private communications (2005).

[Mat73] Matthews and Owens, NIM **111**, 157-168 (1973).

[Mck89] R. D. McKeown, Phys. Lett. B **219**, 140 (1989).

[MD01] N. Mathur and S. J. Dong, Nucl. Phys. Proc. Suppl. **94**, 311 (2001).

[Mei88] Ulf-G. Meissner, Phys. Rept. **161**, 213 (1988).

[Mei97] Ulf-G. Meissner, V. Mull, J. Speth and J. W. Van Orden, Phys. Lett. B **408**, 381 (1997).

[Mes05p] Mac Mestayer, private communications.

[MHD97] M. J. Musolf, H.-W. Hammer and D. Drechsel, Phys. Rev. D **55**, 2741 (1997).

[Mil98] G. A. Miller, Phys. Rev. C **57**, 1492 (1998).

[MK02] D. Marchand and P. King, Proceedings of the PAVI/2002 Conference, Mainz, June 2002.

[MM97] M. Malheiro and M. Melnitchouk, Phys. Rev. C **56**, 2373 (1997).

[MMD96] P. Mergell, Ulf-G. Meissner and D. Drechsel, Nucl. Phys. A **596**, 367 (1996).

[Mor01] M. Morlet, S. Ong and J. Van de Wiele, *Electroproduction Gnerator in the Forward Scattering Configuration of G^0 Experiment*, G^0 Internal Document, G0-doc-212-v1 (2001).

[MT69] L. W. Mo and Y. S. Tsai, Rev. Mod. Phys. **41** 205 (1969).

[Muk98] N. C. Mukhopadhyay et al., Nucl. Phys. A **633** 481 (1998).

[Mus94] M. J. Musolf et al., Phys. Rep. **239**, No. 1 (1994).

[MySQL] See http://www.mysql.com.

[Nak05] K. Nakahara, *Linear Regression Report for the Forward Angle Data*, G^0 Internal Document, G0-doc-556-v1 (2005).

[Nak05a] K. Nakahara, Eur. Phys. J. A **24S2**, 119 (2005).

[Nak05p] K. Nakahara, private communications, 2005.

[Nak06] K. Nakahara, Ph.D. thesis, University of Illinois at Urbana-Champion, in preparation.

[Nis53] K. Nakano and K. Nishijima, Prog. Theor. Phys. **10**, 581 (1953); K. Nishijima, Prog. Theor. Phys. **13**, 285 (1955).

[NJL61] Y. Nambu and G. Jona-Lasinio, Phys. Rev. **124**, 246 (1961).

[Ols00] M. G. Olsson, Phys. Lett. B **482**, 50 (2000).

[OM59] Olsen and Maximon, Phys. Rev. **114**, No. 3, 887 (1959).

[OZI63] S. Okubo, Phys. Lett. **5**, 165 (1963); G. Zweig, CERN Reports TH-401, TH-412 (1964), unpublished; J. Iiuzuka, Prog. Theor. Part. Sci. **37**, 21 (1966).

[Pas05] TJNAF proposal PR05-109, *A Measurement of Nucleon Strange Form Factors at High Q^2*, (K. D. Paschke, P. A. Souder, cospokespersons), presented to JLab PAC 28 (2005).

[Pat99] S. Pate et al., *Report of G0 120 Hz Task Force*, G^0 Internal Document, G0-doc-115-v1 (1999).

[Pav99] M. M. Pavan, R. A. Arndt, I. I. Strakovsky and R. L. Workman, nucl-th/9912034.

[PDG04] S. Eidelman et al., Phys. Lett. B **592**, 1 (2004) and 2005 partial update for the 2006 edition available on the PDG WWW pages `http://pdg.lbl.gov/`.

[Phi05] S. K. Philips, *Beam Polarization Numbers*, G^0 Internal Document, G0-doc-614-v1 (2005).

[Pre95] R. Prepost and T. Maruyama, Ann. Rev. Nucl. Part. Sci. **45**, 41 (1995).

[PS95] M. E. Peskin and D. V. Schroeder, *An introduction to Quantum Field Theory*, Perseus Books, Cambridge, 1995.

[PW92] N. W. Park and H. Weigel (Orsay, IPN), Nucl. Phys. A **541**, 453 (1992).

[Que05] G. Quemener et al., *Q2 Determination in the G0 Experiment*, G^0 Internal Document, G0-doc-548-v1 (2005).

[Qui03a] B. Quinn et al., *Requirements for Beam-Synched Signals for G^0*, G^0 Internal Document, G0-doc-331-v1 (2003).

[Qui03] B. Quinn, *North American Electronics Open Issues*, G^0 Internal Document, G0-doc-380-v1 (2003).

[Qui06] B. Quinn, private communications (2006).

[Rey74] E. Reya, Rev. Mod. Phys. **46**, 545 (1974).

[Rip97] G. Ripka, *Quarks Bound by Chiral Fields*, Clarendon Press, Oxford (1997).

[RMB94] M. J. Ramsey-Musolf and M. Burkardt, Z. Phys. C **61**, 433 (1994).

[RMH98] M. J. Ramsey-Musolf and H.-W. Hammer, Phys. Rev. Lett. **80**, 2539 (1998).

[RMI97] M. J. Ramsey-Musolf and H. Ito, Phys. Rev. C **55**, 3066 (1997).

[Roc02] J. Roche, P. King and J. Liu, *Booklet of the G0 Fastbus data*, G^0 Internal Document, G0-doc-576-v1 (2002).

[Roc02b] J. Roche et al., *Tests of the G0 North American Focal Plane Detector*, G^0 Internal Document, G0-doc-310-v1 (2002).

[Roc04] J. Roche, G^0 Log Entry #72695 (2004).

[Roc04p] J. Roche, private communications.

[Ros50] M. N. Rosenbluth, Phys. Rev. **79**, 615 (1950).

[RS74] E. Reya and K. Schilcher, Phys. Rev. D **10**, 952 (1974).

[RZ05] D. O. Riska and B. S. Zou, nucl-th/0512102.

[Sac62] R. G. Sachs, Phys. Rev. **126**, 2256 (1962).

[Sak69] J. J. Sakurai, Currents and Mesons, Univ. of Chicago Press (1969).

[Shi78] M. A. Shifman, A. I. Vainshtein and V. I. Zakharov, Phys. Lett. B **78**, 443 (1978).

[SKG02] A. Silva, H. C. Kim and K. Goeke, Phys. Rev. D **65**, 014016 (2002).

[Sky61] T. H. R. Skyrme, Proc. Roy. Soc. Lond. A **260**, (127) 1961; Nucl. Phys. **31**, 556 (1962).

[Son96] X. Song, P. K. Kabir, and J. S. McCarthy, Phys. Rev. D **54**, 2108 (1996).

[Spa00] D. T. Spayde *et al.* (SAMPLE), Phys. Rev. Lett. **84**, 1106 (2000).

[Spa01] D. T. Spayde, *Measurement of the Strange Magnetic Form Factor of the Proton Using Elastic Electron Scattering*, Ph.D. thesis, University of Maryland at College Park, 2001.

[Spa04] D. T. Spayde *et al.* (SAMPLE), Phys. Lett. B **583**, 79 (2004).

[Sch98] H. Schmieden, Eur. Phys. J. A 1, 427 (1998).

[Sta01] E. Stangland, R. Flood and H. Dong, G^0 *Helicity Digital Controls*, G^0 Internal Document, G0-doc-572-v1 (2001).

[TBWP] Time-Bandwidth Products, Switzerland, http://www.tbwp.com.

[Tei86] M. C. Teich, K. Matsuo, and B. E. A. Saleh, IEEE Journal of Quantum Electronics, Vol. QE-22, No. 8 (1986).

[Tra98] M. Q. Tran et al., Phys. Lett. B **445** (1998).

[Tsa74] Yung-Su Tsai, Rev. Mod. Phys. **46** 815 (1974).

[TTM80] S. Theberge, A. W. Thomas and G. A. Miller, Phys. Rev. D **22**, 2838 (1980); Phys. Rev. D **24**, 216 (1981).

[TW00] A. W. Thomas and W. Weise, *The Structure of the Nucleon*, Wiley-VCH, Berlin, 2001.

[Wal95] J. D. Walecka, *Theoretical Nuclear and Subnuclear Physics*, Oxford University Press, New York (1995).

[Wei79] S. Weinberg, Physica **96 A** 327 (1979).

[Wel04] *Measurement of the Parity Violating Asymmetry in the $N \rightarrow \Delta$ Transition*, (S. P. Wells, N. Simicevic, cospokespersons), proposal to JLab PAC 26 (2004).

[Wel04b] *Measuring the Two-photon Exchange Amplitude with Vector Analyzing Powers in Elastic Electron-proton Scattering*, (S. P. Wells, P. M. King, cospokespersons), proposal to JLab PAC 26.

[Wil64] W. Willy et al., Phys. Rev. Lett. **13**, 291 (1964).

[Wit79] E. Witten, Nucl. Phys. B **160**, 57 (1979).

[Wit83] E. Witten, Nucl. Phys. B **223**, 433 (1983).

[Won98] Samuel S. M. Wong, *Introductory Nuclear Physics*, 2nd Edition, John Wiley & Sons, New York, 1998.

[WSP91] N. W. Park, J. Schechter and H. Weigel (Syracuse U.), Phys. Rev. D **43**, 869 (1991).

[WT82] L. E. Wright and L. Tiator, Phys. Rev. C **26**, 2349 (1982), L. Tiator and L. E. Wright, Nucl. Phys. A **379**, 407 (1982).

[Wu57] C. S. Wu et al., Phys. Rev. **105**, 1413-1414 (1957).

[Yan03] C. Yan, *Hall C Reference: A Brief Description of the Hall C Beamline*, `http://hallcweb.jlab.org/document/howtos/beamline_optics/` (2003).

[Yan05] C. Yan, N. Sinkine and R. Wojcik, NIM A **539** 1 (2005).

[YM54] Chen-Ning Yang, R. L. Mills, Phys. Rev. **96**, 191 (1954).

[Zhu00] S. L. Zhu, S. J. Puglia, B. R. Holstein and M. J. Ramsey-Musolf, Phys. Rev. D **62**, 033008 (2000).

[ZR05] B. S. Zou, D. O. Riska, Phys. Rev. Lett. **95**, 072001 (2005).